UTS UNIVERSITY OF TECHNOLOGY SYDNEY

BEHAVIOUR OF REINFORCED ULTRA-HIGH PERFORMANCE CONCRETE COMPONENTS SUBJECTED TO LOW-VELOCITY IMPACT LOADING

by Jie Wei

Thesis submitted in fulfilment of the requirements for the degree of

Doctor of Philosophy

under the supervision of Doctor Jun Li and Professor Chengqing Wu

University of Technology Sydney
Faculty of Engineering and IT

September 2021

CERTIFICATE OF ORIGINAL AUTHORSHIP

I, Jie Wei declare that this thesis, is submitted in fulfilment of the requirements for the award of Doctor of Philosophy, in the School of Civil and Environment Engineering at the University of Technology Sydney.

This thesis is wholly my own work unless otherwise referenced or acknowledged. In addition, I certify that all information sources and literature used are indicated in the thesis.

This document has not been submitted for qualifications at any other academic institution.

This research is supported by the Australian Government Research Training Program.

Signature: Production Note:
Signature removed prior to publication.

Date: 10 September 2021

Abstract

Key load-bearing reinforced concrete (RC) members might be against accidental impact loadings during their service period. The impact resisting-performance of these structural components shall therefore be properly evaluated for accidental dynamic loads. To ensure the structural safety, there is an increasing need to improve the crashworthiness of key structural components which are at risk from dynamic impact loads. Ultra-high performance fibre reinforced concrete (UHPC) with superior mechanical properties and damage tolerance demonstrated good impact and blast resistance. As an emerging material with a specially formulated mixture, a thorough understanding of its mechanical performance against quasi-static and impulsive loadings is deemed necessary. Towards this aim, a series of well-instrumented experimental tests and high-fidelity numerical studies are conducted in this study. UHPC and its application in structural protective design against low-velocity lateral impact loads are systematically studied.

Chapter 1 presents the background, motivation, objective and outline of the current work.

Chapter 2 provides a literature review on current study of impact load induced structural responses of RC and UHPC members.

In Chapter 3, axially loaded UHPC and RC components with mono fibre reinforcement were tested against lateral impact loads. The drop weight test was carried out through a drop hammer collided the component from varying heights. UHPC components exhibited minor flexural damage, whereas RC components failed primarily by shearing. To further interpret the experimental data, associated numerical simulation was proposed. A Continuous Surface Cap Material model (CSCM) that

considered material triaxial strength, strain rate behaviour, compressive and tensile properties was developed for UHPC material. After numerical validation, the residual loading capacity of the UHPC members after impact loads was investigated through plenty of numerical tests. Impact mass-velocity (M-V) diagram and its equations were proposed to quick assess the damage of UHPC members.

After confirming the effectiveness of UHPC components in resisting the lateral impact loads, fibre reinforcement effect in UHPC was studied to achieve better cost-effectiveness. In Chapter 4, material property tests were conducted on UHPC with varying fibre reinforcing schemes. As compared to mono type fibre reinforcement, hybrid fibre reinforcement demonstrated better mechanical strength, especially the flexural strength. With notched three-point bending test results, tensile softening curves of UHPC were obtained, which was then used to quantify the fracture energy of UHPC strengthening with hybrid fibres. Then, the dynamic behaviour of RC members and UHPC members with mono and hybrid fibre reinforcement were experimentally characterized through the drop weight tests.

The high mechanical strength and material ductility of UHPC enables structural design with reduced section size and alternative reinforcement. New structural designs, including hollow-core UHPC columns, steel wire mesh reinforced UHPC columns, are investigated against impact loads in Chapter 5. The impact performances of these UHPC members were experimentally and numerically examined. With the validated numerical model, energy absorption curves, dynamic shear force and bending moment distribution diagrams were derived. Based on current data, the cracking and shear failure mechanisms of UHPC members were studied.

To date, the application of UHPC in construction is hindered by the raw material cost and lack of design guidelines. Towards a more effective use of UHPC in structural protective design, in Chapter 6, structural strengthening with UHPC overlay was investigated based on drop-weight impact testing. Bonded and unbonded UHPC overlay with the RC component was considered. While both designs can improve the shear resisting performance of RC components, the unbonded strengthening design prevented early tensile cracking in the UHPC overlay; hence maximised the impact resistance and energy absorption of the strengthening overlay.

Chapter 7 summaries the overall findings of the study and discuss future research work.

Acknowledgement

This doctoral thesis is the result of three and a half years of dedicated work with my supervisor, Doctor Jun Li, to whom I am incredibly grateful for his unwavering patience and guidance. I sincerely appreciate my co-supervisor, Professor Chengqing Wu, for his advice and contributions that greatly improved this work. I particularly thank Professor Hong Guan and Professor Xiaobo Qu who encouraged me to embark on this PhD journey. I also would like to acknowledge Futian Yang and Jie Li who generously offered their expertise and support. Lastly, my family, thank you for always being there.

List of Publications during the Candidature

Wei, J., Li, J., Wu, C., 2019. An experimental and numerical study of reinforced conventional concrete and ultra-high performance concrete columns under lateral impact loads. *Engineering Structures,* 201, 109822.

Wei, J., Li, J., Wu, C., 2020. Behaviour of hollow-core and steel wire mesh reinforced ultra-high performance concrete columns under lateral impact loading. *International Journal of Impact Engineering,* 146, 103726.

Wei, J., Li, J., Wu, C., Liu, Z., Li, J., 2021. Hybrid fibre reinforced ultra-high performance concrete beams under static and impact loads. *Engineering Structures*, 245, 112921.

Wei, J., Li, J., Wu, C., Liu, Z., Fang, J., 2021. Impact resistance of ultra-high performance concrete strengthened reinforced concrete beams. *International Journal of Impact Engineering,* 158, 104023.

Table of Contents

Chapter 1

Introduction

1.1 Background

Reinforced concrete (RC) components, including slabs, beams, and columns may be against dynamic loads (e.g., vehicle crashes, blasts, or terrorist attacks) during their service life. These types of loadings are often classified as low probability events, and as such are not considered in conventional design. However, the dynamic response triggered by these dynamic loads may lead to localized damage. Without an adequate robustness design, the local damage will spread after the sudden loss of one or more critical supporting elements, leading to damage of the disproportionally large or whole parts of structures [1].

Among various kinds of dynamic loadings, impact induced structural responses have been attracting lots of attentions since 20th century from the military to design protective structures against ballistic missiles. Then, the nuclear power industries have evaluated the effect of impact loads on RC members to protect nuclear power reactors. It is noted that, under impact loading, conventional concrete members with flexure design may suffer localized spalling damage, shear damage, flexural response or a combination of these failure behaviours [2]. Different failure modes are attributed to inertia effect, strain rate effect, contact stiffness among the impacting parts, loading rate effect, viscous damping and crack propagation [3]. The poor tensile properties of conventional concrete are the main reasons for the structural brittle damage under impact loads.

Extensive studies have been conducted to explore alternative constructional materials to overcome the brittle nature of conventional concrete. Among them, ultra-high performance concrete (UHPC) is an emerging mixture undergoing fast development over the past few decades. UHPC was firstly developed by Danish contractor Bache in the middle of the 1980s based on Compact Reinforced Concrete [4]. Later, French researchers Bouygues and Lafarge used Bache's idea to develop the new mixture, "Reactive Powder Concrete" (RPC) [5]. The design of RPC was used as commercialized UHPCs such as "Ductal". UHPC is normally characterized the superior compressive strength. Compared with conventional concrete, UHPC shows superior compressive strength, flexural strength and durability. Due to confining and bridging effect from the high content of steel fibres (around 1%-5% volume fraction), strain-hardening behaviour is commonly observed in UHPC in tension, leading to high tensile strength and ductility.

Recently, many studies have evaluated the effect of fibre reinforcement on the behaviour of UHPC. The properties of UHPC is affected through the volume fraction, fibre orientation, fibre aspect ratio, and fibre shapes [6]. While the static flexural performance of UHPC was improved with increasing the fibre volume fractions, the compressive strength was improved with increasing volumetric dosage up to 3 vol%, further increasing the fibre content enhanced its air content and decreased packing density and workability [7]. Different casting methods and different flow velocities also influence the flexural behaviour of UHPC mixtures since flow force and moments tend to rotate fibres parallel to the flow direction [8]. Flexural performance and fracture energy were enhanced on increasing fibre aspect ratio since longer fibre increased bonding area, causing a higher pull-out property [9]. In addition, fibre numbers mainly affected the post-cracking behaviour of UHPC and was insignificantly changed with

the fibre length at the identical volumetric ratio. For example, with the same volume fraction and fibre diameter, the per unit area numbers were 34.00/cm^2 for 13 mm fibres, 33.12/cm^2 for 16.3 mm fibres, and 35.79/cm^2 for 19.5 mm fibres [10]. It is reported that UHPC using deformed (twisted and hooked-end) fibres significantly enhanced the property, and its static tensile strength as well as static post-cracking strain capacity were importantly improved comparing to that with straight steel fibres [11]. However, recent studies have highlighted the incorporation of twisted fibres in UHPC structure under impulsive loading (i.e. impact and blast loading) was not as effective as straight fibres [12] because twist fibres were prone to fracture during dynamic pulling out process.

The commonly used steel fibres are the high unit cost of UHPC. For the typical UHPC reinforced with 2.5 vol% of straight steel fibres, the fibres cost most of the unit price. It is therefore necessary to improve the UHPC performance while keeping the fibre content at a relatively low level (1.5%-3%). Trial attempts were made using deformed fibres (i.e. hooked and twisted) and hybrid fibres. It was noted that UHPC with deformed fibres exhibits a better static flexural and tensile performance [11]. However, recent studies have highlighted the incorporation of twisted fibres in UHPC structure under impulsive loading (i.e. impact and blast loading) was not as effective as straight fibres [13]. Several studies reported that UHPC with hybrid long and short steel fibres could effectively enhance the flexural and tensile strength of UHPC [14-16].

The performance of UHPC structures against impulsive loading has been investigated extensively in recent years. It is noted that high fibre content and passive reinforcement ratio are favourable to the UHPC structural performance under both static and dynamic loading conditions [17-19]. However, it inevitably increases the cost

of UHPC. Therefore, the fibre volumetric ratio should be minimized for adopting the UHPC in the civil construction [20]. Considering the ultra-high compressive strength of UHPC, a hollow-core structural form could be adopted in the UHPC structural design, which provides a solution to reduce the cost. The application of hollow-core design in concrete members maximizes structural efficiency of strength-to-weight as well as the stiffness-to-weight ratio [21]. However, the steel bars' corrosion is a main problem for hollow-core concrete members owing to thinner walls than solid members. This limitation can be easily remedied by the use of UHPC, which has low permeability and very high durability. Alternative reinforcement like steel wire mesh is another solution to balance the cost and performance in UHPC structural design. The self-compacting nature of UHPC makes it possible to be cast into irregular shapes where continuous passive steel tendons are difficult to be applied. In some recent studies, steel wire mesh reinforcement is adopted to maximize the mechanical/physical benefits of UHPC. It is noted that wire mesh reinforcement promoted the localised membrane action to enhance impulsive loading resisting performance [22-24].

UHPC can be adopted as the strengthening or repairing material to extend the life of RC components and reduce the frequent maintenance. RC structural strengthening with UHPC overlays was first used in North America and Switzerland [25]. Several studies explored the effect of strengthening locations (upper or bottom) and layer depth [26, 27] on RC-UHPC beams. It highlighted that the maximum deflection enhanced with the depth of compression UHPC layers, whereas the flexural capacity increased with tension side depths; the flexural properties of beams strengthened on tension sides was superior to that of top strengthened beams. Recent studies have highlighted that UHPC layers strengthened on tension sides could effectively enhance the crack resistance, bearing capacity, rotation capacity and

fatigue resistance [28]. However, limited experimental studies were performed to explore the dynamic response and associated cracking mechanisms of RC beams strengthened by UHPC layers under impact loads.

1.2 Objectives

This study investigates the application of UHPC in structural protective design against impact loading. In the experimental design, UHPC columns with varying reinforcement and cross-section shape, UHPC beams with hybrid fibre reinforcement as well as UHPC strengthened RC components are tested against dynamic impact loads. Structural deformation and failure mechanisms are discussed, and in-depth evaluations of the structural behaviour are performed based on high fidelity numerical modelling. The specific objective is listed as below:

1. Investigate the impact-resistance of RC and UHPC columns; develop the material model and structure model to simulate the UHPC impact tests in LS-DYNA; establish damage criteria to quantify the impact-induced damage; derive the analytical equations for quickly assessing the damage of UHPC columns against low-velocity impact loads.

2. Explore the static compression and flexural properties of the UHPC mixtures with hybrid fibre reinforcement; develop the tensile softening curve and fracture energy of UHPC; study the effect of fibre hybridization on the impact-resisting behaviour of UHPC beams; investigate the dynamic behaviour of UHPC beams subjected to single and multiple impacts.

3. Evaluate the mechanical properties of UHPC with low fibre content; investigate the impact resistance of UHPC columns with new structural design, i.e. hollow cross-section and wire mesh reinforcement; study the failure mechanisms of designed

columns against impact loads; evaluate the influence of key structural parameters on column damage.

4. Study the material mechanical properties and interfacial bonding strength between UHPC and conventional concrete; evaluate the impact resisting performance of reinforce concrete beams strengthened with UHPC layers; investigate crack propagation and failure mechanisms of UHPC-RC beams against impact loading; evaluate the effects of key parameters on UHPC strengthening.

1.3 Outline

Chapter 1 presents research background, objectives and outline in this study.

Chapter 2 presents the literature review on the current investigation of impact load and associated influences on RC structures, UHPC properties, and the UHPC application in structural designs against impact loads.

In Chapter 3, drop hammer tests were conducted on reinforced concrete and UHPC columns. A concrete model was developed based on existing experimental data to simulate UHPC material in commercial software LS-DYNA. After numerical validation, the model was adopted to measure the residual loading capacity of the UHPC column after low-velocity impact loads. Finally, formulae for assessing UHPC column residual loading capacity were proposed through parametric studies.

In Chapter 4, the mechanical property tests were carry out to evaluate the effect of hybrid fibre reinforcement in UHPC. With notched three-point test results, tensile softening curves and fracture energy of hybrid fibre reinforced UHPC were determined through the inverse analysis. Finally, UHPC beams with different hybrid fibres were tested with a drop-weight impact testing machine to characterize the structural dynamic impact resistance.

In Chapter 5, mechanical property tests were conducted on UHPC with 1.5% and 2.5% fibre reinforcement. Drop weight tests and numerical modelling were carried out on UHPC columns with hollow cross-section and steel wire mesh reinforcement. The impact resisting behaviour and failure mechanisms were studied based on test results. Finally, a parametric study was conducted to evaluate the effect of key parameters on hollow-core UHPC columns and steel wire mesh reinforced UHPC columns.

In Chapter 6, RC and UHPC interfacial bonding strength tests were carried out. The RC-UHPC beams were tested under a drop weight test and a numerical model. Crack propagation analysis was conducted based on high-speed video recordings. Shear failure mechanisms were investigated based on experimental and validated numerical results. A parametric numerical study was conducted to evaluate the effects of key parameters on UHPC strengthening against low-velocity impact loads.

Chapter 7 summaries the overall findings of the study and discuss future research work.

Chapter 2

Literature Review

2.1 Impact Load and Its Effects on Reinforced RC Structures

2.1.1 Impact loads

Researchers have long been of interest to evaluate the impact phenomena on structures. The earliest research defined the impact phenomena as a missile collide a geological shield. The early studies proposed empirical models to relate the velocity of missiles and the penetration depth of geological shield [29]. The early investigation on RC structures against impact loads was conducted by the military during and after World War II. Extensive experimental studies were performed to design protective RC structures against ballistic missiles. Later, the demands of nuclear power industries made this topic essential and popular. Nuclear power reactors were required to resist accidental impact loads, such as vehicle collisions, aircraft crashes, and internal accidents including turbine and pipe breaks. Until the 1980s, the nuclear industries contributed to the numerous and systematic research dealt with impact problems. Though constructions of nuclear power factors have decreased ever since, knowledge accumulated and methodology proposed provide the basis of research that followed. Studies of the military and nuclear power industries focused on high-velocity impact loads (150 - 1000 m/s). The purpose of these studies was to propose equations or determining the thickness of structural members to keep the fortification structures at the desired level under a high-velocity impact loading. These studies mainly concentrated on conducting the experimental tests and proposing formulations based on a limited theoretical basis. However, these proposed formulations cannot be

adopted in current engineering constructions since they are limited in the range of experimental data.

Recent studies focus on RC structural members against low-velocity impact loadings from heavy objectives. For instance, RC columns in overpass bridges located near navigable waterways and mountain areas are prone to the impact loading effect of vessel collision and falling rocks, and RC beams are vulnerable to falling objects during the earthquake. In addition, with rising in the number of civil construction, the vehicle collision cases on RC structures have increased and been widely reported worldwide. Hartik et al. [30] reviewed 114 bridge failures in USA during the 38 years (1951-1988). It is noted that 17 (15%) accidents were induced by the vehicle collisions. Wardhana and Hadipriono [31] reviewed 503 accidents during 1989-2000 and noted that, out of 503 failures, 14 (3%) were caused by truck collisions. Fig. 2.1 presents two examples of such incidents. Hao [2] discussed possible failure modes of structures subjected to impact loads. Concrete members may experience flexural response, shear damage, spalling failure or a combination of these failure behaviour. Different failure modes are attributed to inertia effect, strain rate effect, contact stiffness between the impacting parts, loading rate effect, viscous damping and crack propagation [3].

Extensive research were carried out to cover impact loading influences on reinforced concrete structures. The objective of those studies is to build a theory for structural response/failure under impact loads.

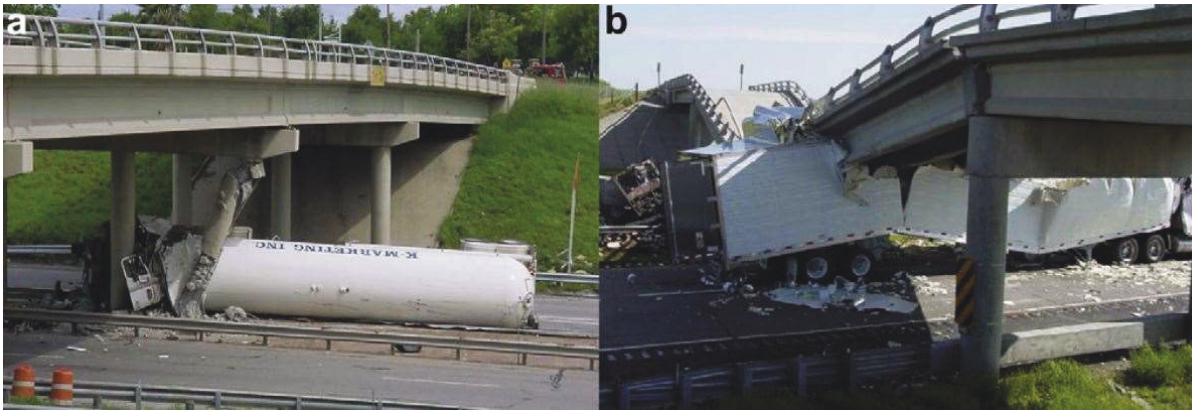

(a) Truck collision (Hartik et al. [30]) (b) Bridge collapse (Wardhana et al [31])

Fig. 2.1. Collapse of the bridge from vehicle collision

2.1.2 Flexure

2.1.2.1 Experimental and numerical study

One of the earliest experimental programs was conducted by Feldman et al. [32] to evaluate RC beams response against impact loads. Authors tested a total of 43 beam specimens, including ten specimens tested under the impact loading at mid-span, and the remaining specimens were tested under two-point loading. Various steel ratios were adopted in specimen design, whereas the grade of steel and concrete strength were kept the same. The beams were 2.44 m or 3.66 m in the span with a depth of 0.152 and a width of 0.305 m. Impact loading was applied through a pneumatic loading device. The authors concluded that the presence of even small amounts of reinforcement was important in the impact resistance of RC beams.

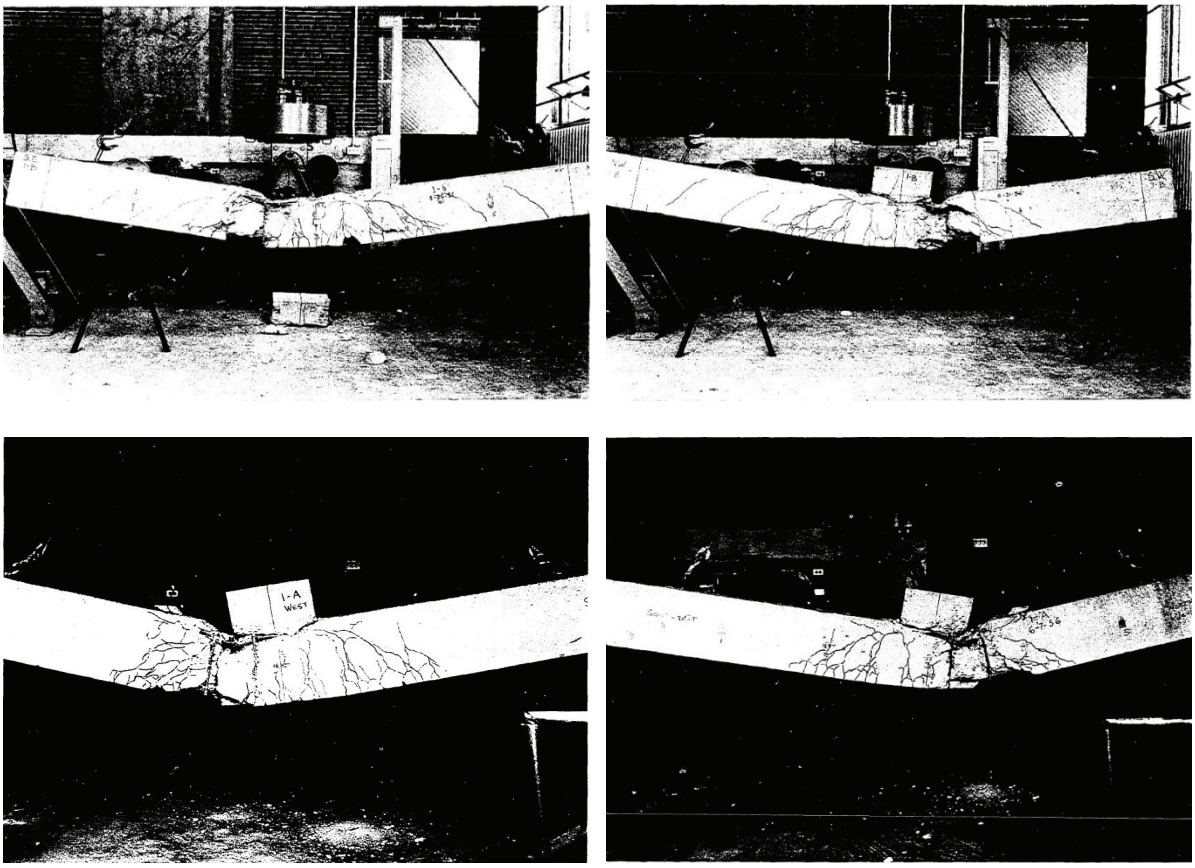

Fig. 2.2. Beam specimens after the impact tests (Feldman et al. [32])

Hughes and Beeby [33] conducted drop weight impact tests on reinforced concrete beams, including 12 simply supported and 8 pin-ended specimens. Two intenders including 60 kg and 100 kg were adopted, and impact velocities ranged from 2.1 - 7.9 m/s. It was noted that while most of the specimens experienced flexural failure, two specimens experienced shear failure with concrete spalling at mid-span under higher impact velocity. The results indicated that the high-velocity impact loading and low transverse steel ratio caused shear phenomena.

Kishi et al. [34] carried out drop hammer tests to estimate the ultimate strength of flexural-failure-response RC beam. The parameter E_a was determined through the area integration under reaction force and mid-span displacement curves. Then, the

authors proposed a parallelogram model (Fig. 2.3) to simplify reaction force versus displacement loops. By assuming a ratio of the maximum reaction capacity R_{ud} to static bending force P_{usd} of two. A ratio of the absorbed energy E_a to the input energy E_{kd} of 0.7, the relationship between the static bending capacity and absorbed energy as well as the residual displacement was derived as follow:

$$P_{usd} = E_a/(2.0\delta_{rd}) = 0.35\, E_{kd}/\delta_{rd} \quad (2.1)$$

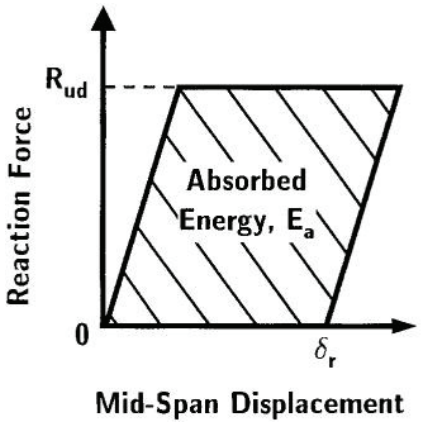

Fig. 2.3. The simplified parallelogram model (Kishi et al. [34])

Fujikake et al. [35] carried out drop-weight tests on 12 reinforced concrete beams. The test specimens was 1700 mm in length and with a cross-sectional dimension of 150 × 250 mm. Three types of deformed bars, including D13, D16 and D22, were adopted as longitudinal reinforcement within the specimens. The weight was 400 kg in mass and fell freely at the mid-span from four heights for each series specimen. It was noted that increasing compressive reinforcement enhanced the flexural resistance of beams against impact loads. With increased drop velocity, the impulse, the maximum force, the force duration, the peak mid-span displacement, and duration to reach the peak displacement were all increased. Authors highlighted that,

for RC beams showing flexural failure against impact loadings, the maximum mid-span deflection could be adopted for quantifying the damage of RC beams.

Chen and May [36] conducted a well-instrumented drop-weight impact program to investigate the behaviour of beams. The drop hammer was 100 kg in mass with a impact velocity of 8 m/s. Specimens were with a length of 3000 mm, 100 mm in width and 200 mm in depth. The test variations included the type of indenter (flat and hemispherical), the support condition (simply and pin ended supported) and the impact interface (directly impact and placed plywood at mid-span). It was noted that, for RC beams failed in flexural, the support had less effect on the impact force. The plywood interface could distribute the impact force at mid-span, which exhibited similar phenomena to the use of the flat indenter.

Tachibana et al. [37] proposed drop weight tests on beams. A total of 21 specimens were cast and divided by three cross-sectional dimensions (150 × 250 mm, 800 × 150 mm and 150 × 400 mm), three-span lengths (1000 mm, 2000mm, 4000 mm) and three longitudinal bars (D10, D13, and D16). Drop weight of various masses (150 kg, 300 kg, and 400 kg) was applied with a velocity varied from 1.1 m/s to 5.9 m/s. All test specimens showed flexural failure. Then, the numerical simulation on the quarter part of the test was carried out to further evaluate the influence of key effects. Based on experimental and numerical test results, the performance-based guidelines were developed. For considered beams with the static bending resistance ranging from 17 kN to 17 kN, and energy ranging from 200 J to 5500 J, the relationship between maximum displacement (δ_{max}, mm) and kinetic energy (E_{col}, J) as well as ultimate flexural resistance could be expressed as (P_{rd}, kN):

$$\delta_{max} = 0.522\, E_{col}/P_{rd} \tag{2.2}$$

In Eq. (2.1), the formulation was established based on two assumptions (absorbed to input energy ratio and reaction force to static capacity ratio). To overcome the drawbacks of the proposed formula and assess its adequacy, Kishi and Mikami [38] conducted the drop-weight impact tests on 36 RC beams. Test specimens varied in cross-sectional dimensions, beam length, reinforcement ratio and concrete strength. The drop weight was 400 kg, and impact velocities varied from 3.2 m/s to 7.7 m/s. It was noted that all test specimens demonstrated flexural failure; increasing input kinetic energy proportionally enhanced the maximum and residual displacements, whereas amplitude could be empirically formulated; a ratio of maximum to the residual displacement of 1.5 was proposed. For considered beams with the input kinetic energy (E, J) less than 15 kJ, flexural load capacity less than 240 kN and a ratio of flexural to shear resistance large than 0.67, the relationship between static flexural load capacity (P_{usc}, kN) and maximum (D_{max}, mm) as well as residual deflections (δ_{rs}, mm) could be expressed as:

$$P_{usc} = 0.42\ E/\delta_{rs} \tag{2.3}$$

$$P_{usc} = 0.63\ E/D_{max} \tag{2.4}$$

2.1.2.2 Analytical studies

Feldman et al. [32] proposed beam deflected in the certain displacement configuration, and this displacement shape at any time could be defined by a single coordinate. Based on the previous experimental observations, the whole drop hammer test system was regarded as a single degree of freedom (SDOF) system (Fig. 2.4). Then, by applying the impact force P on the mass, the equation of equilibrium could be expressed as follow:

$$M_e \times a = P - Q \tag{2.5}$$

where, M_e is equivalent mass; a is the acceleration of the equivalent mass; Q is the spring force; $Q = k\Delta$; k is spring stiffness; Δ is the displacement of the equivalent mass.

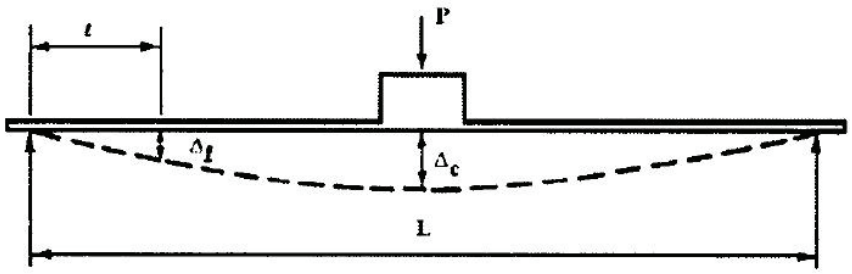

(a) Whole hammer impact system

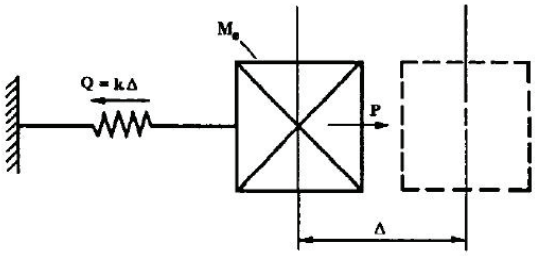

(b) Simplified single degree of freedom

Fig. 2.4. Schematic illustration of the SDOF (Feldman et al. [32])

To deal with the relationship of the displacement and the spring force, which is defined as the dynamic resistance-displacement relationship, Feldman et al. [32] adopted two methods. In the first method, the parameters in Eq. 2.5 could be measured and quantified. The authors adopted the derived spring force and the measured deflection to establish the dynamic resistance-displacement characteristics. In the second method, the authors derived the dynamic resistance-deflection relationship through iteration calculation. The bilinear relationship was first assumed,

and the response was numerically calculated. The iteration process was continued until the model data matched the test results.

Although assumptions and modelling techniques were diversified in the later studies, Comité Euro-international du Béton (CEB, 1998) [39] adopted the Feldman et al.'s method of idealizing the drop-hammer system into SDOF system, and the SDOF approach was widely adopted in the impact analysis. However, several limitations still existed in the application. First, the impact force-time history could not be obtained through the SDOF system since the indenter was simplified as the impact loads directly applied on the beams. Moreover, the resistance-deflection curves of specimens were required to be assumed based on experimental results or iteration analysis. Finally, the SDOF system was applied only for simple structures with flexural patterns and was unsuitable for complex structures.

Later, the SDOF method was developed into the two degrees of freedom (TDOF) method, which considers the drop hammer as a separate weight. As shown in Fig. 2.5, the governing equations of motion were expressed as follow:

$$\begin{aligned} &m_1\ddot{u}_1 + c_1\dot{u}_1 + k_1u_1 = R_2 \\ &m_2\ddot{u}_2 + R_2 = m_2g \\ &R_2 = k_2(u_2 - u_1) + c_2(\dot{u}_2 - \dot{u}_1) \end{aligned} \tag{2.6}$$

where, u_1, $\dot{u}_1$, and $\ddot{u}_1$ are the mid-span deflection, velocity and acceleration of the specimen; u_2, $\dot{u}_2$, and $\ddot{u}_2$ are the deflection, velocity and acceleration of drop hammer; m_1,and m_2 are the mass of the beam and drop hammer, respectively; c_1 and c_2 are the damping of the beam and drop hammer, respectively; k_1 and k_2 are the spring stiffness of beam and drop hammer, respectively. c_1 is usually not considered in the calculation. c_2 and k_2 were defined as follow:

$$c_2 = \sqrt{\frac{m_1 m_2}{m_1 + m_1}} k_2$$

$$k_2 = \frac{EV}{h} \tag{2.7}$$

where, E is the elasticity modulus; V is the penetration volume; h is the thickness of the target.

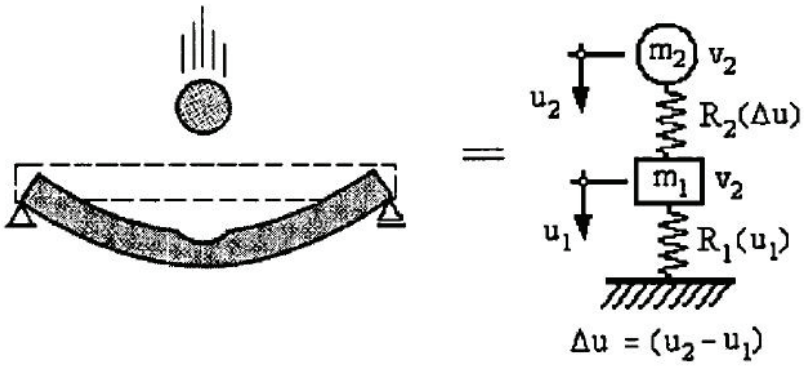

Fig. 2.5. Two degrees of freedom system (CEB [39])

Analytical methods to calculate the resistance-deflection relationship (spring stiffness of beam, k_1) considering strain rate behaviour at the material level has been proposed. Fujikake et al. [35] proposed the section analysis to develop the TDOF system. The RC beam section was divided into fibre elements, and several assumptions were made: (1) the plane section keeps plane after bending; (2) the relationship between concrete and steel is a perfect bond; (3) the shear deformation is ignored; (4) the strain and stress of each fibre element are constant during the calculation. As shown in Fig. 2.6, the beam section was divided into i-th fibre elements, and steel elements were divided into j-th fibre elements. Equations of equilibrium are expressed as follow:

$$N = \sum_{i=1} \sigma_{c.i}\, A_{c.i} + \sum_{j=1} \sigma_{s.j}\, A_{s.j} = 0$$

$$M = \sum_{i=1} \sigma_{c.i}\, A_{c.i} y_{c.i} + \sum_{j=1} \sigma_{s.j}\, A_{s.j} y_{s.j} \tag{2.8}$$

where, $\sigma_{c.i}$ and $\sigma_{s.j}$ are stress distributing on concrete and steel fibre element, respectively; $A_{c.i}$ and $A_{s.j}$ are the area of the concrete and steel fibre element, respectively; $y_{c.i}$ and $y_{s.j}$ are the spacing from the centroid of the concrete and steel fibre element to the neutral axis, respectively. The curvature-moment curve of beam specimens could be obtained by using eq. 2.8, and the curves were converted into the resistance-deflection relationship by using the equation:

$$\phi = \frac{M}{EI} = \frac{12}{L^2}\delta$$

$$P = \frac{4M}{L} \tag{2.9}$$

where, ϕ is the curvature; M is the moment; E is elastic modulus; I refers to moment of inertia; L refers to clear span; δ refers to mid-span displacement. Many researchers have verified the TDOF method by fitting the analytical data with experimental data [19, 35, 40, 41].

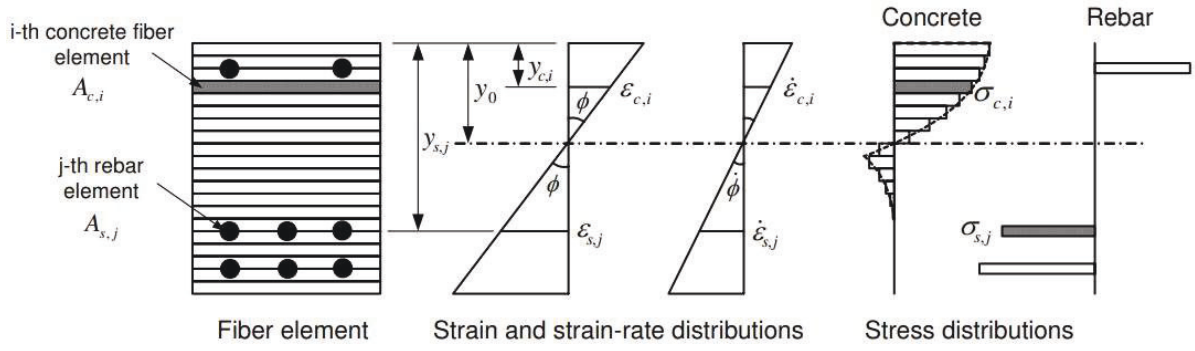

Fig. 2.6. Section analysis (Fujikake et al. [35])

In summary, numerous studies are conducted on RC members failed in flexure, and the flexural mechanism has been well studied. The performance-based TDOF approach is widely adopted in the impact analysis and could provide the RC members response under impact loading with reasonable accuracy.

2.1.3 Shear

As compared to flexural failure, limited research was carried out on the shear failure under dynamic loading. Kishi et al. [42] investigated the performance of 27 beams against impact loads through drop-weight tests. The test specimens had a depth of 150 mm and a width of 250 mm. Three lengths of clear span (1000 mm, 1500 mm and 2000 mm) and two rebar ratios (0.0182 and 0.008) were adopted within the specimens. The weight was 300 kg and fell at the mid-span, and impact velocity varied from 1.1 m/s to 4.9 m/s for each series specimen. It is noted that the beams experienced shear damage with designed shear to bending capacity ratio less than 1. E_a was determined by the area integration under reaction force and mid-span displacement curves. Then, the authors proposed a simplified model (Fig. 2.3) for reaction force versus displacement loops. By assuming a ratio of the maximum reaction capacity to the static shear resistance of 1.5 and, a ratio of the absorbed energy E_{ad} to the input kinetic energy E_{kd} of 0.6, relationship for required shear capacity V_{usd} versus residual displacement δ_{rd} was derived as follow:

$$V_{usd} = 0.8\, E_{kd}/\delta_{rd} \tag{2.10}$$

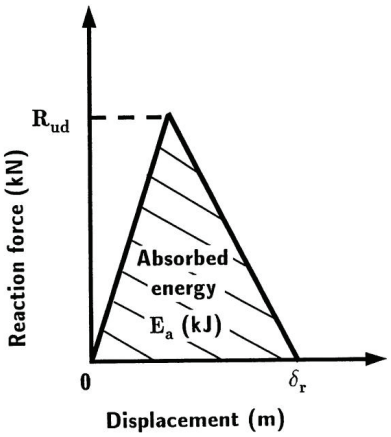

Fig. 2.7. The simplified model (Kishi et al. [42])

Saatci and Vecchio [43] characterised 8 beams under impact loads, and four control beams were tested under static loading. Two indenters with masses of 211 kg and 600 kg were adopted for the repeated impacts. The impact velocity was 7.9 m/s. All specimens were 4880 mm in length, 250 mm in depth and 410 mm in width. It was noted that beams experienced shear response with diagonal shear cracks developed at mid-span and formed a shear plug at mid-span. With the same energy, beam with high resistance could absorb more energy, whereas low with low resistance experienced severe localised failure. The authors highlighted that shear resisting capacity must be considered in the protective design. The developed performance-based SDOF and TDOF methods may not be applicable for predicting the shear response. At beginning, the impact force was resisted by the initial force prior to triggering the boundary reaction. The moving plastic hinges formed along the clear span cause the shear and bending moment diagram time varying, especially in the early contacting phase.

Zhao et al. [44] carried out a well-instrumented drop hammer programme to investigate the shear behaviour of 13 RC beams. The test specimens were 200 mm

in width and 500 mm in depth. The test variations included the beam span length (3000 mm and 5000 mm), the transverse reinforcement ratio (0.094% and 0.188%), the impact weight (848 kg, 1052 kg, 1300 kg, and 1700 kg) and the impact velocity (4.6 m/s, 5.56 m/s, 6.4 m/s and 7.14 m/s). Then, the authors developed the numerical simulation to further interpret experimental results. Based on both experimental and numerical observation, the shear crack patterns were divided into three levels as shown in Fig 2.8: (1) cracks forming a shear-plug at mid-span (Type 1); (2) inclined cracks in the shear span (Type 2); (3) a combination of both Type 1 cracks and Type 2 cracks. It highlighted that the loads concentrated at load area at beginning, causing that the diagonal shear cracks developed and eventually formed Type 1 cracks. For specimens with high shear-resisting capacity, the Type 1 cracks may not be adequately developed. In this situation, Type 2 cracks developed later than Type 1 cracks. Moreover, the increased transverse reinforcement ratio could effectively enhance the shear resistance.

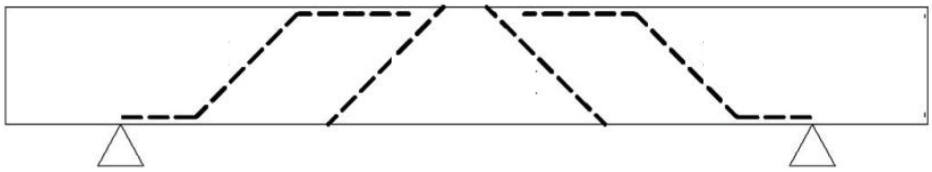

Fig. 2.8. Typical shear crack pattern (Zhao et al. [44])

Later, Zhao et al. [41] numerically conducted drop weight impact programme on beams. The developed models were compared the numerical data with test results. Then, the numerical model was adopted to evaluate effect of span. It was noted that, with the increasing of beam span, more obvious localization features were observed, which controlled the overall behaviour. Since the performance-based SDOF and TDOF methods were not applicable for predicting the localised shear failure, the

authors proposed a three degree of freedom method to evaluate the damage of shear-failure-modes RC beams. The total deformation of the beam was assumed as a mix of the overall flexural and shear plug deformation. As shown in Fig 2.8, the equations of motion are expressed as follow:

$$\begin{bmatrix} m_h & 0 & 0 \\ 0 & m_s & 0 \\ 0 & 0 & m_b \end{bmatrix} \begin{Bmatrix} \ddot{u}_1 \\ \ddot{u}_2 \\ \ddot{u}_3 \end{Bmatrix} + \begin{bmatrix} c_c & -c_c & 0 \\ -c_c & c_c + c_s & -c_s \\ 0 & -c_s & c_s + c_b \end{bmatrix} \begin{Bmatrix} \dot{u}_1 \\ \dot{u}_2 \\ \dot{u}_3 \end{Bmatrix} + \begin{bmatrix} k_c & -k_c & 0 \\ -k_c & k_c + k_s & -k_s \\ 0 & -k_s & k_s + k_b \end{bmatrix} \begin{Bmatrix} u_1 \\ u_2 \\ u_3 \end{Bmatrix} = \begin{Bmatrix} m_h g \\ 0 \\ 0 \end{Bmatrix} \tag{2.11}$$

where, m_h, m_s and m_b are the weight of drop hammer, shear plug and beam; u is the deflection; $\dot{u}$ is the velocity; $\ddot{u}$ is the acceleration; c is damping; k is the stiffness of spring. c_s and c_b are not considered in the study. c_c and k_c are defined as follow:

$$c_c = \sqrt{\frac{m_h(m_s + m_b)}{m_h + m_s + m_b}} k_c \tag{2.12}$$

$$k_c = \frac{EV}{h}$$

k_b is the resistance-displacement relationship of the specimen, which was calculated based on the section analysis. k_s is the resistance-displacement relationship of the shear plug. In their study, k_s was obtained from the finite element software, VecTor2. Although the authors have indicated the proposed model could predict the response of shear-failure-modes RC beams, more studies are required to develop the resistance-displacement relationship of the shear plug based on the theoretical basis.

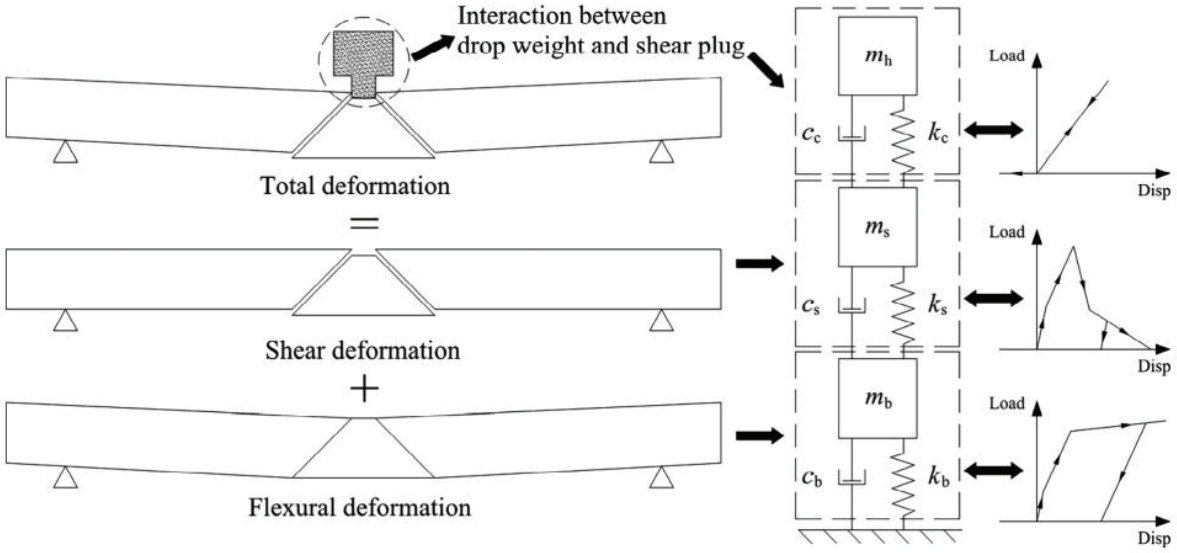

Fig. 2.9. Three degree of freedom system (Zhao et al. [41])

In summary, limited studies were proposed to evaluate the shear performance of RC members against impact loads, and mechanism of shear failure was not fully understood. The current design code AASHTO-LRFD [45] provided a constant value of 2700 kN for the shear resisting capacity on the RC members. However, the estimated static strength could lead to the overestimation of structural performance in real impact scenarios [43]. Systematic research on the shear mechanisms and strengthening methods to enhance the shear-resisting capacity are urgently required.

2.2 Ultra-high Performance Concrete

2.2.1 Material compositions and properties

Over the past few decades, UHPC emerges with superior compressive properties, flexural properties, ductility and durability. The typical composition of UHPC, including superplasticizer, micro fibres, water, fine sand, silica fume, cement, was different from that of conventional concrete in many ways.

For cement adopted in the UHPC mixtures, there are limited design codes in the literature. Wille et al. [46] recommended cement with a $d_{50} \approx 10$ μm for UHPC. Flatt and Houst [47] noted that a cement with a low-alkali (Na_2O and K_2O and) content can ensure a suitable slump life and workability. The normally applied cement in the UHPC mixtures was the low-alkali Portland cement with strength grades of 42.5 R and 52.5 R. Alkaysi et al. [48] investigated the influence of concrete type on mechanical strength. It is noted that the cement with strength grades of 42.5 R and 52.5 R could potentially provide high strength under a low water/binder ratio.

Ultra-fine silica fume was adopted to replace coarse aggregates in UHPC. Silica fume could fill intergranular space to achieve a higher density owing to its particle size (Fig. 2.9). The high pozzolanic reaction effect of silica fume could accelerate the hydration, leading to Calcium-Silicate-Hydrate products, and therefore enhance concrete strength, especially in the early stage. The importance of silica fume on the mechanical properties of mixture was widely investigated by many researchers [49, 50]. It was noted that increasing the content of silica fume enhanced the compression properties of UHPC. However, additional amount of silica fume should be mixed with more superplasticizer to ensure workability.

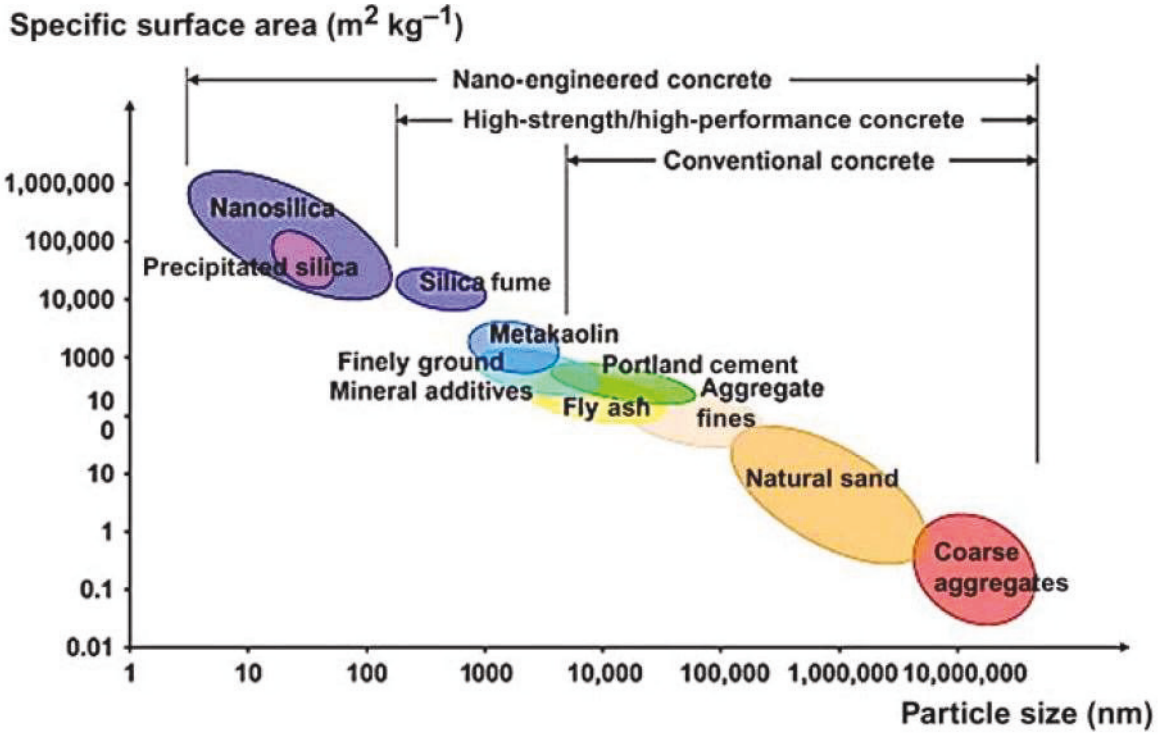

Fig. 2.10. Specific area and particle size of concrete material (Sanchez et al. [51])

Recently, nanoparticles have been adopted in mixture to enhance its performance. The addition of nanoparticles could provide a nanoscale filling effect and pozzolanic effect, resulting in importantly improving the compressive strength without changes of the major compositions. The normally applied nanoparticles in the UHPC mixtures were the nano-SiO_2 and nano-$CaCO_3$. Jo et al. [52] and Qing et al. [53] investigated the influence of additional nano-SiO_2 in the concrete mixture. It is noted that compression strength of mixture added with nano-SiO_2 was larger than control specimens. Liu et al. [54] and Nazari et al. [55] evaluated the performance of UHPC with nano-$CaCO_3$. It was concluded that the additional small amount of nano-SiO_2 could produce higher performance concrete. The filling effect of silica fume and nanoparticles could increase the relative density. The relationship of relative density and compressive strength for high strength concrete without fibre reinforcement is

shown Fig. 2.11. It is indicated that compression properties were enhanced with enhancing density.

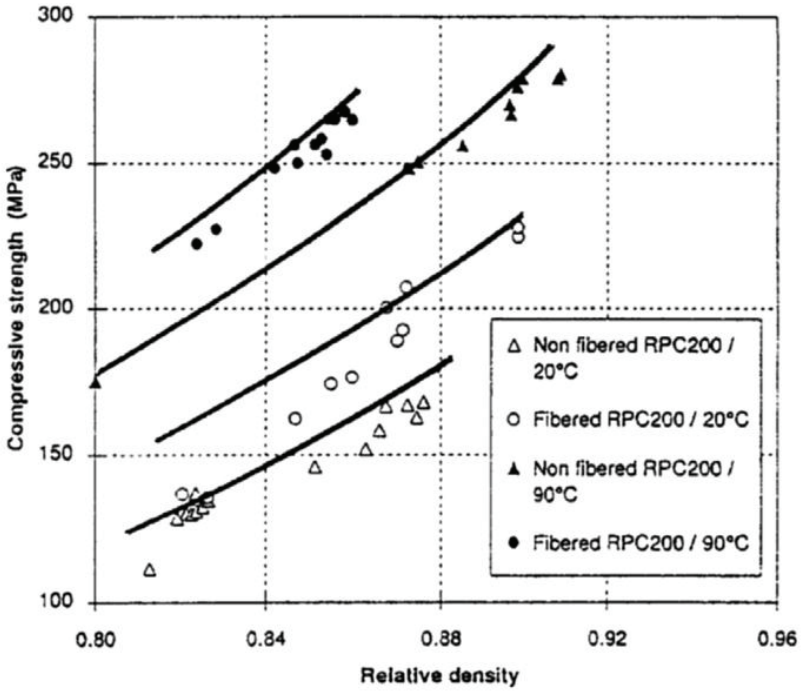

Fig. 2.11. Relative density versus compressive strength curves (Richard et al. [5])

In the UHPC mixture, steel fibres provide high bond-slip strength. When the mixture ruptures, the steel fibres could effectively control the crack development, and the bonding and friction between the mixture and the steel fibres could improve the ductility [6]. In general, due to confining and bridging effect from the high content of steel fibre (around 1% - 4% volume fraction), strain-hardening behaviour is commonly observed in UHPC in tension, leading to high tensile strength and ductility.

Different cast methods would affect the fibre orientation and the material properties. Boulekbache et al. [8] highlighted that different flow velocities rotated the fibres in the UHPC mixtures. In Fig. 2.12, forces were applied to the fibres, causing the fibres to rotate parallel to flow. Yang et al. [56], Ferrara et al. [57], and Kwon et al. [58] conducted UHPC beams with two cast methods: (1) the concrete was pouring at

mid-span and allowing it to flow to two ends of the mould; (2) the concrete was pouring at one side and flowing to the other side.

It is noted that the beams, whereas concrete pouring at one end, provided flexural strength around 15% higher than that pouring at mid-span because the followability of the UHPC provided the force to rotate the fibres parallel to the beam length. Wille and Parra-Montesinos [59] evaluated the effect of flow velocity and cast methods (middle cast and layer cast). It highlighted that increasing flow velocity could directly increase flexural performance; the layer cast method could form a preferred alignment in the thinner layer, which provided a higher flexural capacity.

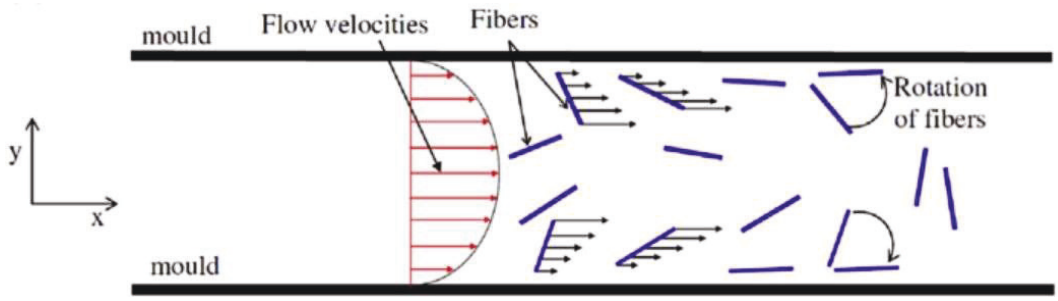

Fig. 2.12. Effect of flow velocity on fibre orientation (Boulekbache et al. [8])

UHPC commonly needs heat treatments at 85 °C for 48 hr to increase the pozzolanic effect of silica fume. However, at a construction site, UHPC is required to be cast in place, and it is difficult to provide a high temperature and moisture environment. Soliman and Nehdi [60] noted that temperatures over 40°C and humidity from 40% to 80% were essential for developing high compression properties. Wille et al. [61] adjusted the mixed proportions of UHPC to achieve high compression properties without heat treatments. It highlighted that the compression properties of the designed UHPC was related to $(w/c) \times air^{1/3}$; a ratio of sand to cement was 1.4;

a weight ratio of silica fume to cement was 0.25; a weight ratio of superplasticizer to cement was from 1.4% to 2.4%; and an optimum w/c ratio was 0.22.

2.2.2 Fibre effect

2.2.2.1 Fibre content

The effectiveness of fibres in enhancing the energy absorption capacity is dependent on the bond-slip behaviour affected by the volume fraction, fibre orientation, fibre shapes and fibre length [62, 63]. The effect of fibre volumetric ratio on the static material properties was studied extensively. Kang et al. [64] conducted experiments on UHPC prisms with various fibre volume fractions (from 0% to 5%). Increasing the fibre content was observed to improve static flexural performance. Yoo et al. [7] investigated mechanical performance of UHPC reinforced with various fibre volumetric ratios from 1% to 4%. It was noted that, increasing in volumetric ratio, ultimate flexural properties enhanced pseudo-linearly. However, the compressive strength and elastic modulus enhanced with the increase in fibre volumetric ratio up to 3 vol%. The mixture with 4 vol% fibre exhibited the poorest compressive performance. In addition, the specimen with 2 vol% fibre provided the best performance in fibre pull-out behaviour, whereas the pull-out properties of UHPC specimen with 3 to 4 vol% fibres were pseudo-linearly decreased. Grünewald [65] pointed out that the interaction force between aggregate and fibres and its packing density importantly decreased with increasing fibre content. Similarly, Yu et al. [66] noted that the increase in fibre content increased its air content and porosity and decreased the relative slump flow of UHPC.

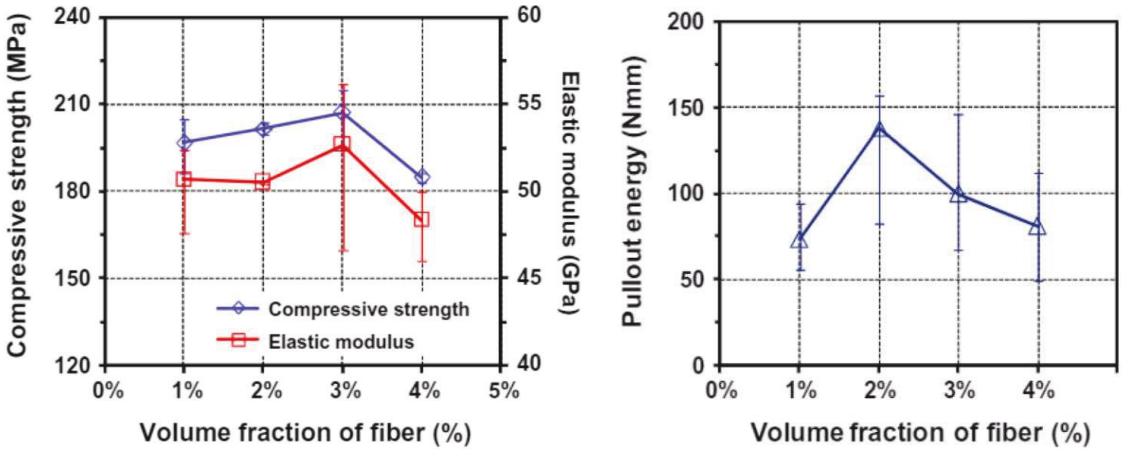

(a) Uniaxial compression tests (b) Pull-out tests

Fig. 2.15. Effect of fibre content on mechanical properties (Yoo et al. [7])

2.2.2.2 Fibre shapes

Recently, several studies were conducted to improve the UHPC performance while keeping the fibre content at a relatively low level (1.5%-3%). Trial attempts were made using deformed fibres (hooked and twisted) and increasing the aspect ratio of straight fibres. Wille et al. [11] revealed that UHPC reinforced with twisted fibres demonstrated higher tensile strength under static loading than UHPC with straight fibres even at a lower fibre volumetric ratio, e.g., UHPC with 1.5 vol% of twisted fibres showed similar tensile performance with UHPC with 2 vol% of straight fibres. Rossi [67] reported UHPC reinforced with twisted fibres had better performance in enhancing the flexural behaviour at static loading conditions than UHPC with hooked fibres since the frictional area of fibre affected the modulus of rupture. However, recent studies have highlighted the incorporation of twisted fibres in UHPC structure under impulsive loading (i.e. impact and blast loading) was not as effective as straight fibres [12]. Yoo et al. [9] experimentally studied the biaxial flexural properties of UHPC with three fibre lengths (13, 16.3, 19.5 mm). The long fibres were observed to have a better biaxial

flexural performance at a 2% fibre volume fraction. Further, Yoo et al. [68] also reported that long straight fibres could effectively improve the maximum and residual deflection capacity subjected to dynamic loads.

2.2.2.3 Hybrid fibres

Nowadays, limited studies investigated the hybrid use of fibres on the mechanical performance of fibre reinforced concrete (FRC). Dawood and Ramli [69] experimentally evaluated the influence of hybrid synthetic, steel, and palm fibres for dynamic tensile performance of FRC through free falling ball tests. Part of the steel fibres was replaced with palm or synthetic fibres, and the volume fraction was kept as 2% for all specimens. The specimens (1.75 vol% steel fibre + 0.25 vol% synthetic fibre and 1.75 vol% steel fibre + 0.25 vol% palm fibre) were found to have a better impact resistance than the SFRC specimen. However, with the more steel fibres replaced, the poorer impact-resistance was observed. Therefore, it is noted that when a small portion of steel fibres was replaced, hybrid fibres could retain a good level of impact resistance. Skazlic and Bjegovic [14] revealed that UHPC prisms with hybrid hooked and straight steel fibres displayed higher flexural strength than that with a single type of straight fibres with the same volumetric ratio of 3%. Kim et al. [15] reported influence of hybrid long and short fibres for mechanical behaviour of UHPC. Volume friction of macro fibres was fixed as 1%, and the volumetric ratio of micro-fibre increased from 0% to 1.5%. The prisms with hybrid fibres had greater displacement capacity and toughness than those with 1 vol% macro fibres. The improvement of flexural performance was attributed to the combined effect of fibre content and fibre hybrid. Yoo et al. [16] investigated the flexural properties of UHPC with the hybrid long (30 mm), medium (19.5 mm) and short (13 mm) straight steel fibres with a constant fibre

content of 2%. The hybrid fibres with long and short fibres were observed to deteriorate the flexural performance, whereas those with long and medium fibres improved flexural behaviour.

2.2.3 Dynamic material behaviour of UHPC

2.2.3.1 Dynamic compression response

The dynamic compressive behaviour of UHPC is well evaluated. Most of them measured dynamic compression strength by the split-Hopkinson pressure bar (SHPB) tests. Su et al. [13] evaluated the influence of nanomaterials for the UHPC dynamic compression response by group comparison. In their studies, the nanomaterials included nano-$CaCO_3$, nano-SiO_2, nano-Al_2O_3 and nano-TiO_2 with the same volumetric ratio of 3%. It was noted enhancing the strain rate could directly enhance compressive strength for all types of specimens; the addition of nano-$CaCO_3$ in the UHPC mixture presented the highest strain-rate sensitivity and biggest compressive strength increment. However, UHPC with nanomaterials was less sensitive than NC because the strain-rate sensitivity was less obvious in concrete with lower porosity [6]. In addition, fibre addition was noted to have an impact on the material rate sensitivity. Rong et al. [70] and Lai et al. [71] evaluated the influence of the fibre content for dynamic compressive response of UHPC. In the studies, fibre content ranged from 0% to 4%. It is noted enhancing the strain rate could directly enhance compressive strength for all types of specimens, and the highest strain-rate sensitivity of compression properties was UHPC without fibre reinforcement. As shown in Fig. 2.13, increasing the fibre content could effectively improve the maximum compressive stress, the maximum strain and strain capacity.

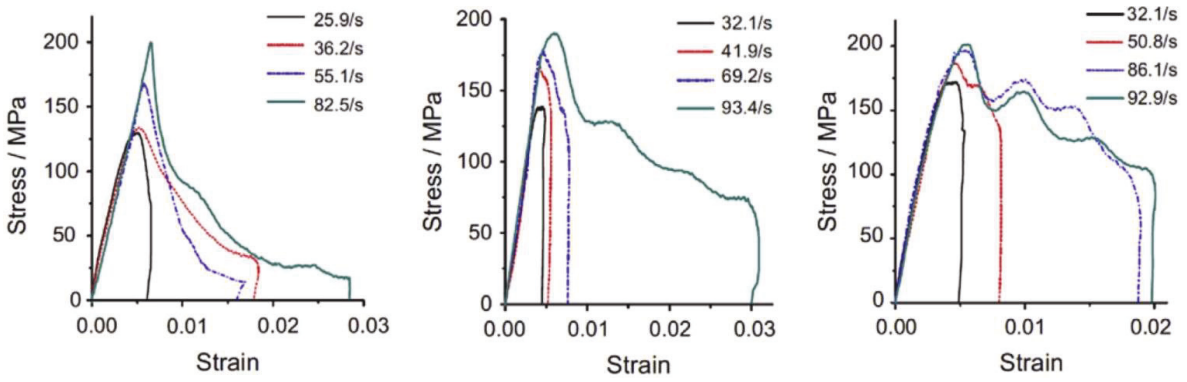

(a) UHPC with no fibres (b) UHPC with 3% fibres (c) UHPC with 4% fibres

Fig. 2.13. Dynamic compressive response (Rong et al. [70])

Fujikake et al. [72] given the equations of DIC of UHPC with a volume content of 2% fibres:

$$DIF = \frac{f'_{c,d}}{f'_c} = \begin{cases} \left(\frac{\dot{\varepsilon}}{\dot{\varepsilon}_{sc}}\right)^{0.0055\left[\log\left(\frac{\dot{\varepsilon}}{\dot{\varepsilon}_{sc}}\right)\right]^{0.951}} & \text{for } \dot{\varepsilon} \geq \dot{\varepsilon}_{sc} \\ 1 & \text{for } \dot{\varepsilon} < \dot{\varepsilon}_{sc} \end{cases} \quad (2.13)$$

where, $f'_{c,d}$ is dynamic compression strength; f'_c is static compression strength; $\dot{\varepsilon}$ is strain rate; $\dot{\varepsilon}_{sc} = 1.2 \times 10^{-5}$ /s.

2.2.3.2 Dynamic tension response

Douglas and Billington [73] conducted the monotonic tension tests to evaluate the dynamic tension behaviour for UHPC with strain rates ranged from quasi-static to 0.2 s^{-1}. It was noted tension behaviour of UHPC were influenced by the increased loading rate and the specimen geometry. Toutlemonde et al. [74] and Wille et al. [75] investigated the influence of the fibre content for the dynamic tension behaviour by fibre pull-out tests. It is observed that the volumetric ratio impacted the strain-rate sensitivity; with the increase in strain rate from 10^{-4} to 10^{-1} s^{-1}, the tension energy capacity and ultimate tensile strength increased by around 40% and 20%,

respectively. Tai et al. [76] and Tran et al. [12] evaluated the influence of the fibre types (straight and twisted fibres) on the dynamic tension behaviour. It was noted that under increasing strain rates, the tensile strength and strain capacity were greatly enhanced (Fig. 2.14). Although UHPC with twist fibres exhibited the higher static tension strength, UHPC with long fibres presented the higher dynamic tension strength, strain capacity and toughness, because the twist fibres were prone to fracture during the pull-out tests.

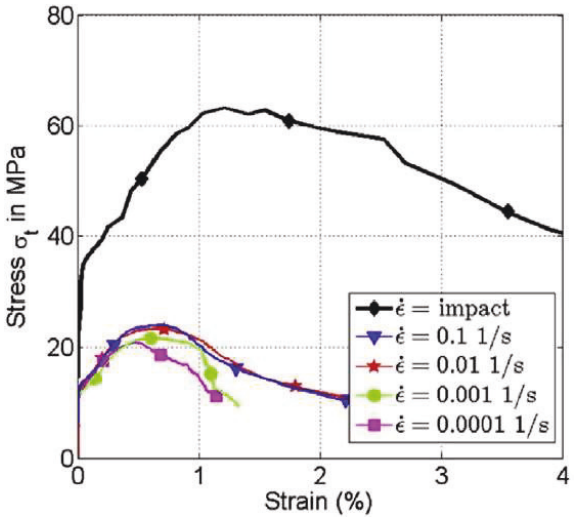

Fig. 2.14. Dynamic response for UHPC with straight steel fibres (Tran et al. [12])

Fujikake et al. [72] given the equations for DIC of UHPC with a volumetric ratio of 2% steel fibres:

$$DIF = \frac{f'_{t,d}}{f'_t} = \begin{cases} \left(\frac{\dot{\varepsilon}}{\dot{\varepsilon}_{st}}\right)^{0.0013\left[\log\left(\frac{\dot{\varepsilon}}{\dot{\varepsilon}_{st}}\right)\right]^{1.95}} & \text{for } \dot{\varepsilon} \geq \dot{\varepsilon}_{st} \\ 1 & \text{for } \dot{\varepsilon} < \dot{\varepsilon}_{st} \end{cases} \quad (2.14)$$

where, $f'_{t,d}$ is the dynamic tension strength; f'_t refers to static tension strength; $\dot{\varepsilon}$ refers to strain rate; $\dot{\varepsilon}_{st} = 1.0 \times 10^{-6}$/s.

2.3 Application of UHPC in Protective Design

2.3.1 UHPC components subjected to impact loads

Several studies have reported the UHPC members against impact loading experiments. Fujikake et al. [77] evaluated behaviour of five I-type UHPC beams against impact loads through drop hammer tests. The specimens were simply supported and were 1700 mm in length 150 mm in width and 250 mm in depth. The deformed bars with a diameter of 13 mm and yield strength of 296 MPa were adopted as longitudinal bars within specimens. The compression properties and Young's modulus were 214.7 MPa and 55 GPa, respectively. The drop hammer was 400 kg and fell at the mid-span from the releasing height ranged from 0.8 m to 1.6 m. It is noted that all specimens presented the typical flexural failure; increasing drop velocities would proportionally increase the mid-span deflection. Then the authors developed the performance-based TDOF with considering strain rate behaviour of UHPC material. The analytical results matched the experimental results with reasonable accuracy.

Yoo et al. [19] carried out a well-instrumented drop hammer programme to study the impact behaviour of four UHPC beams. The drop hammer was 270 kg with a velocity of 5.6 m/s. Test specimens were simply supported and were 2900 mm in length, 200 mm in width and 270 mm in depth. The test variations included four reinforcement ratios (0%, 0.53%, 1.06% and 1.71%). The compression and tension strengths of UHPC were 200 MPa and 17.7 MPa, respectively. The diameter and yield strengths of longitudinal bars were 12.7 mm and 630 MPa. It is observed that all specimens exhibited the flexural response; enhancing the steel ratio provided the enhancement of impact resistance; the UHPC beams with higher steel ratio presented lower maximum and residual mid-span deflection. Then, the authors developed the

SDOF method considering the material stain rate effect to provide displacement-time response for UHCP beams. The analytical predicted the maximum deflection accurately matched the test data. However, the calculated time at the ultimate deflection was faster than the experimental values.

Fan et al. [78] carried out drop hammer program to evaluate the impact performance of UHPC columns through adopting the drop-weight test system. 8 large-sized columns were cast and tested, including two UHPC columns, three different UHPC strengthened RC columns, and three control RC columns. The steel weight was 568 kg falling freely at the mid-span. The specimens had a span of 2200 mm and a circular cross-section diameter of 200 mm. The test variations included concrete perperties (150 MPa for UHPC and 30 MPa for conventional concrete), two longitudinal ratios (0.96% and 1.92%), two transverse ratios (0.72% and 1.3%), three axial load levels, (0, 200, and 400 kN) and two impact velocities (4.42 m/s and 6.86 m/s). It is noted that UHPC could effectively improve the shear resisting capacity since RC columns experienced severe localised damage while UHPC columns showed flexural response under the same impact energy; increasing the axial loads improved the compressive membrane action, resulting in the increment of impact resistance; applying the UHPC jacket in the impact zone could enhance the impact resistance, but the shear failure was still triggered in the remaining part of the specimens without UHPC jacket strengthening. Then, the authors developed FE models to reproduce the impact hammer tests on UHPC columns. The CSC material model considering strain-rate behaviour was proposed for UHPC. The developed modelling matched experimental results with reasonable accuracy.

Xu et al. [79] reported the dynamic behaviour of two RC and UHPC columns. Deformed bars with 12 mm diameter and yield strength of 500 MPa were applied as

longitudinal bars. Stirrup bars were roller plain bars with a 10 mm diameter and 500 MPa yield strength. The drop hammer was 400 kg with an velocity of 5.42 m/s. The protective closed-cell aluminium foam (CCAF) layer with a length of 400 mm and a cross-sectional size of 75 × 165 mm was applied for both the RC and UHPC columns. It is observed that the addition of CCAF protective layer on the RC columns shifted the failure modes from the shear damage for RC members to the flexural-shear failure; the UHPC column presented superior crashworthiness with the failure modes shifted from the shear damage for the RC column to the flexural response for the UHPC column; the UHPC column with the CCAF layer presented the highest impact resistance. Then, the authors developed the numerical simulation to further interpret experimental results. The K&C material model was utilized in the LS-DYNA software. The proposed models were validated with measured results. The paramedic results highlighted that CCAF layer thickness was significantly influenced the target dynamic behaviour under impact loading. However, the application of the CCAF layers are carefully choose for cost-effective design.

Jia et al. [80] evaluated the dynamic response of 11 reinforced UHPC columns and two control RC columns under impact loading through the low-velocity lateral impact machine. The steel weight was 568 kg falling freely at the mid-span. The specimens had a span of 2200 mm and a rectangle cross-section size of 300 mm. The deformed bars with a diameter of 22 mm and yield strength of 368 MPa were adopted as longitudinal reinforcement within the specimens. The compressive strength and Young's modulus were 148 MPa and 48.6 GPa, respectively. The test variations included impact velocity ranged from 6.26 m/s to 8.85 m/s and the axial force level from 140 kN to1400 kN. It highlighted UHPC members presented outstanding impact-resistance since RC columns experienced shear failure while UHPC columns

experienced minor flexural damage; both impact energy and axial loads had significant effects on the performance of UHPC beams against the impact loads. Then, the authors developed the CSC model based on the constitutive model and strain rate effect to simulate UHPC material in LS-DYNA. The proposed CSC model was verified by all current drop hammer tests on UHPC members.

2.3.2 Structural strengthening with UHPC

2.3.2.1 Hollow-core structural design

In previous construction practices, hollow-core concrete members are applied widely for bridge design. The use of hollow-core design in concrete columns maximizes structural efficiency for strength-to-weight as well as the stiffness-to-weight ratio [21]. These columns required lower carrying demand on the foundation, consequently decreasing application costs. Many researchers studied performance of hollow-core concrete members, including flexural and shear strength as well as ultimate axial strength [81-83]. It is evident that the hollow core is primarily responsible for the low axial loading capacity and also the different structural behaviour when compared with solid columns. In addition, steel bars' corrosion is a problem for hollow-core concrete members because their thinner walls than solid columns. These limitations of hollow-core concrete columns can be easily remedied by the use of UHPC instead of conventional concrete

2.3.2.2 Structural design with steel wire mesh reinforcement

The self-compacting nature of UHPC makes it possible cast components into irregular shapes where continuous passive steel tendons are difficult to be applied. In some recent studies, steel wire mesh reinforcement is adopted to maximize the

mechanical/physical benefits of UHPC. Nie et al. [84] tested the flexural behaviour of steel wire mesh reinforced beams. It is noted that beams exhibited a better flexural properties. Due to the contribution of steel wire mesh, the structure stiffness was enhanced, and fewer cracks were observed. Huang et al. [22] adopted steel wire mesh to strengthen the RC T-type beam. It is found that the stiffness, ductility of the members were increased owing to steel wire mesh strengthening. Li et al. [23] conducted investigations on wire mesh reinforced slab against the explosion loading. It is noted that wire mesh promoted the localised membrane action to enhance the blast resisting performance. Meng et al. [24] tested RC slabs and steel wire mesh reinforced geopolymer slabs with a dimension of 1300 × 1300 × 100 mm. These slabs were exposed to 50 kg of equivalent TNT at the standoff of 3~7 m. It is observed wire mesh reinforced geopolymer concrete slab demonstrated less concrete failure.

2.3.2.3 UHPC strengthened RC members

RC structural strengthening with UHPC overlays was first developed in North America and Switzerland [25, 85]. Brühwiler et al. [86] and Habel et al. [87] experimentally tested large-sized RC-UHPC subjected to four-point loading. It was found that the UHPC layer enhanced the service condition stiffness, effectively restrained the development of cracks, and increased flexural capacity. Safdar et al. [27] conducted four-point flexural tests on composite RC-UHPC beams to investigate the effect of strengthening locations (upper or bottom) and layer depth. It was noted that the flexural capacity increased with the tension layer depth, and flexural behaviour of bottom strengthened beams was superior to that of top strengthened beams. Yin et al. [88] and Paschalis et al. [89] carried out studies to investigate the flexural behaviour of RC beam with UHPC layers on the tension side. The test results demonstrated that

UHPC layers significantly increased the crack resisting performance and stiffness of RC beams; increasing layer depth of UHPC could effectively enhance flexural capacity; a small value of interface slip proved effective interfacial bonding between UHPC and NSC. Noshiravani et al. [28] explored the bearing capacity of RC-UHPC beams. The test results indicated addition of UHPC layer increased structural rotation capacity; the capacity of the beam carrying the redistributed stresses was dependent on both steel reinforcement and interfacial bonding strength. Murthy et al. [90] evaluated the performance of RC-UHPC beams under fatigue loading. The maximum number of cycles to failure of RC-UHPC beams under fatigue was indicated to be importantly larger than that of control RC beams. The UHPC layers improved the ductility and fatigue resistance of RC beams against cyclic loads. Al-Osta [91] experimentally studied the flexural properties of RC-UHPC composite beams with two interface preparation methods (i.e. by sandblasting surface and smooth surface with an epoxy adhesive). The specimens under each technique were strengthened by three strengthening configurations, including tensile side, two longitudinal sides and three sides (both tensile side and two longitudinal sides) strengthening. It was found that there was no significant difference between two interface preparations technique, however, the sand blasted surface strengthening beams demonstrated an overall better flexural performance. Moreover, the RC beams with UHPC layers strengthening at three sides exhibited the highest flexural capacity improvement.

2.4 Summary and Identification of the Gap

This chapter presents a general review of current impact studies of reinforced concrete members. It can be concluded that the flexural behaviour of RC members against impact loading are well learned. The corresponding performance-based

analytical studies can predict the response of RC members under impact loading with reasonable accuracy. However, limited studies were carried out to investigate dynamic performance of shear-failure-modes RC beams, and the mechanism of shear failure was not fully understood. With high volume micro fibre reinforcement, UHPC shows greatly improved tensile properties, both of which favour the flexural and shear resisting capacity. Hybrid long and short steel fibres could effectively favour the static energy absorption capacity of UHPC. However, fewer studies were carried out on the structural performance of UHPC members with hybrid fibres under dynamic loadings. Although several studies were carried out to investigate the dynamic performance of UHPC members, failure mechanisms of UHPC members are required to be studied. Moreover, from the cost perspective, the new structural designs should be proposed to increase the practical application of UHPC.

Chapter 3

Behaviour of Reinforced Conventional Concrete and Ultra-high Performance Concrete Columns under Impact Loading

3.1 Introduction

RC column, as a typical load-carrying structural member, is widely adopted in car parks and buildings that are close to main roads. These easily accessible columns are prone to vehicular collision [3, 92, 93]. Moreover, RC columns in overpass bridges located near navigable waterway and mountain areas should also be designed against impact loading effect of vessel collision and falling rocks [94-96]. Numerous experiments are adopted to study the dynamic behaviour of RC members under impact loadings. Most of these studies were conducted on RC beams [35, 41, 42, 44], while fewer studies were performed on RC columns. The impact-resistance of RC beams and columns is different owing to the presence of boundary restraints and axial loads. Differences in structural responses and damage modes between impact and quasi-static tests were mainly attributed to the inertia effects at structure level [44, 97] and the strain rate effects at material level [98, 99].

Under impact loading environment, the concrete structure members may fail in local failure rather than desired flexural failure. The current design code cannot capture the complex mechanism of impact events. For instance, the designed shear resistance of RC bridges from AASHTO-LRFD [100] is a constant static value. The estimated static strength could lead to overestimation of structural performance in real impact scenarios [92]. In addition, the deformation/rotation-based damage criterion which is widely adopted in dynamic damage assessment may not be appropriate for

columns subjected to impact loads because of the localized shear damage and concrete fragmentation. For concrete structures subjected to blast loads, a performance-based damage assessment was discussed. Shi et al. [101] applied residual capacity as the damage criterion. The residual axial capacity measured through numerical studies. Li et al. [102] carried out the study to measure the residual loading capacity of UHPC columns after blast loads. Later, Li et al. [103] applied residual capacity as damage criterion to quantitate the structure damage after blast loads. This performance-based criterion has been well developed and adopted in the preliminary design of protective structures under blast-loading scenarios.

Until now, there is limited study on UHPC columns under low-velocity impact loads and their corresponding residual loading capacity. This study concentrates on developing the analytical equations for quickly assessing the damage of UHPC columns against low-velocity impact loads. To achieve this, the drop weight tests were first conducted on RC and UHPC columns. Subsequently, the nonlinear finite-element dynamic analysis was performed. The validated numerical models were adopted to measure the residual capacity of UHPC after low-velocity impact loads. Finally, proposed formulae for assessing UHPC column residual loading capacity were developed.

3.2 Experimental Program

3.2.1 Concrete preparation

Mix proportions of material are presented in Table 3.2. Ultra-fine silica fume was adopted to replace coarse aggregates in UHPC. Silica fume could fill intergranular space to achieve a higher density. The high pozzolanic reaction effect of silica fume could accelerate the hydration, leading to Calcium-Silicate-Hydrate (C-S-H) product

and therefore enhance the concrete strength, especially in the early stage. Nanoparticles were adopted at a 3% volume dosage. The addition of nanoparticles could provide nanoscale filling effect and also pozzolanic effect. 1.5% volume dosage of steel fibre was mixed in the UHPC matrix. The properties of these copper-coated smooth fibres were listed in Table 3.1.

Fibre type	Diameter D_f (mm)	Length L_f (mm)	Aspect ratio (L_f/D_f)	Density (kg/m^3)	Tensile strength (MPa)	Elastic modulus (GPa)
Smooth fibre	0.20	6	30	7800	>2850	200

Table 3.1 Properties of copper-coated micro steel fibres.

	Conventional concrete (kg/m^3)	UHPC (kg/m^3)
Cement	551.9	750
Fine sand	843.1	1030
Coarse aggregate	745.9	-
Water	282.7	190
Silica fume	-	225
Nano particles	-	21.7
Superplasticizer	-	16
Steel fibre	-	114

Table 3.2 Mix proportion of Conventional concrete and UHPC.

The casting procedure of UHPC is listed as follow. First, fine sand, cement, nanoparticles and silica fume are dry mixed for 5 mins in a concrete mixer. Second, 70% of water was gradually added and these constituents continued to be mixed for 3 min. Third, superplasticizer and remaining 30% water were added. The mixer kept working until the constituents achieved good flowability. Finally, fibres were manually added in the concrete mixer. Fibres mixing process was slow to ensure that steel fibres were well dispersed. After 48 hours curing in hot water (90 degree), the specimens were then cured until testing.

In the current research, mechanical property tests were proposed to study the material performance of conventional concrete and UHPC. Test results are shown in Fig. 3.1 (a). Compared with conventional concrete, UHPC showed a greater ultimate strength, strain and ductile behaviour. Compressive strengths of conventional concrete and UHPC were 40 MPa and 136 MPa, respectively. The elastic modulus was measured using strain gages attached on the specimens following ASTM C469-14 [104]. The elastic moduli of conventional concrete and UHPC were 32.5 and 45.5 Gpa, respectively. In flexural bending tests, test beam samples of conventional concrete and UHPC had a length of 400 mm (300 mm clear span and 100 mm loading span) with a 100 mm × 100 mm cross-section. The central deflection was averaged from two parallel LVDTs installed on both sides of the specimen. The flexural responses of conventional concrete and UHPC were significantly different. For conventional concrete samples, the flexural crack propagated rapidly from bottom to top and the specimen split into two parts. For UHPC samples, the flexural performance was significantly improved. With crack propagating, the specimen remained attached. The flexural force versus displaceemnt curve is shown in Fig. 3.1 (b), and flexural

strengths were calculated based on ASTM C78 [105], The flexural strengths of conventional concrete and UHPC were 4.0 MPa and 14.4 MPa, respectively.

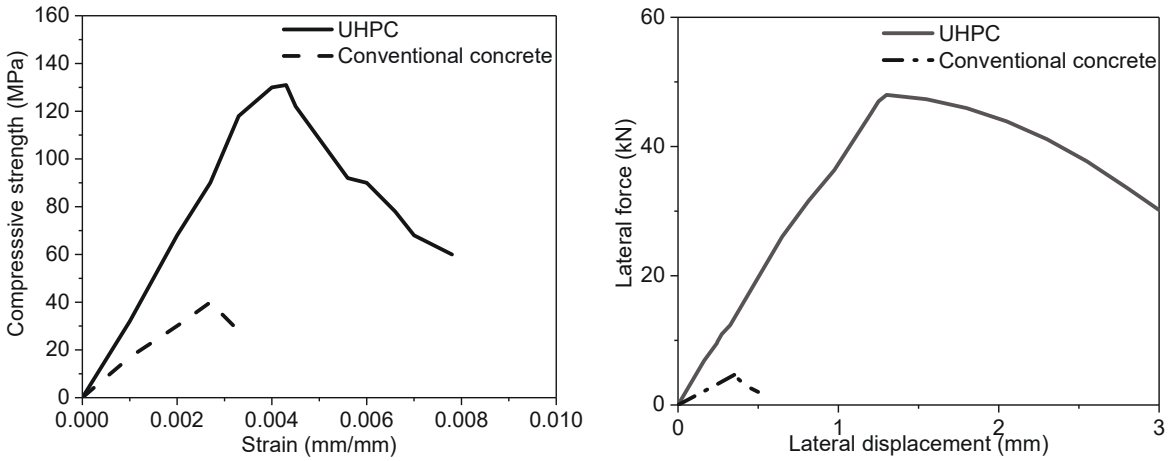

(a) stress versus strain curves (b) force versus displacement curves

Fig. 3.1. Mechanical property drop hammer impact test results

3.2.2 Sample preparation

To investigate the behaviour of columns against impact load, a total of six columns (three RC columns and three UHPC columns) with a 2 m span were prepared for drop weight tests. The specimens were divided into two series according to column cross-section shapes (“S” for square, “C” for circular). The geometric configuration and reinforcement layout are shown in Fig. 3.2. Deformed bars with 12 mm diameter and yield strength of 500 MPa were applied. Stirrup bars were roller plain bars with a 10 mm diameter and 500 MPa yield strength. The concrete cover for columns was 25 mm. The specimens were named as follow (Table 3.3): (1) “S” and “C” represent square and circular shape of column cross section. (2) “h” and number afterward represent the height of impact weight (unit: m).

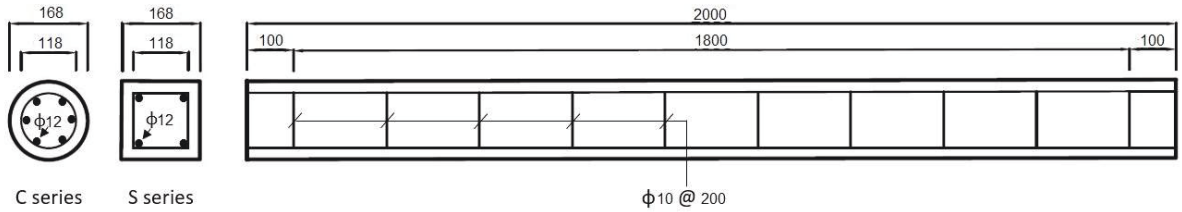

Fig. 3.2. RC and UHPC column configuration (unit: mm)

Test specimen	Concrete type	Cross section shape	Impact weight (kg)	Impact height (m)	Axial load (kN)
RC-S-h1.5	NC	Square	411	1.5	200
RC-S-h1.25	NC	Square	411	1.25	200
UHPC-S-h1.5	UHPC	Square	411	1.5	200
UHPC-S-h1.75	UHPC	Square	411	1.75	200
RC-C-h1	NC	Circular	427	1	200
UHPC-C-h1	UHPC	Circular	427	1	200

Table 3.3 Specimen design in drop weight test program.

3.2.3 Drop weight test setup

The impact tests are proposed on a drop hammer system with an adjustable drop weight (up to 1090 kg) and drop height (up to 20.6 m). After manually triggering the electromagnetic release mechanism, the drop hammer would fall freely along the guide rail. The designed impact velocity could be achieved by adjusting the drop height. Two types of indenter (Fig.3.3) were adopted in the drop weight tests to simulate the point contact. The hemispherical indenter was used for S series tests, and wedge-shaped indenter was used for C series tests.

The effect of axial load on column design should be considered especially when the large flexural failure occurs. In the present study, the axial loads are used through the pneumatic jack. Axial load ratio for a typical low-to-medium buildings is from 0.2 to 0.4 [106]. Therefore, a 200 kN force was adopted for all RC and UHPC specimens

Fig 3.4 presented test setup. Supporting frames were bolted to rigid foundations. The fully fixed boundary condition was applied through clamping systems. Each device included upper and lower parts that were fixed with four M18 bolts to prevent lateral movement. The clear span of test specimens was 1.4 m (total length 2 m), and the total length of clamped boundary was 0.5 m. The remaining 0.1 m was designed to apply the axial load. Two LVDTs were adopted to monitor the column deflection. In addition to transverse force, a load cell was mounted between drop hammer and indenter. The data acquisition frequency of LVDTs and load cell was 100 kHz.

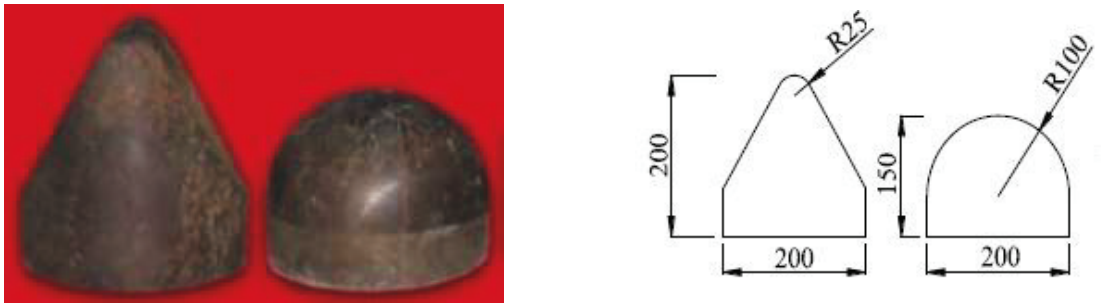

Fig.3.3. Two types of indenter (units: mm) [107]

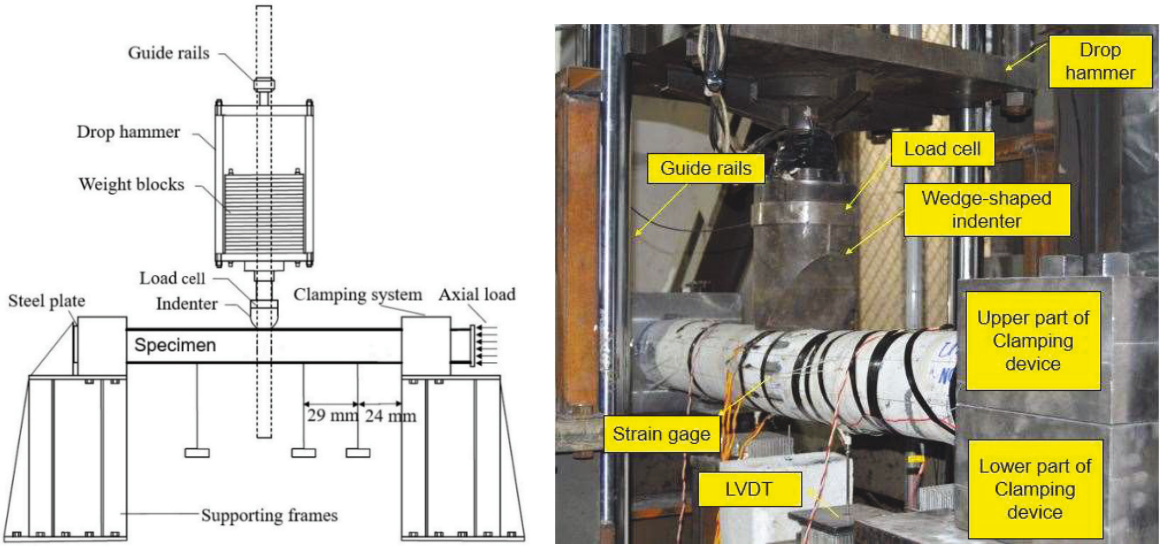

(a) Schematic illustration of test setup (b) Practical test setup

Fig 3.4. Low-velocity drop weight impact test setup

3.2.4 Impact test results

Fig 3.5 presents the specimens after the impact tests. For the conventional concrete column RC-S-h1.5, it was shattered with extensive concrete fragmentation at mid-span and flexural cracking on the upper surface close to the boundary. The longitudinal bars at mid-span were exposed and showed a clear buckling due to axial compression. With the decrease in impact velocity from 5.42 m/s to 4.95 m/s, the response of the column RC-S-h1.25 shifted from local concrete shattering to diagonal shear failure.

Fig. 3.5. Column failure patterns

For the UHPC-S-h1.5 column under the same impact velocity (5.42 m/s), one major flexural crack with a width more than 10 mm was observed at mid span. Minor flexural cracks with a width less than 10 mm were observed close to the clamping boundary. No fragmentation was observed on the UHPC column. Similar observations were made on UHPC-S-h1.75. With the impact height increased from 1.5 m to 1.75 m, the column retained a minor flexural damage mode with limited concrete crush on the compression surface.

For circular column “C” series tests, the RC-C-h1 column exhibited catastrophic shear failure mode under impact loading, while the UHPC-C-h1 column exhibited minor flexural damage, similar to the UHPC-S-h1.5. The comparison results from C series again indicated the good performance of UHPC column under impact loads.

The impact force and column deflections are to be presented in later section together with the numerical modelling.

3.3 Numerical Simulation

3.3.1 Numerical test setup

In the current study, numerical simulations were performed in commercial software LS-DYNA. The drop weight test setup and indenters were modelled in detail (Fig 3.6). Beam elements were employed for longitudinal and stirrup bars while solid elements were adopted in concrete. Since experimental results indicated that concrete local damage occurred on RC columns under impact loadings, a small 5 mm mesh size was applied for columns, clamping devices, reinforcement and indenter to capture highly localized damage. A relatively coarse 40 mm mesh size was applied for the drop hammer frame. The element size mentioned above was determined by mesh sensitivity tests which were discussed in the following section 3.2.5. To model experimental boundary conditions, the clamping boundary was constrained at all directions while the steel plate (right one) for axial compression application was constrained at x and y-axis. The axial load was applied prior to the impact scenario.

The reinforcements and concrete matrix were assumed to be perfect bonded. The keyword *CONTACT_AUTOMAI_SURFACE_TO_SURFACE was applied between indenter and column, column and clamping devices, column and steel plates. To reduce calculation efforts, initial impact velocity was adopted. The conversion formula was: $v_i = \sqrt{2gh}$, where v_i is the impact velocity upon contact; g is the standard gravity; h is the initial drop height. The velocity was applied by defined the keyword * VELOCITY_GENERATION in LS-DYNA.

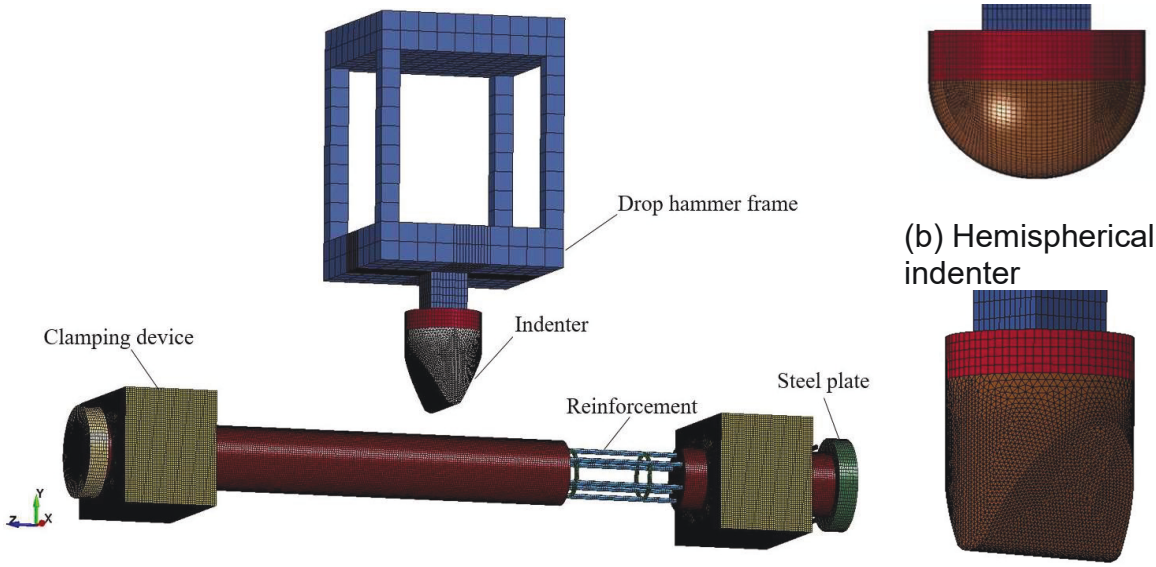

(a) Numerical drop weight test setup

(b) Hemispherical indenter

(c) Wedge-shaped indenter

Fig. 3.6. Numerical low-velocity drop hammer impact test setup

3.3.2 Material properties

In LS-DYNA program, various material models (including CSCM, MAT_159, the Concrete Damage Rel3 model (KCC, MAT_72_REL3), and the Winfrith model (MAT_84)) are available to describe concrete behaviour under dynamic loads. Fan and Yuan [108] conducted numerical simulations using the CSCM model and Winfrith model. Test results indicated that the peak hammer-beam contact forces were overpredicted by Winfrith model, while both average and peak forces from CSCM model showed well results. For the KCC model, it has been widely adopted to simulate conventional concrete under blast loads. However, Yoo et al. [19] noted that UHPC beams that modelled with the KCC model overpredicted the mid-span displacement. For CSCM model, feasibility of this model of modelling RC structures are demonstrated by previous studies [109-112]. In the present study, the CSCM model was selected and modified for UHPC.

3.3.2.1 CSCM model for RC

The current version of the CSCM model is developed from the MAT_GEOLOGIC_CAP_MODEL (MAT_025). This model was improved to simulate roadside safety structure (e.g., anti-ram bollards and concrete bridge columns) against vehicle collision. The CSCM model considers plenty of mechanical properties such as strain rate effect (through viscoplastic rate effect formulation), material softening and modulus reduction through damage algorithm, material failure and hardening (through three invariant strength surfaces), and so on. Detailed properties of CSCM model are discussed in its user's manual [113]. In LS-DYNA program, two versions of the CSCM model, i.e., *MAT_CSCM and *MAT_CSCM_CONCRETE are available. *MAT_CSCM_CONCRETE features a function with an input of minimum three parameters. And it is suggested for NSC with strength between 28 and 58 MPa [113]. For the other versions, total 45 parameters should be obtained from material tests. In the present study, *MAT_CSCM is used to model UHPC, and the key parameters are discussed in the following section. Conventional concrete is modelled by *MAT_CSCM_CONCRETE.

Since experimental test results have shown highly localized damage (shear failure and concrete spalling) during the tests, the so-called "element erosion" algorithm was adopted in the simulation to avoid mesh distortion. It is worth noting that "element erosion" has no physical meaning, and therefore it needs to be used with caution. In the present study, for rectangular columns, the simulation experienced computational overflow due to local mesh distortion, and therefore the erosion algorithm was adopted. For circular columns, simulations could continue without

massive mesh distortion. Thus, the erosion algorithm was not adopted. After conducting several trial simulations, the value of 0.2 is adopted for element erosion.

3.3.2.2 CSCM model for UHPC

UHPC is a cement-based material and shares similar features with other concrete-like materials. However, the material model needs to be carefully validated for UHPC to represent its unique features. In the current study, calibrations are carried out based on previous material tests on UHPC.

3.3.2.2.1 Triaxial compression, torsion and extension surface

The equation for the triaxial compression (TXC) yield surface in the CSCM material is shown as follow:

$$F_s(I_1) = (\alpha - \lambda exp^{-\beta I_1} + \theta I_1) \quad (3.1)$$

$$I_1 = \sigma_a + \sigma_b + \sigma_c \quad (3.2)$$

where F_s is the shear failure surface; α, λ, β, θ are calculated from fitting to the four types of stress states (Fig. 3.7) measured from TXC tests via an iterative procedure; σ_i is the principal stress $(\sigma_a \geq \sigma_b \geq \sigma_c)$. For four types of stress states, the first measured one is unconfined compression (point C in Fig. 3.7). The second one and third one are biaxial and triaxial tension (point B and A in Fig. 3.7). As experimental tests on the biaxial and triaxial tensile behaviour of UHPC are not available, the values of biaxial and triaxial tension strength are assumed to be the same as the uniaxial tensile strength, which is based on the same assumption for conventional concrete to determine biaxial and triaxial tension strength. The final stress state is the TXC state at a high confining pressure. To collect triaxial compressive strength of UHPC at different confining pressure, Ren et al. [114] conducted TXC on UHPC specimens. By

selecting the data on UHPC of 129 MPa (Fig. 3.8), the fitting equation is listed as follow:

$$\frac{\tau_0}{f_c'} = 0.271 + 0.709\frac{\sigma_0}{f_c'} \tag{3.3}$$

where shear strength $\tau_0 = \sqrt{\frac{2J_2}{3}}$; normal strength $\sigma_0 = \frac{I_1}{3}$. The correlation factor R^2 is 0.9972. The triaxial compression strength at specific pressure can be achieved by adopting Eq. (3.3). It is difficult to determine these TXC failure surface parameters based on just four stress states as the curve is highly nonlinear. Therefore, additional stress states are required. Experiments indicated that, at the high confining pressure, the fitting curve is closed to a straight line [114]. More stress states at high pressure (e.g.,$I_1 = 2f_c',\ 3f_c' \text{ and } 4f_c'$) estimated by Eq. (3.3) are used to curve fit the shear failure surface for triaxial compression. Based on the aforementioned stress states, four strength parameters can be calculated by fitting on the compression failure surface at different strength grades with the least-square method. The calculation results for *α, λ, β, θ* are 44.67 MPa, 35.32 MPa, 0.0125 MPa^{-1}, 0.2897, respectively.

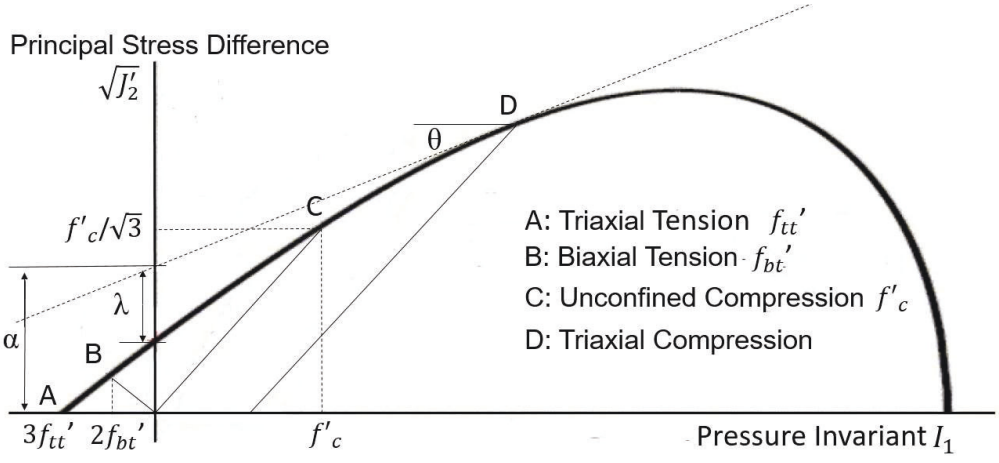

Fig. 3.7. Meridian lines of compression failure surface

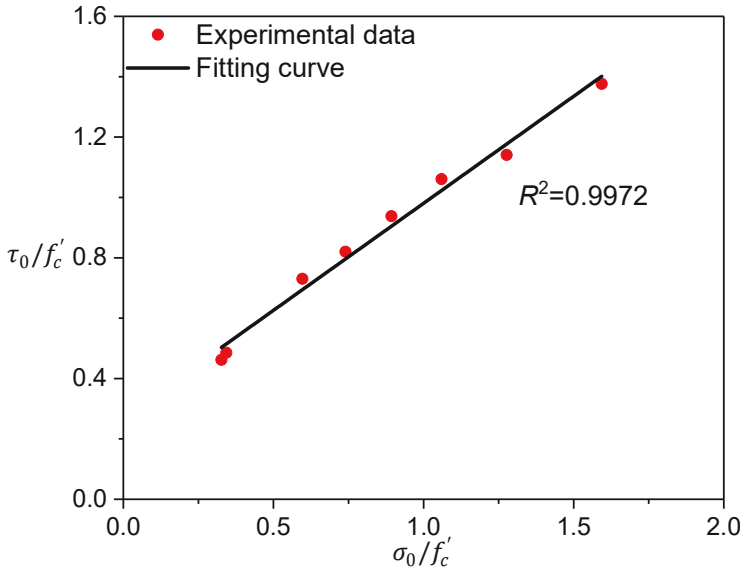

Fig. 3.8. Triaxial compression test data [114]

The strength ratio for the triaxial torsion (TOR) and extension (TXE) yield surface is determined by the Rubin scaling functions in accordance with TXC strength as follow:

$$Q_1 = \alpha_1 - \lambda_1 e^{-\beta_1 I_1} + \theta_1 I_1 \tag{3.4}$$

$$Q_2 = \alpha_2 - \lambda_2 e^{-\beta_2 I_2} + \theta_2 I_2 \tag{3.5}$$

where Q_1 is the TOR/TXC strength ratio; Q_2 is the TXE/TXC strength ratio; eight strength parameters ($\alpha_1, \lambda_1, \beta_1, \theta_1$ and $\alpha_2, \lambda_2, \beta_2, \theta_2$) are used to fit the equation based on TOR and TXE tests. Since little torsion experiments were carried out for conventional concrete or the concrete-like material, constitutive theory for UHPC should be applied to determine the strength parameters ($\alpha_1, \lambda_1, \beta_1, \theta_1$). Based on the model theory, constant values $Q_1(I_1 = 0) = 0.5774$ and $Q_2(I_1 = 0) = 0.5$ were assumed to ensure the compression and tension surface can smoothly intersect. Since $Q_1(I_1) \leq 1$ in nature and I_1 could be infinite [115], the parameter θ_1 was then set to 0 for UHPC. When I_1 is infinite, the yield surface shape is nearly circular, which

means $\alpha_1 = 1$. Due to $Q_1(I_1 = 0) = 0.5774$, the parameter $\lambda_1 = 1 - 0.5774 = 0.4226$. The parameter β_1 is set as 0.0126 based on user manual recommendation [116]. The parameters $(\alpha_2, \lambda_2, \beta_2, \theta_2)$ for TXE are also determined by constitutive theory for concrete-like material, which yields $\alpha_2 = \alpha_1 = 1$, $\theta_2 = \theta_1 = 0$, and $\beta_2 = \beta_1 = 0.0126$. Since $Q_2(0) = 0.5$, $\lambda_2 = 1 - 0.5 = 0.5$.

3.3.2.2.2 Cap hardening parameters

Cap hardening parameters (*R*, X_o, *W*, D_1, D_2) are fitted on the pressure-volumetric curves which collected from Hydrostatic compression tests [113]. X_o refers to cap initial location. To determine the value for X_o, Guo et al. [117] have fitted a formula based on Hydrostatic compression tests conducted by Murray et al. [116]. The formula was adopted in the current UHPC model and shown in Eqs. (3.6) and (3.7).

$$\varepsilon_v^p = W(1 - e^{-D_1(X - X_0) - D_2(X - X_0)^2}) \tag{3.6}$$

$$X_o = 0.0204 \times f_c'^2 - 1.232 \times f_c' + 104.87 \text{ (MPa)} \tag{3.7}$$

where ε_v^p is the plastic volume strain; *W* is the maximum plastic volume strain; X_o is the initial cap location; D_1 is the linear cap hardening parameter; D_2 is the quadratic cap hardening parameter; f_c' is the compressive strength of UHPC. For cap aspect ratio *R*, since the compression failure surface and the cap surface usually interacted at the point $(f_c', \frac{f_c'}{\sqrt{3}})$ (Point C, in Fig. 3.7), the formula to determine *R* is estimated as follow:

$$R = (X_o - f_c')/(f_c'/\sqrt{3}) \tag{3.8}$$

where, *R* is the cap shape. Although UHPC has low a porosity, the applications made by UHPC may not be fully compacted in fact. A value of 0.05 was set to provide a reasonable shape of the cap surface to drop-weight tests, which is also suggested by

Williams et al. [118]. The linear shape parameter D_1 and the quadratic shape parameter D_2 are gained from assumptions. Default values of 6 × 10^{-10} (MPa^{-1}) and 0 were set for D_1 and D_2, respectively.

3.3.2.2.3 Damage and strain rate parameters

Concrete or concrete-like material exhibits strain softening behaviour under a low-pressure regime. The damage algorithm in the CSCM model is used to simulate this behaviour. Moreover, the damage algorithm also considers a modulus reduction. Five parameters (B, GFC, D, GFT, GFS) used in the damage algorithm should be determined. The parameter B is softening parameter. Although plenty of uniaxial compression tests have been carried out, few studies pay attention to compression softening behaviour. JSCE [119] has no recommendations for compression softening portion of UHPC. It indicates that the compression softening behaviour has limited influence on the performance of UHPC under impact loads. Therefore, a value of 100 was adopted for B. For parameter D, it controls the brittle softening behaviour. UHPC has significant different tensile properties as compared to conventional concrete. The strain hardening behaviour and bridging effect of steel fibres could greatly improve the post-peak tensile resistance on UHPC. In the current study, a value of 0.1 was set for parameter D after trial simulations. The fracture energy refers to the area located under the stress-displacement curve from peak stress to totally softening. Due to lack of test data, the value of GFC could be determined by fitting the stress-strain curve with test data. For GFT, simplified tension stress-strain (Fig. 3.9 (b)) which is similar to Mao et al. [120] and Guo et al. [117] was used. The values for GFC and GFT are 10000 (Pa·m) and 2000 (Pa·m), respectively. The parameter GFS is suggested to be equal to GFT according to the user manual [116]. The fitting parameters of fracture energy were determined for UHPC with single fibres (15 mm) at a 2.5% volume

dosage. Different fibre types, fibre lengths and fibre dosages would affect the fitting parameters.

The mechanical properties of concrete-like material are greatly different between dynamic and static loadings. The strength enhancement under high strain rate loading condition is called the strain rate effect. In the CSCM model, viscoplastic rate effect equations are applied to model the strain rate effect of concrete-like materials [113]. In viscoplastic formulations, the dynamic strength for direct pull ($f'_{t,d}$) and unconfined compression ($f'_{c,d}$) simulations could be expressed as follow:

$$f'_{t,d} = f'_t + E\dot{\varepsilon}\eta \tag{3.9}$$

$$f'_{c,d} = f'_c + E\dot{\varepsilon}\eta \tag{3.10}$$

where E is Young's modulus; $\dot{\varepsilon}$ is effective strain rate and defined in Eq. (3.13); the viscoplastic fluidity parameter η is determined by four user-specified input parameters. Parameters η_{ot} (rate effect parameter) and N_t (rate effect power) are used to fit uniaxial tensile stress data, and η_{oc} and N_c are used to fit uniaxial compression stress data. The relationships of these parameters are shown as follow:

For pressure in tension:

$$\eta = \eta_{ot} + \text{trans}(\eta_t - \eta_{ot}),\ \text{trans} = \left(\frac{-J_1}{\sqrt{3J'_2}}\right)^{pwrt},\ \eta_t = \frac{\eta_{ot}}{\dot{\varepsilon}^{N_t}} \tag{3.11}$$

For pressure in compression:

$$\eta = \eta_{oc} + \text{trans}(\eta_c - \eta_{ot}),\ \text{trans} = \left(\frac{-J_1}{\sqrt{3J'_2}}\right)^{pwrc},\ \eta_c = \frac{\eta_{oc}}{\dot{\varepsilon}^{N_c}} \tag{3.12}$$

where *pwrc* and *pwrt* are defined as transition parameters. J_1 and J_2' are referred to the first and the second stress invariant.

The effective strain rate in the viscoplastic model is defined as follow:

$$\dot{\varepsilon} = \sqrt{\frac{2}{3}\{(\dot{\varepsilon}_1 - \dot{\varepsilon}_2)^2 + (\dot{\varepsilon}_2 - \dot{\varepsilon}_3)^2 + (\dot{\varepsilon}_3 - \dot{\varepsilon}_1)^2 + \dot{\varepsilon}_{12}{}^2 + \dot{\varepsilon}_{13}{}^2 + \dot{\varepsilon}_{23}{}^2\}} \quad (3.13)$$

where $\dot{\varepsilon}_1$, $\dot{\varepsilon}_2$ and $\dot{\varepsilon}_3$ are the first, second and third principal strain rate, respectively; and $\dot{\varepsilon}_{12}, \dot{\varepsilon}_{23}, \dot{\varepsilon}_{13}$ are the shear strain rates.

Most of research defined strain rate effect through Dynamic Increase Factor (DIF). Based on Eqs. (3.11) and (3.12), the DIF can be respectively written as:

For tensile strength: $DIF = \frac{f'_{t,d}}{f'_t} = 1 + \frac{E\dot{\varepsilon}\eta_{ot}}{f'_t\dot{\varepsilon}^{N_t}}$ (3.14)

For compressive strength: $DIF = \frac{f'_{c,d}}{f'_c} = 1 + \frac{E\dot{\varepsilon}\eta_{oc}}{f'_t\dot{\varepsilon}^{N_c}}$ (3.15)

For UHPC, DIF can be calculated by the equations proposed by Fujikake et al [121]:

For tensile strength:

$$DIF = \frac{f'_{t,d}}{f'_t} = \begin{cases} \left(\frac{\dot{\varepsilon}}{\dot{\varepsilon}_{st}}\right)^{0.0013\left[\log\left(\frac{\dot{\varepsilon}}{\dot{\varepsilon}_{st}}\right)\right]^{1.95}} & \text{for } \dot{\varepsilon} \geq \dot{\varepsilon}_{st} \\ 1 & \text{for } \dot{\varepsilon} < \dot{\varepsilon}_{st} \end{cases} \quad (3.16)$$

For compressive strength:

$$DIF = \frac{f'_{c,d}}{f'_c} = \begin{cases} \left(\frac{\dot{\varepsilon}}{\dot{\varepsilon}_{sc}}\right)^{0.0055\left[\log\left(\frac{\dot{\varepsilon}}{\dot{\varepsilon}_{sc}}\right)\right]^{0.951}} & \text{for } \dot{\varepsilon} \geq \dot{\varepsilon}_{sc} \\ 1 & \text{for } \dot{\varepsilon} < \dot{\varepsilon}_{sc} \end{cases} \quad (3.17)$$

where $\dot{\varepsilon}_{st} = 1.0 \times 10^{-6}$ /s and $\dot{\varepsilon}_{sc} = 1.2 \times 10^{-5}$ /s. Four user-specified input parameters (η_{ot}, N_t, η_{oc} and N_c) could be determined by fitting data on strain stress curve made based on Eqs. (3.16) and (3.17). The final results show $\eta_{oc} = 1.83 \times 10^{-4}$, $N_c = 0.504$, $\eta_{ot} = 1.76 \times 10^{-5}$, and $N_t = 0.56$.

3.3.2.3 Single element test

By following the aforementioned procedure, the CSCM material model for UHPC in the current study could be achieved. Before applying the developed UHPC model in the impact simulation tests, single element tests including uniaxial compressive and uniaxial tension tests were carried out. In the single element tests, keyword *PRESCRIBED_MOTION was adopted to achieve the displacement control. More details about uniaxial compression and tensile tests could be found in the study of Schwer et al [122].

Fig. 3.9 (a) shows the test results for the single element with an element size of 5 mm under unconfined uniaxial compressive tests. Compared with the strain-stress curve (Fig. 3.1 (a)) of measured from experimental tests, it can be found that the developed CSCM material model could provide an accurate uniaxial compressive strength of UHPC. The strain-stress curve of uniaxial tensile stress is shown in Fig. 3.9 (b).

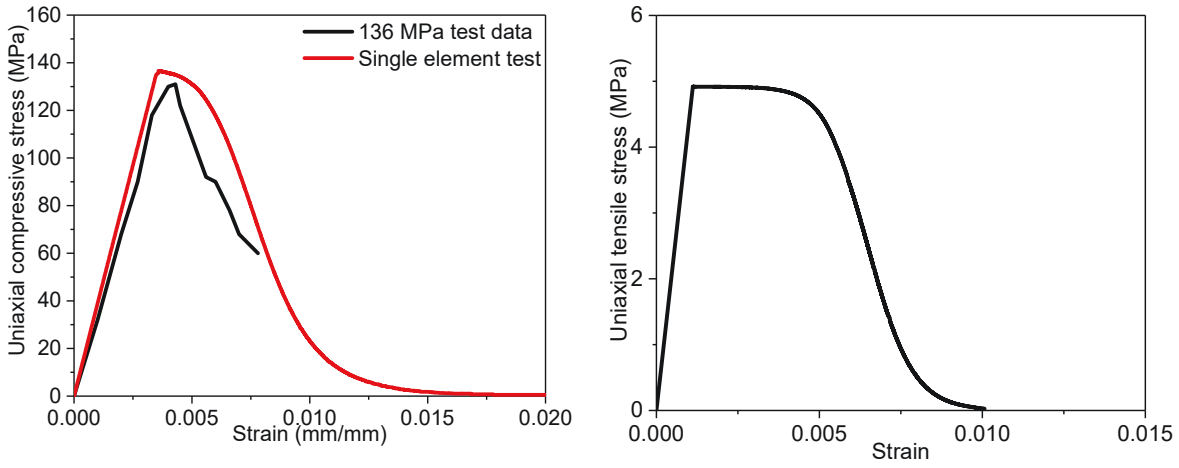

(a) compressive strain-stress curve (b) Uniaxial tensile strain-stress curve

Fig. 3.9. Single model under uniaxial compressive and tensile tests

3.3.2.4 Numerical uniaxial compression and four-point bending test

The numerical test was conducted on the UHPC cube with a dimension of 100 mm × 100 mm × 100 mm, which is shown in Fig. 3.10 (a). The element sizes for the concrete matrix and supports was 5 mm. It can be seen from Fig. 3.10 (b) that well results in terms of the compressive stress and strain was achieved.

A numerical test was also carried out. The specimen was a UHPC prism with a dimension of 100 mm × 100 mm × 400 mm, as shown in Fig. 3.11 (a). The clear span was 300 mm and the gap between the two area was 1/3 of the clear span. The element size for the concrete matrix and supports was 5 mm. The comparison between the testing and simulated results of the lateral force versus displacement curves are shown in Fig. 3.11 (b); two curves matched well.

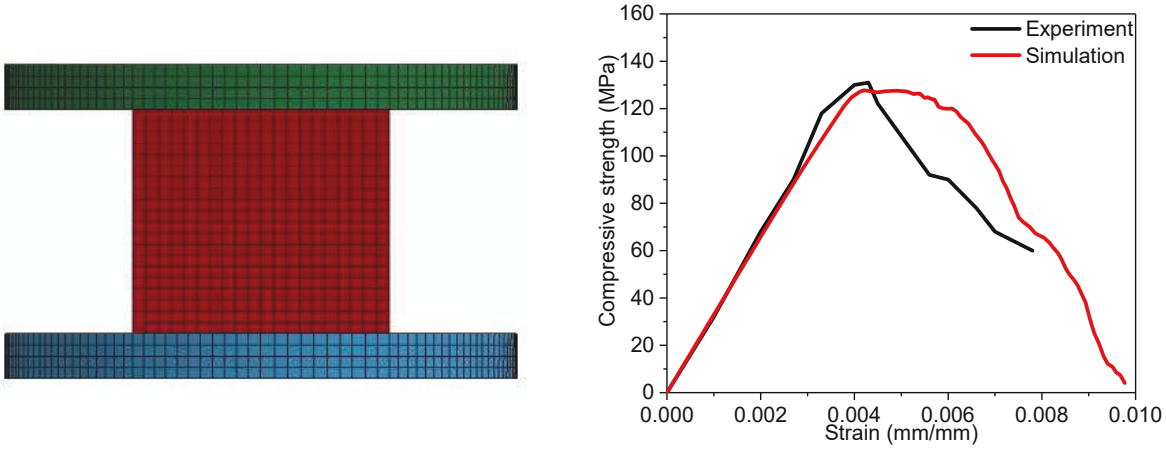

(a) Numerical simulation (b) Compressive stress-strain curves

Fig. 3.10. Numerical uniaxial compression test

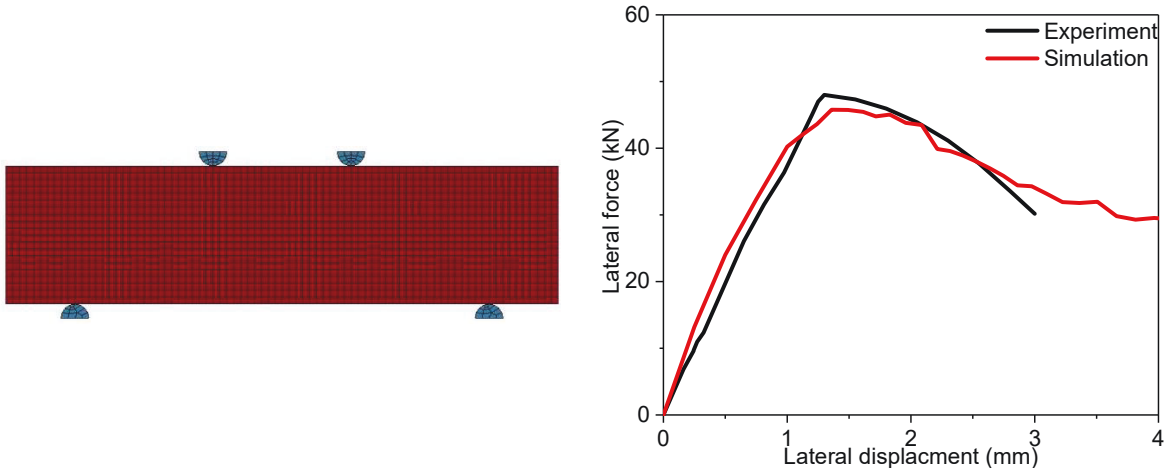

(a) Numerical simulation (b) Lateral force versus deflection

Fig. 3.11 Numerical four-point bending test

3.3.2.5 Other material model

The reinforcement was simulated by MAT_24 which considered the rebar strain hardening. For the remaining part (indenter, clamping devices, steel plates, drop hammer frame), the elastic model *MAT_ELASTIC (MAT_1) was used. All input parameters were determined from experiments and tabulated in Table 3.4. The strain rate effect on steel bars could be calculated according to [123]:

$$\frac{f_{r,d}}{f_{r,s}} = DIF = (\frac{\dot{\varepsilon}}{10^{-4}})^{\delta} \quad (3.18)$$

where $f_{r,d}$ is the dynamic strength of the reinforcement; $f_{r,s}$ is static reinforcement stregnth; for ultimate strength, $\delta = 0.019 - 0.009f_y/60$; for yield strength, $\delta = 0.074 - 0.040f_y/60$, and f_y is the bar yield strength in ksi (for f_y in MPa, the 60 ksi should be replaced by 414 MPa).

Part	Model	parameter	value
Longitudinal bars Stirrup bars	MAT_PIECEWISE_ LINEAR_PLASTICITY	Mass density Young's modulus Poisson's ratio Yield stress Tangent modulus	7800 (kg/m^3) 2.0e11 (Pa) 0.3 5.0e8 (Pa) 5.0e6 (Pa)
Indenter Clamping devices Steel plates Drop hammer frame	MAT_ELASTIC	Mass density Young's modulus Poisson's ratio	7800 (kg/m^3) 2.0e11 (Pa) 0.15

Table 3.4 Other parameters defined in the numerical simulation model.

3.3.2.6 Mesh sensitivity tests

To capture the impact induced stress wave propagation and associated localized deformation and damage, sufficiently small element size is required in structural modelling against localized impact. Refining mesh size could converge the computational solutions. As shown in Fig. 3.12, three element sizes were applied in mesh sensitivity tests. It is noted that 10 mm mesh size overpredicted deformations. Moreover, with the element sizes decreasing, the simulation results converged to the experimental tests. To balance the accuracy and efficiency, the 5 mm element size was adopted for the column. The numerical results did not well capture the experimental data. The possible explanations were: first, the fully fixed boundary was

adopted on the UHPC columns during numerical tests. However, the steel clamping devices experienced marginal deformation during the experimental tests. Second, the numerical simulation adopted the perfect bond between the steel reinforcement and UHPC rather than the practical bond-slip model. The partially released boundary and bond-slip behaviour could lead to a longer loading phase and forced vibration phase.

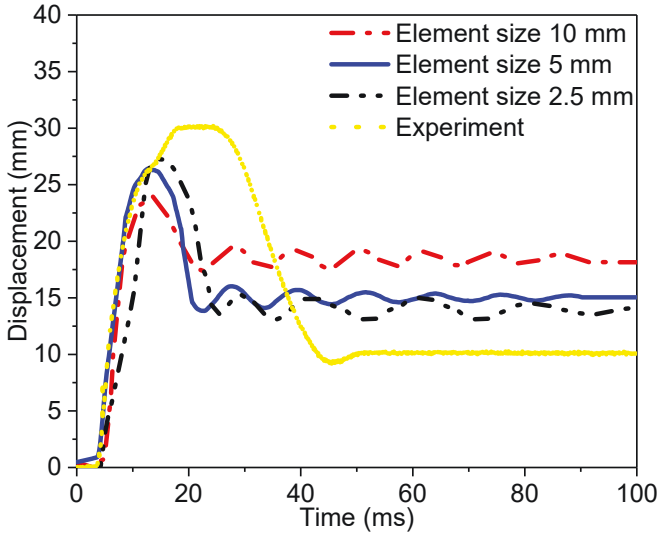

Fig. 3.12 Mesh sensitivity tests on UHPC-S-h1.5

3.3.3 Modelling results

3.3.3.1 Damage mode comparison

RC column specimens all exhibited concrete spalling under impact location. In Fig. 3.13, side view of the column RC-S-h1.5 after low-velocity impact load is shown. It can be highlighted that the specimen column was totally shattered with a large part of concrete fragmentation at mid-span. The vertical cracks near clamping devices developed from top to bottom due to negative bending moment. The numerical model captures the overall deformation of the column with reasonable accuracy.

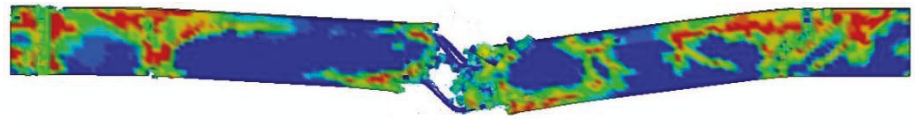

(a) numerical result

(b) experimental result

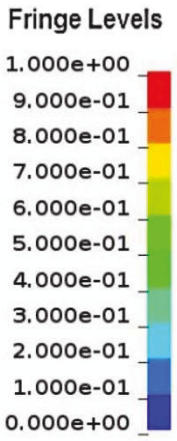

Fig 3.13. RC-S-h1.5 response

Fig 3.14 shows the test specimen RC-S-h1.25 response. With decreasing the velocity, the failure mode shifts from concrete shattering to diagonal shear. The column collapsed under the combined action of impact and axial compression. The numerical model captures the diagonal shear and the ultimate collapse of the test specimen.

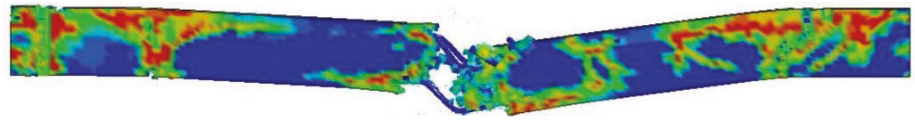

(a) numerical result

(b) experimental result

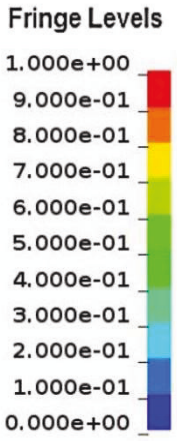

Fig 3.14. RC-S-h1.25 response

Fig. 3.15 and Fig. 3.16 show the test specimens UHPC-S-h1.5 and UHPC-S-h1.75 response. In the experimental observation, only one visible crack at mid-span and several shear cracks near the clamping system were observed. The numerical model captured the overall deformation and damage of the column with reasonable accuracy.

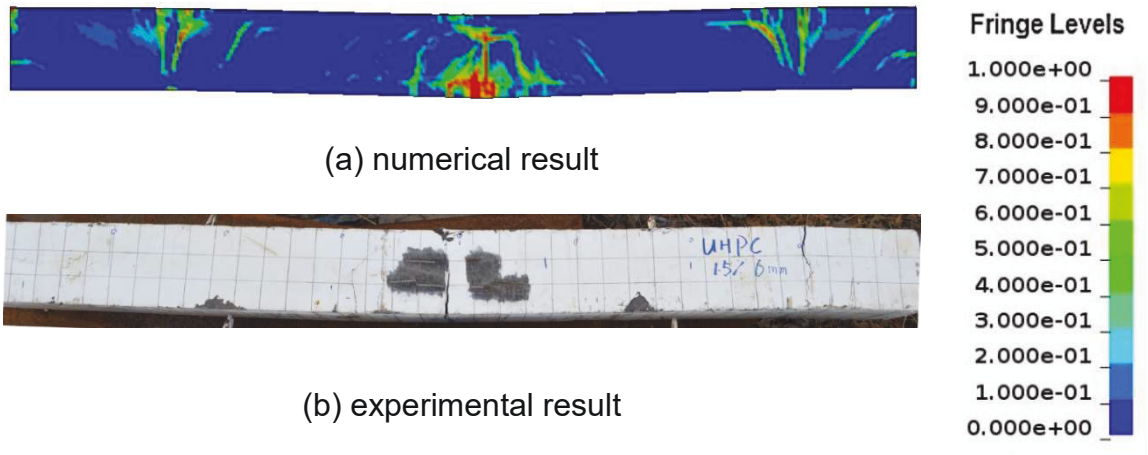

(a) numerical result

(b) experimental result

Fig 3.15. UHPC-S-h1.5 response

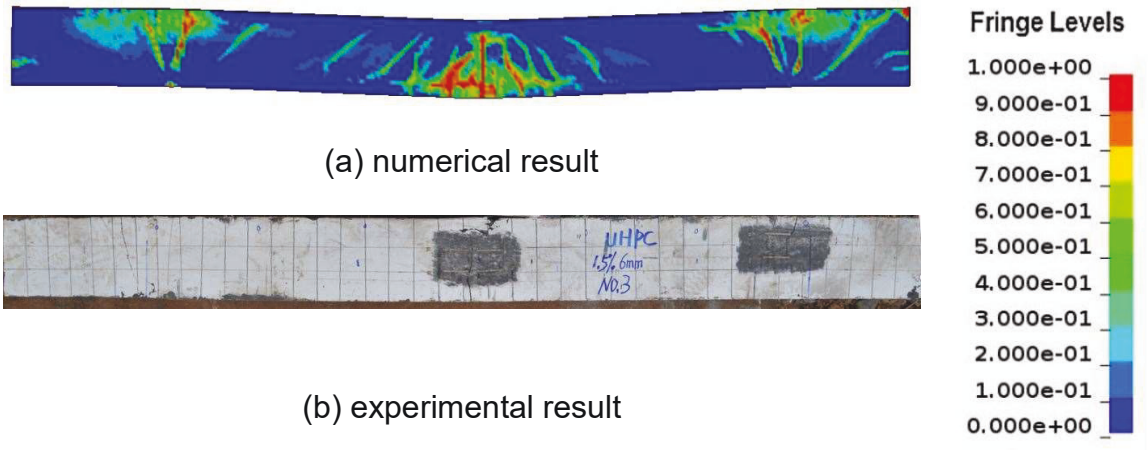

(a) numerical result

(b) experimental result

Fig 3.16. UHPC-S-h1.75 response

Fig. 3.17 and Fig. 3.18 present the failure modes for the test specimen RC-C-h1 and UHPC-C-h1. For the RC-C-h1, the test specimen experienced large deformation. The numerical model captures the collapse of the test column. For UHPC-C-h1, the test specimen experienced a minor flexural damage. The numerical model accurately captures the penetrating flexural cracks from experimental observations. Moreover, for the RC-C-h1, a shear plug was formed at mid-span. For the cracks near clamping system, they were developed from bottom to top surface and formed an inclination

angle of 45 degrees. The developed CSCM could accurately predict the damage when the deformation is small.

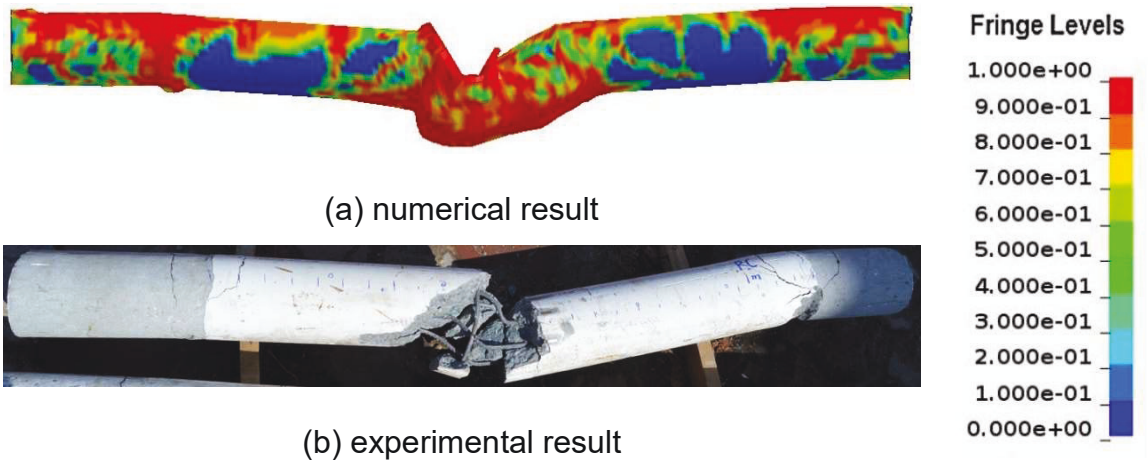

(a) numerical result

(b) experimental result

Fig 3.17. RC-C-h1 response

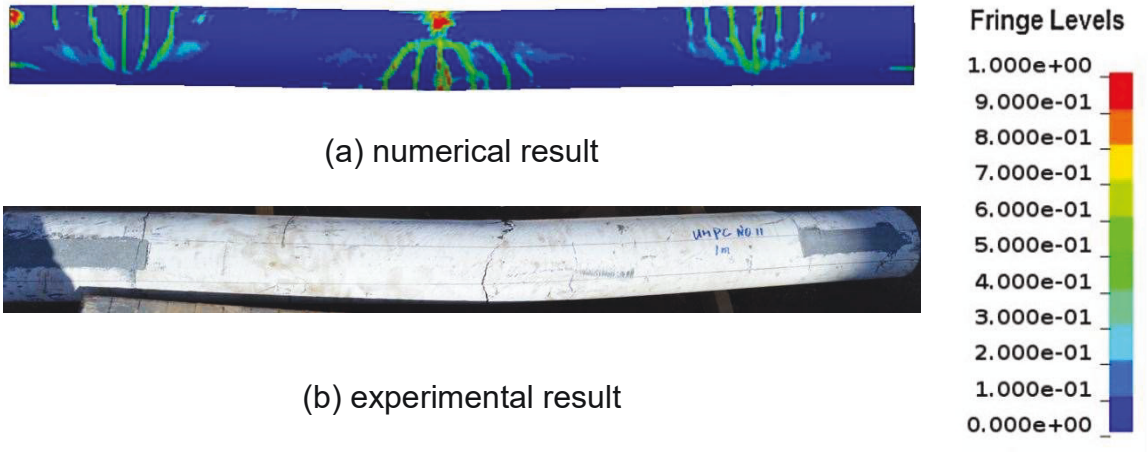

(a) numerical result

(b) experimental result

Fig 3.18. UHPC-C-h1response

3.3.3.2 Impact force and displacement histories comparison

The impact force histories were recorded from the contact force at the interface between test specimens and indenter. The deflection histories were extracted from node displacement histories in the perpendicular direction, and the locations of measured nodal points in FE simulations are the same with the test setup. The results of experiments and numerical simulations for specimens are shown in Fig. 3.19. From

Fig. 3.19, it is noted that for UHPC columns (UHPC-S-h1.5, UHPC-S-h1.75 and UHPC-C-h1), the first peak impact force matched reasonably well with the experimental results. The subsequent main force pulse was overpredicted and the durations of impact loading phase were shorter than experimental results.

For displacement histories, the numerical simulations also showed a shorter forced vibration phase. The possible error could be explained as: first, the fully fixed boundary was adopted on the UHPC columns during numerical tests. However, according to high-speed camera record, the steel clamping devices experienced marginal deformation during the experimental tests. The partially released boundary could lead to a longer loading phase and forced vibration phase. Second, the existence of debris between column and indenter could decrease the impact force but increase the loading phase. Third, the inertia of the mechanical LVDT possibly delayed the measured forced vibration phase. Other than that, the impact force and flexural behaviour were well reproduced by the simulation. For conventional concrete specimens failed in shear (RC-S-h1.5) the displacement histories collected from numerical simulations slightly deviated from the experimental responses due to massive element erosion.

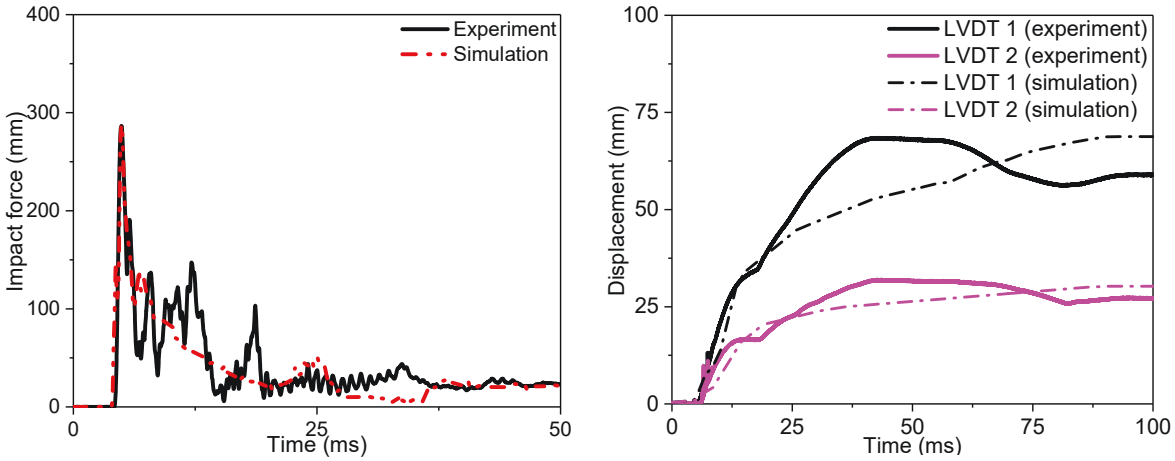

(a) RC-S-h1.5

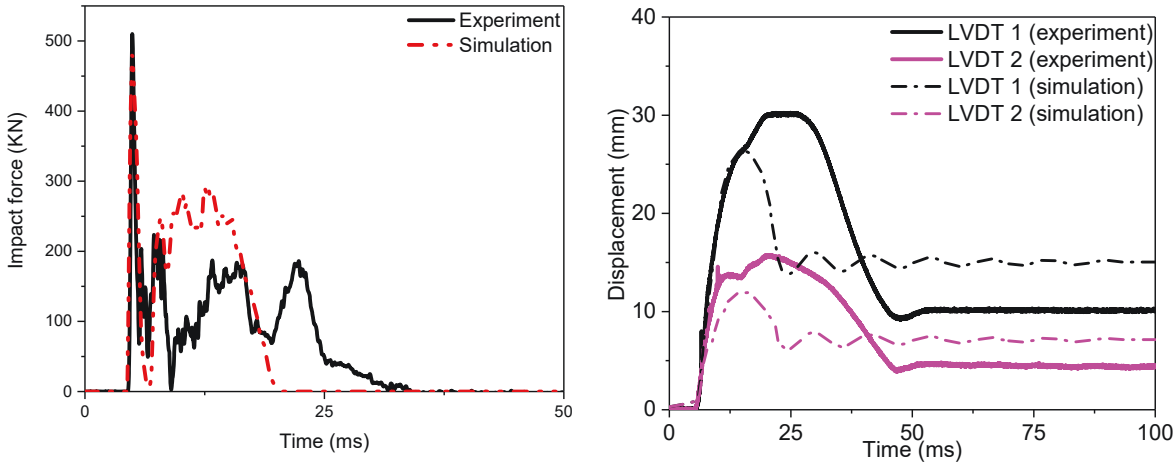

(b) UHPC-S-h1.5

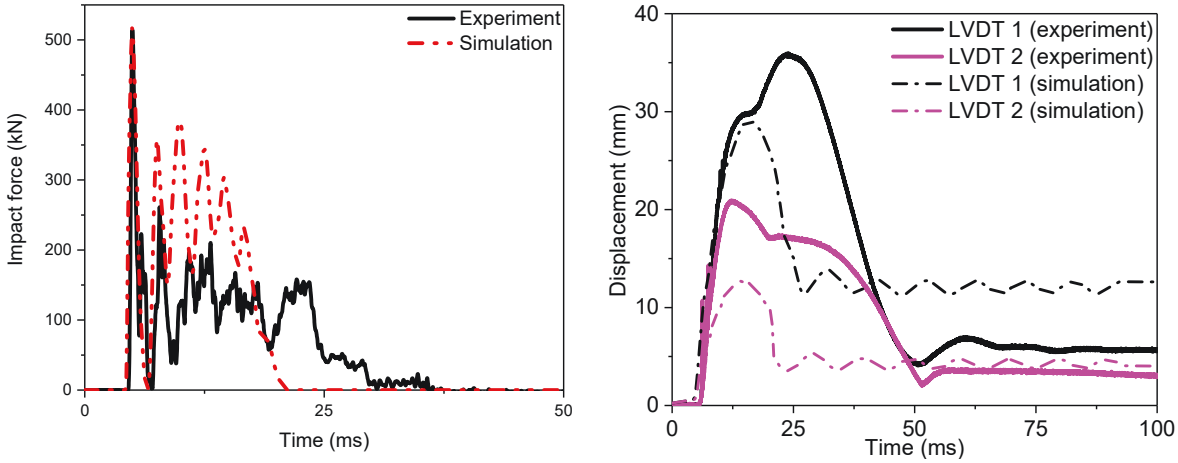

(c) UHPC-S-h1.75

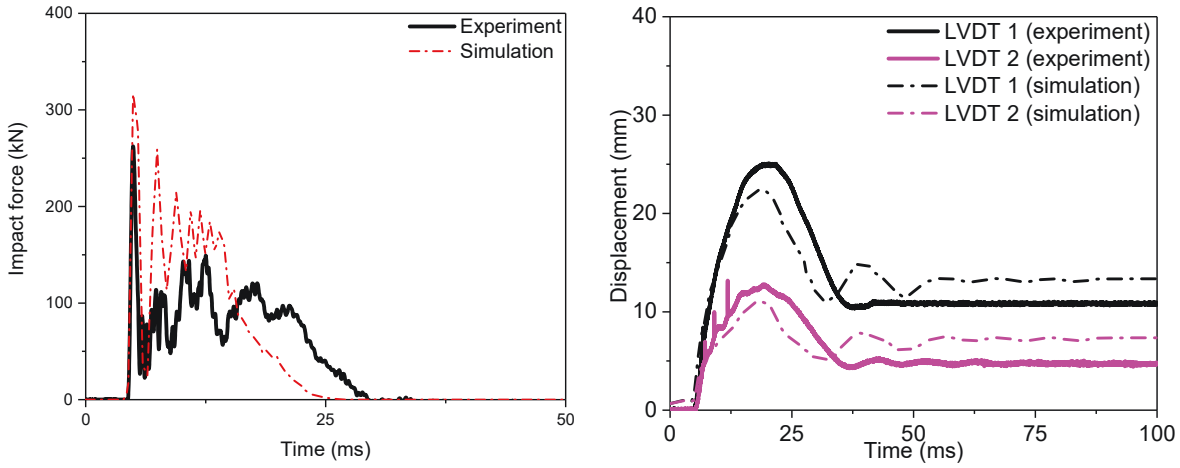

(d) UHPC-C-h1

Fig. 3.19. Comparison between experiments and simulations

3.4 Mass-velocity Diagram for UHPC Columns

In this section, to quantify the structural damage after impact loads, a performance-based damage criterion was adopted. Then, extensive numerical study was performed to generate the damage diagram for UHPC columns.

3.4.1 Damage criteria for UHPC columns

Columns are mainly designed to carry axial loads in structures. Evaluating the residual loading carrying capacity is suitable for both global damage (flexural failure) and local damage (penetration, punching shear and scabbing). The damage index *D* based on the degradation of axial loading carrying capacity was discussed by Shi et al. [101] for post-blast columns study. In the current study, the damage index is adopted for post-impact UHPC columns and defined as:

$$D = (1 - \frac{N_{re}}{N_{max}}) \times 100\% \quad (3.19)$$

where N_{re} is residual axial loading capacity of post-impact columns; N_{max} is the maximum axial loading capacity; *D* is damage index. For N_{max}, a previous study [124] adopted equation to calculate the maximum loading capacity.

$$N_{design} = 0.85 f_c' (A_g - A_s) + f_y A_s \quad (3.20)$$

where f_c' is the concrete compressive strength; A_g refers to the cross-section area; A_s refers to the longitudinal reinforcement area.

Failure mode of undamaged UHPC column (UHPC-S-h1.5) under axial compression is shown in Fig. 3.20 (a). From numerical observation, under pure axial loading conditions, the column fails under end concrete crush. No flexural failure or shear failure was observed during or after axial compression tests. A similar observation is found in [102, 125]. For the axial loading capacity of undamaged UHPC columns, the numerical results shown in Fig. 3.21 remain above on the capacity calculated from Eq. (3.20). Similar experimental observations could also be found in [102, 125]. As shown in Fig. 3.21, the curve of the post-impact column started from 200 kN. The 200 kN axial load was applied prior to the impact test and kept constant during the test. Therefore, the axial load for the post-impact test started from 200 kN rather than 0 kN. Eq. (3.20) was the equation to calculate the maximum loading capacity of conventional concrete. Due to the lack of guidelines, there are no equations for UHPC. Moreover, the axial loading capacity calculated from the current design code is significantly low, and the numerical results are adopted as N_{max} in the present study.

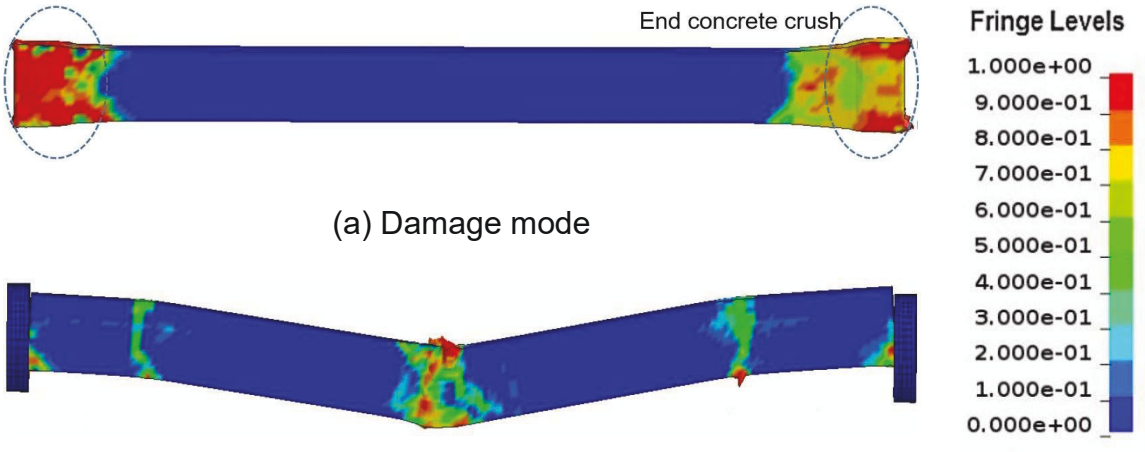

(a) Damage mode

(b) Flexural failure at mid span of the post-impact column

Fig. 3.20. Failure mode of the UHPC-S-h1.5 column

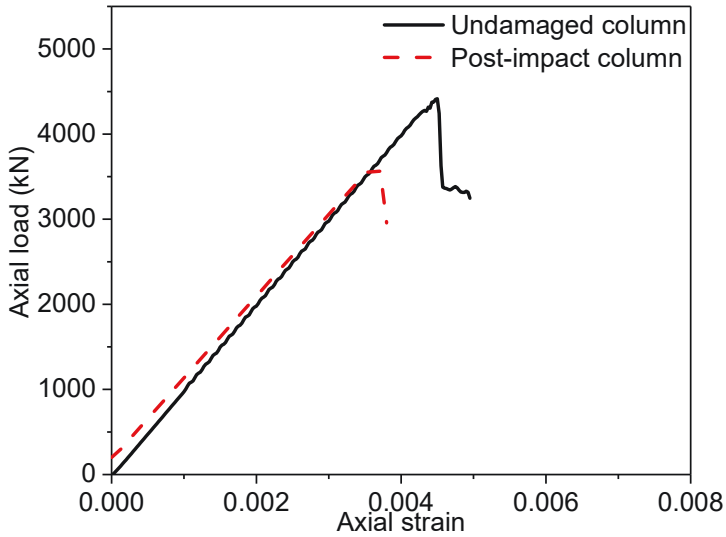

Fig. 3.21. Axial load-strain curves for the UHPC-S-h1.5 column

For residual axial loading capacity N_{re}, it was simulated by the post-impact numerical model. The numerical test setup was resented in Fig. 3.22. The column UHPC-S-h1.5 in the post-impact tests was resented in Fig. 3.20 (b). From numerical observations, the column which underwent 5886 kJ (400 kg impact mass and 5.42 m/s impact velocity) equivalence impact loading remains straight until the flexural damage

with rebar buckling suddenly occurred at mid-span. The load-deflection curve of the post-impact column was resented in Fig. 3.21, and the column preserved 81.9% of its original axial load-resistant capacity. In the current study, the damage degree was defined in three grades, that is, 20%, 40%, 60%. Moreover, D = 0 to 0.2, D = 0.2 to 0.4, D = 0.4 to 0.6 and D = 0.6 to 1 are defined as low damage, medium damage, high damage and collapse, respectively.

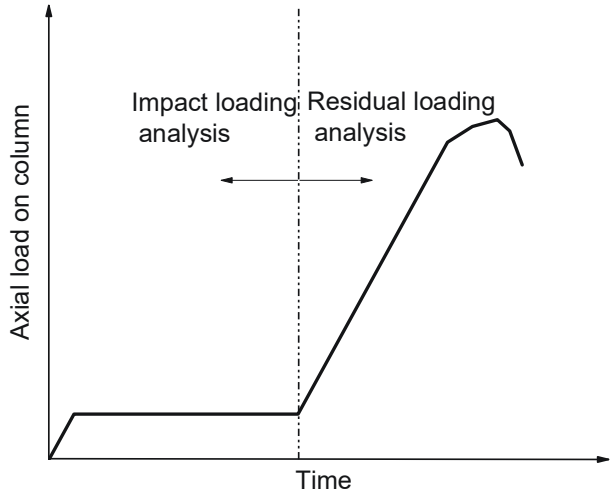

Fig. 3.22. Loading scheme on UHPC column

3.4.2 M-V diagram for the UHPC columns

Mass-velocity diagrams are adopted for quick investigations of structural damage under the given impact loading scenario. The values around damage boundaries will be adopted for a curve fitting. The M-V diagrams based on extensive numerical simulations of the rectangular UHPC columns (UHPC-S-h1.5 and UHPC-S-h1.25) are shown in Fig. 3.23.

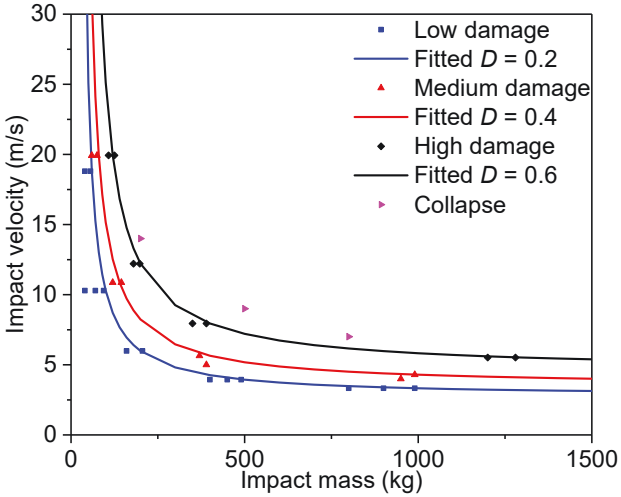

Fig. 3.23. Numerical results and fitting curves

For the fitted curves of M-V diagrams, they could be expressed analytically as

$$(M - M_O)(V - V_O) = A(M_O + V_0)^B \tag{3.21}$$

where M_O is the mass asymptote for damage index *D*; V_O refers to the velocity asymptote; *A* and *B* are constant values, affected by column. The values of parameters (M_O, V_O, *A* and *B*) for different damage levels are listed in Table 3.5. By comparing the values of parameters *A* and *B* with different damage levels, it is noted that *A* and *B* are almost the same. Therefore, the parameters *A* and *B* are assumed to be independent of damage index *D.* 4 and 1.5 are adopted for *A* and *B*, respectively.

D	M_O (kg)	V_O (m/s)	*A*	*B*
0.2	24.5	2.74	3.8	1.55
0.4	31.0	3.46	4.0	1.51
0.6	40.7	4.55	4.2	1.46

Table 3.5 Parameters *A* and *B* defined in the equation.

3.4.3 Parametric studies

With numerical models, further studies were conducted to investigate the influence of different values on the mass-velocity diagrams of rectangular UHPC columns. These parameters include different width, depth, height, concrete strength, longitudinal reinforcement ratio and axial loads. The range of these parameters is shown in Table 3.6. It is noted that since the UHPC columns experienced flexural damage during tests and the test results indicated that UHPC effectively resisted shear failure, the effect of stirrup is not considered in the current study.

Width *w* (mm)	Depth *d* (mm)	Height *h* (m)	Concrete strength f_c' (MPa)	Steel ratio (ρ)	Axial loads *N* (kN)
168	168	1.4	135	0	0
230	230	1.8	145	0.008	200
300	300	2.6	160	0.022	400

Table 3.6 Parameter range used in the parametric study.

3.4.3.1 Column width

The comparisons of the mass asymptote (M_O) and velocity asymptote (V_O) of the mass-velocity diagrams for UHPC columns with three different width levels (168 mm, 230 mm, 300 mm) are listed in Table 3.7. From Table 3.7, it is evident that with the increase in column width, both mass and velocity asymptotes of M-V diagrams are increasing. It is evident that column with a larger cross-section has higher impact resistance due to large mass and section modulus.

Width (mm)	*D* = 0.2		*D* = 0.4		*D* = 0.6	
	M_O (kg)	V_O (m/s)	M_O (kg)	V_O (m/s)	M_O (kg)	V_O (m/s)
168	24.5	2.74	31.0	3.46	40.7	4.55
230	26.4	2.98	36.7	4.33	46.1	5.42
300	28.7	3.01	43.1	4.74	53.1	5.82

Table 3.7 Column width effect.

3.4.3.2 Column depth

To investigate the influence of UHPC column depth on the M-V diagrams, three different column depths, i.e., 168, 230 and 300 mm are studied. The mass asymptote (M_O) and velocity asymptote (V_O) of the mass-velocity diagrams are listed in Table 3.8. With an increase in column depth, both mass and velocity asymptotes of M-V diagrams increase. Compared with width, column depth has more pronounced influence on the impact resistance.

Depth (mm)	*D* = 0.2		*D* = 0.4		*D* = 0.6	
	M_O (kg)	V_O (m/s)	M_O (kg)	V_O (m/s)	M_O (kg)	V_O (m/s)
168	24.5	2.74	31.0	3.46	40.7	4.55
230	31.8	3.28	44.7	5.03	62.8	6.78
300	42.4	4.77	70.1	7.83	104.3	11.3

Table 3.8 Column depth effect.

3.4.3.3 Column height

The influence of column height on the mass and velocity asymptotes of the M-V diagram is investigated. UHPC columns with three different heights (1.4, 1.8, 2.6 m) were tested, and values of two asymptotes are listed in Table 3.9. By comparison of the mass and velocity asymptotes, it is noted that, with increasing column height, both asymptotes slightly decrease. The results indicate that slender columns are more prone to impact induced flexural failure.

Height (m)	*D* = 0.2		*D* = 0.4		*D* = 0.6	
	M_O (kg)	V_O (m/s)	M_O (kg)	V_O (m/s)	M_O (kg)	V_O (m/s)
1.4	24.5	2.74	31.0	3.46	40.7	4.55
1.8	21.3	2.39	30.1	3.37	39.0	4.36
2.6	18.6	2.08	28	3.13	37.8	4.23

Table 3.9 Column height effect.

3.4.3.4 Concrete strength

UHPC with three different strength levels (135, 145, and 160 MPa) were studied. The M and V are listed in Table 3.10. From Table 3.10, it can be seen that concrete strength has a positive influence on the mass and velocity asymptotes. Because enhancing the concrete strength would improve column's bending resistance.

3.4.3.5 Longitudinal reinforcement

The results (Table 3.11) show that enhancing reinforcement ratio in compression can improve the M and V of the mass-velocity curve. Because the longitudinal reinforcement ratio will greatly improve the column's bending strength. It will also improve shear resisting strength and axial loading capacity. It is interesting to note that

even without longitudinal reinforcement, the UHPC columns preserve a good impact resistance, and this finding further highlights the benefits of using UHPC in protective structural design.

Strength (MPa)	*D* = 0.2		*D* = 0.4		*D* = 0.6	
	M_O (kg)	V_O (m/s)	M_O (kg)	V_O (m/s)	M_O (kg)	V_O (m/s)
135	24.5	2.74	31.0	3.46	40.7	4.55
145	25.0	2.79	31.8	3.56	42.1	4.71
160	25.3	2.83	33.3	3.73	43.2	4.84

Table 3.10 Concrete strength effect.

Reinforcement ratio	*D* = 0.2		*D* = 0.4		*D* = 0.6	
	M_O (kg)	V_O (m/s)	M_O (kg)	V_O (m/s)	M_O (kg)	V_O (m/s)
0	17.3	1.94	21.9	2.45	27.1	3.04
0.0036	21.8	2.44	27.8	3.11	35.5	3.96
0.008	24.5	2.74	31.0	3.46	40.7	4.55
0.018	28.5	3.18	39.2	4.38	59.3	6.63
0.022	29.9	3.34	41.1	4.59	61.0	6.82

Table 3.11 Reinforcement ratio effect.

3.4.3.6 Axial loads

The effect of axial loads on mass-velocity diagrams is evaluated by comparing the corresponding mass and velocity asymptotes for UHPC columns with different axial loads (0, 200, 400 kN). The results (Table 3.12) reveal that increasing axial loads

could increase mass and velocity asymptotes. However, it should be mentioned that this result is obtained based on that the range of the axial ratio is from 0 to 0.1. If the axial load ratio is larger than 0.1, this observation might not be true. This is because with the increased axial load level, the effect of P-Delta on flexural damaged column may no longer be negligible.

Axial loads (kN)	*D* = 0.2		*D* = 0.4		*D* = 0.6	
	M_O (kg)	V_O (m/s)	M_O (kg)	V_O (m/s)	M_O (kg)	V_O (m/s)
0	22.4	2.50	28.6	3.19	37.4	4.18
100	23.8	2.66	30.0	3.36	40.1	4.48
200	24.5	2.74	31.0	3.46	40.7	4.55
400	25.8	2.88	38.3	4.29	45.3	5.06

Table 3.12 Effect of axial loads on mass and velocity asymptotes.

3.4.4 Proposed formulae to generate M-V diagram

3.4.4.1 Derivations of the analytical formulae

With test data, proposed equations were proposed to calculate mass and velocity asymptotes of mass-velocity curves when the critical damage boundaries are 0.2, 0.4 and 0.6, respectively. The functions of the mass asymptotes $M_o(D)$ and velocity asymptotes $V_o(D)$ were derived through the least-squares fitting method, and they are derived in accordance with column width *w,* column depth *d*, column height *h*, concrete strength f_c', longitudinal reinforcement ratio in compression *ρ,* and axial loads, *N.* They are defined in Eqs. (3.22) - (3.24). Since the range of the column parameters is limited in the parametric studies, the range of parameters adopted for proposed analytical

formulae is defined as follow: 168 mm ≤ w ≤ 300 mm, 168 mm ≤ d ≤ 300 mm, 1.4 m ≤ h ≤ 2.6 m, 135 MPa ≤ f_c' ≤ 160 MPa, 0 ≤ ρ ≤ 0.022, 0 kN ≤ N ≤ 400 kN.

$$\begin{aligned} M_o(0.2) = \ & \exp\left(1.54w + 4.49d - 0.20h + 3.23\left(\frac{f_c'}{1000}\right) + 19.31\rho \right. \\ & \left. + 0.32\left(\frac{N}{1000}\right) + 1.78\right) \\ V_o(0.2) = \ & \exp\left(1.22w + 4.44d - 0.20h + 3.49\left(\frac{f_c'}{1000}\right) + 19.48\rho \right. \\ & \left. + 0.31\left(\frac{N}{1000}\right) - 0.4\right) \end{aligned} \tag{3.22}$$

$$\begin{aligned} M_o(0.4) = \ & \exp\left(2.53w + 6.16d - 0.08h + 2.85\left(\frac{f_c'}{1000}\right) + 22.86\rho \right. \\ & \left. + 0.78\left(\frac{N}{1000}\right) + 1.36\right) \\ V_o(0.4) = \ & \exp\left(2.50w + 6.12d - 0.09h + 2.67\left(\frac{f_c'}{1000}\right) + 22.49\rho \right. \\ & \left. + 0.79\left(\frac{N}{1000}\right) - 0.77\right) \end{aligned} \tag{3.23}$$

$$\begin{aligned} M_o(0.6) = \ & \exp\left(2.07w + 7.17d - 0.06h + 2.82\left(\frac{f_c'}{1000}\right) + 32.80\rho \right. \\ & \left. + 0.45\left(\frac{N}{1000}\right) + 1.50\right) \\ V_o(0.6) = \ & \exp\left(2.04w + 6.90d - 0.06h + 2.84\left(\frac{f_c'}{1000}\right) + 32.71\rho \right. \\ & \left. + 0.45\left(\frac{N}{1000}\right) - 0.64\right) \end{aligned} \tag{3.24}$$

In Eqs. (3.22) - (3.24), $M_o(D)$ is in kg; $V_o(D)$ is in m/s; f_c' is in MPa; w, d and h are in meters; N is in kN. Fig. 3.24 draws the mass-velocity curves derived from Eqs. (3.21) - (3.24) with the fitting curves shown in Fig. 3.23. It is noted that the mass-velocity curves calculated from proposed analytical formulae match well with the curves fitted from numerical data.

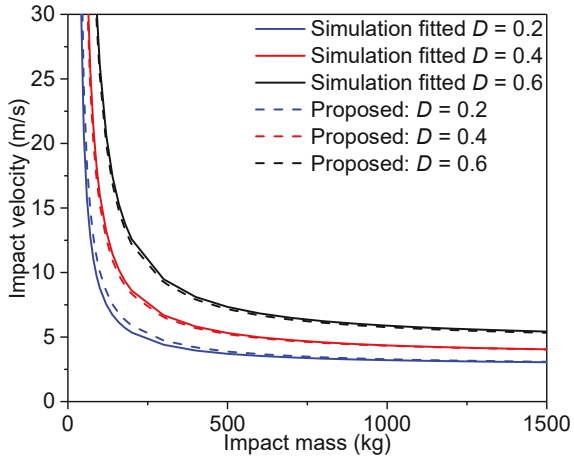

Fig. 3.24. Comparison of the fitting curves from numerical data and analytical formulae

3.4.4.2 Comparison with other experimental results

Since limited low-velocity impact tests were carried out for UHPC columns with square cross section, the analytical formulae Eqs. (3.21) - (3.24) were adopted for the drop weight tests on UHPC beams conducted by Yoo et al.[19]. In their study, four specimens (UH-N, UH-S-0.53%, UH-S-1.06% and UH-S-1.71%) were prepared and tested against repeated drop-weight impacts. Different test specimens contained different reinforcement ratio (0%, 0.53%, 1.06% and 1.71%). The compressive strength for UHPC is 152.5 MPa and all specimens were 2900 mm long with a cross section of 200 × 270 mm. For low-velocity impact tests, the test machine with a drop weight of 270 kg as well as a fixed impact velocity of 5.6 m/s was adopted, and the clear loading span was 2500 mm. The test results of residual displacement by 1st drop at mid-span for four specimens were 9.2 mm, 7.8 mm, 4.1 mm and 2.1 mm, respectively. The mass-velocity diagrams for four specimens were proposed by Eqs. (3.21) – (3.24) and drawn in Fig. 3.25. The column configuration included w = 0.2 m, d = 0.27 m, h = 2.5 m, f_c' = 152.5 MPa, N = 0 kN, ρ = 0 for (a), ρ = 0.0053 for (b), ρ =

0.0106 for (c), and ρ = 0.0171 for (d). As shown in Fig. 3.25, damage index D < 0.2 means the UHPC beams experienced low damage during low-velocity tests. Since no residual loading capacity tests were carried out for these post-impact beams [19], the support rotation damage criteria was adopted. The ASCE guideline provides response criteria for reinforced concrete. For support rotation θ (degree), θ ≤ 1, 1 < θ ≤ 2, and 2 < θ ≤ 4 were defined as low response, medium response and high response, respectively. For UHPC beams, the residual displacements at mid-span were 9.2 mm, 7.8 mm, 4.1 mm and 2.1 mm, respectively. Thus, the support rotations were 0.42, 0.36, 0.19, and 0.1, respectively. All support rotations are less than 1, which means the UHPC beams experienced a low level damage. Based on the above validation, it is believed that the mass-velocity diagram generated by proposed analytical formulae could predict the structural damage.

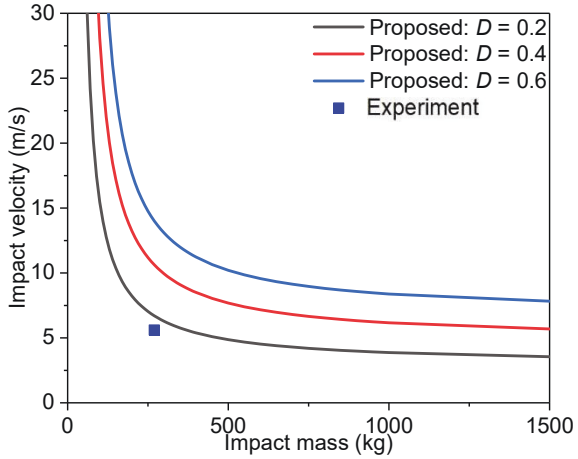

(a) Specimen 1

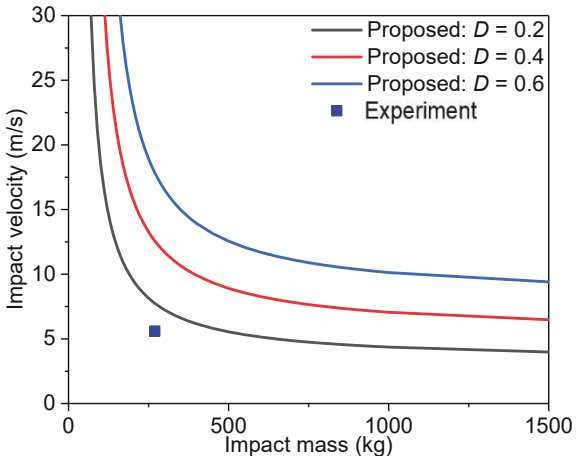

(b) Specimen 2

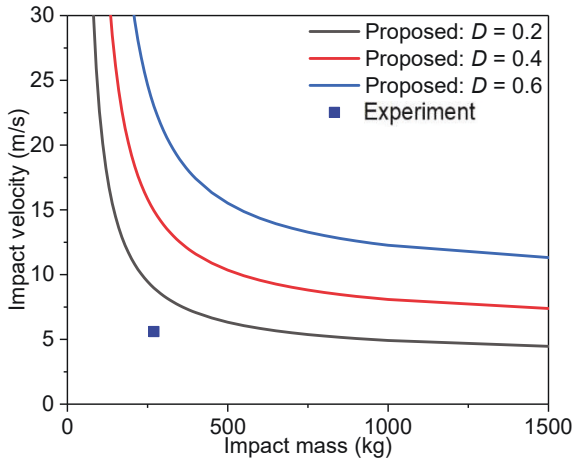

(c) Specimen 3

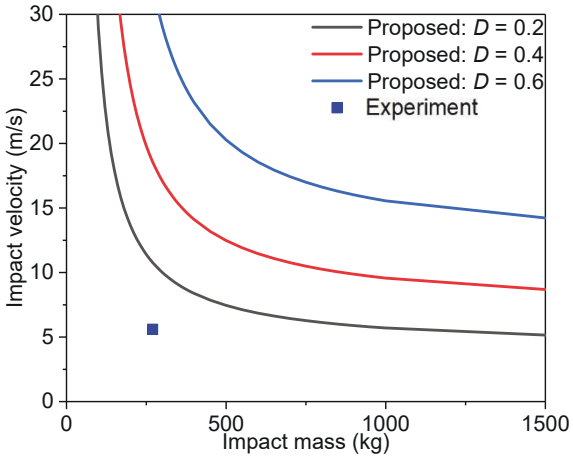

(d) Specimen 4

Fig. 3.25. Mass-velocity diagrams for the UHPC beams

3.5 Summary and Identification of the Gap

In this chapter, impact tests on reinforced UHPC and RC columns were studied by the drop weight machine. To evaluate the influence of cross-section shapes (square and circular) on both UHPC and RC columns, two specimen series (“S” and “C”) were prepared and tested. Then, the Continuous Surface Cap Material model (CSCM) for UHPC in LS-DYNA has been validated. The residual loading capacity of UHPC columns was assessed and used to define the column damage level. The mass-velocity diagrams based on this performance-based criterion were derived from extensive numerical simulations, and its analytical formulae were proposed. The main results yield the following conclusions.

1. Reinforced UHPC columns showed high impact resistance. From experimental observation, both square and circular RC columns experienced brittle shear failure with a large part of concrete fragmentation, while square and circular UHPC columns showed flexural response.

2. Numerical simulation with developed CSCM material model captures the damage patterns and impact force as well as displacement histories, especially for the UHPC specimens failing in flexural failure. Further study on the shear and tensile behaviour under triaxial loading condition is deemed necessary for a more comprehensive understanding of this emerging material.

3. Performance-based criteria, i.e., the residual loading capacity was used to assess the damage of the UHPC column after impact scenario. The proposed analytical equations can be used to generate the impact mass versus velocity diagram for quick assessment of UHPC column damage.

Chapter 4

Behaviour of Hybrid Fibre Reinforced Ultra-high Performance Concrete Beams under Impact Loading

4.1 Introduction

Recently, lots of studies are carried out to enhance the concrete strength. It was noted, with increasing the concrete strength, the brittleness becomes increasingly prominent. The incorporation of discontinuous short fibres could improve material toughness, fracture energy and ductility [102, 126-129]. Among all fibre reinforced concretes, the recently developed UHPC demonstrates superior compression strength, tension strength and ductility. The high micro-fibres content could mitigate crack propagation and bridge over the cracked concrete matrix, both of which are beneficial to the energy absorption capacity of UHPC subjected to dynamic and static loads [6, 130-134].

Several studies have indicated that the hybrid fibres with long and short fibres were observed to improve the flexural performance. However, most of these studies were paid attention to the influence of fibre hybridization on the behaviour of UHPC [14-16, 135-137], whereas fewer studies were carried out on the structural performance of UHPC members with hybrid fibres under dynamic loadings.

One notable feature of UHPC is its tensile post-cracking behaviour. Although main attention are paid to improving tensile properties, fewer studies were performed to quantify its post-cracking energy absorption capacity, which is also termed as fracture energy. Generally speaking, the fracture energy represents the area underneath the stress versus Cracking Opening Displacement (σ-COD) curve. To gain

this curve, a dedicated test was required. The ideal test method was the uniaxial tensile test, which could directly obtain the tension-softening curve of UHPC. However, the uniaxial tensile test is time-consuming, and the test is usually conducted through specialised equipment. Except for the direct tensile test, the three-point test conducted for prisms with a notch bottom has been adopted by many researchers. The experimental results were then inversed to σ-COD curve by means of analytical, empirical and numerical models. Amin et al. [138] determined σ-COD for FRC. The model can be characterized by two parts, including the calculation of the ascending branch until the ultimate strength and controlling steepness of the decreasing branch. Based on this model, the authors [139] calculated the σ-COD and fracture energy of FRC. Simo et al. [140] used the embedded discontinuity method (EDM) technique based on the numerical model to undertake the size-dependent fracture parameters and tension-softening behaviour of FRC prisms. Kang et al. [64] combined the analytical model and numerical study to gain the poly-linear tension-softening curves of UHPC, and then the simplified bi-linear softening curves were developed.

Until now, the influence of the hybridization of micro and macro straight steel fibres on the mechanical performance and impact resistance of UHPC members are not fully understood and therefore further investigation is required. For the research, to examine the effect of the hybrid straight fibres for mechanical properties of UHPC, three types of straight steel fibres with different lengths were adopted. The specific objectives include: (a) the compressive strength capacity and elastic modulus; (b) flexural strength and toughness. In addition, the σ-COD curve and fracture energy of UHPC incorporating various fibre hybridizations were developed through inverse analysis. Subsequently, UHPC beams with different hybrid fibre were cast and tested

with a drop-weight impact testing machine to characterize the dynamic impact resistance, including failure pattern and absorbed energy.

In the present study, the main objectives include: 1. Investigate the static performance with hybrid fibre and a single type of fibre reinforcement. 2. Develop the tensile softening curve and fracture energy of UHPC. 3. Study the effect of hybrid fibre reinforcements for dynamic behaviour of UHPC beams. 4. Evaluate the dynamic behaviour of UHPC beams against single and multiple impacts.

4.2 Experimental Test Program

4.2.1 Materials and preparations

42.5 Grade cement and silica fume were applied for cementitious mixture in present study. Density of the cementitious mixture were summarized in Table 4.1. Maximum particle size of silica fume is 0.2 μm, and it has the intergranular space filling effect to achieve high density. The w/b of 0.19 was implemented. Aggregates adopted dry and clean river sands with the size of 0.3-0.5 mm. Superplasticizer was used to improve fluidity. Nano-particles were applied to provide the nanoscale filling effect. Three types of micro straight steel fibres with various length (6, 10, 15 mm) were incorporated. The main properties of straight fibres were detailed in Table 4.2. Table 4.3 shows the four mixture proportions, including two single type fibre reinforcement and two hybrid fibre reinforcement at a constant 2.5% volume dosage. The mixture proportions were named as follow: (1) the letters “S”, “M” and “L” denote 6 mm short fibres, 10 mm medium fibres, and 15 mm long fibres, respectively. (2) The number afterwards represents the fibre volume percentage. S2.5 denotes the mixture with single short fibres (6 mm) at a 2.5% volume dosage. L1.5S1 refers to the mixture with hybrid long fibres (15 mm) at a 1.5% volume dosage and short fibres at a 1% volume

dosage. L1.5M1 represents the mixture with hybrid long fibres (15 mm) at a 1.5% volume dosage and medium fibres (10 mm) at a 1% volume dosage. L2.5 denotes the mixture with single long fibres at a 2.5% volume dosage.

Composition	CaO (%)	Al_2O_3 (%)	SiO_2 (%)	Fe_2O_3 (%)	MgO (%)	SO_3 (%)	K_2O (%)	C (%)	Density (kg/m^3)
Cement	62.74	6.11	22.19	3.46	2.98	2.52	-	-	3110
Silica fume	0.38	0.25	97.23	0.12	0.10	-	0.86	1.06	2150

Table 4.1 Material properties.

Fibre type	d_f (mm)	l_f (mm)	Aspect ratio (l_f/d_f)	Density (g/cm^3)	f_{ft} (MPa)	E_f (GPa)
Smooth fibre	0.20	6/10/15	30/50/75	7.8	>2850	200

where, d_f = fibre diameter, l_f = fibre length, f_{ft} = tensile strength of fibre, E_f = elastic modulus of the fibre.

Table 4.2 Steel fibres.

The mixer is the CMP500 mixer from CO-NELE Company with a maximum capacity of 500 L and mixing power of 18.5 KW. The amount of each component could be obtained through calculating the volume of designed specimens. Cement, nanoparticles, river sands and silica fume were first dry mixed for around 8 min at a speed of 12 revolutions per minute. Then, the superplasticizer and water were gradually poured and mixed for another 8 min. When the fresh concrete showed good

flowability, the fibres were slowly dispersed by hand, and the mixer remained at the speed of 6 revolutions per minute. After casting, the specimens were ambient cured for 36 hours prior to demolding. Then, steam curing with high temperature (80 degrees) was conducted for 48 hours after demolding. Finally, all specimens were curing until testing.

Series	Relative weight ratios to cement				Steel fibre (V_f, %)		
	Cement	Fine aggregates	Nano-particles	Silica fume	15mm fibre	10mm fibre	6mm fibre
S2.5	1.00	1.37	0.03	0.30	0%	0%	2.5%
L1.5S1	1.00	1.37	0.03	0.30	1.5%	0%	1%
L1.5M1	1.00	1.37	0.03	0.30	1.5%	1%	0%
L2.5	1.00	1.37	0.03	0.30	2.5%	0%	0%

where, V_f refers to fibre volumetric ratio.

Table 4.3 Mixture proportions of UHPC.

4.2.2 Material test setup and instruments

4.2.2.1 Uniaxial compressive tests

To investigate the compressive behaviour (e.g., ultimate compressive strength, stress-strain curve and elastic modulus) under static loading, the cylindrical specimens with a 200 mm height and a 100 mm diameter were tested in a group of three. The final results were averaged from tests. The cylindrical specimens were tested by the hydraulic machine. During test, a linear increased compression force was adopted until the specimen failure. Fig. 4.1 (a) presents the setup of uniaxial compressive tests. The deformation of the specimens was averaged from two dial indicators installed on

both sides of the test specimen. Strain gauges were attached to the specimens to measure elastic modulus.

4.2.2.2 Four-point bending tests

To evaluate performance of the UHPC mixture, the prisms with a 100 mm x 100 mm square cross-section size and a 400 mm span were cast and tested through the hydraulic machine. Average flexural strength from two samples in each batch was reported. Two-stage loading scheme was applied for the prism specimens. First, a linearly increased force used at 0.1 kN/s until 10 kN. Then, a compression load controlled by the deflection at 0.3 mm/min was exerted until the specimen damage. Fig. 4.1 (b) shows the test setup for four-point bending tests. Two parallel dial indicators installed on both sides of each beam were applied to obtain the average central deflection.

4.2.2.3 Three-point flexural tests

Three-point tests were adopted to derive the discrete relationship between crack opening distance and stress and quantify UHPC fracture energy. The prisms with a 100 mm x 100 mm square size and 0.4 m span were cut with a notch via a diamond cutter. The notch had a width of 4 mm and a depth of 20 mm. The testing device and loading scheme were set as the same as the four-point tests. Average flexural strength from two samples in each batch was reported. Fig. 4.1 (c) shows the test setup and equipment. The mid-span vertical deflection was recorded by two dial indicators. The CMOD was recorded via two laser displacement sensors. The measurement point was kept at the same height as the beam bottom face of. The CMOD of the beam was calculated through the geometrical equivalence.

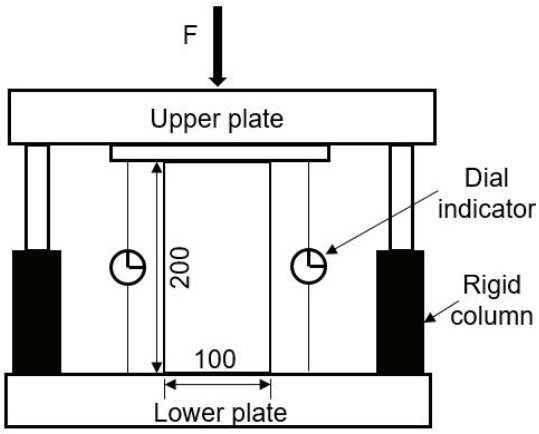

(a) Compression setup

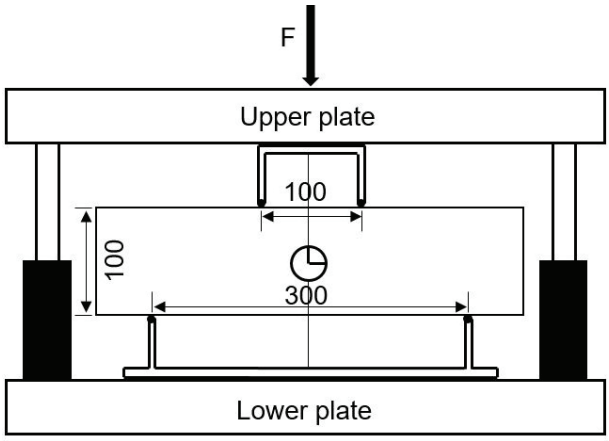

(b) Four-point setup

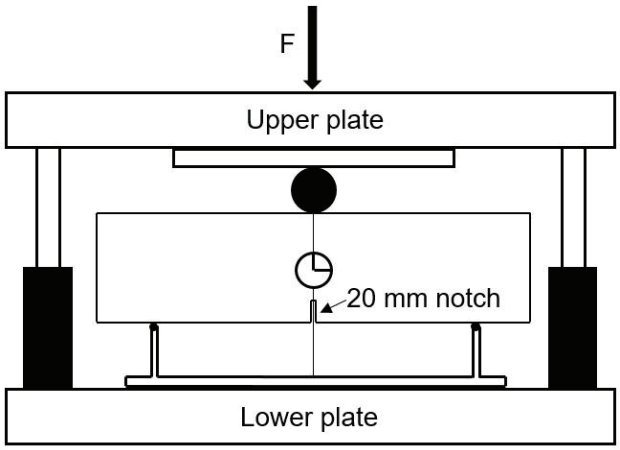

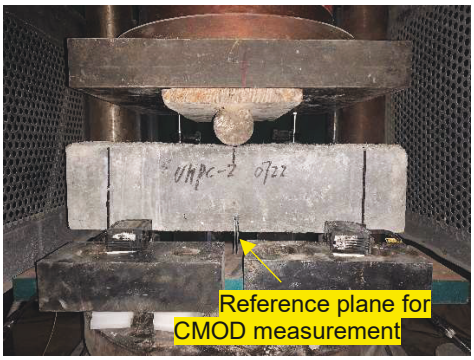

(c) Three-point bending test

Fig 4.1. Material mechanical property test setups

4.2.3 Drop hammer impact test

4.2.3.1 Detail of test specimens

Table 4.4 shows five large-sized UHPC beams involved in the impact tests. These test specimens were grouped into three pairs according to different fibre hybridization. The meaning of letters “S”, “M”, “L” and the number afterwards is the same as that in mechanical tests. The letters “a” and “b” are applied to distinguish the identical specimens in each pair. For UHPC beams with hybrid fibres (L1.5M1 and L1.5S1), each pair included identical specimens, cast simultaneously with the same concrete batch.

Specimens had a 168 × 168 mm square cross-section and 2 m span. The reinforcement layout and geometric configuration are presented in Fig. 4.2. The bars were placed symmetrically in the four corners and spanning the entire length. Deformed bars with a 12 mm diameter were adopted as longitudinal bars. A 25 mm protective cover was adopted. Closed stirrups with a 200 mm spacing and a 10 mm diameter were applied. The performance of reinforcing bars are concluded in Table 4.5.

Beam	Steel fibre (%)			$f'_{c,cyl}$ (MPa)	Drop hammer	
	15 mm fibre	10mm fibre	6 mm fibre		*h* (m)	v_0 (m/s)
L2.5-a	2.5	0	0	147.1	1	4.43
L1.5M1-a	1.5	1	0	134.7	1	4.43
L1.5M1-b	1.5	1	0	134.7	0.05/0.5/0.5	0.99/3.13/3.13
L1.5S1-a	1.5	0	1	129.5	1	4.43
L1.5S1-b	1.5	0	1	129.5	0.05/0.5/0.5	0.99/3.13/3.13

where, $f'_{c,cyl}$ refers to uniaxial compressive strength for cylindrical specimens; *h* refers to drop hammer height; v_0 refers to impact velocity.

Table 4.4 Summary of test specimens.

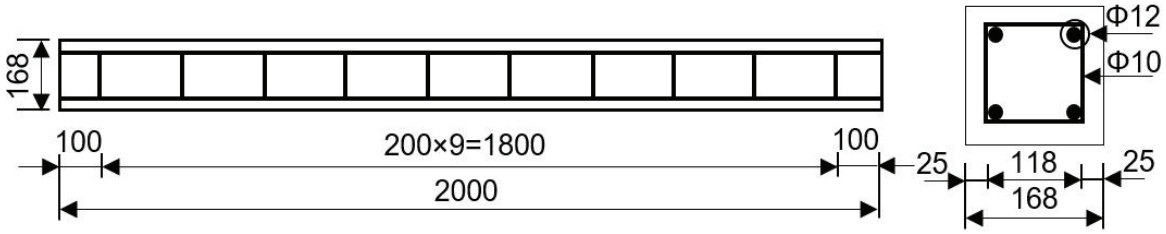

Fig. 4.2. Specimen dimensions (unit: mm)

	Density (kg/m^3)	Yielding strength (MPa)	Elastic modulus (GPa)	Diameter (mm)	Poisson's ratio
Long bar	7800	500	198	12	0.27
Stirrup	7800	300	198	10	0.27

Table 4.5 Properties of reinforcing bars.

4.2.3.2 Test setup

Fig. 4.3 shows a schematic illustration of the drop hammer impact testing machine. In general, the setup includes three parts: the drop-hammer impact system, measuring system and specimen support system. The drop-hammer impact system includes a hemispherical indenter, drop hammer frame, load cell and guide rails. A maximum release height of 5 m was designed for the drop hammer machine. The designed impact energy is attained through adjusting the height of the drop hammer. In the present study, a hemispherical indenter with diameter of 0.1 m was applied. Mass of the drop weight is 641 kg. For "a"-series specimens, the specimens were subjected to one single impact. The drop hammer fell from the height of 1 m, resulting in a 4.43 m/s impact velocity. For "b"-series specimens, the specimens were subjected

to multiple impacts. The beams were first tested with an impact from a height of 0.05 m (0.99 m/s), followed by two tests with an impact height of 0.5 m (3.13 m/s).

The fully fixed boundary on the column was provided by the steel clamping devices. In the test setup, the beam has a clear span of 1.4 m by leaving an overhang of 0.05 m at each end. The clamping device has a length of 0.25 m at two ends. The overhangs were intended to simulate the fully anchored longitudinal bars at supports. The beams were placed on the steel clamping devices designed to achieve clamped boundary. The lower part of clamping devices was supported by heavy steel pedestals fixed to floor. Upper part of clamping device was compressed by the 30-mm-thick steel plates. The steel plate was fixed to the steel pedestal through four 32-mm-diameter high strength steel bars and screw caps at each support.

For the measuring system, the data collected were captured at a 100 kHz sampling rate by a data acquisition system. The impact force histories was recorded by the load cell embodied in frame. The lateral displacements of the beams were monitored using two LVDTs. To protect the LVDTs, the LVDT-1 and LVDT-2 were placed 530 mm and 240 mm away from the boundary. A camera (Model: Phantom V310) is applied to measure dynamic process at a frame rate of 2500. In addition, the time history of lateral displacement at mid-span could be collected by the high-speed camera and compared with those obtained from the LVDTs.

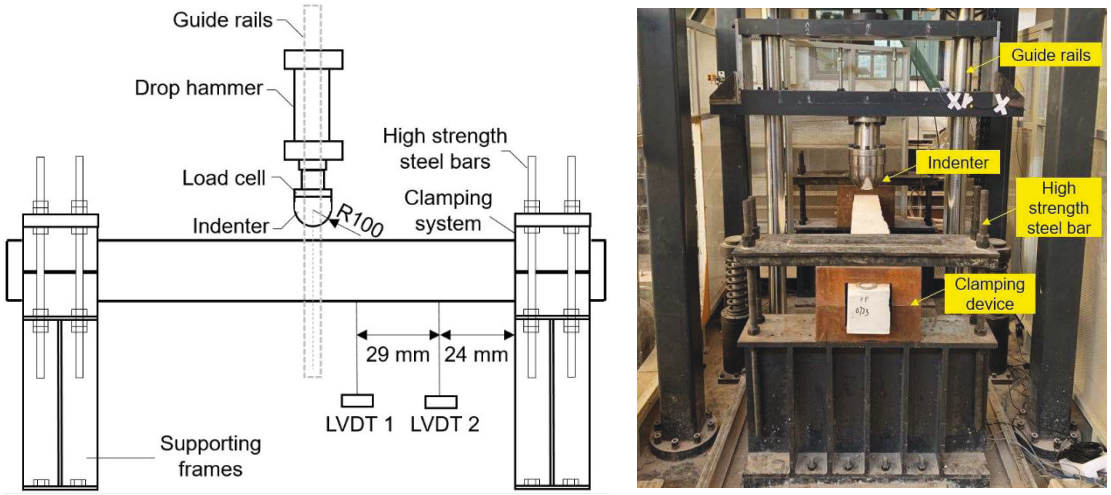

(a) Schematic illustration of test setup (b) Practical test setup

Fig. 4.3. Low-velocity drop hammer impact test setup

4.3 Material Test Results and Discussion

4.3.1 Compressive behaviour

The measured ultimate compression strengths from test beams are concluded in Table 4.6. The highest compressive strength was 147.1 MPa for prism L2.5, which was 18.2%, 11.9%, and 8.4% higher than S2.5, L1.5S1, and L1.5M1 specimen, respectively. The average stress-strain curve of cylindrical UHPC with hybrid fibres was presented in Fig. 4.4. Elastic modulus can be obtained by the stress-strain response according to ASTM C469M [141], and can be calculated by applying the equation:

$$E_c = \frac{0.4 \times f_{cu} - f_{c1}}{\varepsilon_2 - 0.00005} \quad (4.1)$$

where f_{cu} refers to the ultimate compressive stress; f_{c1} refers to the stress corresponding to the longitudinal strain of 0.00005; ε_2 refers to the longitudinal strain. Calculated elastic modulus for S2.5, L1.5S1, L1.5M1, and L2.5 were 44.2 GPa, 46.5 GPa, 48.3 GPa, and 52.1 GPa, respectively. For UHPC specimens with the same fibre

content, the longer fibre enhanced both elastic modulus and compressive strength. Yu et al. [142] evaluated the compressive behaviour of UHPC specimens reinforced with hybrid steel long length (13 mm) and short length (6 mm) fibres. It was observed that the sample with single long fibres (2 vol.%) and the sample with hybrid macro (1.5 %) and micro fibres (0.5 %) exhibited higher compression strength (around 140 MPa). With more short fibres incorporated, the compressive strength pseudo-linearly decreased. The sample with short fibres (2 vol.%) showed the lowest compressive strength (117.1 MPa). This is mainly because, compared to long steel fibres, the short fibres are ineffective in mitigating the propagation of macro-fibres. In addition, the long fibres have a larger bonding area between the fibres and the concrete matrix [16].

Unlike conventional concrete showing curved line before the peak stress, the UHPC material exhibited almost linear strength increment. The reason for the nonlinear stress-strain relationship prior to the peak stress because of the interfaces among the cement paste and aggregate. With increase in the stress, concrete starts to develop internal micro-cracking at those interfaces, and hence the stress-strain curve starts to bend over. When the applied stress increases beyond about 70% of the ultimate concrete strength, mortar cracking connecting the interfacial cracks initiates, and the stress-strain curve bends over at an increasing rate. UHPC presents a more homogeneous structure due to the elimination of large sized aggregates. Micro-fillers such as silica fume improve interfacial bonding. A large amount of steel fibres also contributes to the bridging effect over micro-cracking. These factors lead to a more linear stress-strain behaviour under compressive prior to peak stress. In the previous study on similar steam cured UHPC, the stress-strain relationship reaches 80 of the compression strength [143].

Series	Peak stress (MPa)			Average peak stress (MPa)	Standard deviation (MPa)
	1	2	3		
S2.5	112.5	129.8	118.7	120.3	7.2
L1.5S1	124.3	128.5	135.8	129.5	4.8
L1.5M1	124.3	144.5	135.2	134.7	8.3
L2.5	145.8	142.7	152.7	147.1	4.2

Table 4.6 Compression test results.

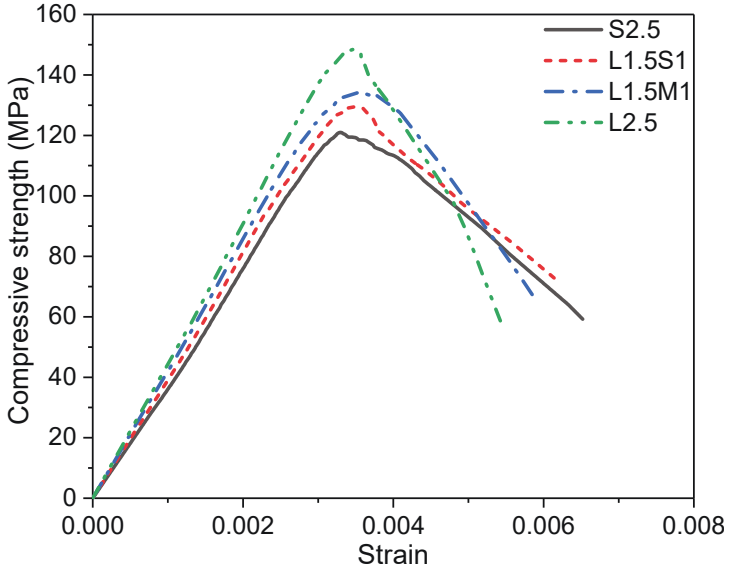

Fig. 4.4. Average compressive result

4.3.2 Flexural behaviour

4.3.2.1 Test results

Fig 4.5 presents result curves of four-point tests. To gain the average data, the displacement was first assumed to add in 1 μm increments. Subsequently, the corresponding force was estimated through linear interpolation. Finally, the force was

averaged from the measured data at the identical deflections in all the samples with the same material mixture. Regarding ultimate force and post-peak ductility, the flexural performance of UHPC prisms with hybrid fibres is higher than UHPC prisms with a single type of fibre reinforcement. Replacing 1% of the long fibres with short fibres (L1.5S1) led to an important improvement in flexural properties. The prisms using the short fibres (S2.5) had lower flexural performance than that using the long fibres (L2.5).

For the UHPC prisms under four-point loading, the flexural strength can be expressed by applying the equation [144]:

$$f = \frac{PL}{bD^2} \tag{4.2}$$

where, *P* is the externally applied force; *D* refers to depth; *b* refers to width; and *L* refers to clear span. The ultimate flexural strengths f_u and displacements δ_u at the ultimate flexural strength are concluded in Table 4.7. The mixture with hybrid long and short fibres had noticeably improved values of f_u and δ_u over the other UHPC prisms. The largest f_u of 29.21 MPa was obtained for L1.5S1, which was about 11.8% and 27.9% higher than that for the L1.5M1 and L2.5 prisms, respectively. The prism S2.5 exhibited the lowest f_u, 19.29 MPa, which is 18.4% lower than that of the L2.5 prism.

Series	Four-point tests		Three-point tests				
	f_u (MPa)	δ_u (mm)	f_u (MPa)	δ_u (mm)	CMOD_u (mm)	f_{LOP} (MPa)	CMOD_{LOP} (mm)
S2.5	19.29	1.01	20.57	0.95	0.52	16.89	0.0154
L1.5S1	29.21	2.13	30.92	1.88	1.46	15.96	0.0148
L1.5M1	26.12	1.78	27.17	1.38	1.17	15.61	0.0147
L2.5	22.83	1.65	23.35	1.28	1.01	15.25	0.0143

Table 4.7 Summary of flexural strength of UHPC prisms.

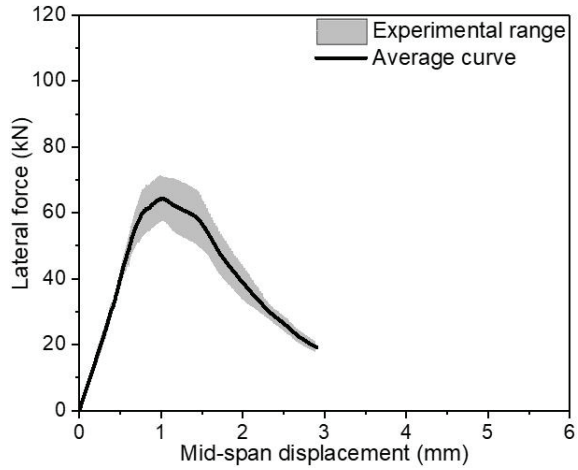

(a) S2.5

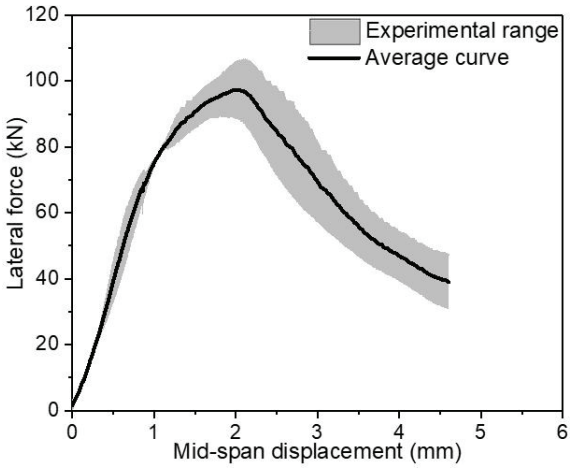

(b) L1.5S1

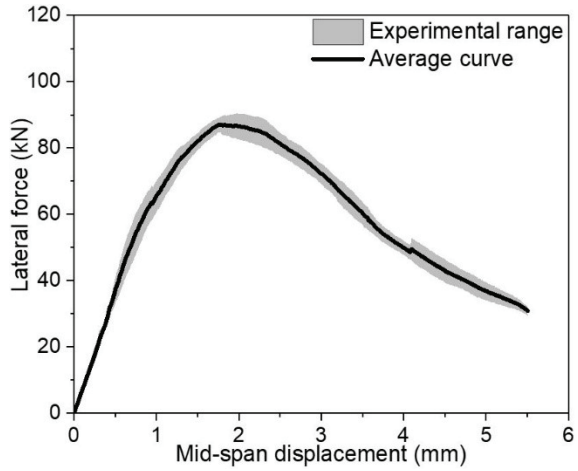

(c) L1.5M1

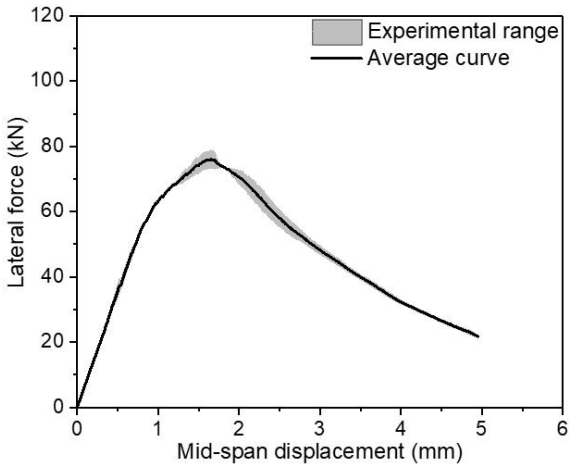

(d) L2.5

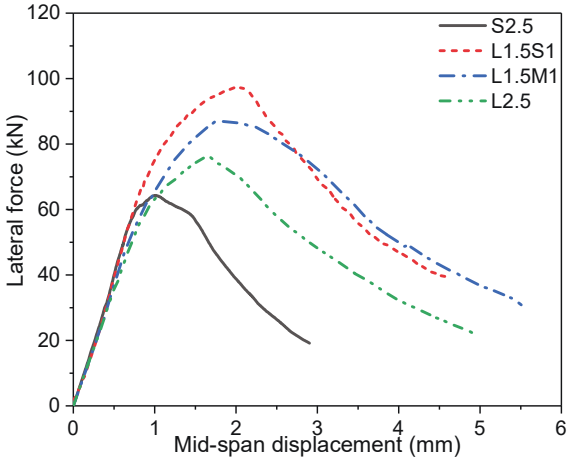

(e) Comparison of UHPC with different fibre reinforcement

Fig. 4.5. Force versus mid-span deflection curves

The three-point flexural tests were adopted to quantify the material fracture energy. Fig 4.6 shows the lateral force versus mid-span deflection and CMOD, respectively. In terms of flexural performance, three-point test results also highlighted that the mixture with hybrid fibre had a better performance than that reinforced with a single type of fibre. Relationship of force and CMOD in the early loading phase is illustrated in Fig 4.7. The point of the limit of proportionality (LOP) was used to define the first cracking point in the present research. All UHPC prisms demonstrated deflection hardening after LOP. The values of CMOD and force at LOP were almost the same for UHPC prisms at the identical volume fraction.

For UHPC notched prisms under central point loading, the flexural stress can be expressed using the equation [145]:

$$f = \frac{3PL}{2b(D - a_0)^2} \tag{4.3}$$

where, a_0 refers to depth. Flexural strength and its corresponding displacement at the points of ultimate force and LOP are listed in Table 4.7. Considering crack was triggered by the matrix and relatively independent of the fibre mixture [16, 139], an averaged initial crack strength, f_{LOP} of 15.93 MPa and the corresponding crack mouth opening distance CMOD_{LOP} of 0.0148 were obtained for all UHPC prisms.

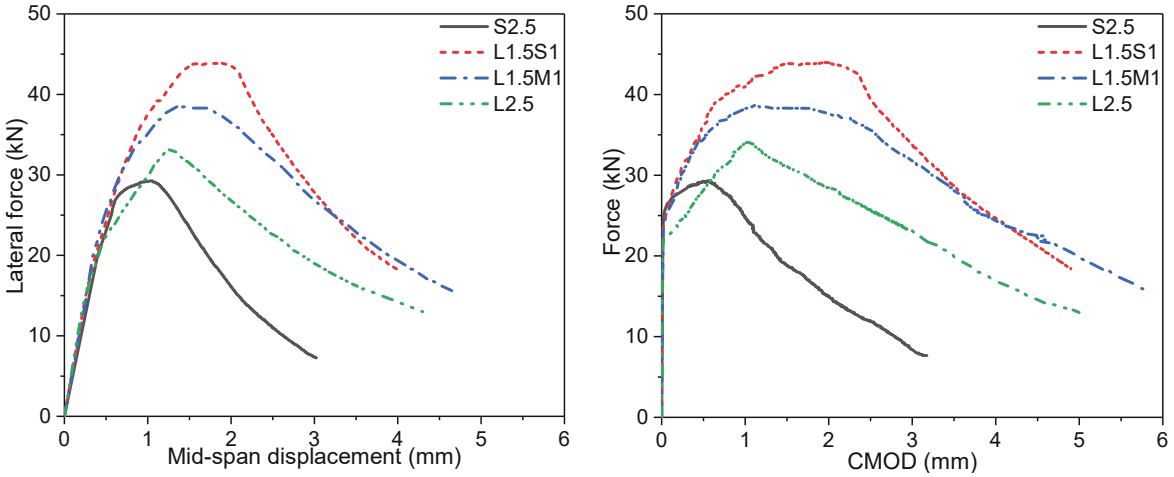

(a) Force versus displacement (b) Force versus CMOD

Fig 4.6. Results of three-point tests

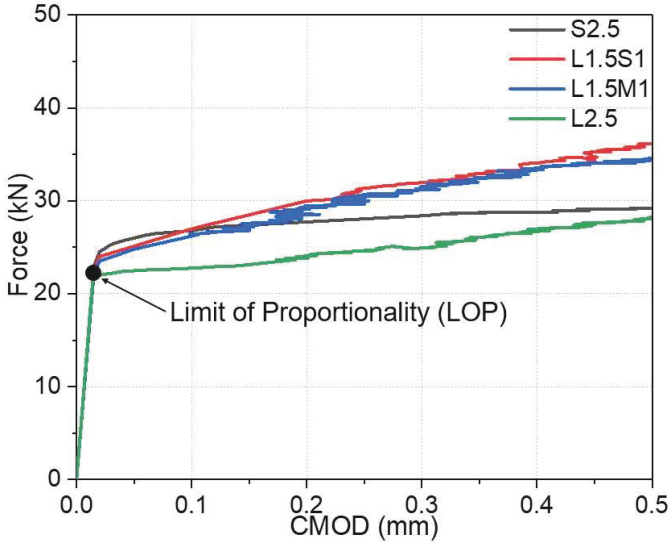

Fig. 4.7. Initial force versus CMOD curve

4.3.2.2 Toughness

Toughness was referred to area under force versus deflection curve (Fig. 4.5) of four-point tests up to a certain displacement point and applied to quantify the energy absorption capacity. According to ASTM C1609M [146], the toughness at two displacement points, including *L*/150 (2 mm) and *L*/600 (0.5 mm) were first

investigated. Then, the toughness at an extra displacement point of *L*/60 (5 mm) was determined since the strain-softening behaviour of the present UHPC prisms shows a superior energy absorption capacity even at a large displacement. Fig. 4.8 shows the toughness at three displacement points. At the displacement point of *L*/600, the UHPC prisms with short fibres had the largest toughness, and the toughness slightly reduced when replacing short fibres with medium and long length-fibres. Yoo et al. [7] experimentally evaluated flexural performance of UHPC with hybrid fibres. It was noted that replacing the long fibres with medium and short fibres slightly enhanced the toughness at the displacement point of *L*/600. For UHPC prisms with the constant fibre content, the prisms with shorter fibres would increase the fibre number and decreased the fibre spacing at the crack surface, which slightly increased post-cracking stiffness. For displacement points of *L*/150 and *L*/60, the toughness of prisms reinforced with hybrid fibres is larger than that with a single type of fibres reinforcement. In addition, the largest toughness at the deflection point of *L*/60 was 309.7 kNmm for L1.5S1, approximately 5%, 25%, 59% higher than L1.5M1, L2.5 and S2.5, respectively.

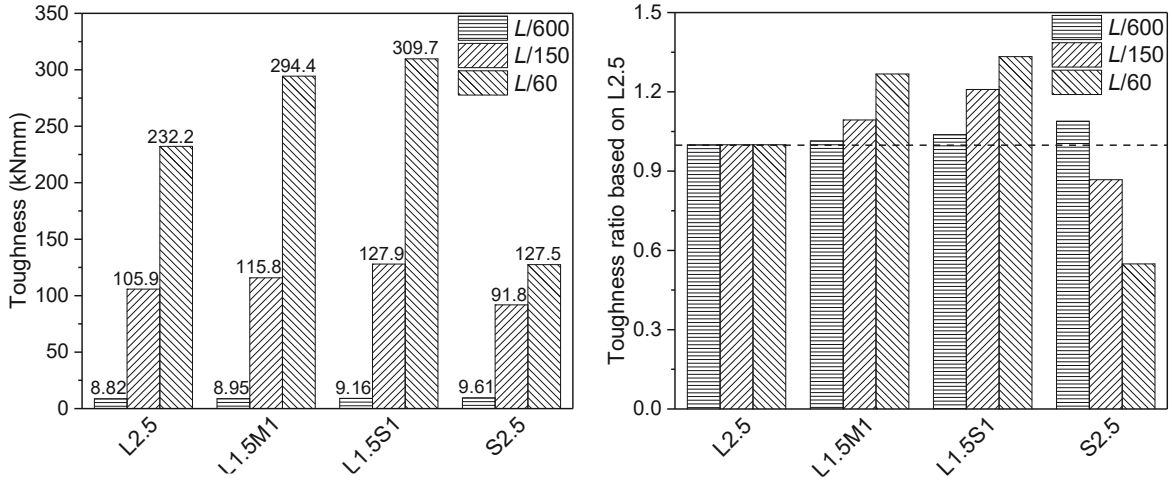

(a) Toughness (b) Toughness ratio based on L2.5

Fig. 4.8. Toughness at various displacement points

4.3.2.3 Fracture energy

In conventional concrete, the flexural strength decreases rapidly after the occurrence of initial crack. However, in UHPC, after crack initiation, the steel fibres bridge over the cracks, and some residual strength is available. Flexural strength is inadequate to exactly explain the failure mechanism of UHPC. In the literature, analytical models based on the inverse analysis have been proposed over the last two decades to find stress (σ)-crack opening distance (COD). The inverse analysis used the force-CMOD curves from the three-points flexural tests, and this approach was later extended to engineered cementitious composites (ECC) [147] and steel fibre reinforced concrete (SFRC) [148-150].

In general, for the inverse analysis, the first step is assuming the shape of the σ-COD curve. If the σ-COD curve is complex, lots of parameters need to be determined. The following iteration process becomes time-consuming. According to the JSCE [151] and previous studies [7, 64], a simplified shape of post-cracking curves of UHPC was determined in the present study and shown in Fig. 4.9. Then, as shown in Fig. 4.10 (a), the i+1 th point in the σ-COD curve was determined by fitting the i+1 th point in the force-CMOD curve, calculated through sectional analysis, with the experimental results.

Fig. 4.10 (b) shows the sectional analysis applied in the inverse analysis. *D* represents the total depth of the prism. θ represents the plane rotation of the prism. d_e represents the depth without notch. αd_e represents the crack length. βd_e represents the distance between notch root and neutral axis. ω represents the crack width at the notch root. The measurement point (CMOD) was at the mouth of the notch rather than the root of the notch. On the compression side, with progressive crack

opening, the neutral axial rises in the section. The compressive stress σ_c is linearly-elastic and calculated by the following equation:

$$\sigma_c(x) = f_{ct} \times \frac{x - \beta d_e}{(\beta - \alpha) d_e} \tag{4.4}$$

where, f_{ct} represents the tensile strength of UHPC when the occurrence of the first crack. On the tension side, for the part of the prism (i.e., from βd_e to αd_e), the concrete was intact and carrying tension. The portion of tension stress σ_{tc} is calculated by the following equation:

$$\sigma_{tc}(x) = f_{ct} \times \frac{\beta d_e - x}{(\beta - \alpha) d_e} \tag{4.5}$$

Below the αd_e, the concrete is cracked, and the steel fibres carried post-crack tension stress σ_{tf}. This value was found from developed σ- ω curve. According to geometry, COD $\omega(x)$ at the level x is calculated by the following equation:

$$\omega(x) = \frac{\alpha d_e - x}{\alpha d_e} \times \omega \tag{4.6}$$

The equilibrium of forces in the whole section is:

$$\int_0^{\alpha d_e} \sigma_{tf}(x) b \mathrm{dx} + \int_{\alpha d_e}^{\beta d_e} \sigma_{tc}(x) b \mathrm{dx} + \int_{\beta d_e}^{d_e} \sigma_c(x) b \mathrm{dx} = 0 \tag{4.7}$$

The equilibrium of moments in the whole section is:

$$\int_0^{\alpha d_e} \sigma_{tf}(x)(\beta d_e - x) b \mathrm{dx} + \int_{\alpha d_e}^{\beta d_e} \sigma_{tc}(x)(\beta d_e - x) b \mathrm{dx} + \int_{\beta d_e}^{d_e} \sigma_c(x)(x - \beta d_e) b \mathrm{dx} = M \tag{4.8}$$

where, b represents the width of the prism. For the three-point bending, the relationship of the COD (ω) and the externally applied moment (M) are calculated [152].

The sectional analysis could be done through Eqs. (4.4) - (4.8) to determine its external applied bending moment, M, and corresponding crack opening distance, ω. As shown in Fig. 4.10 (c), considering rigid body rotations about the crack height (αd_e), COD can be related to the in plane rotation of the prism (θ), which is $\mathrm{COD} = 2 \times \alpha d_e tan\theta$. The deflection of the notch can be expressed as: $\Delta_n = a_0 sin\theta$. CMOD is the sum of these two components ($\mathrm{COD} + 2\Delta_n$). Then, the required external applied force, P, and crack mouth opening distance, CMOD are taken as:

$$P = \frac{4M}{L}$$
$$\mathrm{CMOD} = 2 \times (\alpha d_e tan\theta + a_0 sin\theta) \tag{4.9}$$

where, L represents the clear span; a_0 represents the depth of the notch.

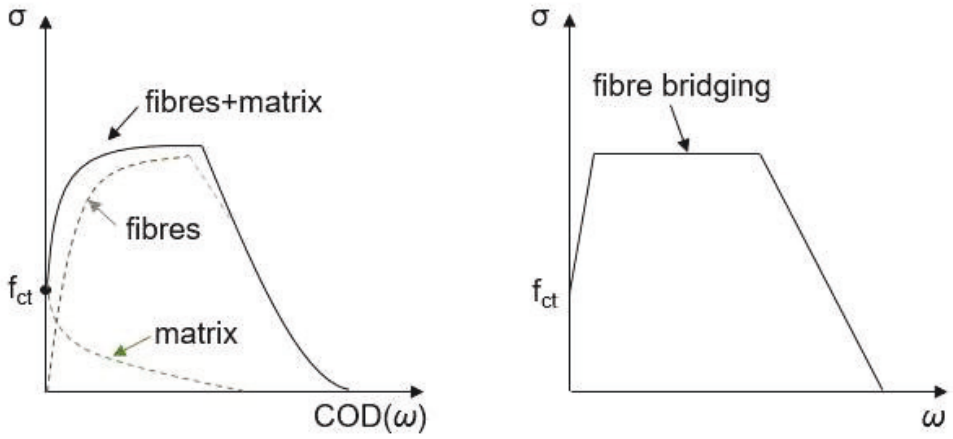

Fig. 4.9. Stress and COD (ω) for UHPC

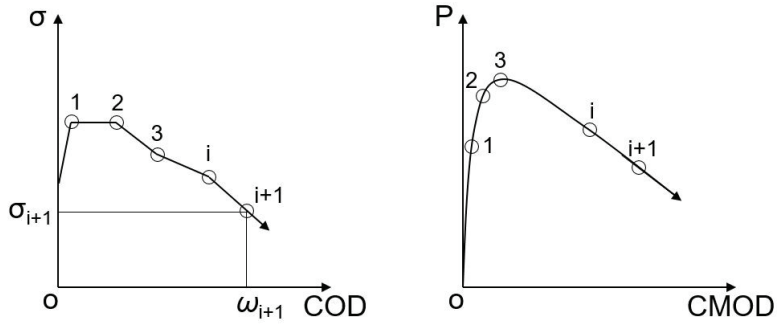

(a) Inverse analysis

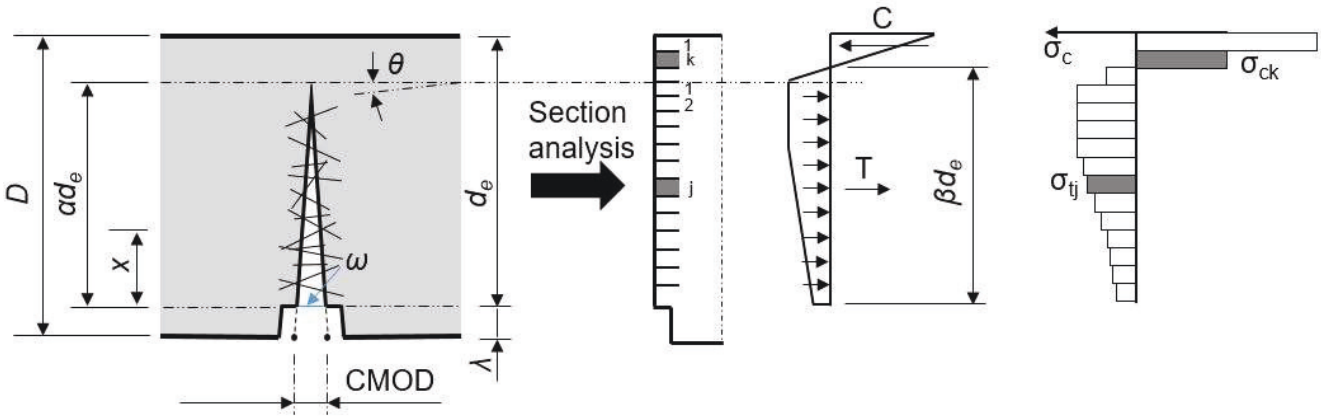

(b) Sectional analysis using slices

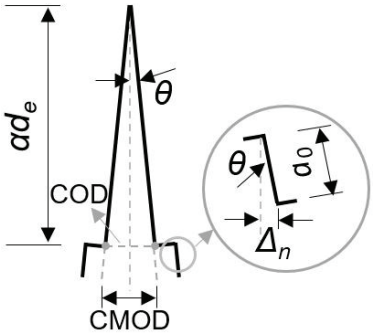

(c) Crack propagation in the UHPC prism

Fig. 4.10. Incremental procedure adopted in inverse analysis

The specific steps of inverse analysis include:

i. Suppose the value of the post-crack tension stress, σ_i at its corresponding crack opening distance, ω_i.

ii. Suppose the length of the crack, αd_e.

iii. Suppose the depth of the neutral axis, βd_e.

iv. Iterate on the depth of the neutral axis to satisfy the equilibrium of forces (i.e., Eq. (4.7)).

v. Calculate the bending moment, M (i.e.. Eq. (4.8)).

vi. Calculate the externally applied force, P, and CMOD (i.e.. Eq. (4.9)).

vii. Match the analytical and experimental force-CMOD curves by adjusting the post-crack tension stress, σ_i and repeat from step (i).

viii. Increment crack opening distance, ω_{i+1} and repeat from step (i) to complete the force-CMOD curve.

The fracture energy is area under the developed σ-COD curves. Fig. 4.11 shows the developed σ-COD curves. The analytical force-CMOD curves gained from inverse analysis procedure along with experimental force-CMOD curves are also shown in Fig. 4.11. The fracture energy of S2.5, L2.5, L1.5M1 and L1.5S1 was 12.41, 28.49, 33.13 and 35.67 N/mm.

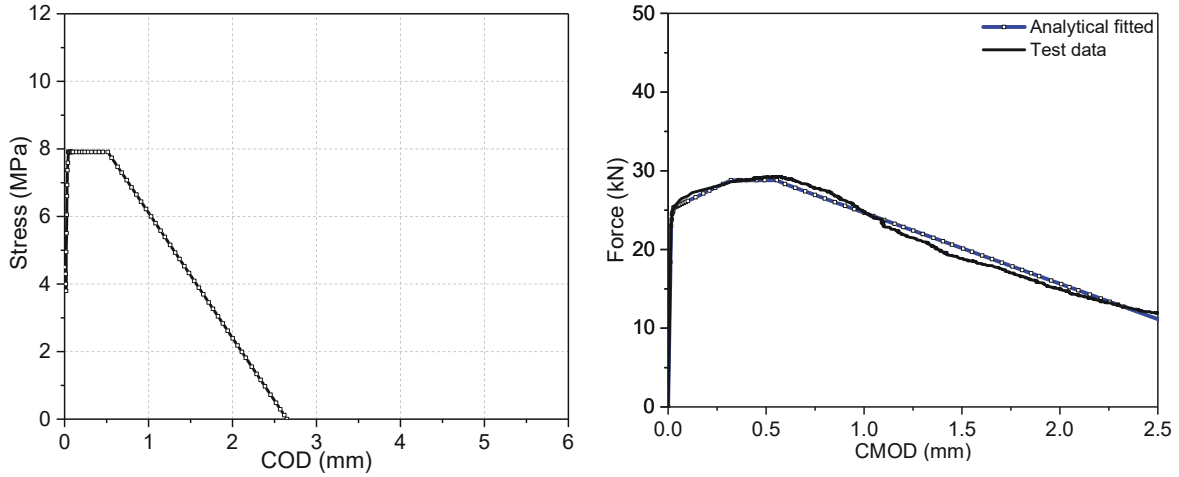

(a) S2.5

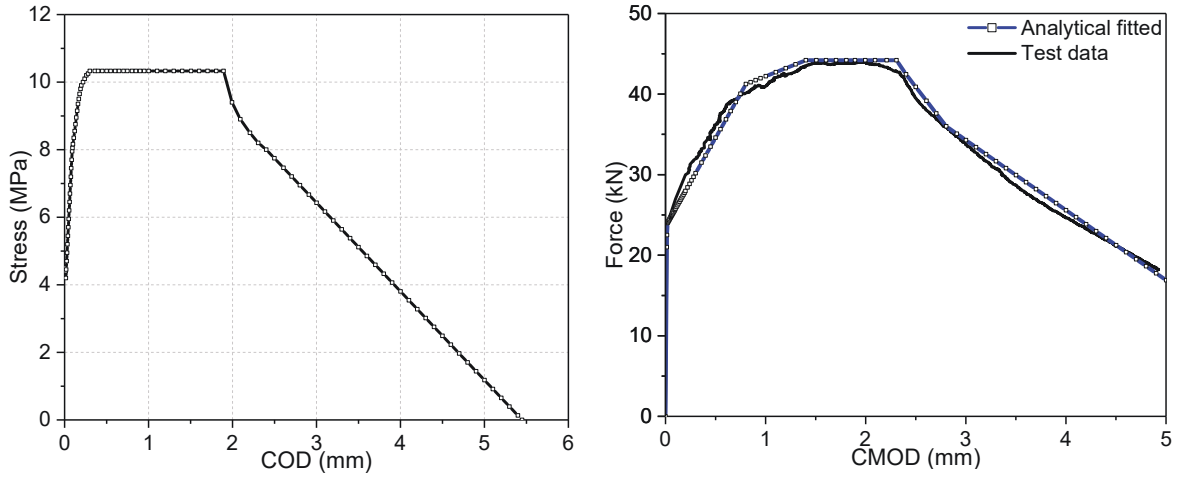

(b) L1.5S1

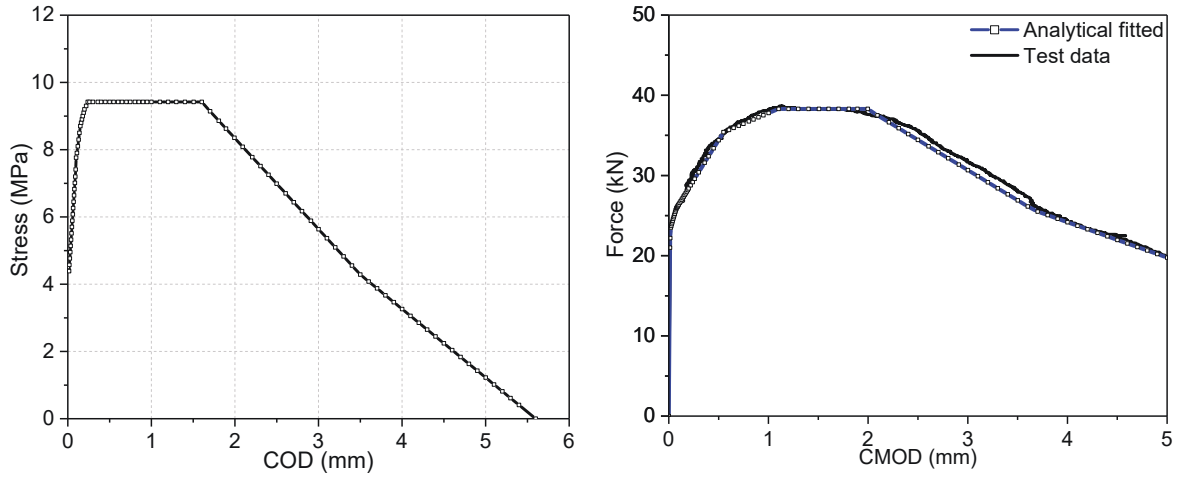

(C) L1.5M1

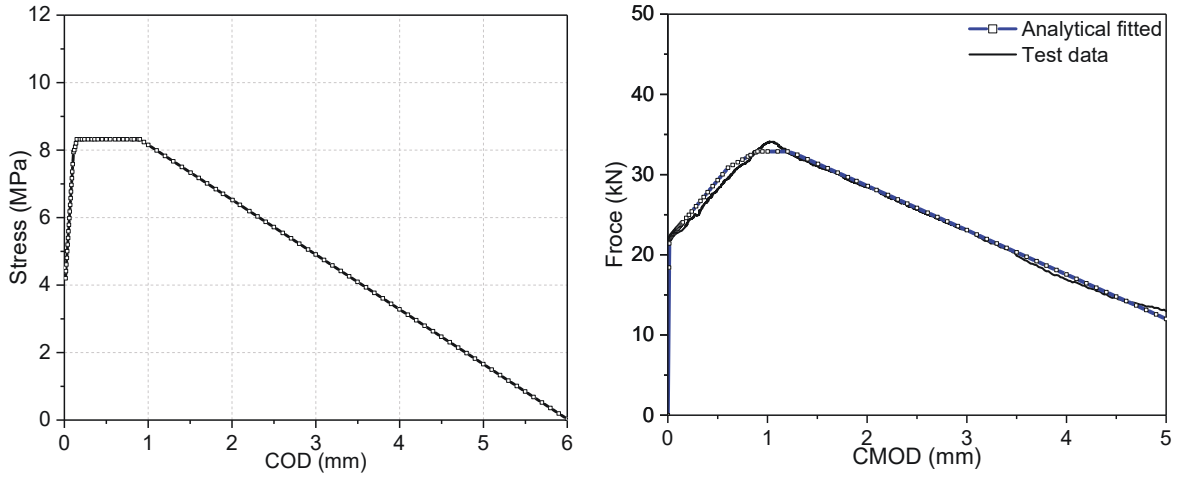

(d) L2.5

Fig. 4.11. Inverse analysis results (σ versus COD and force versus CMOD)

4.3.2.4 Discussion

The results noted the UHPC prisms reinforced with hybrid fibres importantly enhanced the flexural properties (i.e., ultimate flexural strength, toughness and fracture energy). The hybrid fibre reinforced specimen L1.5S1 obtained the highest flexural properties.

It has been a consensus that there existed intrinsically weak zones in UHPC [153]. Under tensile loading, the micro-cracks were developed initially at the weak

zones. During the process, the stress gathered at crack tip. Region surrounding steel fibres would generate reverse cohesive force. The cohesive force mitigated the localized stress concentration, restrained crack propagation, and therefore increased the strength. With increasing the tensile loading, the micro-cracks gradually developed into macro-cracks, and then eventually caused the specimen failure. In the present study, after the matrix starting to crack, the steel fibres provided residual strength. For the UHPC prisms reinforced with single fibres, long steel fibre reinforcement could improve the flexural performance; however, it is not able to restrain the development of micro-cracks. For UHPC prisms reinforced by short fibres only, its peak tensile strength, post-peak ductility and energy absorption are greatly reduced due to insufficient bonding with the surrounding matrix. For the UHPC prisms reinforced with hybrid fibres, the short fibres first restrained the emerging micro-cracks. Then, with increasing external force, the micro-cracks grew and merged into macro-cracks. The short fibres around the cracks were gradually pulled out, while long fibres became more effective in crack bridging. Long fibres could therefore improve the ductility and provide a stable post-crack response, and more time and energy were required to damage the UHPC reinforced with hybrid fibres.

Although fibres are more efficient in enhancing the flexural properties, they are also effective in bridging the cracks in compressive tests leading to improved compressive strength. Similar to the present study, decreasing in compression strength with enhancing in short fibre reinforcement content was observed in previous studies [142, 154], and it was attributed to the lower efficiency of short fibre reinforcements in restricting the development of cracks. It is worth noting that compared with compressive strength, flexural strength and energy absorption capacity

are deemed more important for UHPC materials and hence are the major focus in the present discussion.

The other effect contributed to high flexural properties of specimens with hybrid fibres was wall-effect. Wall-effect was defined as the behaviour that, when casting the fibre-reinforced concrete, the steel fibres closed to the border tended to align parallel to the walls [135, 155]. If the casting of concrete in a certain flow velocity was applied, the long fibres were always well oriented between borders [8] (Fig. 4.12), and the short fibres could also restrict the rotation of long fibres, further enhancing the wall-effect. Therefore, more fibres align in the direction parallel to the borders, leading to a significant improvement of flexural properties.

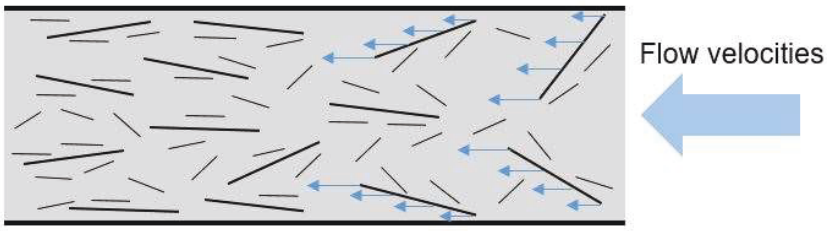

Fig. 4.12. Fibre orientation of hybrid fibres

4.4 Drop Hammer Impact Test Results and Discussion

4.4.1 Crack patterns

Crack patterns were presented in Fig. 4.13. All UHPC beams displayed a flexural response with cracks propagated vertically along with the depth of the beams. Major flexural crack speared from bottom surface, whereas serval minor cracks around boundary speared from the top surface, which is due to the negative bending moment at the boundary.

In authors' previous study, under the relatively lower impact energy (5040 J), the reinforced C40 concrete column RC-S-h1.25 (the same column configuration) showed

the diagonal shear and complete collapse [78]. When a drop-hammer impacted the specimen, the stress generated at the loading point and propagated towards the boundary. The stress wave travelled back and forth several times until a stable stress state was established, and then the boundary reaction was activated and global deformation started. Before the stress wave triggered the boundary reaction, the inertia force provided the structural resistance rather than boundary reaction force. As discussed in the previous study [156], at beginning, the time varying shear force was largely concentrated near the loading point in the initial contact phase, which caused early shear cracks in the specimen. However, this high amplitude shear force only lasted a very short period and quickly decayed, and the shear force distribution gradually achieved a uniform state along the beam span. The induced shear force at the impacting location could easily exceed the structural shear capacity, leading to localized shear damage or total collapse of the conventional concrete structure. In the present study, UHPC beams showed the considerably superior shear resistance, and the global flexural response was observed rather than localized shear damage.

(a) L2.5-a

(b) L1.5M1-a

(c) L1.5S1-a

(d) L1.5M1-b

(e) L1.5S1-b

Fig. 4.13. Failure modes under impact loading

4.4.2 Impact force time history

Fig. 4.14 shows the test results, and peak impact force and impulse are listed in Table 4.8. These curves can be classified as four phases including peak force phase (Phase 1), plateau force phase (Phase 2), rebounding phase (Phase 3), and free vibration phase (Phase 4). Examination on the video recorded via high-speed camera further explained the impact force versus time curves of UHPC beams. As shown in Fig. 4.15, during Phase 1, the drop hammer impacted the beam (L1.5S1-a) with the initial impacting velocity. Due to the huge differences of velocity between drop weight and specimen, the portion of the beam was immediately accelerated, and the ultimate impact force was triggered during the phase. In addition, one minor tensile crack on the bottom surface started to emerge. During the plateau phase (Phase 2), the impact force and beam velocity were approximately the same. The deformation of the beam dissipated the kinetic energy stored in the drop hammer. When the hammer velocity decreased to zero, the Phase 2 ended, and the impact energy of drop hammer was totally absorbed, leading to a widened flexural crack. In other words, the resistant force to stop weight was mainly contributed by both the boundary condition and the lateral

stiffness of the beam. During the rebounding phase (Phase 3), the energy transferred to the beam was released through the reserved motion of hammer and beam. When the hammer left the contact-impact zone, the Phase 3 ended. Finally, the specimen vibrated freely to dissipate the residual energy.

For UHPC beams subjected to one single impact, the peak force of UHPC beams with the hybrid fibre reinforcement is larger than that reinforced with the single type of fibre. Compared to the specimen L2.5-a, the peak force of the specimens L1.5S1-a and L1.5M1 increased by 16.6% and 21.4%, respectively. Under static loading, the mixture L2.5-a had the highest elastic modulus and compressive strength. However, the mixture L2.5-a had the lowest peak contact force. This is because the dynamic compressive behaviour of UHPC with hybrid fibres was more sensitive to strain rate. Wu et al. [153] evaluated dynamic compressive performance of UHPC reinforced with hybrid long fibres (13 mm) and short fibres (6 mm) by Split Hopkinson pressure bar tests. The specimens with hybrid fibres and the single type of fibres showed evident strain rate effect. Besides, the specimens with hybrid fibres had higher dynamic increase factor (DIF), e.g., under the impact loading of 13.9 m/s, DIFs for L1.5S0.5, L1S1 and L0.5S1.5 were 1.43, 1.5 and 1.55, respectively, whereas DIF for L2S0 was 1.32. In addition, the observation from dynamic compressive stress-strain curves noted that the elastic modulus was enhanced under high loading rates.

For UHPC beams reinforced with hybrid fibres subjected to multiple impacts, the impact force and impulse of L1.5M1-b were overall lower than that of L1.5S1-b. For the first impact of L1.5M1-b, due to operation error (a relatively low-frequency acquisition at a 20 kHz sampling rate was set for the load cell), the load cell did not capture the accurate peak impact force. Researchers have recently reported that an insufficient sampling rate of the sensors might miss the peak impact force [157, 158].

Pham et al. recommended a minimum sampling rate of 50 kHz were adopted for drop-weight tests [159].

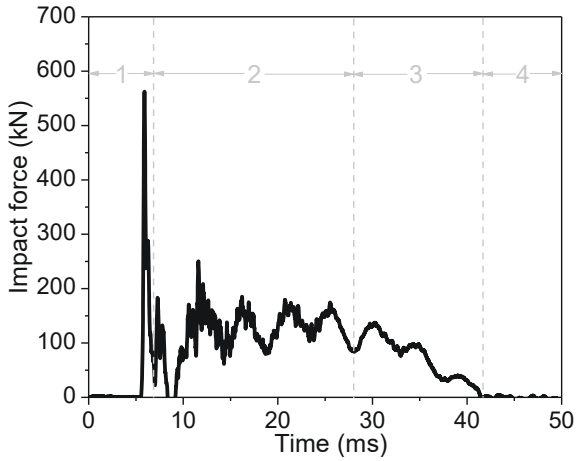

(a) L2.5-a

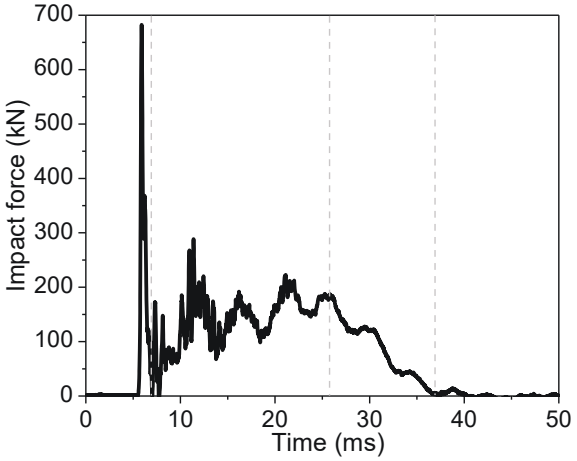

(b) L1.5M1-a

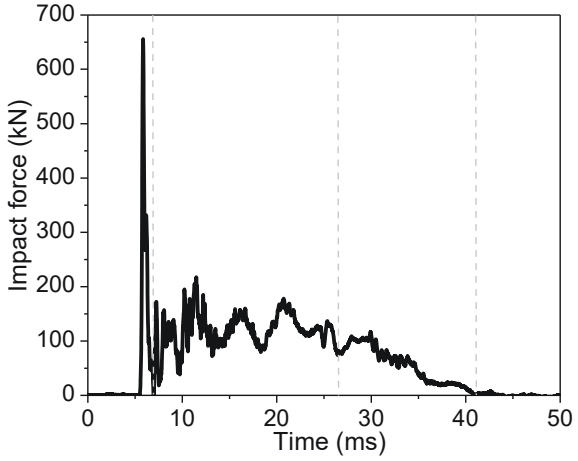

(c) L1.5S1-a

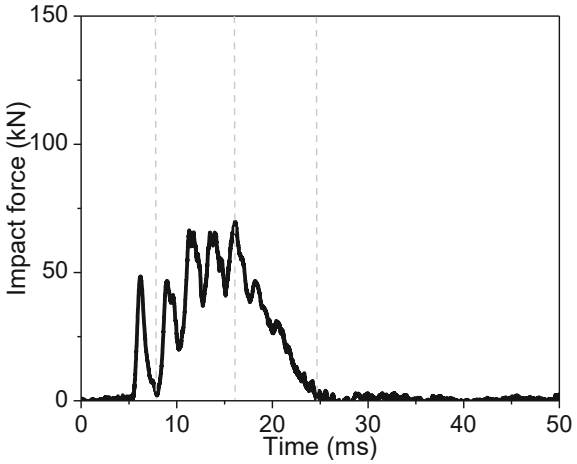

(d) L1.5M1-b (first impact)

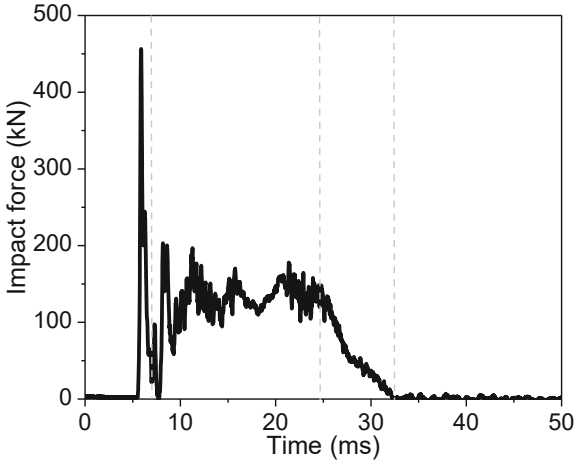

(e) L1.5M1-b (second impact)

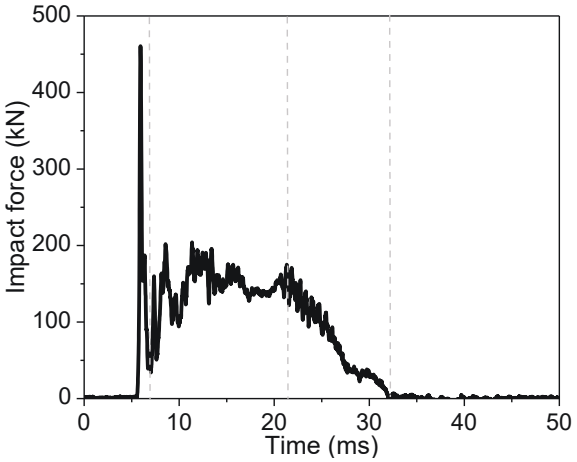

(f) L1.5M1-b (third impact)

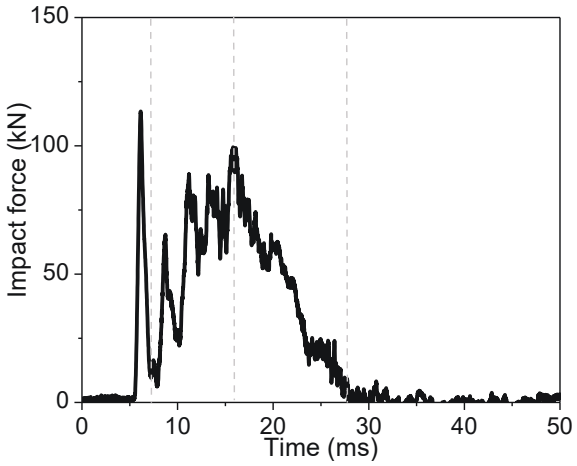

(g) L1.5S1-b (first impact)

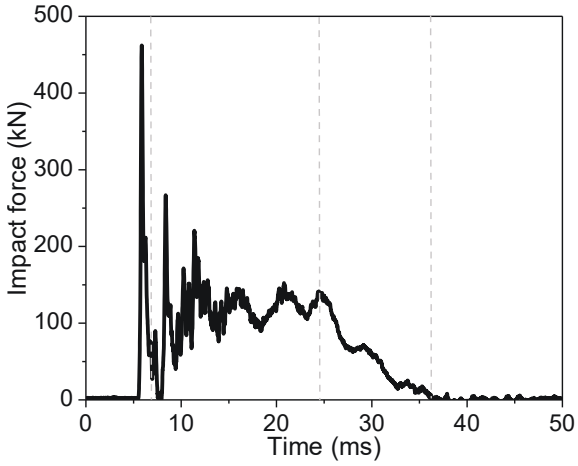

(h) L1.5S1-b (second impact)

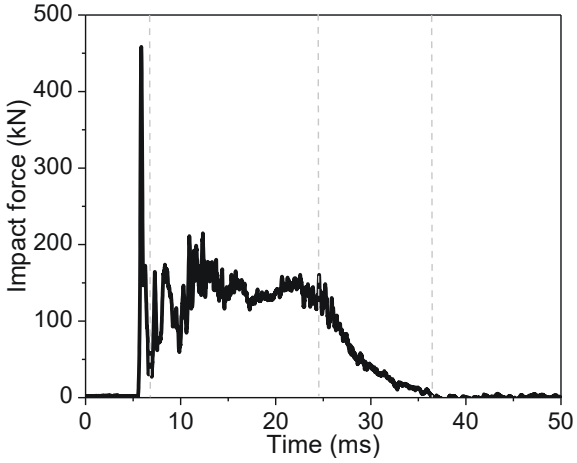

(i) L1.5S1-b (third impact)

Fig 4.14. Impact force time history of drop hammer test

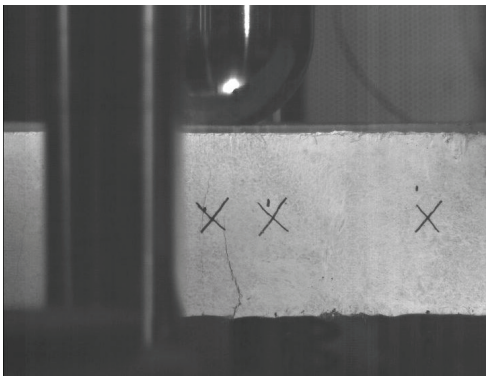

(a) t = 1.13 ms (end of Phase 1)

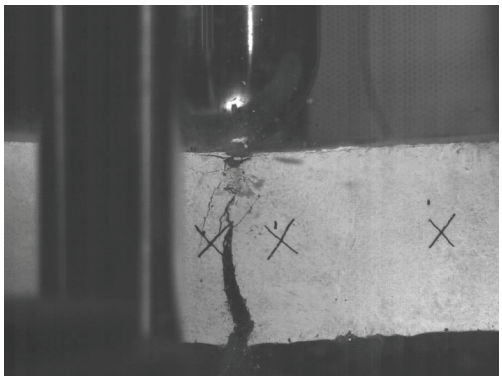

(b) t = 21.34 ms (end of Phase 2)

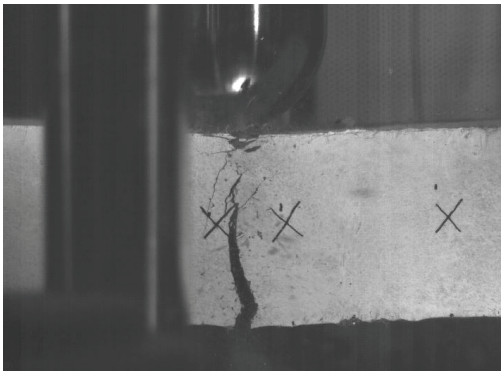

(c) t = 36.27 ms (end of Phase 3)

Fig 4.15. Dynamic process of the UHPC beam L1.5S1-a

During the impact test, the secondary impacts occurred after the rebound. The test results presented in the study were time history curves within 100 ms focusing on the primary/first impact. Fig. 4.16 shows the impact force and displacement time history of L2.5-a within 350 ms. There was a secondary impact occurring at 243 ms. The secondary impact force had a peak of 62.81 kN. Due to the secondary impact, the deflection at LVDT-1 increased from 33.04 mm to 39.71 mm; but returned to 33.04 mm and remained stable. Due to the relatively low impact energy and no further permanent damage caused, the effect of secondary impact was neglected in the following discussion.

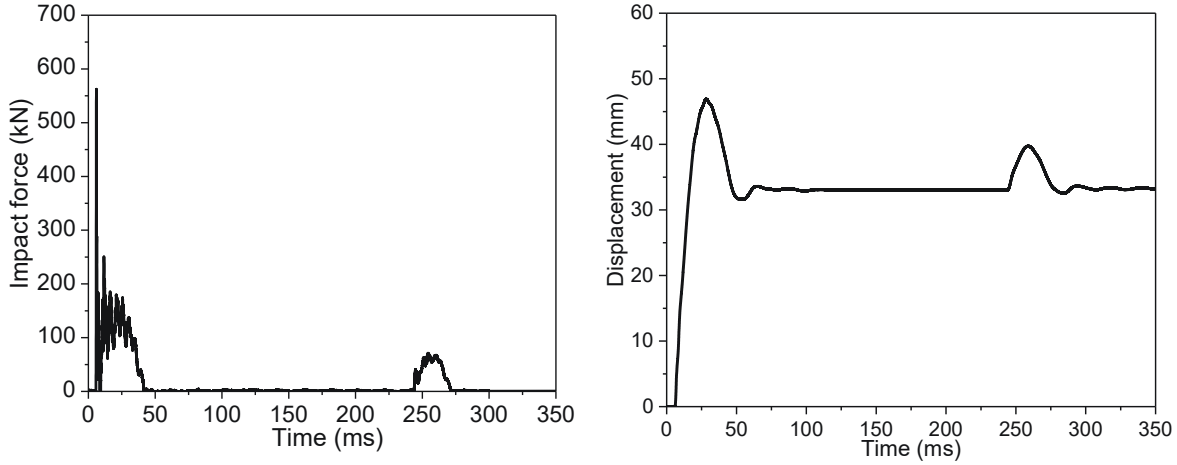

(a) Impact force time history (b) Displacement time history at LVDT 1

Fig. 4.16. Experimental results of L2.5-a

Series	Peak impact force (kN)	Peak mid-span deflection (mm)	Residual mid-span deflection (mm)	Peak deflection LVDT-1 (mm)	Peak deflection LVDT-2 (mm)
L2.5-a (1 m; 4.43 m/s)	562.31	52.75	36.41	48.87	38.04
L1.5M1-a (1 m; 4.43 m/s)	682.43	44.27	27.69	43.21	33.79
L1.5S1-a (1 m; 4.43 m/s)	655.85	44.69	29.58	43.47	33.97
L1.5M1- b (1st) (0.05 m; 0.99 m/s)	69.84*	2.81	0.42	2.67	1.19
L1.5M1- b (2nd) (0.5 m; 3.13 m/s)	456.42	24.73	14.73	23.23	18.18
L1.5M1- b (3rd) (0.5 m; 3.13 m/s)	460.48	35.76	19.88	34.42	30.35
L1.5S1-b (1st) (0.05 m; 0.99 m/s)	113.42	5.93	1.68	5.81	4.68
L1.5S1- b (2nd) (0.5 m; 3.13 m/s)	452.07	27.36	17.52	26.15	19.79
L1.5S1- b (3rd) (0.5 m; 3.13 m/s)	458.43	40.43	23.35	38.65	34.21

* Faulty data

Table 4.8 Lateral impact test results.

4.4.3 Mid-span displacement time history

Fig. 4.17 shows the test results, and the deflection values were summarized in Table 4.8. The recorded mid-span displacement time curves could be catalogued into three phases, including the ascending phase, descending phase and residual phase. The displacement first ascended to the ultimate value and then gradually descended to the residual value. Afterwards, the residual values remained with an insignificant vibration until the end of the test.

For UHPC beams subjected to one single impact, the UHPC beams with hybrid fibres had overall smaller deflection than the beam L2.5-a. The maximum deflection and residual deflection for L2.5-a were 52.75 mm and 36.41 mm, which were reduced by 16.1% and 23.9% in L1.5M1-a, and by 15.3% and 18.7% in L1.5S1-a. The UHPC beam with mixed long and medium fibre reinforcement could effectively reduce the maximum and residual displacements. For UHPC beams subjected to multiple impacts, the beam L1.5M1-b had an overall smaller maximum and residual displacement at mid-span.

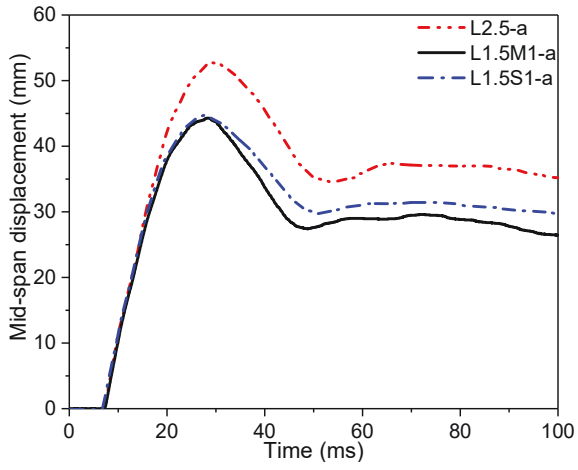

(a) Single impact

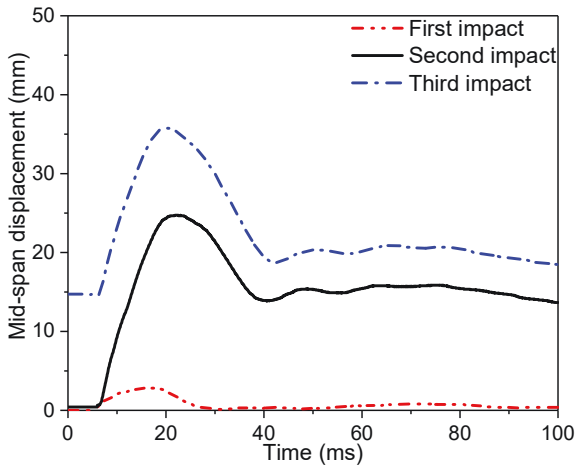

(b) Multiple impacts on L1.5M1-b

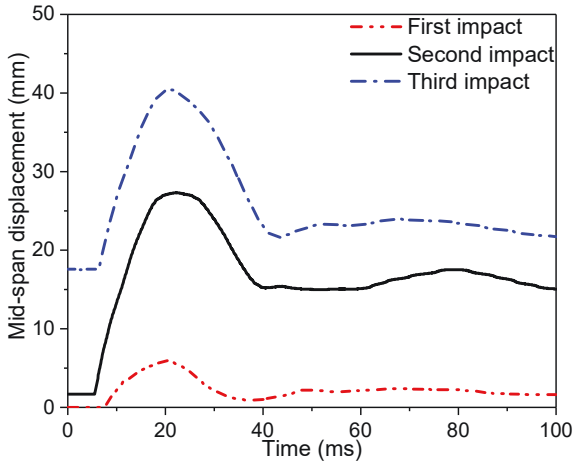

(c) Multiple impacts on L1.5S1-b

Fig. 4.17. Test results

Combing the histories of the impact force and deflections, the force-displacement curve could be gained. The absorbed energy of UHPC beams at the end of the impact process was then calculated from the integration of the area under force-deflection curves. Fig. 4.18 shows the absorbed energy and energy ratio (absorbed energy divided by the input impact energy) of UHPC beams subject to impact loading. A large part of the impact energy was absorbed by UHPC beams through permanent deformations and concrete fracture, and partial impact energy was dissipated by other means (i.e., frictional energy and sound energy). For UHPC beams subjected to one single impact, the absorbed energy ratio of specimens reinforced with hybrid fibres is smaller than that with one single type of fibre reinforcement. For UHPC beams subjected to multiple impacts, except for the first drop, L1.5M1 absorbed more energy than L1.5S1. For the first impact of L1.5M1, the load cell did not capture the accurate impact force history, leading to erroneous energy absorption.

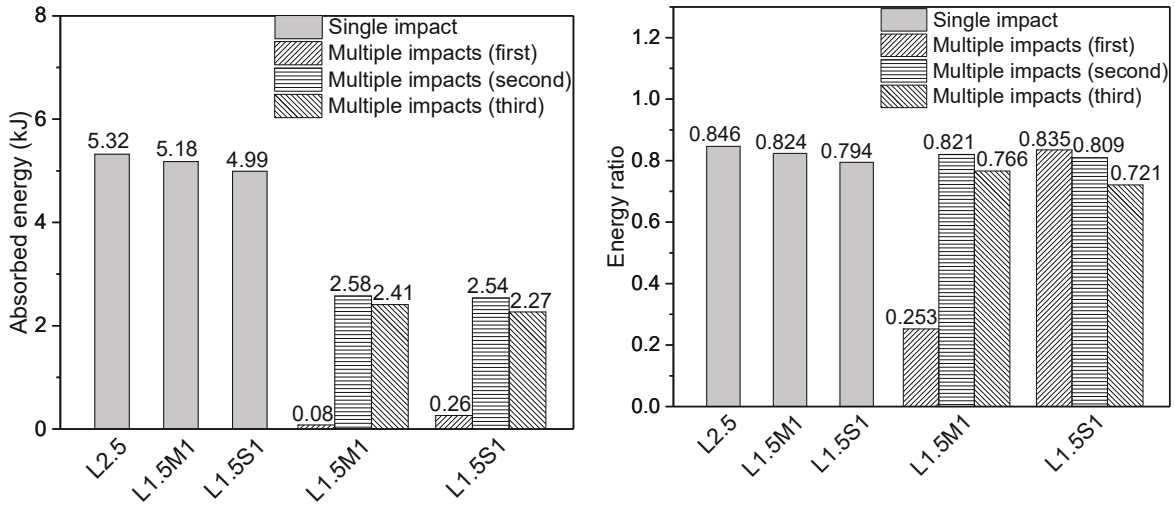

(a) Absorbed energy (b) Energy ratio based on impact energy

Fig. 4.18. Absorbed energy of UHPC beams

4.4.4 Discussion

The results above showed the UHPC beams reinforced with hybrid fibres improved the dynamic impact resistance (low maximum and residual deflection). Although the first peak impact force of specimens with hybrid fibres was larger than that with a single type of fibre, no shear cracks were observed. In future work, the effect of fibre hybridization on the dynamic shear capacity needs to be quantified.

The L1.5M1 mixtures demonstrated higher dynamic impact resistance than L1.5S1, which is different from static flexural properties. Under impact loading, the number of micro-cracks and macro-cracks increased simultaneously, whereas limited micro-cracks grew into macro-cracks subjected to static loads. In addition, the combined effect of fibre geometry, quantity and spacing influenced the quality of the UHPC mixtures. It is noted that the tension properties increased with fibre length while decreased with an increase in fibre spacing [160, 161]. Compared with static properties, the dynamic properties were more sensitive to the interior structure of the

UHPC mixtures. The best impact resistance could be achieved only when the combined effect reached an optimal state.

4.5 Summary and Identification of the Gap

Experimental studies, including quasi-static compressive tests, four- and three-point tests, were characterised to study the influence of fibre hybridization on behaviour of UHPC. The tensile softening curves and fracture energy were then obtained. Subsequently, drop weight impact tests on UHPC beams with hybrid fibres were conducted. With the results presented above, several conclusions are given:

(1) Longer length of fibre improved both compressive strength and elastic modulus. Among all specimens with straight steel fibre, specimen reinforced with 2.5% single type long fibre showed the best compressive behaviour. On the other hand, fibre hybridization importantly enhanced the flexural properties of UHPC. The L1.5S1 mixture demonstrated increased flexural strength which was 21.8% and 33.9% higher than L2.5 and S2.5, respectively.

(2) To obtain the adequate tension-softening curves for UHPC considering fibre hybridization, the inverse analysis was performed. Based on the softening curves, the material fracture energy was obtained, and the fracture energy of UHPC with hybrid fibres was larger than that reinforced with a single type of fibre. The L1.5S1 mixture showed increased fracture energy which was 20.1% and 65.2% higher than L2.5 and S2.5, respectively.

(3) Reinforced UHPC beams exhibited a high impact resistance. From experimental observation, UHPC beams showed minor flexural damage. As compared to UHPC beams with single long length fibre reinforcement, the UHPC beams with hybrid fibres demonstrated the improved impact resistance, i.e., low maximum and

residual deflection. The UHPC beams with hybrid fibres showed a higher peak impact force which was probably because of the increased material modulus under high loading rate.

Chapter 5

Behaviour of Hollow-core and Steel Wire Mesh Reinforced Ultra-high Performance Concrete Columns under Impact Loading

5.1 Introduction

Recently, many studies have been conducted to explore the impact resistance of RC structures through experiments and finite element (FE) modelling [35, 36, 97, 162]. These studies focus on failure mechanisms and structural dynamic behaviour responses. It is evident that under a concentrated impact load, concrete structures may experience localized damage that includes penetration, punching shear, concrete scabbing and spallation. These undesired brittle failure modes are primarily associated with the low tensile properties of the conventional concrete.

Over the past few decades, UHPC has been developed and widely discussed. With high volume micro fibre reinforcement, UHPC shows greatly improved tensile strength and ductility, both of which favour its energy absorption capacity [6, 151]. The structural static performance containing different micro fibre content has been investigated. For the structural dynamic performance, the micro fibre reinforcement has been noted to have a significant impact on structural performance under dynamic loads; increasing the reinforcement ratio improves impact resting performance of UHPC beams.

As noted in the above review, high fibre content and passive reinforcement ratio are favourable to the UHPC structural performance under both static and dynamic loading conditions. However, they inevitably increase the cost of UHPC. In a common UHPC with 2% volume fraction of steel fibres, about 60 - 80% of the total price is due

to fibres. Therefore, the fibre volumetric ratio are minimized for the UHPC adopted in practice [163]. Hollow-core structural form and structure form strengthened with steel wire mesh provide a possible solution to reduce the cost.

In present study, UHPC with 1.5% fibre addition was developed and compared with its counterpart with 2.5% fibre reinforcement in terms of their static mechanical performances. Then, hollow-core columns and steel wire meshed reinforced columns that cast with UHPC with 1.5% fibre addition were designed and tested under drop-weight impact tests. Subsequently, finite-element modelling was performed. Based on the validated numerical model, energy evolution, dynamic shear force and bending moment distribution were obtained to study the failure mechanisms of designed columns. Residual axial capacity numerical tests were then conducted to define the damage of post-impact UHPC columns. A parametric study was carried out on designed UHPC columns to study the effect of key structural parameters on the damage level.

5.2 Methodology

In the present study, the main targets include: 1. Investigate the mechanical properties of UHPC with low fibre content; 2. Study the impact resistance of UHPC columns with new structural design, i.e., hollow cross-section and wire mesh reinforcement; 3. Explore the failure mechanisms of designed columns under impact loading; 4. Provide damage criteria to quantify the impact-induced damage; 5. Evaluate the effect of key structural parameters on column damage.

The methodology to achieve the aforementioned targets is listed as follow: 1. Mechanical property tests were conducted on UHPC with 1.5% and 2.5% fibre reinforcement; 2. Experimental and numerical tests were conducted on UHPC

columns with hollow cross-section and steel wire mesh reinforcement; 3. Energy evolution, dynamic shear force and bending moment distribution were generated from validated numerical model. Dynamic cracking recorded was adopted to validate the failure mechanisms analysis; 4. Residual axial loading capacity tests were conducted through modelling; 5. A parametric study was conducted to investigate the influence of hollow section shapes, hollow ratio, axial load level and longitudinal reinforcement ratio for hollow-core UHPC columns and the effects of layers of steel wire mesh for steel wire mesh reinforced UHPC columns.

5.3 Experimental Investigation

5.3.1 Material properties

The mix proportions of UHPC adopted in this study are listed in Table 5.1. The cementitious materials included ordinary Portland cement and silica fume. The low water-binder ratio (w/b = 0.19) was implemented to reduce the permeability and improve compressive strength. Superplasticizer was adopted as a water-reducing admixture to ensure the flowability of the fresh UHPC. Fine aggregates with a mean particle size below 0.5 mm and nano-particles were adopted as the filler. 1.5% and 2.5% volume percentages of smooth steel fibres were incorporated. The properties of steel fibre are summarized in Table 3.1.

To ensure uniform distribution, the fibres were manually dispersed during the UHPC casting. After the first 24 hours curing at room temperature, the specimens were steam-cured at a high temperature (90 degrees) for another 48 hours. Finally, ambient curing was performed on the UHPC specimens until testing.

Relative weight ratios to cement					Steel fibre (V_f, %)
cement	Silica fume	Water	Fine aggregates	Nano-particles	
1.00	0.30	0.25	1.37	0.03	1.5% and 2.5%

where, V_f refers to volumetric ratio to the whole volume.

Table 5.1 Mix design of UHPC.

Uniaxial compressive tests were employed to calculate compression strength and elastic modulus of UHPC. Test specimens with dimensions of 0.1 × 0.1× 0.1 m are casted. The servo-hydraulic compression testing machine with a capacity of 3000 kN was adopted. Strain gauges were attached at the sides of the specimen to measure the elastic modulus. Uniaxial compression test results are summarized in Table 5.2 and showed in Fig. 5.1. The uniaxial compressive strength was 135 MPa and 148 MPa for UHPC with 1.5% and 2.5% fibre, respectively, and the elastic modulus calculated in accordance with ASTM C469-14 [164] was 45.5 GPa and 47.6 GPa, respectively. Four-point bending tests were performed to examine the flexural behaviour of UHPC. UHPC prisms had a length of 0.4 m (100 mm loading span and 300 mm clear span) and a cross-section of 100 mm × 100 mm. A load was applied using a universal testing machine with a capacity of 2000 kN through displacement control. The flexural strength was calculated according to ASTM-C78 [165], and the results are listed in Table 5.2. The flexural strength was 10.1 and 14.4 MPa for UHPC with 1.5% and 2.5% fibre reinforcement. UHPC with 1.5% fibre reinforcement also demonstrated very similar moduli when compared with UHPC with 2.5% fibre reinforcement. It is noted, with a higher dosage of fibre reinforcement, the standard deviations of the

compressive and flexural strength are evidently higher, which may imply difficulties in achieving a homogeneous material mixture.

In the current mixture design, the cost of 1.5% fibre UHPC is about 25% lower than 2.5% fibre UHPC while the compressive strength difference is only 7%. Although the flexural strength difference is 40%, 10.1 MPa flexural strength is already significantly higher than conventional concrete. In the actual structural design, the structural flexural capacity would be further enhanced by the passive rebar and wire meshes. In the following study, UHPC with 1.5% fibre reinforcement is used.

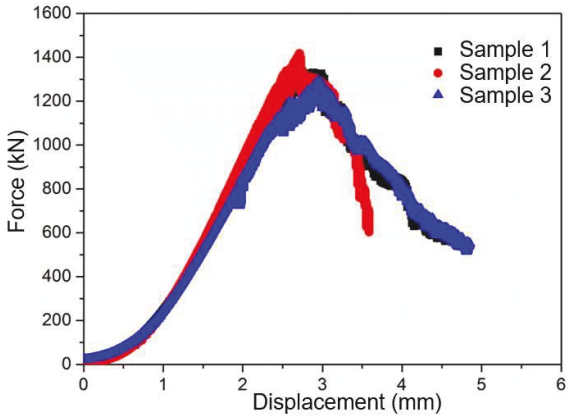

(a) UHPC with 1.5% 6 mm steel fibre

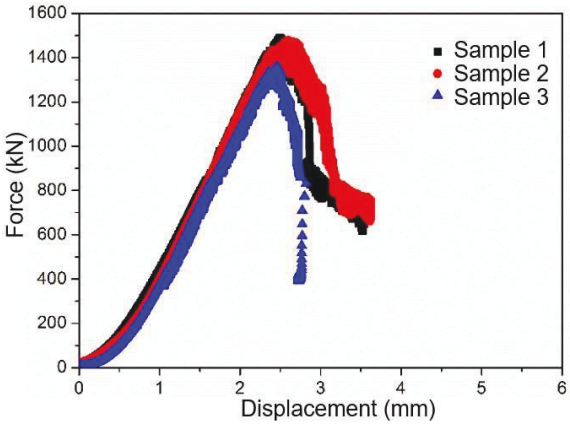

(b) UHPC with 2.5% 6 mm steel fibre

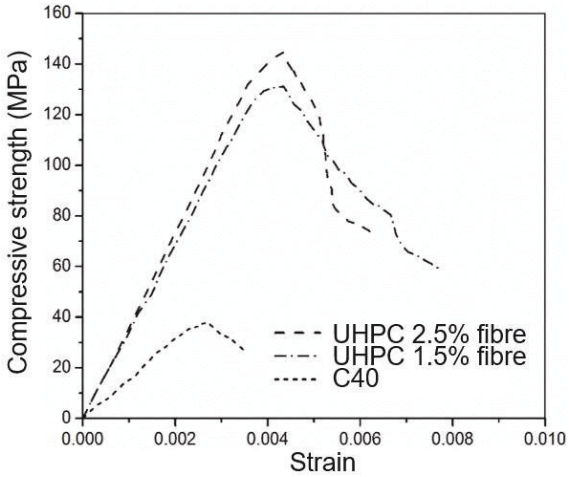

(c) Averaged compressive stress strain curve

Fig. 5.1. UHPC under uniaxial compression

Test method	Specimen type	Specimen number	Strength (MPa)	Average strength (MPa)
Compression test	2.5% fibre UHPC	1	147	148
		2	149	
		3	148	
	1.5% fibre UHPC	1	142	135
		2	129	
		3	135	
Flexural test	2.5% fibre UHPC	1	11.1	14.4
		2	16.2	
		3	15.9	
	1.5% fibre UHPC	1	9.7	10.1
		2	10.4	
		3	10.1	

Table 5.2 Results of material property tests.

5.3.2 Specimen construction

Table 5.3 lists the four large-scale column specimens for the drop-weight impact tests, including two UHPC hollow-core columns, and two steel wire mesh reinforced UHPC columns. The letters “R” and “C” denote the rectangular and circular hollow section, respectively. The numbers “10” and “6” denote different layers of steel wire mesh reinforcement. Each column had a 2000 mm span with a 168 mm × 168 mm rectangular cross-section.

The hollow-core column configuration and reinforcement detail are shown in Fig. 5.2 (a), (c) and (d). The four steel rebar with a 0.012 m diameter were used as longitudinal reinforcement. The cover thickness of specimens was 25 mm. Stirrup bars with a diameter of 10 mm and a spacing of 200 mm were applied for providing shear

resistance. In this experimental program, to investigate the impact resistance of different shape of hollow-core UHPC columns, UHPC-R and UHPC-C had the same hollow ratio (around 10%). The length of the rectangle and the diameter of the circular hollow hole were 54 mm and 60 mm, respectively.

Column	The shape of hollow hole	Hollow ratio (%)	Steel wire mesh strengthening	Drop hammer	
				v_0 (m/s)	Mass (kg)
UHPC-R	rectangular	10	N/A	4.95	411
UHPC-C	circular	10	N/A	4.95	411
UHPC-10	N/A	0	10 layers	4.95	411
UHPC-6	N/A	0	6 layers	4.95	411

where, f_c' = column strength, v_0 = initial velocity of the drop hammer.

Table 5.3 Summary of specimens.

For steel wire mesh reinforced UHPC columns, all steel wire meshes were cut into the same size of 2000 mm × 148 mm (Fig. 5.2 (b)). The steel wire mesh was made of 304 steel, and the diameter was 1 mm. The gird mesh size was 6.35 mm × 6.35 mm. The primary material properties are summarised in Table 5.4. The strengthening layout is shown in Fig. 5.2 (e) and (f). Although the steel wire meshes were designed to be evenly distributed, it was difficult for a single steel wire layer to be positioned at the designed location. The steel wire meshes were tied into cages, fastened by steel-string and positioned in the wooden mould. The gap between the steel wire layers was carefully controlled. The concrete cast and compacting were also conducted in the wooden mould. The curing treatment, including steam curing in a humid condition (95% humidity) at 90 ℃ for 48 hours was adopted for UHPC specimens. Then, column specimens were ambient cured for 28 days.

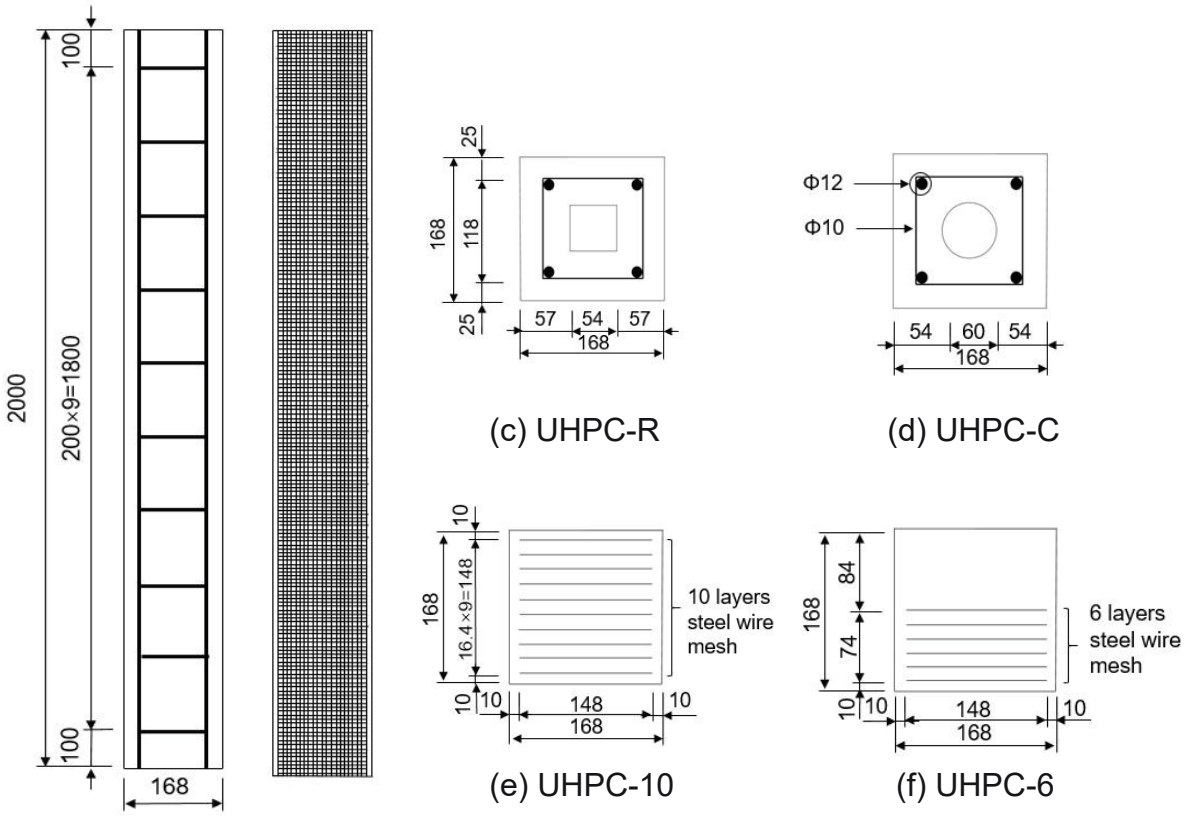

Fig. 5.2. Specimen dimensions (unit: mm): (a) reinforcement details for UHPC hollow-core and RC columns (b) reinforcement details for steel wire mesh reinforced UHPC columns

	Steel wire mesh	Longitudinal bars	Stirrup bars
Density (kg/m^3)	7900	7900	7900
Elastic modulus	198	198	198
Poisson's ratio	0.27	0.27	0.27
Yield strength (MPa)	500	500	300
Diameter	1	12	10

Table 5.4 Steel wire mesh, steel bars and stirrup bars.

5.3.3 Testing setup

The drop hammer test setup includes a support system, an axial load system and a drop weight system. Support system, as shown in Fig. 5.3, consisted of clamping devices, supporting frames and rigid foundation. The supporting frames were fixed to floor. The lower clamping part of a clamping device was then fixed to the support frame by high strength bolts. The upper and lower clamping parts were fixed with four M18 bolts to achieve the fully fixed boundary condition. For the axial loading system, it was designed to be self-reacting, which included a hydraulic jack and a hydropneumatic accumulator. Prior to the test, a constant of 200 kN was gradually applied by the hydraulic jack on a test specimen. During the test, the axial load would change due to the shortening of the specimen under the lateral impact. The hydropneumatic accumulator was adopted to mitigate the influence of axial deformations on axial loads and maintain the axial load at a constant level.

For the impact system, the drop hammer testing device was employed. The maximum release height of the drop hammer is 20.6 m. The maximum weight of the drop hammer is 1050 kg, including hammer frame (390 kg), weight blocks (30 kg each) and indenter. The designed impact energy could be achieved by adjusting the number of weight blocks and impact height. In the present study, the drop hammer with a weight of 411 kg and a drop height of 1.25 m was applied for all testing specimens. As shown in Fig. 5.4, the clear span is 1400 mm, and the length of two clamping devices was 500 mm. The remaining 100 mm was designed for the axial load application. Two LVDTs were adopted to measure the time history of column deflection. A high-frequency (100 kHz) data acquisition system was used to record impact test data.

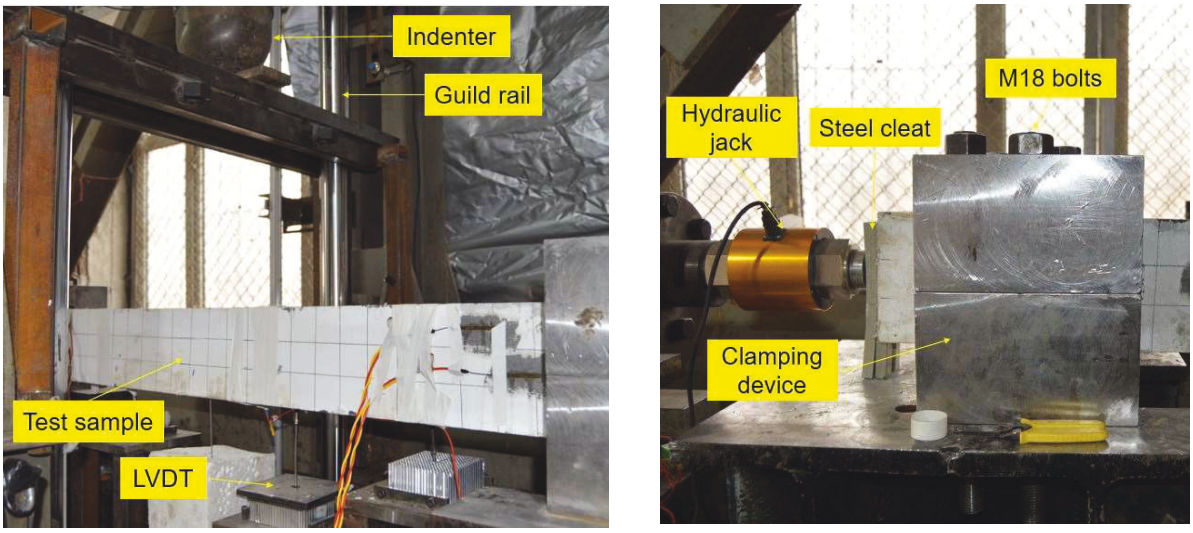

(a) Picture of the test setup (b) Axial load and support system

Fig. 5.3. Low-velocity impact test setup

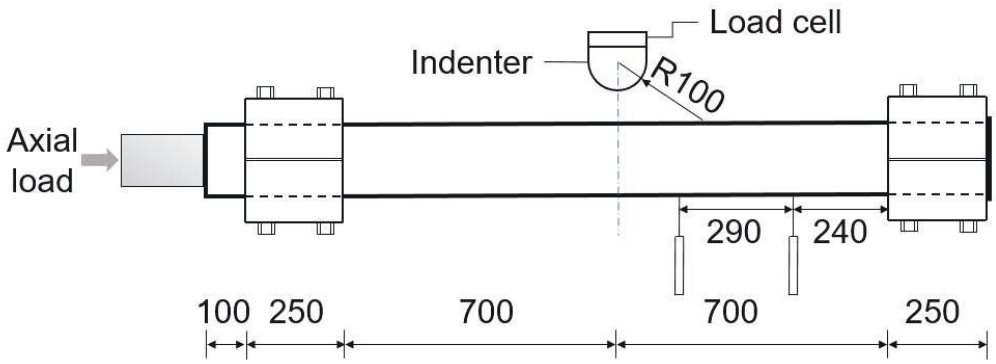

Fig. 5.4. Low-velocity impact test layout (units: mm)

5.3.4 Impact test results

The crack pattern after impact tests is shown in Fig. 5.5. All test specimens exhibited minor flexural damage with one major flexural crack located beneath the impact location. Several minor flexural cracks from the top surface were observed near the clamping devices. Limited concrete crushed around the loading point, and no fragmentation was observed.

The impact force and column deformation are to be presented and discussed together with numerical results in the following section.

(a) UHPC-R

(b) UHPC-C

(c) UHPC-10

(d) UHPC-6

Fig. 5.5. Column failure patterns

5.4 Finite Element Modelling

5.4.1 Finite element model

The numerical simulation study was conducted using LS-DYNA. Fig. 5.6 (a) presents the finite element (FE) model for numerical test setup. Some details on modelling UHPC hollow-core column and steel wire mesh reinforced UHPC column are shown in Fig. 5.6 (b) and (c), respectively. Solid element was employed to model the concrete. Hughes-Liu beam element was employed for the steel wire mesh and

reinforcing steel bars. A 5 mm mesh size was used in the centre part of the column (0.6 m in length direction) and the indenter while a coarse 10 mm mesh size was used for the remaining part of the column and the support system. A 6.35 mm mesh size was used for steel wire meshes. The mesh size was determined by convergence tests in the following section 5.3.3. The reinforcements and concrete were assumed to be perfect bonded. The steel wire mesh and concrete were bonded to each other with *CONSTRAINED LAGRANGE IN SOLID.

The keyword *CONTACT AUTO SURFACE TO SURFACE was adopted to model the contact between drop hammer and column specimen, specimen and the clamping devices, specimen and steel plates. The boundary condition of specimens was modelled, as shown in Fig. 5.6 (d). The steel plate (bottom one) was constrained at all directions while the clamping devices were constrained at x-axis. The axial loads were realized with a uniform surface pressure on a steel plate (the right one) through *LOAD NODE SET function. To reduce the computational cost, the free-falling process was replaced by the initial impact velocity in the numerical test. The conversion formula was: $v_i = \sqrt{2gh}$, v_i refers to the initial impact velocity; g refers to the standard gravity; h refers to the drop height.

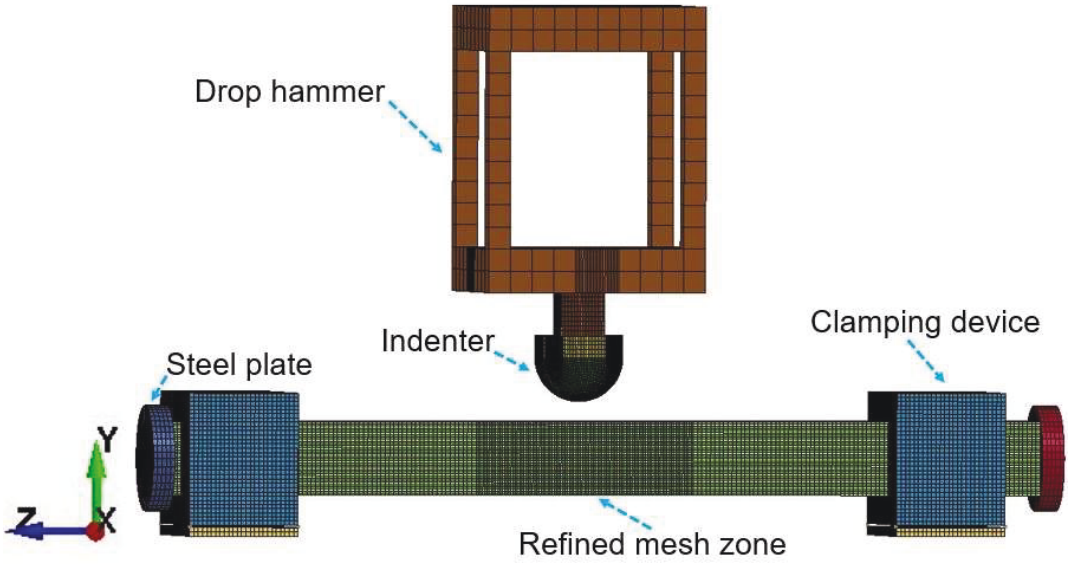

(a) Entire FE model for drop hammer impact test analysis

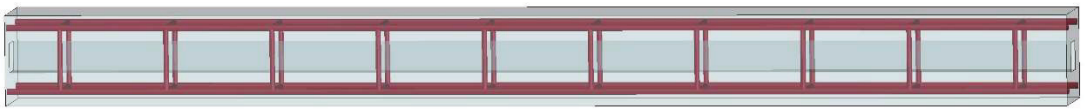

(b) UHPC hollow-core column

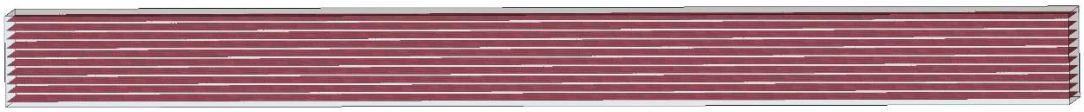

(c) Steel wire mesh reinforced UHPC column

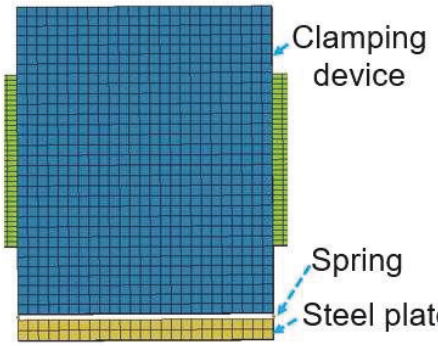

(d) Partially released boundary

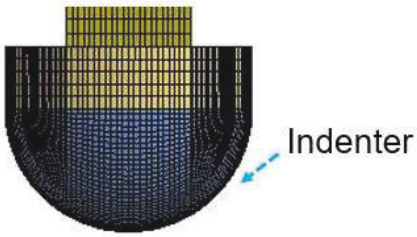

(e) Hemispherical indenter

Fig. 5.6. FE model for column impact simulations

To improve computational efficiency, the steel members including the drop hammer system and the clamping system were simulated by the elastic material *MAT ELASTIC (MAT_1). The elastic-plastic model *MAT PIECEWISE LINEAR PLASTICITY which allows defining strain-stress curve was adopted to model the reinforcement and steel wire mesh. Other parameters were determined from experiments and tabulated in Table 5.4. The strain rate effect was calculated in accordance with Eq. (3.18).

Many material models (e.g., MAT CONCRETE DAMAGE REL3 (MAT_72R3) and MAT CSCM (MAT_159)) were proposed to describe the behaviour of conventional concrete. Among them, the continuous surface cap model (CSCM) was developed from MAT GEOLOGIC CAP MODEL (MAT_25) and improved to simulate the roadside safety structures against vehicle collision. The current study employed the CSCM for concrete simulation. Although there are total 45 parameters need to be determined, the developers incorporated a set of concrete properties as default values into the CSCM model. Detailed properties of conventional concrete were discussed in the user's manual [113]. The previous study suggested the use of default parameters for concrete with strength among 28 MPa and 58 MPa [116].

Compared with the study on conventional concrete, there is limited application of CSCM model on simulating the behaviour of UHPC. Since CSCM had an excellent performance on modelling the concrete-like material under low velocity impact loading, Wei et al. [166] extended it to UHPC based on existing experimental test data and constitutive model theory. The modified CSCM model was adopted for UHPC. The strain rate effect of UHPC was adopted from the equations (Eqs. (3.16) and (3.17)) derived from the tests conducted by Fujikake et al. [121].

5.4.2 Convergence test and modified boundary condition

For the mesh size of the steel wire mesh, it will cause the incorrect load transfer if the size is larger than 6.35 mm since the load is transferred between nodes and the steel wire mesh element shares common nodes with each other. However, the mesh size less than 6.35 mm requires enormous computational resources and time. The steel wire mesh model was built with a 6.35 mm beam element. Concrete mesh size is determined based on the convergence test. As shown in Fig 5.7, simulation of the column with 6 layers of steel wire mesh under 411 kg drop hammer with a 4.95 m/s initial impacting velocity was carried out with three mesh sizes for the central part of the column, i.e., 5 mm, 2.5 mm and 10 mm. The displacement of the central nodal displacement converges with the decreasing the concrete element size. To balance the computational efficiency and the accuracy, 5 mm was choose.

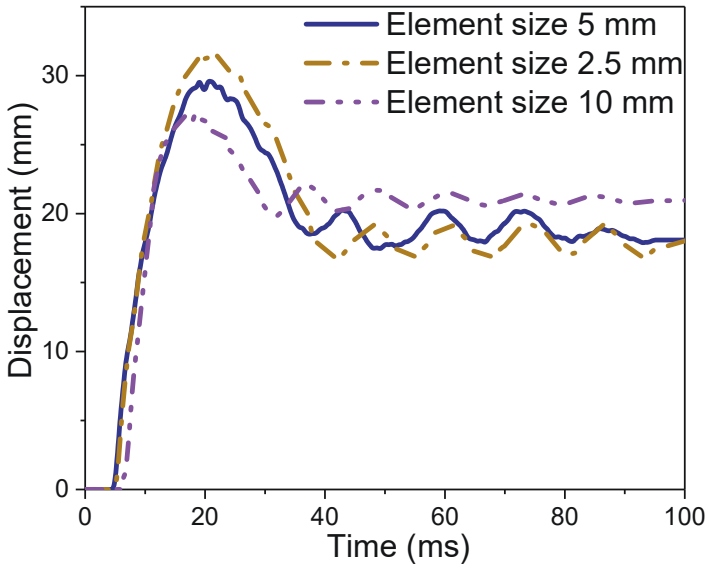

Fig.5.7. Convergence test on UHPC-6

In the previous study, the fully fixed boundary condition was set for numerical impact tests [166]. However, according to the high-speed camera record, the clamping

devices behaved as partially fixed to the rotation, rather than fully fixed as intended. Fig. 5.9 shows the test results for the UHPC-S-h1.5 (solid column with the same cross-section size and reinforcement as the hollow-core specimen) with velocity and kinetic energy of 5.4 m/s and 6.03 kJ. As shown in Fig. 5.9, the partially released boundary led the numerical results to show a shorter duration of loading phase in force histories and a shorter forced vibration phase in displacement histories. Similarly, partially released behaviour of boundary condition is also consistent with the previous study. Aoude et al. [167] conducted experimental tests of column specimens under different blast loading corresponding to different pressure-impulse combinations by means of a shock-tube. In their tests, the experimentally recorded strains at the support locations were adopted. It was founded that, compared with a fully fixed support against rotation, the partially released supports just provided between 33 and 46 % of the moment/rotational resistance. In the current study, although the boundary condition was designed to be fully fixed, the partially released behaviour could also be observed through a high-speed camera. Hence, a modified support system was developed in the numerical model. As shown in Fig. 5.6 (d), two steel plates were built under the clamping devices. The steel plates were constrained at all directions. The clamping devices were constrained at x-axis rather than all directions. Four springs were built at four corners to connect a bottom steel plate and a clamping device. Since few studies focused on the initial rotational stiffness of the partially released supports, the stiffness of the springs was determined from trial and error and set as 80000 kN m/rad in the numerical simulation (Fig. 5.8). The numerical test was conducted on the UHPC column with the partially released support system under 411 kg drop hammer with an initial velocity of 5.42 m/s impacting scenario. The numerical test results (Fig. 5.9) show better agreements with experimental data.

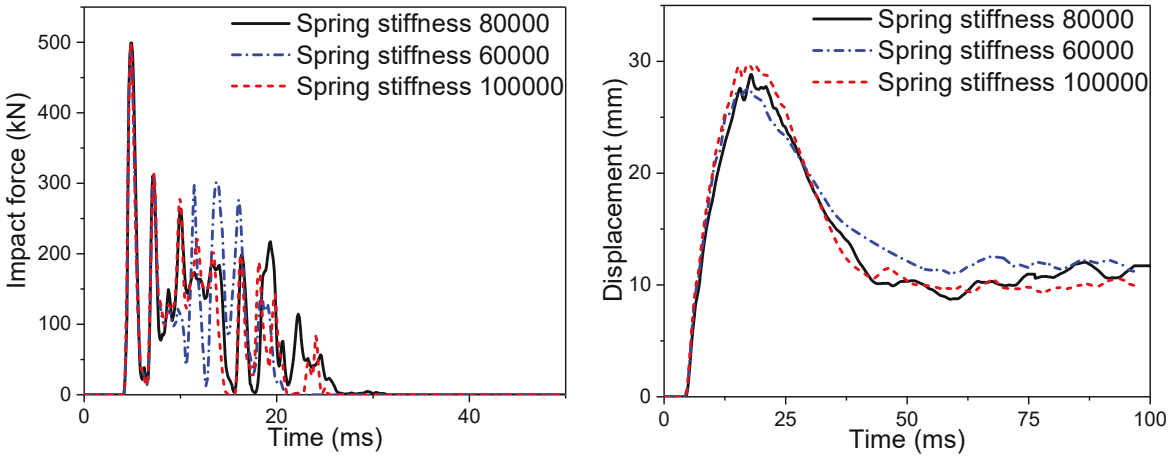

Fig. 5.8. Trial and error tests for spring stiffness

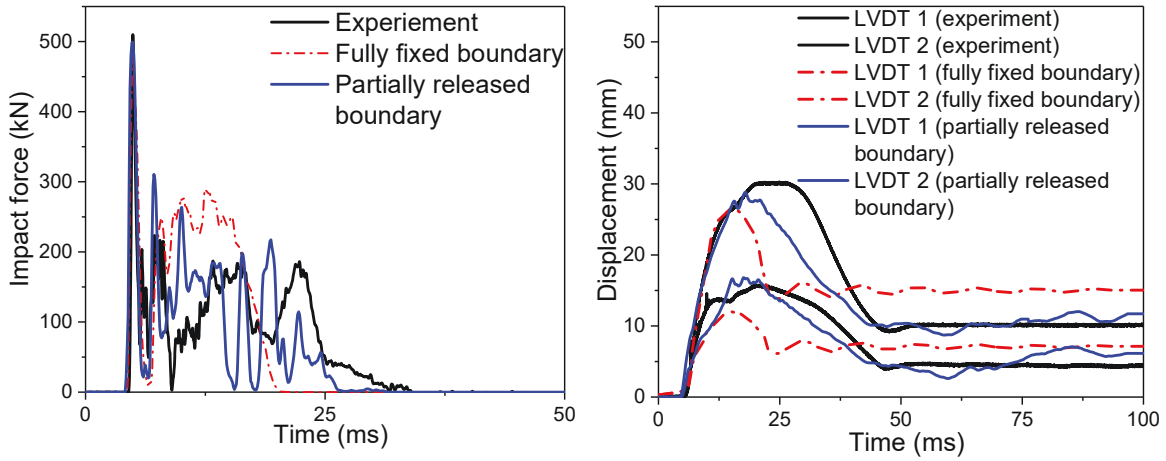

Fig. 5.9. Experimental and numerical results of UHPC-S-h1.5 [166]

5.4.3 Numerical validation and discussion

5.4.3.1 Numerical validation

Simulation results with the test results are presented in Fig. 5.10. The impact force histories were obtained from the contact interface between indenter and test specimen. The displacement histories were extracted from the nodal movement, which has the same locations as the experimental setup. The simulated impact force well matched (i.e., UHPC hollow-core columns and steel wire mesh reinforced UHPC

columns). With the same velocity, the instantaneous peak force of hollow-core columns (around 400 kN) is smaller than that of steel wire mesh reinforced UHPC columns (around 500 kN). The subsequent main impact impulse was mainly depended upon the flexural stiffness of the impact column.

For steel wire mesh reinforced UHPC columns, while the LVDT-2 data was reasonably reproduced by the simulation, the data from LVDT-1 which is closer to the impact location is not properly captured. It is considered the inadequate modelling of the bond-slip behaviour between the wire mesh and the surrounding UHPC matrix caused inaccurate results. Under point impact, the crack initiated on the column bottom face where the maximum tensile strength was reached. The crack propagated upward and resisted by the fibre bridging effect and then the wire meshes. Due to the small diameter and smooth surface of the wire mesh, a significant amount of bond-slip occurred upon widening of the crack. The frictional bond slip in the local area was not modelled in the simulation, leading to more energy dissipation in the global plastic deformation. Hence, the larger residual deflection was noticed in the simulation.

As mentioned in Chapter 3, the partially released boundary and the bond-slip relationship would significantly affect the structural dynamic behaviour. In Chapter 5, the partially released boundary was achieved with a modified support system. The numerical results of the UHPC column with the partially released support system show better agreements with the experimental data. However, the initial rotational stiffness of the partially released supports was determined from trial and error rather than theoretical basis. The spring stiffness and bond-slip relationship will be developed based on the theoretical basis in my future studies.

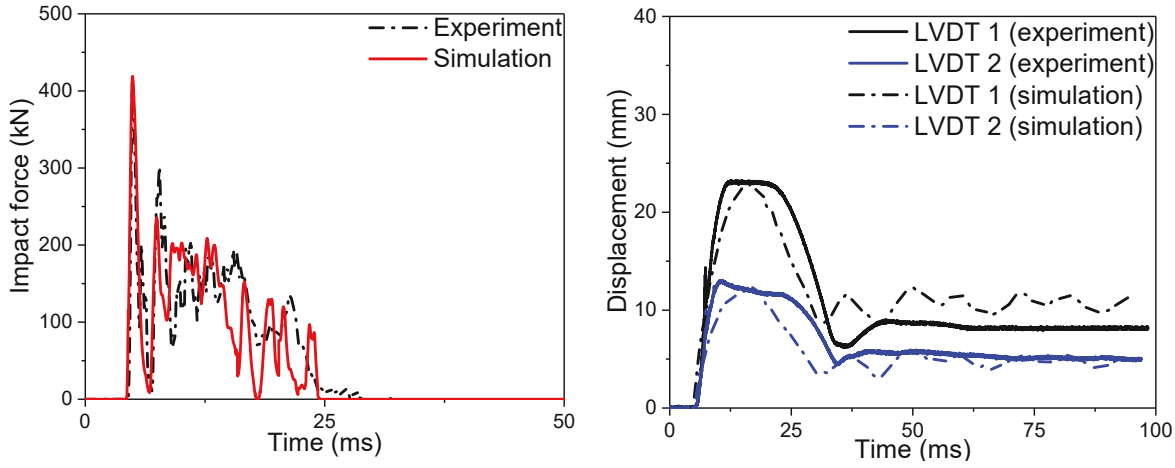

(a) UHPC-R

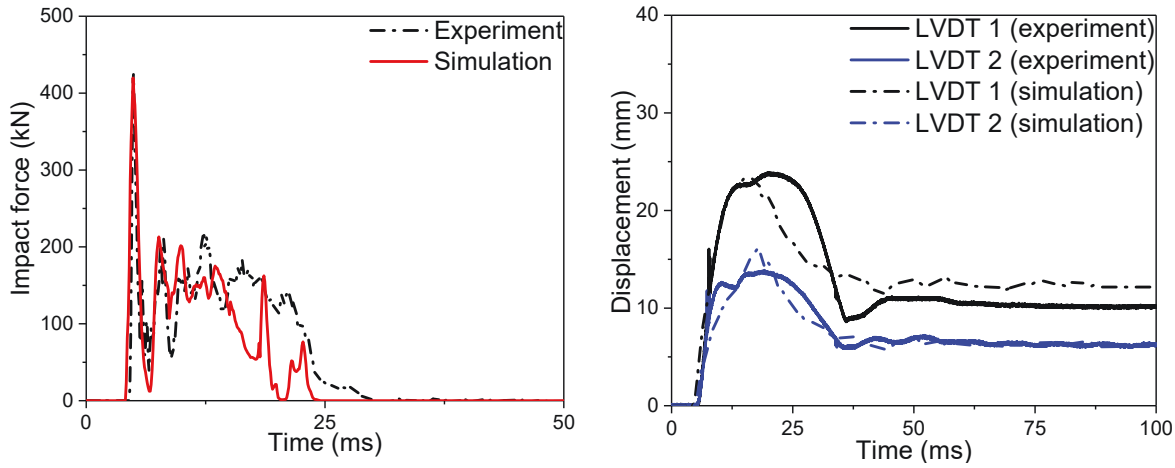

(b) UHPC-C

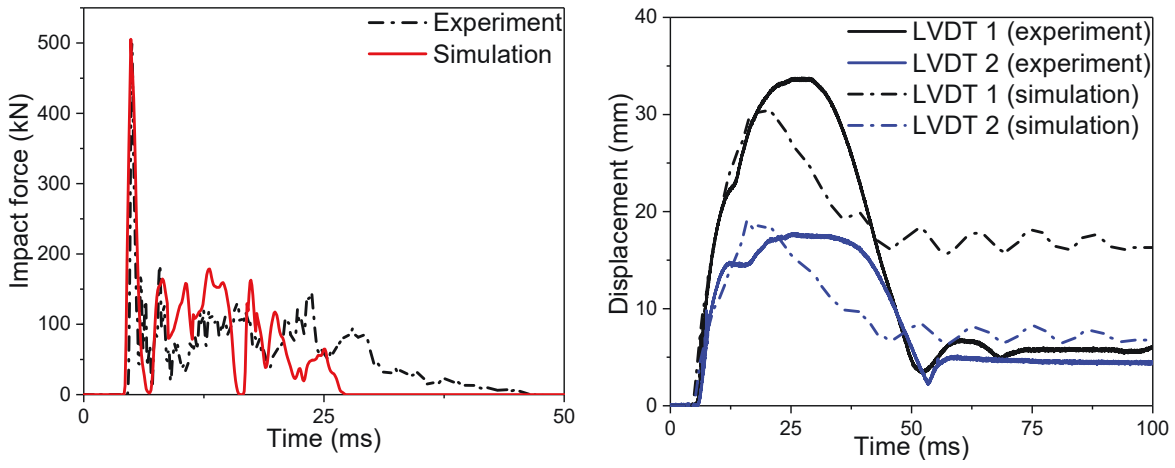

(c) UHPC-10

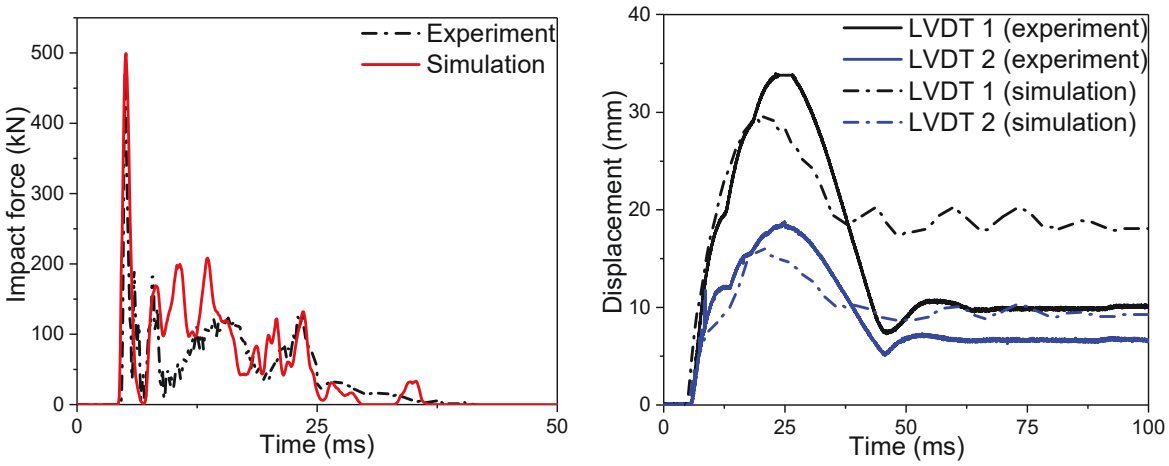

(d) UHPC-6

Fig. 5.10. Comparison between experiments and simulations

The peak impact force, impulse and maximum as well as residual displacement data, are summarised in Table 5.5. It can be noticed that, except for the residual displacement of LVDT 1, the developed FE model yields reasonably accurate prediction with the maximum error of less than 20%.

No.	Test peak force (kN)	FE peak force (kN)	Error (%)	Test max LVDT 1 (mm)	FE max LVDT 1 (mm)	Error (%)	Test residual LVDT 1 (mm)	FE residual LVDT 1 (mm)	Error (%)
UHPC-R	420.9	425.7	1.1	22.96	22.84	-0.5	8.53	10.12	18.6
UHPC-C	427.9	420.1	-1.8	23.56	23.23	-1.4	9.93	11.87	19.5
UHPC-10	500.2	505.3	1	33.74	30.79	-8.7	5.81	16.75	188
UHPC-6	504.1	514.2	2	33.98	29.59	-12.9	9.98	18.53	85.7

Table 5.5 Summary of numerical and experimental results.

Fig. 5.11 shows the damage patterns obtained from the FE model. The “Fringe Levels” referred to the damage parameters ranges from 0.5 to 1 for complete damage.

The numerical model captures damage of the columns with reasonable accuracy. However, numerical difficulties still retain. The first one is adjusting the damage parameters for the relatively new UHPC material. In CSCM, fracture energy is contained in the damage algorithm to describe strain softening. However, the relevant tests on compressive/shear fracture are rarely seen in the open literature for conventional concrete, not to mention the UHPC with fibre reinforcement. The second challenge is the concrete fracture simulation. FE method is not capable of simulating large deformation. In future work, the mesh-free methods such as SPH is planned to illustrate the UHPC cracking and fragmentation under impulsive loads.

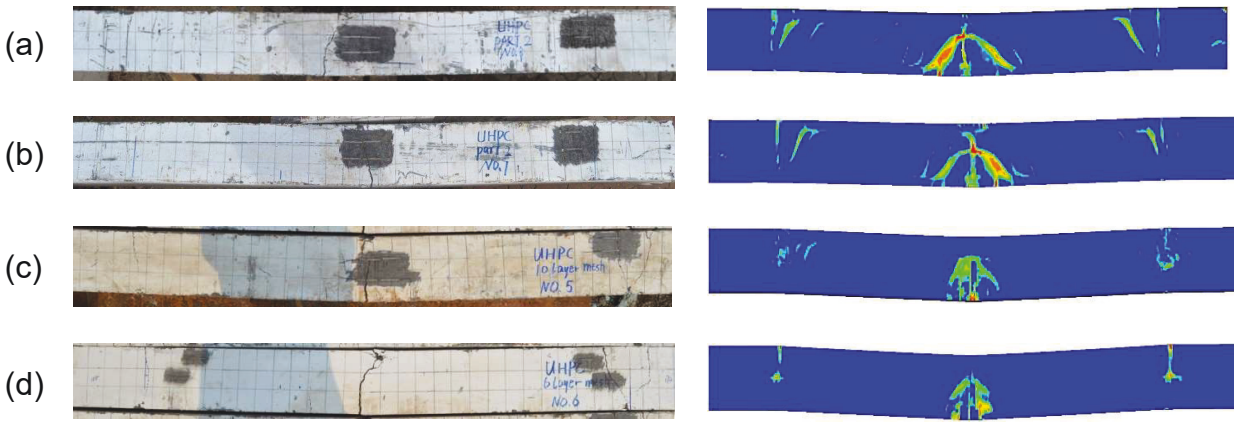

Fig. 5.11. Failure modes comparison: (a) UHPC-R; (b) UHPC-C; (c) UHPC-10; (d) UHPC-6

Fig. 5.12 (a) shows the energy evolution during the impact process of UHPC-R, obtained from the validated numerical model. The kinetic energy, starting from 5.04 kJ, was partly converted into the internal energy of UHPC material (1.69 kJ) and the reinforcing bars (1.32 kJ) through the plastic deformation. It is noted that the system kinetic energy was 0.44 kJ at the end of the drop process while the UHPC column returned to static. This non-zero kinetic energy was associated with the drop hammer

that bounced back after impact. The energy absorbed by the UHPC material itself was larger than reinforcing bars. The energy dissipated from concrete fracture and friction with boundary was 1.59 kJ which constituted around 31% of the initial kinetic energy of the drop hammer. Fig. 5.12 (b) shows the energy evolution at the end of the impact process for all testing specimens as well as the solid column (with the same reinforcement as the hollow-core specimen). For hollow-core UHPC columns, the internal energy stored within the UHPC column was roughly the same (around 3 kJ). As compared to the solid UHPC column, the energy absorbed by hollow-core UHPC columns were less, whereas more energy was dissipated by concrete fracture and friction. For steel wire mesh reinforced UHPC columns, as compared to the solid column, the internal energy stored in steel wire mesh was evidently less than conventional rebar. Most of the energy was absorbed by UHPC material (74 % for UHPC-10, and 80 % for UHPC-6), resulting in a larger plastic deflection.

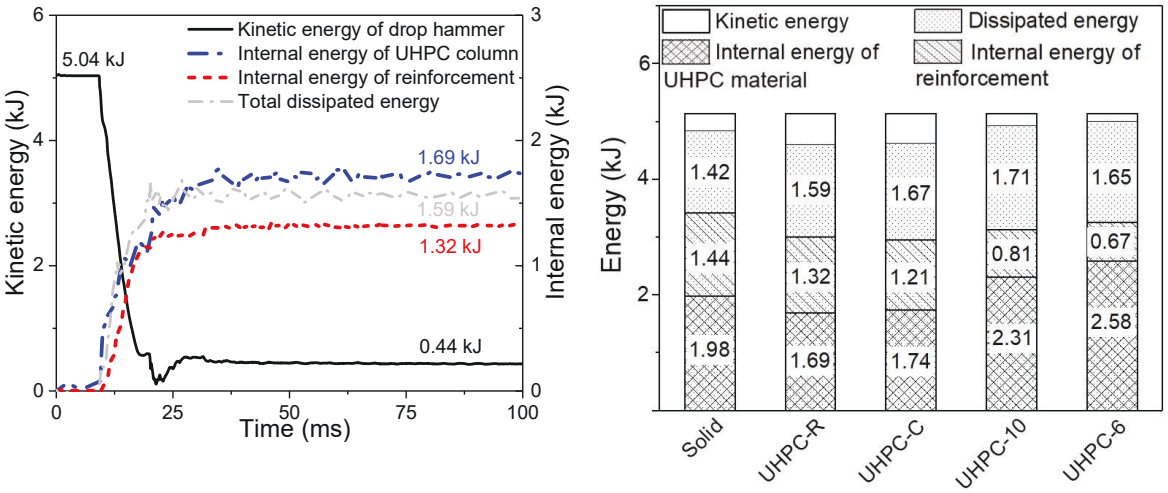

(a) Energy evolution of UHPC-R (b) Comparison among test specimens

Fig. 5.12. Energy evolution of test specimens and the solid column

5.4.3.2 Shear force and moment diagram

Lots of attention have been paid for the peak impact force since it is important in the occurrence of shear failure. Therefore, a more detailed study on the dynamic shear force distribution is required, which could be described by examining the stress wave propagation. When the drop hammer started impacting the column, stress waves were generated at the loading point and propagated along with the structure, away from the loading point and towards the column ends. The time duration before the boundary reaction activates can be obtained from the numerical model (Fig. 5.13).

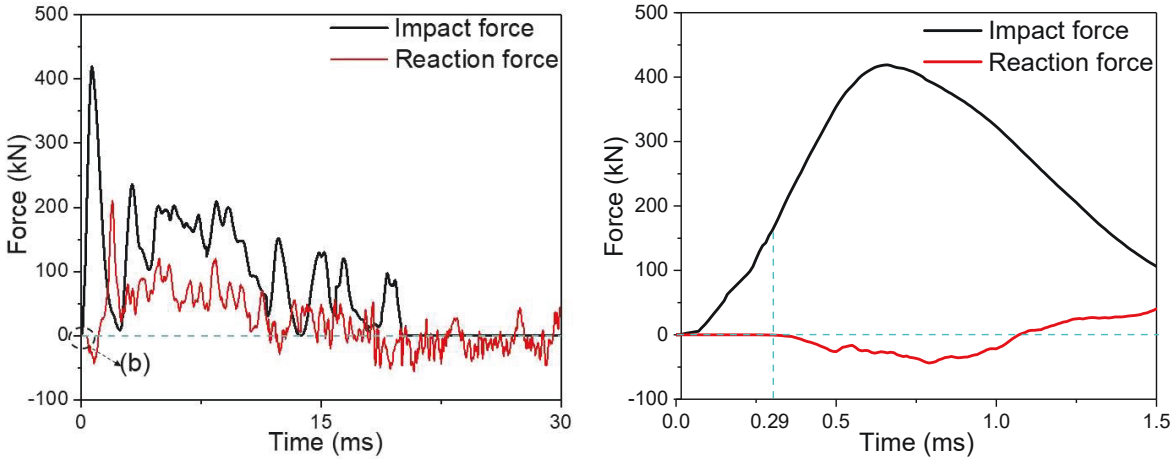

(a) Impact and reaction force (b) Force history within 1.5 ms

Fig. 5.13. Time history for impact force and reaction force (UHPC-R)

It is noted that, prior to 0.29 ms, the structural resistance is provided by the inertia force rather than boundary reaction. Actually, the main difference between dynamic analysis and quasi-static analysis is inertia effect and its distribution along the beam [2]. Fig. 5.14 (a) showed the shear force and moment distribution diagram (UHPC-R) prior 0.29 ms. It is evident that both shear force and bending moment distribution are time dependent. This behaviour occurs because the inertia force distribution is time dependent. At this early stage of the impact, only partial column was accelerated, and

inertia force is provided by accelerated part of the column. The inertia force distribution developed with stress wave propagating towards the supports. There has been a consensus that the distribution of inertia force along the concrete member was linear under impact [168-170]. The negative moment showing in the moment diagram caused the cracks on the top surface. The equation to obtain bending moment initiating cracks is:

$$M_{cr} = \frac{f_{t,d} w d^2}{6} \tag{5.1}$$

where, $f_{t,d}$ represents the dynamic tensile strength of concrete, w and d represent the width and depth of the beam section. In the current study, the bending moment for cracks initiation is around 6 kN × m. Therefore, several initial cracks appeared from the bottom at mid-span and gradually developed into a minor crack from 0.24 ms. Examination on the high-speed camera image, Fig. 5.15 (a) shows one minor visible crack with a width less than 1 mm was observed near the mid-span at 0.24 ms. At 0.29 ms, the flexural crack developed (Fig. 5.15 (b)), and there are no cracks developed from the top prior to 0.29 ms.

JSCE [151] recommended that a model be applied to the shear resistance of UHPC members. In this model, the total shear is resisted by the concrete (V_c), stirrup (V_s) and steel fibres (V_f) with V_c and V_s determined through empirical means and V_f obtained from PSM-VEM model proposed by Voo and Forster [171] and Voo et al. [172, 173]. The design shear capacity (V_d) was obtained by the equation below.

$$\begin{aligned} V_d &= V_c + V_S + V_f \\ V_c &= \beta_d \cdot \beta_p \cdot \beta_n \cdot f_{vcd} \cdot b_w \cdot d/\gamma_d \\ V_s &= [A_w f_{wyd}(sin\alpha_s + cos\alpha_s)/s_s]z/\gamma_b \\ V_f &= K_{fd} \cdot f_{tf} \cdot b_w \cdot z \cdot cot\theta \end{aligned} \tag{5.2}$$

where, $\beta_d = \sqrt[4]{1/d}$ (*d*: m) (when β_d > 1.5, β_d is taken as 1.5); d presents effective depth; $\beta_p = \sqrt[3]{100\rho_w}$ (when β_d > 1.5, β_d is taken as 1.5); $\rho_w = A_s/(b_w \cdot d)$; A_s presents the area of tension bars; b_w presents the width of the member; $\beta_n = 2$ in general; $f_{vcd} = 0.7 \times 0.2 \times \sqrt{f'_{cd}}$; f'_{cd} presents designed compressive strength of concrete; $\gamma_d = 1.3$ in general; A_w presents the area of the shear bars; f_{wyd} presents designed yield strength of the shear reinforcing steel; α_s presents an angle of the shear reinforcing steel to the member axis; s_s presents the spacing of shear reinforcing steel; $z = d/1.15$; $\gamma_b = 1.1$ in general; $K_{fd} = 0.82$ in general; $f_{tf} = K_{f,max} \cdot \alpha_f \cdot \rho_f \cdot \tau_b$; $K_{f,max} = 0.5 - 0.645/{\alpha_f}^{0.45}$; α_f presents aspect ratio of the fibre; ρ_f presents the volumetric fraction of fibres; $\tau_b = 0.6\sqrt{f_{cm}}$; f_{cm} presents mean compressive cylinder strength; θ presents the angles of the compressive strut relative to the member axis. In the present study, the designed shear force capacity for UHPC-R was calculated as 183 kN. At 0.29 ms, the shear force was 80 kN, which has not reached the designed capacity. The specimen experienced minor flexural damage at the early stage. However, if the impact velocity is significantly large, causing the impact duration significantly short, the impact forces will be balanced completely by the inertial force provided by part of structures. In this situation, excessive damage of concrete and yield of reinforcement is required to absorb part of impact energy. In the meanwhile, shear failure or concrete spalling damage has a high-frequency of occurrence rather than designed flexural damage.

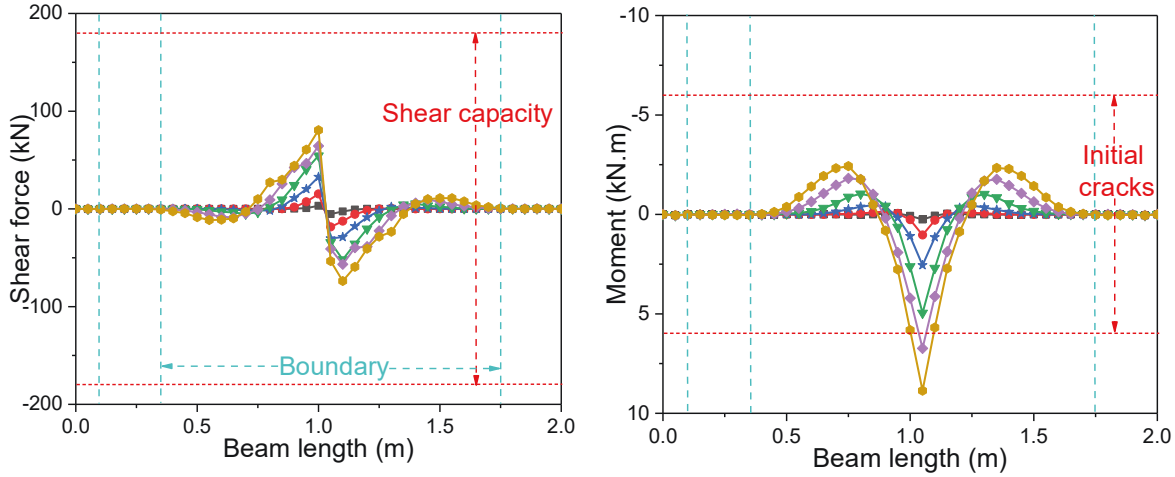

(a) Shear force and bending moment at the early stage

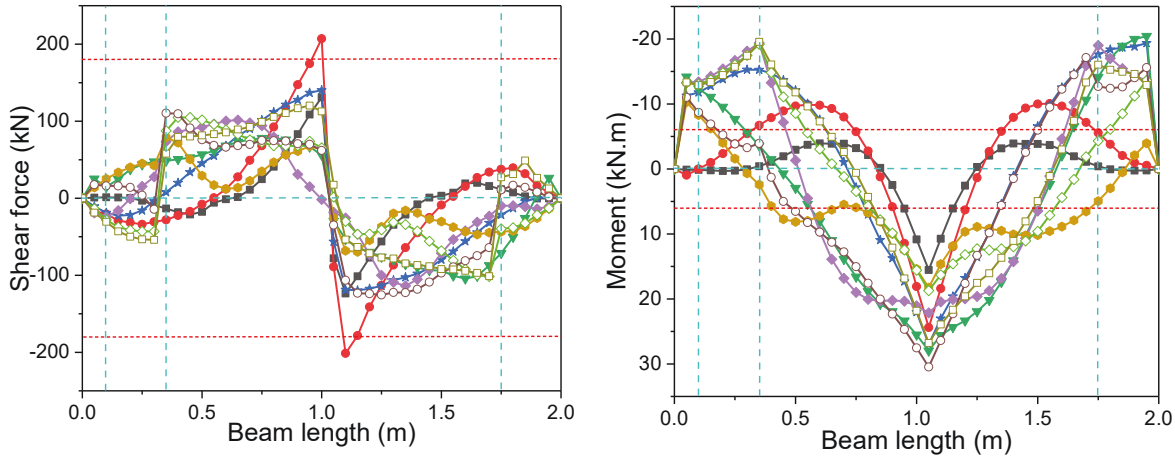

(b) Shear force and bending moment at the later stage

Fig. 5.14 (b) shows the shear force and moment distribution diagram in the later stage. After 0.29 ms, the stress wave already reached the boundary and triggered boundary action. The impact resistance was provided by the entire structure rather than part of the column. At 0.5 ms, the peak impacted force reached. The minor flexural crack at mid-span developed and one shear crack formed an inclination angle of 45 degrees (Fig. 5.15 (c)). Several minor cracks on the top surface of the column started to appear close to the clamping boundary since the negative bending moment is larger than 6 kN × m. The initial peak shear force was reached and equalled to 203

kN. At 6 ms, the maximum bending moment was attained. Fig. 5.15 (d) shows one major crack was developed with a width less than 5 mm.

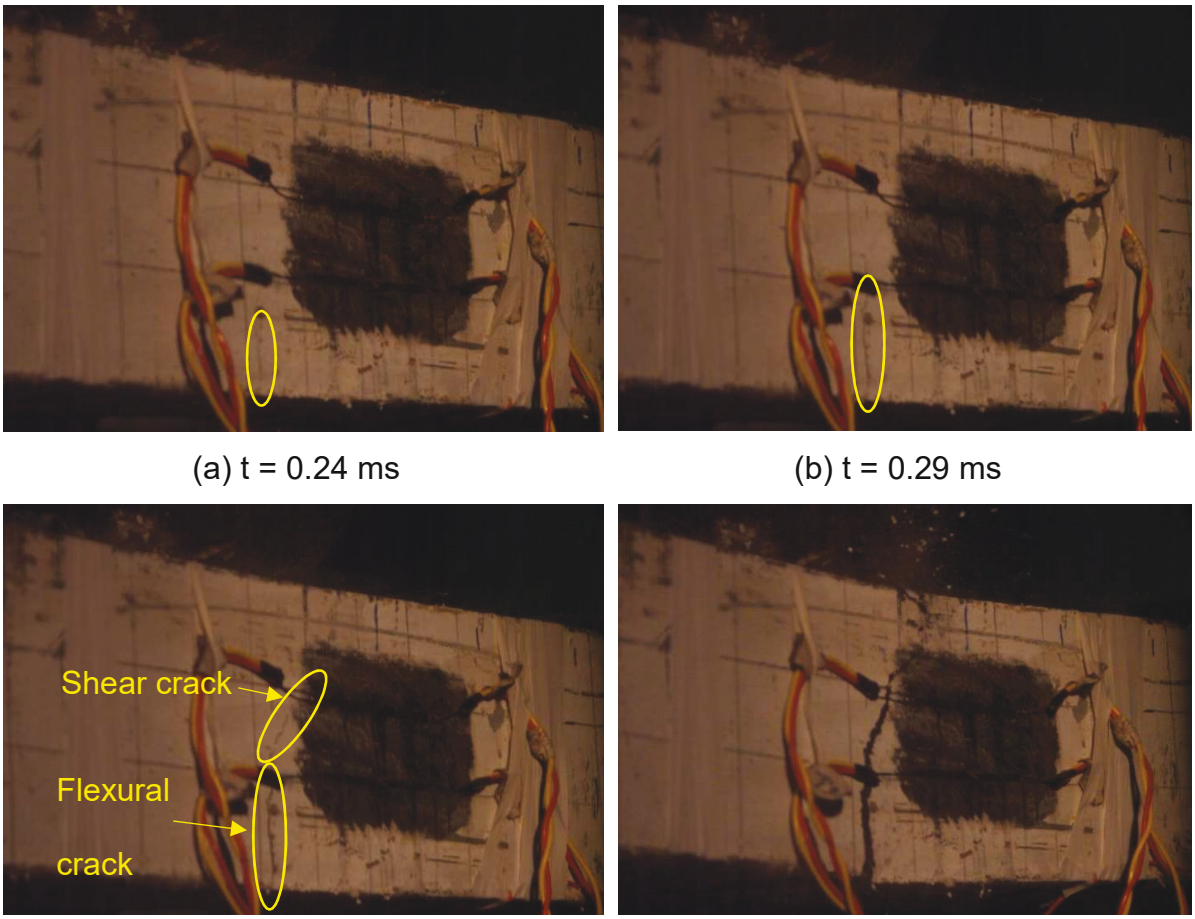

(a) t = 0.24 ms (b) t = 0.29 ms

(c) t = 0.5 ms (d) t = 6 ms

Fig. 5.15. Dynamic process of UHPC column (UHPC-R)

Fig. 5.16 presents the maximum shear and bending moment distribution diagrams for all test specimens as compared to the solid column under the same impact scenario. In Fig. 5.16, the maximum absolute value for the whole impacted process was adopted in the diagram. For example, at 0.55 m (Fig. 5.14 (b)), the bending moment shows both of positive and negative moment during impact process and ranged from -10.05 kN × m to 8.24 kN × m. Hence, -10.05 kN × m is adopted for the maximum bending moment at 0.55 m in Fig. 5.16. Compared with the solid column, the hollow-core UHPC columns exhibits an overall lower shear force and bending

moment. The shapes of hollow-core had limited influence on impact resistance. Further studies on the influence of the shape of hollow core would be present in the parametric study. For steel wire mesh reinforced UHPC columns, since the specimen experienced flexural damage, the shear force distribution was similar as compared to the solid column. It is noted the flexural resistance of the steel wire mesh reinforced columns was not as good as the solid columns.

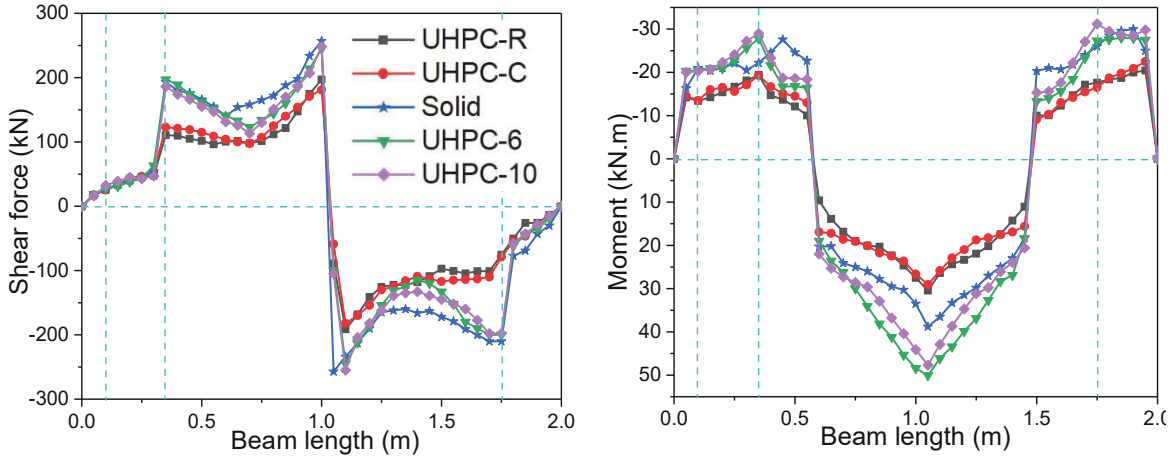

5.4.4 Residual axial capacity test for post-impact column

Since column structures are primarily designed to carry axial loads, the residual axial load capacity of columns after lateral impact scenario is necessary to quantify so that collapse risk could be evaluated. The criteria based on residual axial capacities is applied to quantify the damage extent of hollow-core columns, and steel wire mesh reinforced columns. Similar to Shi et al. [101], a damage index (D_i) is used for post-impacted UHPC columns and defined in Eq. (3.19).

To estimate ultimate axial load capacity, Table 5.6 lists different formulas described by different specifications. Based on these formulas, the axial load capacity is contributed from confined concrete and longitudinal bars. However, Fan et al. [174] measured experimental axial capacities of RC columns, and they pointed out that the

axial load-carrying capacity provided from specification was underestimated. Li et al. [102] tested the ultimate load capacity of UHPC columns. The experimental capacities were also higher than capacities predicted by the specification. Since the possible limitations of code perdition might result in an underestimation of damage index, the numerical capacities are used as N_{max} in this study.

Specification	Calculation formula
America (ACI 318)	$N_{design} = 0.85f_c'(A_g - A_s) + f_y A_s$
Europe (EN 1992-1-1)	$N_{design} = 0.833f_c' A_g + f_y A_s$
Japan (JGC15)	$N_{design} = 0.85f_c' A_{cor} + 2.5f_y A_{sso} + f_y A_s$

where, N_{design} is ultimate capacity; f_c' is the compression strength; A_g is cross-section area; A_s is reinforcing bars' area; A_{cor} is core concrete area; A_{sso} is the area of the spiral bars

Table 5.6 Formula for calculating ultimate axial load capacity of designed columns.

After impact simulation, the residual axial capacity test was conducted by FE modelling tests. After the impact scenario simulation, *RESTART function was applied for the quasistatic residual loading capacity simulation. *RESTART function allows user to restart the simulation by providing defining changes to the model such as deleting contacts, materials, switching materials from rigid to deformable and so on. Moreover, the restart file just keeps the deformation of the column so that the effect of free vibration is not considered. More detail description of *RESTART is discussed in its user's manual [175]. In the restart analysis, the drop hammer was deleted. The post-impact column was placed on the clamping devices with an axial load applied gradually until failure to the evaluation of residual capacity N_{re}.

Numerical test results are listed in Table 5.7 and Fig. 5.17 presents the comparisons of the damage extent of test specimens and the solid column. Under a 411 kg drop hammer falling from 1.25 m height, the solid column showed low damage. The hollow-core UHPC columns with a 10 % hollow ratio also demonstrated a good impact resistance with low flexural damage. The steel wire mesh reinforced UHPC columns experienced medium damage.

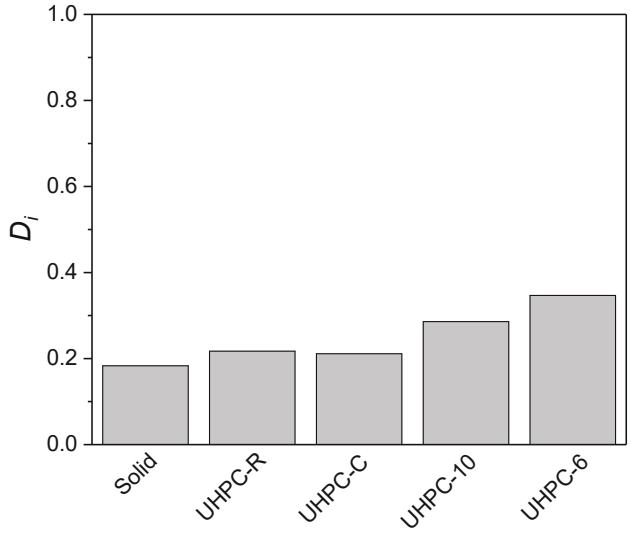

Fig. 5.17. Damage extent of test specimens and solid column

5.5 Parametric Study

5.5.1 Numerical simulation matrix

To evaluate the effect of key design parameters on the impact resistance and residual strengths of UHPC columns, a parametric study was conducted through the FE model described previously. For hollow-core UHPC columns, key parameters included hollow ratio = 5%, 10%, 15% and 20%; initial impact velocity = 4.95 m/s, 5.86 m/s and 6.64 m/s; shapes of hollow hole = rectangular and circular; axial load level = 10% (400 kN), 15% (600 kN) and 20% (800 kN); longitudinal reinforcement ratio ρ_s = 0.012, 0.025 and 0.033. Sections details of UHPC columns with different hollow ratios

are shown in Fig. 5.18. “R” and “C” represent a rectangular and circular shape of the hollow hole. The number afterwards denotes a hollow ratio. “W” “D” and “R” in brackets represent width, depth and diameter, respectively. For compression, the control solid UHPC columns were set and tested with different initial impact velocity. For steel wire meshed UHPC columns, key parameters included the layers of steel wire mesh reinforced under centre axis = 4, 5, 6; the layers of steel wire mesh reinforced whole column section = 8, 10, 12. As summarized in Table 5.7, totally 39 tests are simulated on hollow-core UHPC columns, and steel wire mesh reinforced UHPC columns.

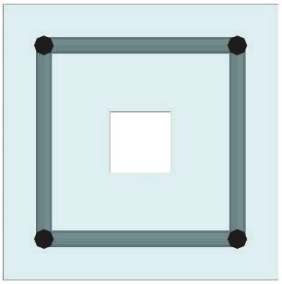

R5% (W37-D37)

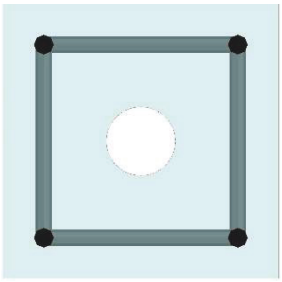

C5% (R42)

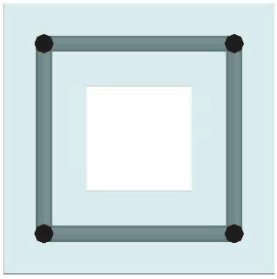

R15% (W65-D65)

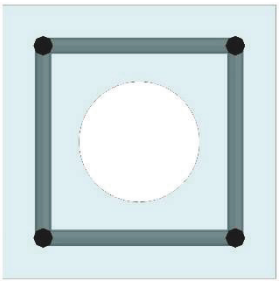

C15% (R73)

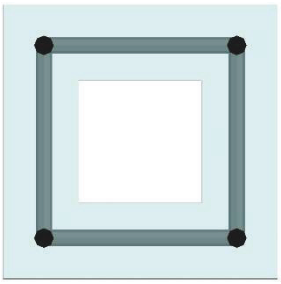

R20% (W75-D75)

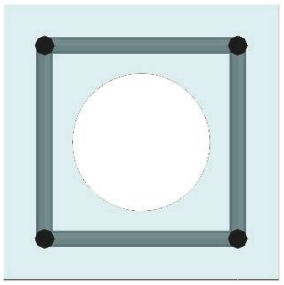

C20% (R84)

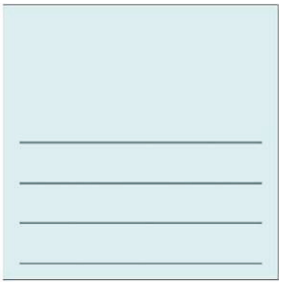

UHPC-4

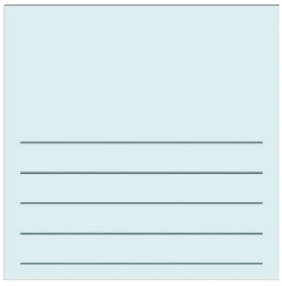

UHPC-5

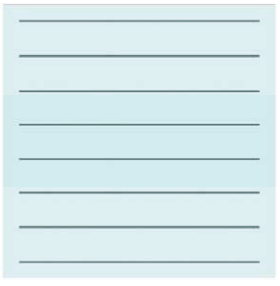

UHPC-8

UHPC-12

Fig. 5.18. Schematic of different UHPC column configurations (unit: mm)

Series	ID	Types	Variables			Deflection		Load capacity	
			V_i (m/s)	N (kN)	ρ_s	d_{max} (mm)	d_{re} (mm)	N_{max} (kN)	N_{re} (kN)
Control	1	-	4.95	200	0.018	32.2	15.6	4471	3652
UHPC	2	-	5.86	200	0.018	38.7	21.2	4471	3320
column	3	-	6.64	200	0.018	46.7	27.1	4471	2870
Hollow-	4	R5%	4.95	200	0.018	26.3	14.4	4094	3256
core	5	C5%	4.95	200	0.018	26.8	14.1	4117	3293
UHPC	6	R10%	4.95	200	0.018	27.5	15.1	3773	2953
column	7	C10%	4.95	200	0.018	27.9	14.7	3787	2987
	8	R15%	4.95	200	0.018	28.5	15.9	3352	2604
	9	C15%	4.95	200	0.018	28.7	15.7	3378	2633
	10	R20%	4.95	200	0.018	29.3	16.6	3021	2308
	11	C20%	4.95	200	0.018	29.7	16.3	3049	2322
	12	R5%	5.86	200	0.018	35.1	16.7	4094	2878
	13	C5%	5.86	200	0.018	35.7	15.9	4117	2896
	14	R10%	5.86	200	0.018	36.1	19.3	3773	2541
	15	C10%	5.86	200	0.018	36.6	18.7	3787	2563
	16	R15%	5.86	200	0.018	37.6	21.3	3352	2135
	17	C15%	5.86	200	0.018	38.1	20.6	3378	2164

	18	R20%	5.86	200	0.018	39.8	23.5	3021	1815
	19	C20%	5.86	200	0.018	40.5	22.9	3049	1840
	20	R5%	6.64	200	0.018	45.1	24.3	4094	2428
	21	C5%	6.64	200	0.018	45.8	23.9	4137	2477
	22	R10%	6.64	200	0.018	47.5	28.6	3773	2095
	23	C10%	6.64	200	0.018	47.7	26.9	3787	2114
	24	R15%	6.64	200	0.018	49.1	29.5	3352	1687
	25	C15%	6.64	200	0.018	49.8	30.6	3378	1711
	26	R20%	6.64	200	0.018	52.6	36.3	3021	1213
	27	C20%	6.64	200	0.018	53.1	35.3	3049	1238
	28	C10%	4.95	400	0.018	24.4	14.9	3787	3061
	29	C10%	4.95	600	0.018	22.1	14.1	3787	3110
	30	C10%	4.95	800	0.018	20.9	13.5	3787	3146
	31	C10%	4.95	200	0.012	29.5	18.6	3787	2860
	32	C10%	4.95	200	0.025	25.1	16.2	3787	3052
	33	C10%	4.95	200	0.033	23.3	13.8	3787	3122
Steel wire	34	UHPC-4	4.95	200	-	37.4	21.5	3964	2510
mesh	35	UHPC-5	4.95	200	-	36.9	21.1	4009	2584
reinforced	36	UHPC-6	4.95	200	-	36.6	20.7	4056	2650
UHPC	37	UHPC-8	4.95	200	-	32.7	18.9	4151	2922
column	38	UHPC-10	4.95	200	-	31.6	17.6	4207	3004
	39	UHPC-12	4.95	200	-	30.5	16.1	4239	3065

where, V_i = initial impacting velocity; N = axial loads applied before impact test; ρ_s = longitudinal reinforcement ratio; f_{max} = first peak impact force; I = impulse (the area under force time history); d_{max} = maximum displacement; d_{max} = residule displacement.

Table 5.7 Summary of the FE results.

5.5.2 Effects of major parameters

5.5.2.1 Effects of hollow hole shapes

The impact resistance for UHPC columns with rectangular and circular hollow holes was examined under different impact loading, including 4.95 m/s, 5.86 m/s and 6.64 m/s. Fig. 5.19 illustrates the displacement comparison. Overall, UHPC columns with circular hollow section perform better although the difference is marginal. Although the area of rectangular and circular hollow holes in the cross-section is the same, the flexural stiffness of the circular hollow-core column is slightly larger than that of the rectangular hollow-core column, leading a larger lateral stiffness of the circular hollow-core column. Since the difference between rectangular and circular hollow-core columns is not obvious and the circular hollow-core columns have overall smaller residual displacement and damage extent D_i, the following analysis adopts data of circular hollow-core columns.

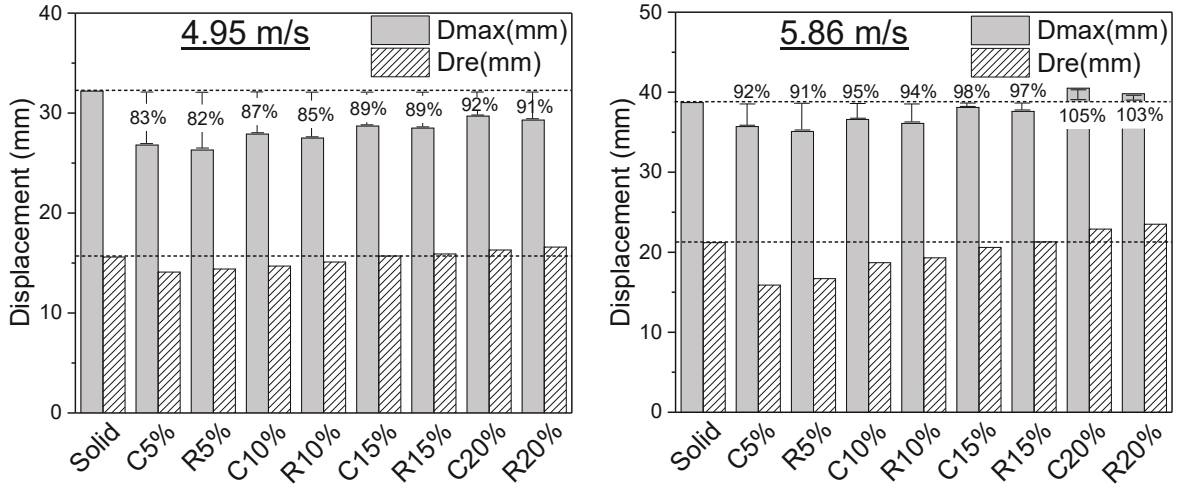

(a) (b)

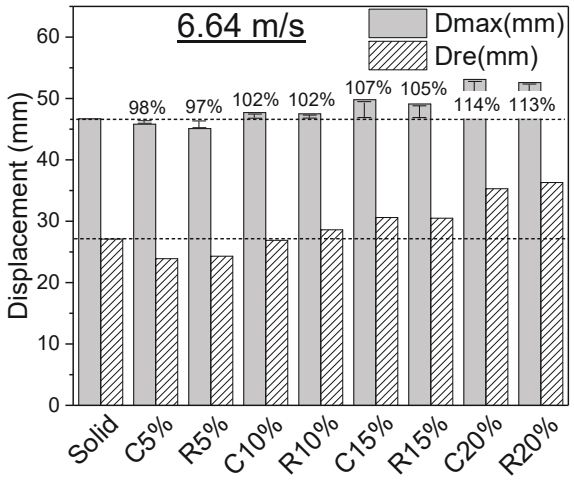

(c)

Fig. 5.19. Displacement for UHPC columns with rectangular and circular hollow holes under different impact loading scenario (a) 4.95 m/s (b) 5.86 m/s (c) 6.64 m/s

5.5.2.2 Effects of the hollow ratio

UHPC columns with four hollow ratios, ranging from 5% to 20%, and control solid UHPC columns were investigated. Fig. 5.20 (a) illustrates the comparison of the first peak impact force of UHPC columns with different hollow ratio. In this comparison, under the same impact scenario, the first peak impact force decreased with increasing the hollow ratio. The same behaviour was observed on the specimen under higher loading rates. This is because increasing the hollow ratio could decrease the moment of inertia and stiffness of the column structures. Fig. 5.20 (b) illustrates the comparison of defined damage D_i of hollow-core HUPC columns. It is noted that, under low impact velocity (5 m/s), although an increase in the hollow ratio would reduce the maximum axial load carrying capacity, the damage D_i is similar. With increasing the impact velocity, hollow-core UHPC columns experienced more evident damage. When the initial impact velocity reached to 6.64 m/s, C20% experienced severe damage while the other three columns could keep more than 50% of its maximum capacity. Based

on the above observation, considering both economic benefit and impact resistance, C15% is considered to be a better design.

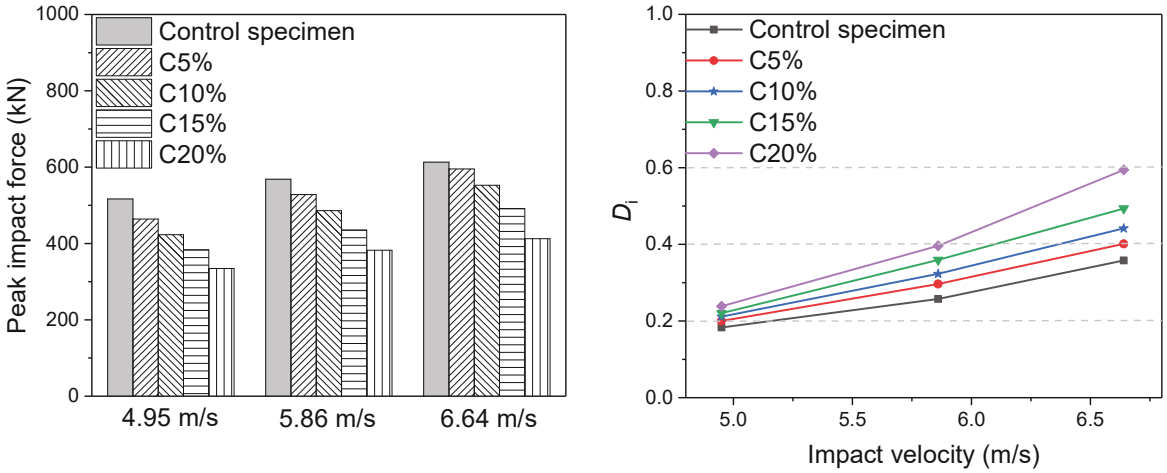

(a) (b)

Fig. 5.20. Effects of hollow ratio on (a) peak impact force and (b) damage extent D_i

5.5.2.3 Effects axial load level

Four axial load levels, varying from 200 kN to 800 kN of axial capacity (N_{max}) of the C10% column, were evaluated. Fig. 5.21 (a) shows the damage extent D_i of the columns. Generally, the damage decreased with increasing the axial load ratio from 200 kN to 800 kN. This behaviour occurred because the applied axial loads tended to improve the confinement effect of UHPC during the test, leading to an increase in moment capacity and hence impact resistance. However, it is noted that the results are obtained based on the axial load ratio from 0.05 to 0.2. If the axial load ratio is larger than 0.2, the results might not be true because the secondary P-Delta would bring a more pronounced detrimental effect on the flexural damaged column.

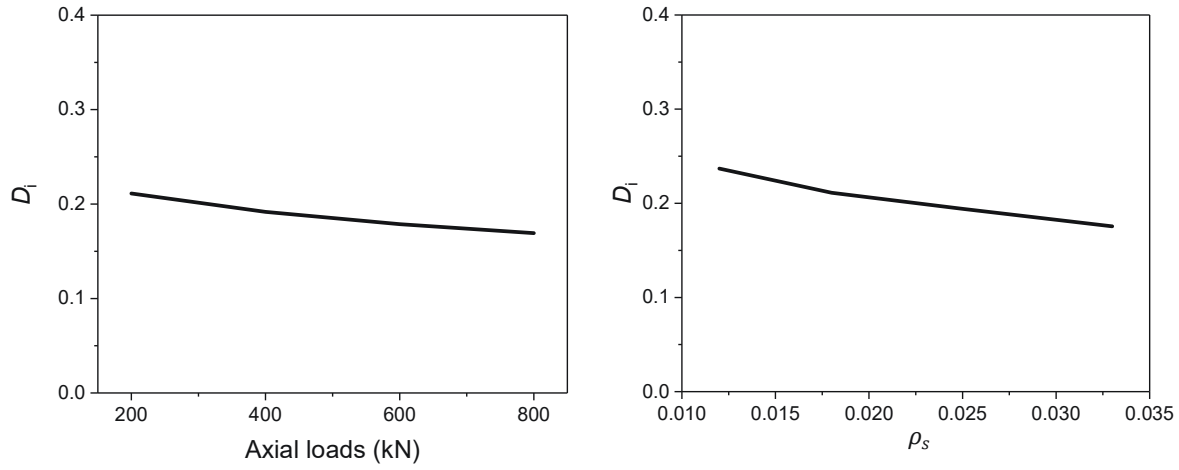

(a) (b)

Fig. 5.21 Influences of (a) axial loads and (b) longitudinal reinforcement ratio on D_i

5.5.2.4 Effects of longitudinal reinforcement ratio

Four values of longitudinal reinforcement ratio, varying from 0.012 to 0.033, are evaluated. Fig. 5.22 (b) shows damage extent D_i of the columns with different longitudinal reinforcement ratio. The results show enhancing the reinforcement ratio in compression could decrease damage extent, which is expected.

5.5.2.5 Effects of layers of steel wire mesh

For steel wire mesh reinforced UHPC columns, two strengthening methods were designed including steel wire mesh strengthening under centre axis (layers = 4, 5, and 6) and strengthening the whole column section (layers = 8, 10, 12). Fig. 5.22 illustrates the comparison of displacement and damage extent of UHPC columns with different steel wire mesh layers. In this comparison, for steel wire mesh reinforced in tension zone only, increasing layers had no obvious effect on bending resisting strength. It is noted that steel wire mesh reinforced in both tension and compression could improve the bending strength and reduce residual displacement. For damage extent $\mathrm{D_i}$, increasing layers also had slight effects on axial residual capacity. This was attributed

to the fact that the axial capacity of a steel wire mesh reinforced UHPC column depends on the confined concrete rather than the amount of steel wire mesh.

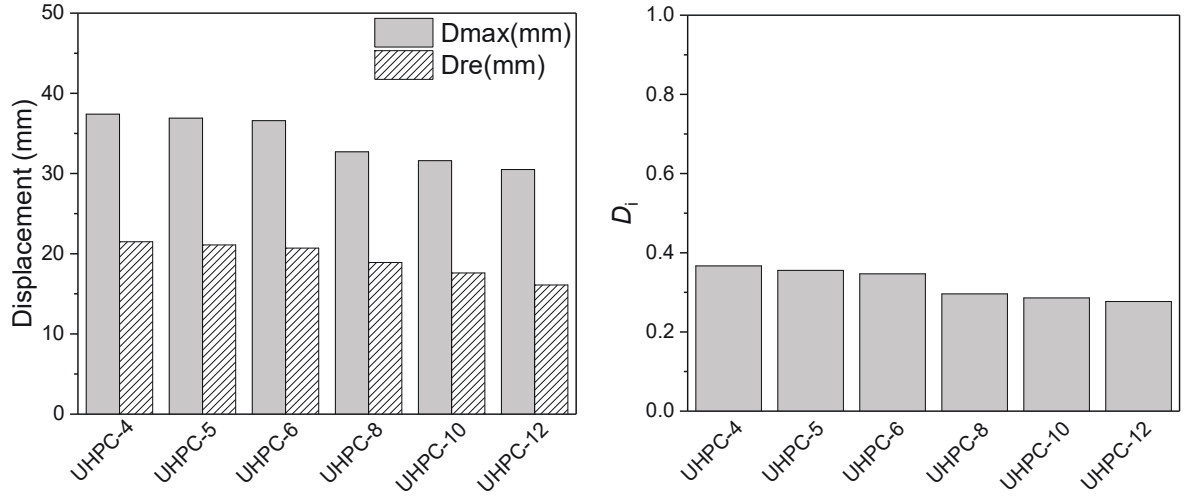

(a) (b)

Fig. 5.22. Effects of layers of steel wire mesh on (a) displacement and (b) D_i

5.6 Summary and Identification of the Gap

Drop hammer impact tests on axially loaded hollow-core, and steel wire mesh reinforced UHPC columns have been performed. Subsequently, a finite element modelling method are proposed to investigate the residual loading capacity of the column. The influences of key parameters on the impact resisting behaviour of UHPC based columns were parametrically investigated. Several conclusions are given from this work:

1. The crashworthiness of axially loaded UHPC columns was considerably superior. Test specimens showed minor flexural damage with limited concrete crush around the loading point. This highlighted the excellent impact resistance of UHPC material.

2. High-fidelity FE models were developed to reproduce the behaviour of UHPC columns subjected to impact loading. The modified boundary condition that reflects a partial fixture demonstrated a good agreement with experimental results. The simulation for steel wire mesh reinforced UHPC columns remain an issue unsolved. The bond-slip behaviour between the wire mesh and surrounding UHPC matrix was considered as the reason for the inaccurate results. Further studies need to be performed to develop the bond-slip behaviour.

3. Residual axial loading capacity of post-impact was numerically tested and adopted as damage criteria to quantify column damage extent. For hollow-core UHPC columns, different hollow shapes have limited influence on their residual axial loading capacity when the hollow ratio was constant. Their impact resistance is influenced by hollow ratio, loading rate, axial load level and longitudinal reinforcement ratio. For steel wire mesh reinforced UHPC column, the column with steel wire mesh strengthening in the whole columns has a better impact resistance than that strengthening only in the tension zone. The layer number has no obvious effects on residual axial loading capacity.

Chapter 6

Behaviour of Ultra-high Performance Concrete Strengthened Reinforced Concrete Beams under Impact Loading

6.1 Introduction

UHPC can be adopted as the strengthening or repairing material to extend the life of RC components and reduce the frequent maintenance. As noted in the above literature, the addition of UHPC layers enhanced crack resistance, flexural capacity, rotation capacity and fatigue resistance. However, limited experimental studies were conducted to explore the dynamic response and associated cracking mechanisms of RC beams strengthening by UHPC layers. Therefore, drop hammer impact tests were performed on UHPC strengthened concrete beams. Material and interfacial bonding strength tests were carried out. Three designs of RC-UHPC beams were casted and tested under a well-instrumented drop weight test. Crack propagation analysis is conducted with high-speed video recordings. Subsequently, a high-fidelity finite element model was performed. Shear failure mechanisms were investigated based on experimental and validated numerical results. A parametric numerical study was proposed to evaluate the influences of key parameters on UHPC strengthening against low velocity impact loads.

6.2 Experimental Program

6.2.1 Materials

In the study, NSC was composed of cement, sand, aggregate and water, and designed according to AS 1012.2-2014 [176]. The maximum particle size of coarse

aggregate is 20 mm. The mix configurations of concrete are shown in Table 6.1. UHPC was made of 42.5 Grade Portland cement, nano-particles, silica fume with a maximum particle size of 0.2 μm, dry river sand with the size of 0.4-0.5 mm, tap water and superplasticizer. The water to binder ratio was 0.19. To improve the tensile performance of UHPC, smooth steel fibres with a volume dosage of 2.5% was used. The steel fibres were 15 mm in length and 0.2 mm in diameter. The tensile strength and elastic modulus of steel fibre were 2850 MPa and 200 GPa, respectively.

Ingredient	NSC (kg/m^3)	UHPC (kg/m^3)
Portland cement	551.9	750
Silica fume	-	225
Fine sand	843.1	1030
Coarse aggregate	745.9	-
Water	282.7	190
Polycarboxylate water reducer	-	16
Nano particles	-	21.7
Steel fibres (2.5%Vol.)	-	190

Table 6.1 Mix proportions of conventional concrete and UHPC.

The strengths of NSC and UHPC were obtained from tests designed according to the relevant codes (ASTM C469M [177] and ASTM C78 [178]). The compressive behaviour was explored by testing cylindrical specimens with a 200 mm height and a 100 mm diameter. These specimens were characterised by the servo hydraulic testing machine (maximum capacity: 2000 kN). A loading rate of 60 kN/min is first adopted until 800 kN, then a displacement-controlled load with 0.3 mm/min loading rate was

exerted. The specimen number was three, and the final results were averaged from tests. The measured stress-strain curves from uniaxial compression tests are shown in Fig. 6.1 (a). The elastic modulus was measured by strain gauges attached to cylindrical specimens, and was calculated following ASTM C469M [177]. The measured compressive properties of UHPC and NSC are summarized in Table 6.2.

Prism specimens with a dimension of 100 mm x 100 mm x 400 mm were fabricated and tested through the hydraulic machine. All specimens were prepared from the same batch, and were cured with the same conditions. Average flexural strength from three prism specimens in each batch was reported. Mid-span deflection was measured through two parallel LVDTs installed on both sides of specimens. The measured average force versus central deflection curves of NSC and UHPC are shown in Fig. 6.1 (b). The flexural strength of NSC and UHPC could be calculated following ASTM C78 [178], and summarized in Table 6.2.

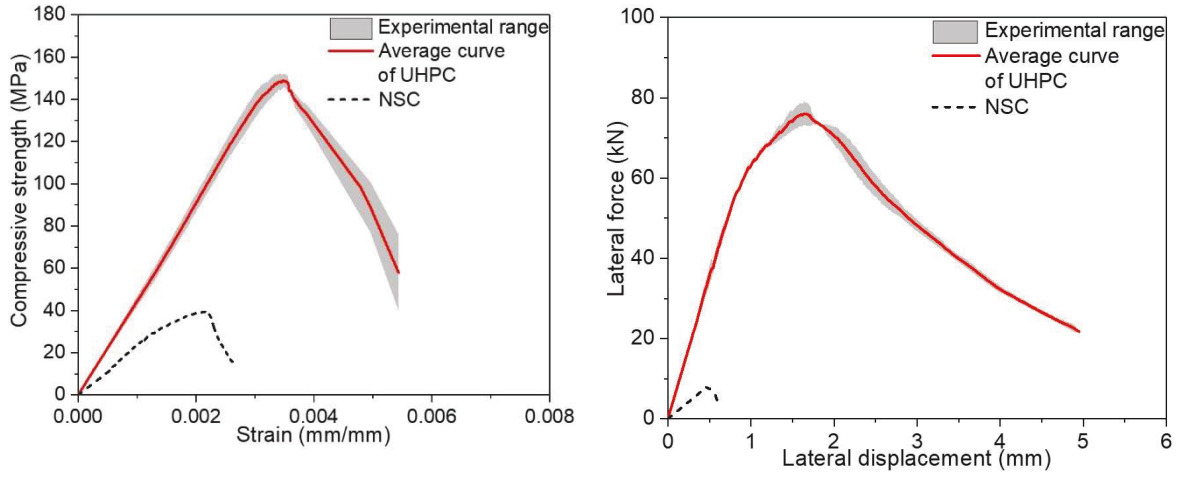

(a) Compressive stress-strain curve (b) Force versus displacement curve

Fig. 6.1. Measured curves of NSC and UHPC

Materials	No.	Compressive strength (MPa)	Average strength (MPa)	Elastic Modulus (GPa)	No.	Flexural strength (MPa)	Average strength (MPa)
NSC	1	39.6	39.5	32.5	1	3.9	4.1
	2	38.2			2	4.4	
	3	40.7			3	4.0	
UHPC	1	145.8	147.1	52.1	1	22.7	22.8
	2	142.7			2	22.1	
	3	152.7			3	23.7	

Table 6.2 NSC and UHPC properties.

6.2.2 UHPC-NSC interfacial strength test

To measure the interfacial bond strength, the slant shear and splitting tensile tests were conducted. The slant shear test was designed following ASTM C882 [179]. Although the test method was intended to explore the bond strength of epoxy-resin and latex bonding systems, researchers have successfully utilized this method to characterize the shear and compressive capacity of composite concrete specimens [180, 181]. In the study, the slant shear test was conducted on cylindrical specimens with a 200 mm height and a 100 mm diameter. After being cured at room temperature for 28 days, NSC cylindrical specimens were cut at an angle of 30° from the vertical direction (Fig. 6.2 (a)). Then, the surface is roughened by sandblasting. The specimens were then moulded and cast with fresh mixed UHPC. Finally, the UHPC-NSC specimens were ambient cured until the testing. The setup was shown in Fig. 6.2 (a). The universal testing machine was used at 0.5 mm/min. All specimens were tested

in a group of six, and averaged strength was reported in Table 6.3. Relationship among applied load and strength are expressed as follows:

$$\sigma_s = \frac{4F}{\pi D h_s}(\cos\theta)^2$$
$$\tau_s = \frac{4F}{\pi D h_s}\sin\theta \times \cos\theta \quad (6.1)$$

where, σ_s is compressive stress, Pa; τ_s is shear stress, Pa; F is the ultimate load, N; D is spacemen diameter, m; h_s is slant height, 0.2 m in the study; θ is the angle between the interface and horizontal, 60° in the study. ACI 546-06 [182] recommended the bond strength to select appropriate repair materials. For the slant shear test, the metrics are: 400 to 1000 psi (2.8 to 6.9 MPa) for 1 day; 1000 to 1800 psi (6.9 to 12 MPa) for 7 days; 2000 to 3000 psi (14 to 21 MPa) for 28 days. In the present study, the bond strength of 5-day-old specimens was 5.59 MPa, which was deemed satisfactory.

ASTM C496 [183] provides a test method to determine the splitting tensile strength of concrete strength. Since the failure of the UHPC-NSC specimen usually occurs at the interface, the interfacial bond strength is therefore linked to the measured split tensile strength values. If the failure occurs away from the bond line, the bond strength is higher than the failure load. If the failure occurs at the bond line, the measured tensile force is the actual interfacial bond strength [182]. In the study, six cylindrical specimens with a 200 mm length and a 100 mm diameter were designed for the splitting tension test. The fabrication procedure of splitting tensile test specimens was the same as slant shear test specimens, except that NSC specimens were vertically cut at mid span and the other half was cast with UHPC (Fig. 6.2 (b)). The test data were listed in Table 6.3. The strength is calculated as follows:

$$f_{st} = \frac{2F}{\pi l D} \tag{6.2}$$

where, f_{st} is splitting tensile strength, MPa; l is the length of specimens, m. The metrics defined in ACI 546-06 [182] are: 70 to 150 psi (0.48 to 1 MPa) for 1 day; 150 to 250 psi (1 to 1.7 MPa) for 7 days; 250 to 300 psi (1.7 to 2.1 MPa) for 28 days. Similarly, Sprinkel and Ozyildirim [184] presented the metrics to define the bond quality. The metrics are: excellent: ≥ 2.1 MPa; very good: 1.7 to 2.1 MPa; good: 1.4 to 1.7 MPa; fair: 0.7 to 1.4 MPa; poor: 0 to 0.7 MPa. For the specimens tested, the mean bond strength was 1.67 MPa, which fits within the thresholds of specification.

(a) Slant shear test

(b) Splitting tensile test

Fig. 6.2. UHPC-NSC interfacial bond strength tests (unit: mm)

Slant shear test				Splitting tensile test			
No.	Ultimate applied force (kN)	Shear strength (MPa)	Standard Deviation (MPa)	No.	Ultimate applied force (kN)	Tensile strength (MPa)	Standard Deviation (MPa)
1	206.1	5.59	0.23	1	47.4	1.67	0.19
2	191.6			2	45.1		
3	216.4			3	62.6		
4	198.7			4	53.1		
5	195.3			5	57.8		
6	208.9			6	49.6		

Table 6.3 Interfacial strength test results (5 days).

Like most of the similar tests presented in the literature, the material parameters in the current work include compressive strength, elasticity modulus, flexural strength and interfacial bonding. Each specimen type was tested three times to ensure the reliability of the test results. The mean value and standard deviation were reported in Table 6.2 and Table 6.3. It is well known that the parameters of structure and loading would inevitably have certain variability, regardless of how much control was implemented in the experiments. To account for the uncertainties and variability in the analysis, structural reliability analysis shall be performed. However, it must be emphasized that statistical information about UHPC is still very limited. Early studies on UHPC material properties have been used in structural reliability analysis. Different mean values, coefficient of variation and distribution were assumed in such analysis. In addition, the post-cracking tensile strength of UHPC depended on many parameters

(e.g., distribution and orientation of embedded fibres), and could result in a large scattering response. More statistical studies on UHPC material properties are therefore deemed necessary for the structural reliability analysis.

6.2.3 Fabrication and preparations of test specimens

A total of seven large-size beam specimens were casted for the drop hammer impact test. These beam specimens were grouped into four series in accordance with different strengthening methods, including two RC beams, one B15 beam (Fig. 6.3 (b)), three B20 beams (Fig. 6.3 (c)), and one T15B15 beam (Fig. 6.3 (d)). The beam specimens were named as follow: (1) the letters “B” and “T” represent that the UHPC layer was strengthened at the bottom and top surfaces of the RC beam, respectively; (2) the number afterwards denotes the depth of the UHPC layer.

The RC beams were cast and ambient cured for more than 100 days. The geometric configuration of RC beams is shown in Fig. 6.3 (a). Each beam had a 168 mm rectangular cross-section and a 2000 mm span. The 12 mm diameter deformed bars were symmetrically arranged at four corners of the beam specimen. A 25 mm thickness of concrete cover was employed. To provide shear resistance, stirrups with a 10 mm diameter were placed at a 200 mm spacing. For the B15 and T15B15 specimens, the bottom and top surfaces of RC beam specimens were roughened by sandblasting. Then, the RC specimens were moulded and cast with the UHPC layer at a 15 mm thickness. For the B20 specimens, after roughening, 5 mm spacing was left at mid-span by placing an Expanded Polystyrene (EPS) foam prism with a dimension of 1400 × 168 × 5 mm beneath the beam bottom surface (Fig. 6.3 (c)), and then cast with the UHPC layer with a total of 20 mm thickness.

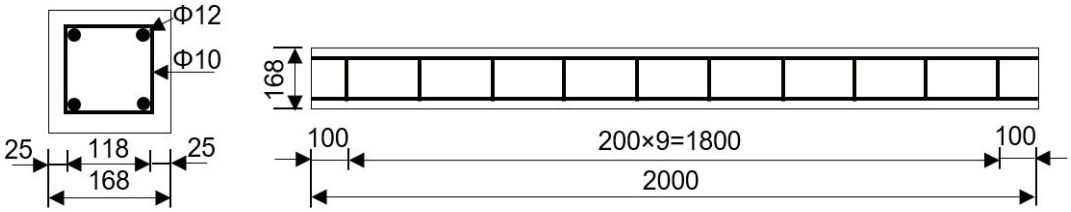

(a) reinforcement layout (unit: mm)

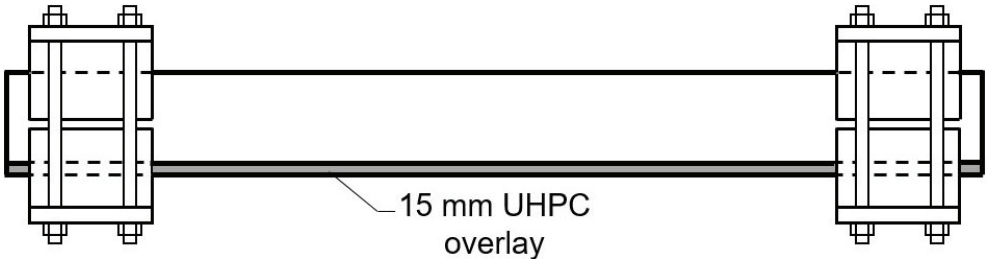

(b) B15

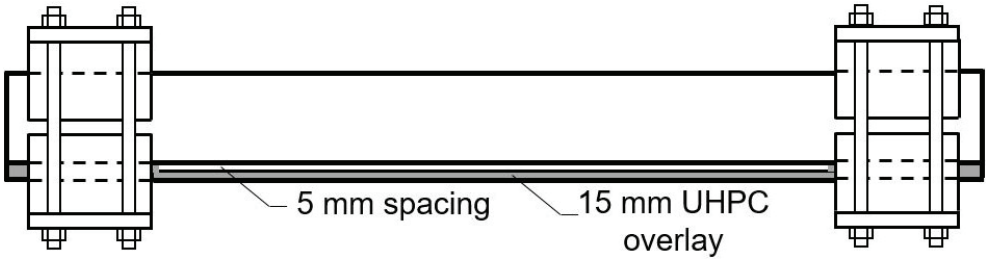

(c) B20

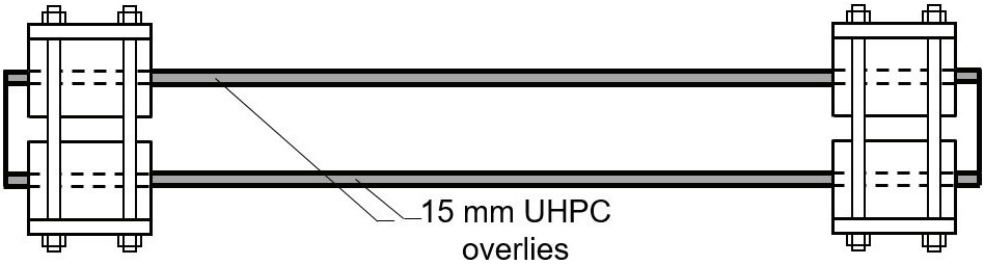

(d) T15B15

Fig. 6.3 Detailed scheme for NSC-UHPC specimens

6.2.4. Test setup and instrumentation

Fig. 6.4 shows the drop hammer impact test setup and arrangement of instrumentation in the beam specimens. The drop hammer machine includes a drop

hammer frame, clamping system and measuring system. The weight of the drop hammer frame is 641 kg. Higher weight could be adjusted by attaching weight blocks onto the frame. The maximum drop height was designed as 5 m. The load cell with a 1.2 MHz sampling rate was bolt fixed between the indenter and drop hammer frame. The hemispherical indenter with a diameter of 100 mm was used in the study. The drop hammer will fall freely along the guide rails when the release system is triggered. The clamping system was designed to provide fully fixed boundary conditions. As shown in Fig. 6.4 (b), the beam specimens were placed on the steel clamping devices, which was supported by the steel frames. The strong floor fixed with steel frames. The clamping devices was constrained by a heavy steel plate with a thickness of 30 mm. Then, the heavy steel plate was fixed to the supporting frame by high strength steel bars and screw caps.

The deflection of test beam specimens was measured by LVDTs, high-speed camera (Model: Photron FASTCAM SA-Z) and IL Series multi-function laser sensor (Model: IL-1000) produced by Keyence Company. Due to the concern that impact-induced concrete spalling may destroy the LVDTs at mid-span, the LVDT-1 and LVDT-2 were placed 500 mm and 240 mm away from the right clamping device, respectively. The laser sensor was also placed 500 mm away from the clamping device, and the measured values were used to validate values measured by LVDT-1. The high-speed camera was applied to record the deflection movement at 10000 frames per second. The deflection of the measuring points could be collected through the point tracking technology in Photron FASTCAM Viewer software (PFV), as compared to values measured by other sensors. The data acquisition system was used to capture data at a sampling rate of 100 kHz.

Table 6.4 presents the test matrix. These beam specimens were grouped into three series ("*a*" and "*b*" series) in accordance with different loading schemes. For *a*-series specimens, beams with a 1.4 m clear span were subjected to one single impact. The drop height was 0.5 m and the impact location was at mid-span. For *b*-series specimens, beams were subjected to repeated impacts. The drop height of the two impacts was 0.25 m.

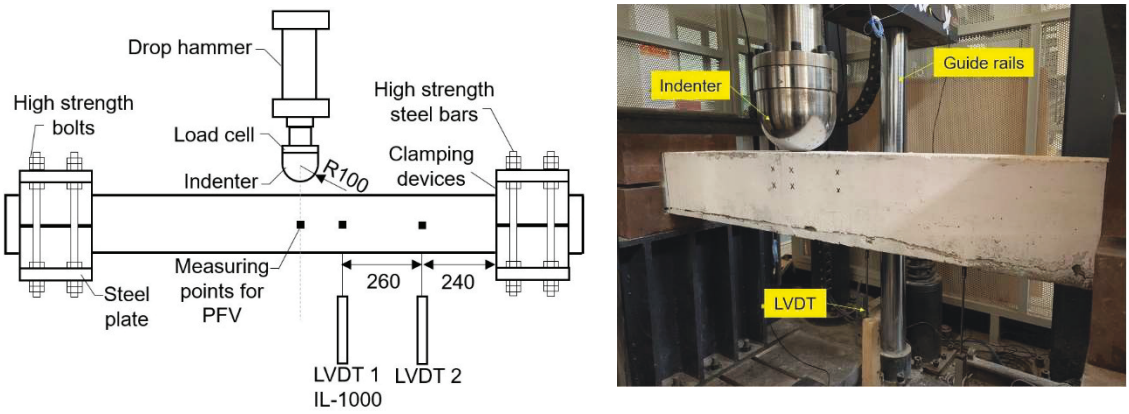

(a) Schematic view of setup (b) Picture of setup

Fig. 6.4 Drop hammer impact test setup (unit: mm)

Type	Drop height (m)	Impact velocity (m/s)	Hammer mass (kg)	Clear span (m)
RC-a	0.5	3.13	641	1.4
B15-a	0.5	3.13	641	1.4
B20-a	0.5	3.13	641	1.4
T15B15-a	0.5	3.13	641	1.4
RC-b	0.25/0.25	2.21/2.21	641	1.4
B20-b	0.25/0.25	2.21/2.21	641	1.4

Table 6.4 Lateral impact test matrix.

6.2.5 Test results

6.2.5.1 Crack patterns and failure mode

Fig. 6.5 exhibits the failure modes of all beams under impact loading. Based on the observation from crack development, the shear failure patterns of beam specimens could be divided into two series as shown in Fig. 6.6: (1) diagonal cracks developing to the shear plug (Type i); (2) inclined cracks forming in the shear span (Type ii). Zhao et al. [44] noted that Type ii cracks were dominant failure cracks when beam specimens were subjected to relatively low impact energy. With increasing the imported kinetic energy, Type i cracks were more evident and developed to dominant failure cracks while Type ii cracks was unimportant or not visible at all.

In the case of specimens in *a*-series, the beam RC-a exhibited severe shear failure modes. The beam was fractured with concrete spalling around mid-span, and the longitudinal bars were exposed. For B15-a, the Type i cracks were dominant and forming a shear plug at mid-span. The failure mode of the RC beam shifted from local concrete shattering to shear failure. The crack patterns of B20-a were similar to those of B15-a but without the formation of shear plugs, indicating the B20 strengthening method was more effective. For T15B15-a, both top and bottom surfaces were strengthened by 15 mm UHPC layers. Compared with B15-a, since the deformation of the top UHPC layer dissipated a portion of impact energy, the crack patterns of the RC beam shifted from Type i to Type ii.

The failure modes of the specimens subjected to repeated impacts were similar to those of the a-series. For b-series specimens, RC-b exhibited concrete shattering while B20-b exhibited diagonal shear failure at mid-span with evidently reduced deflection.

(a) RC-a

(b) B15-a

(c) B20-a

(d) T15B15-a

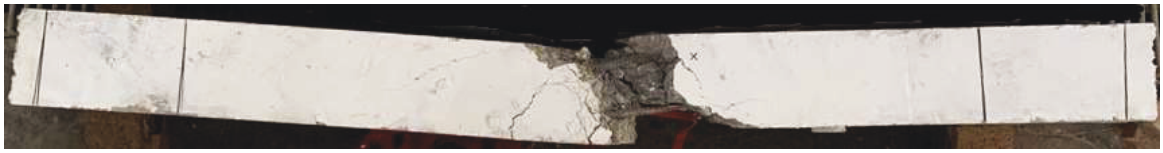

(e) RC-b

(f) B20-b

Fig. 6.5. Failure patterns under impact loading

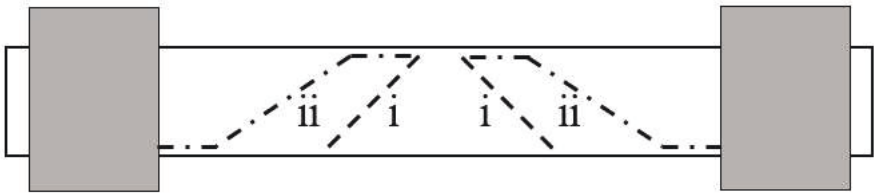

Fig. 6.6. Typical shear failure crack pattern in RC beams

6.2.5.2 Crack propagation

Dynamic process of crack development shows the notable differences between two strengthening methods, i.e., bottom strengthening with and without a designated interfacial gap. Due to the limited resolution of the high-speed camera, cracks development in the partial beam was recorded. Fig. 6.7 presents the typical dynamic responses from B15-a and B20-a. For T15B15-a, since the major cracks were developed in the left half span of the beam, the crack propagation was not captured. For RC-a, due to operation error, the dynamic process was not recorded.

As shown in Fig. 6.7 (a), at the beginning of the dynamic process, both flexural and diagonal shear cracks emerged at mid-span in B15-a. It is noted the flexural cracks extended into the UHPC layer. Then, the diagonal shear cracks widened into a shear plug rapidly. At 7 ms, the diagonal crack extended into the interfacial zone, and the UHPC layer started to disintegrate from the bonded interface. Despite early cracking, the UHPC layer provided additional shear resistance that altered the failure from shattering into the shear plug. In addition, the existence of the UHPC layer effectively controlled the breakup and launching of debris under impact loading.

As compared to B15-a, a similar vertical crack emerged at the beginning of the dynamic process in B20-a. Owing to the 5 mm spacing, the effective moment capacity was enhanced; thus, the less evident flexural crack was observed, as shown in Fig. 6.7 (b). Also, due to the non-bonded interface, the flexural crack did not extend in the

UHPC layer, leading to a fully developed resistance from the UHPC strip. Before the breakage of the UHPC layer (9 ms), due to its tensile resistance and fibre bridging effect, the UHPC layer effectively mitigated shear crack, and delayed the formation of localized shear plug as compared to B15-a and RC-a. As the dynamic process continued, shear cracks kept extending but the crack development was not as evident as that of B15-a; the beam demonstrated an overall flexural deformation.

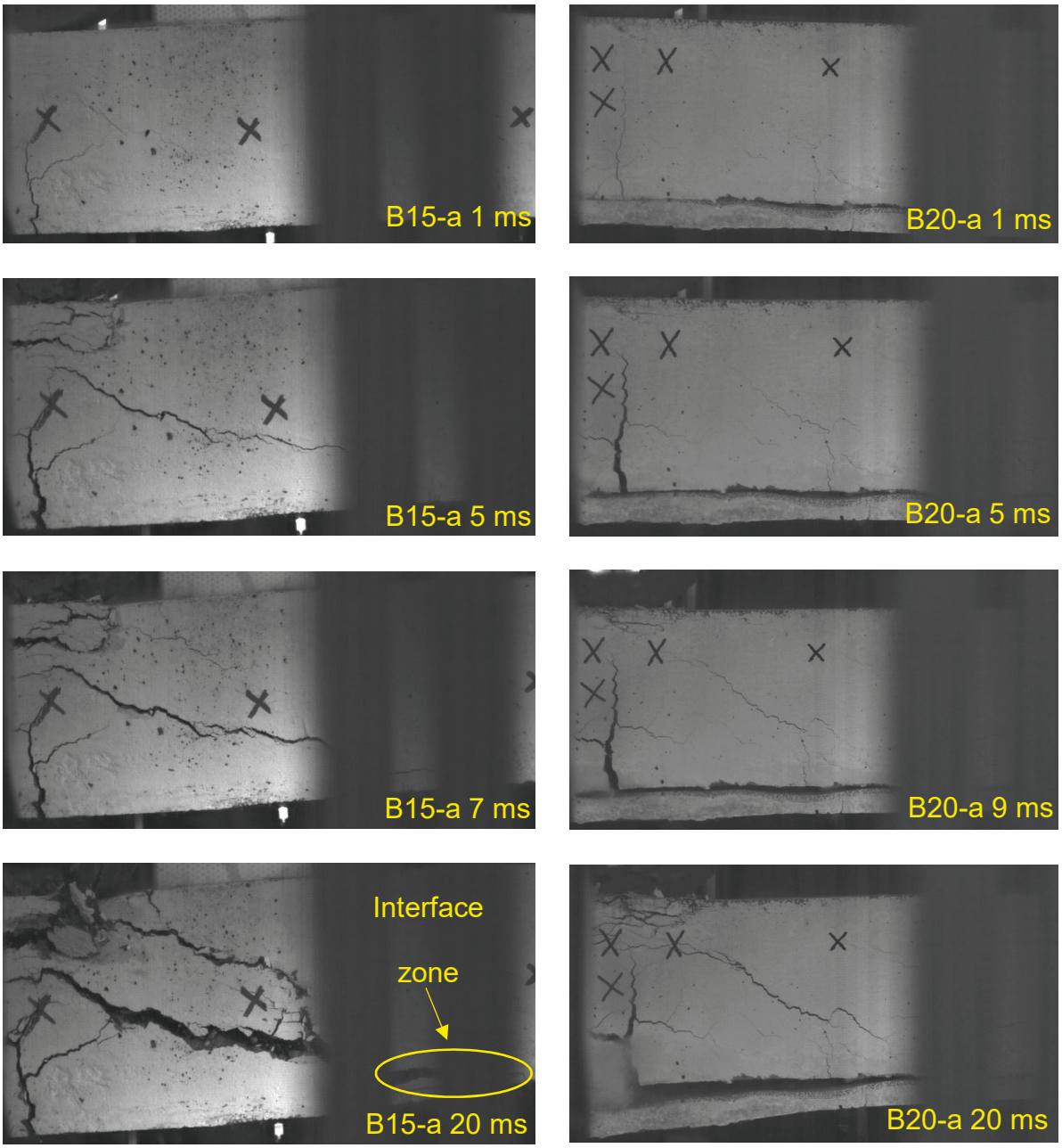

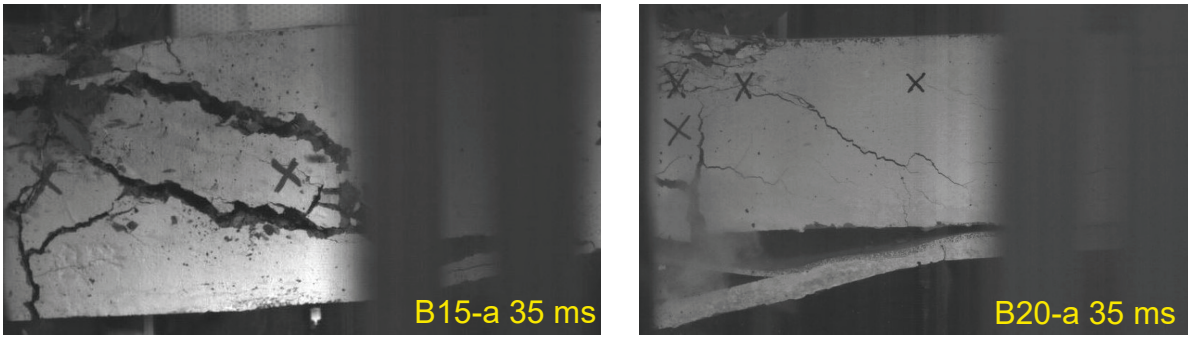

(a) B15-a (b) B20-a

Fig. 6.7. Dynamic failure process of a-series specimens

Many engineering structures such as bridge piers and railway sleepers might suffer repeated impact loads during their service life. The accumulated damage could lead to structural failure. To explore the structural performance under this loading, tests were performed in the present study, and the results were compared to the single impact scenario with identical input energy. Prior to the repeated impact tests, the specimens RC-b and B20-b were first tested with an impact from a height of 0.05 m (1 m/s) to investigate the elastic behaviour of the specimens and test the measurement system. As the maximum residual mid-span displacement was less than 2 mm and no cracks were observed in the specimens, the effect of this impact was neglected in the following discussion.

Fig. 6.8 exhibits the dynamic process of RC and B20 beams under repeated impact loads. Fig. 6.8 (a)-(b) displays crack propagation in specimens in the first impact test with an impact from a height of 0.5 m (2.21 m/s). For RC-b, mid-span flexural cracks and diagonal shear cracks formed rapidly in a short time. Then, the shear cracks kept widening, forming a shear plug and developed into the primary cracks. For B20-b, prior to the breakage of the UHPC layer (13 ms), the strengthening layer effectively restrained the crack development and delayed the forming of the

shear plug. Fig. 6.8 (c)-(d) shows crack propagations in the second impact test with an impact velocity of 2.21 m/s. Since the impact energy exceeded the remaining impact capacity, the RC-b beam experienced extensive damage. The shear cracks split the beam into several parts, causing concrete spalling at mid-span and a complete loss of impact resistance. For B20-b, the shear crack rapidly formed the shear plug and developed into predominant cracks. Due to the breakage in the first impact, the UHPC layer can no longer provide additional resistance to the impact.

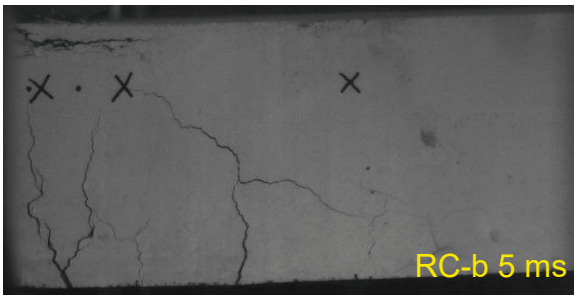

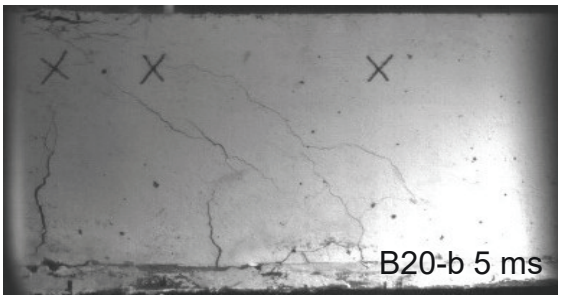

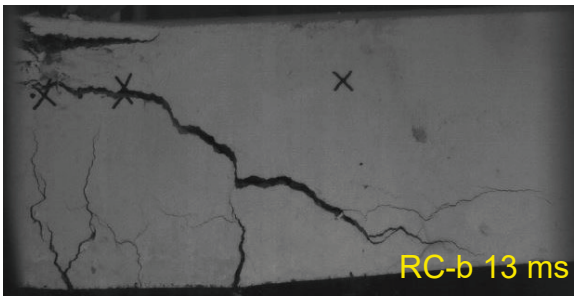

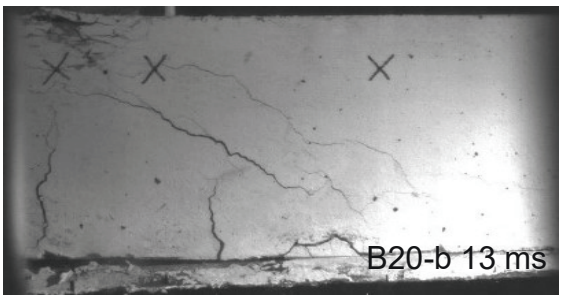

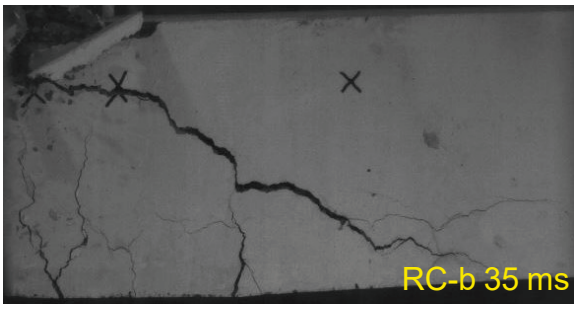

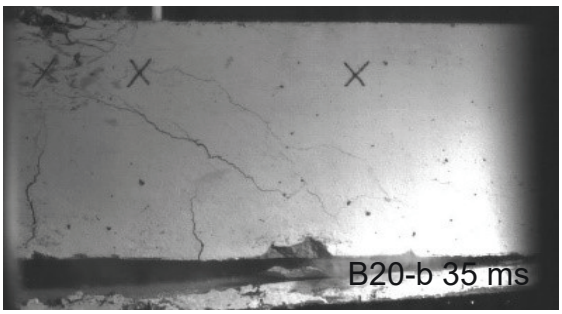

(a) RC-b (first impact)

(b) B20-b (first impact)

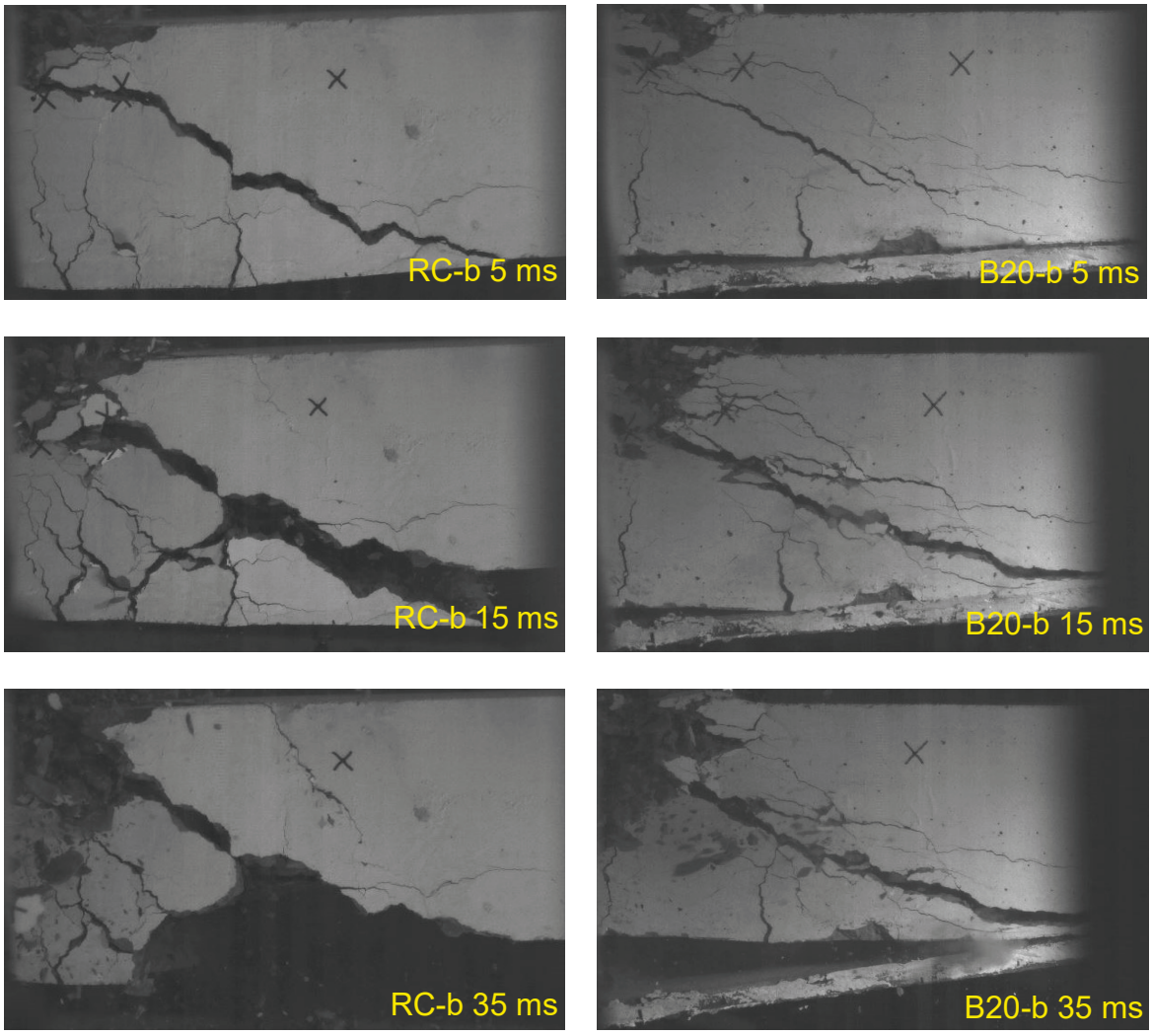

(c) RC-b (second impact) (d) B20-b (second impact)

Fig. 6.8 Dynamic failure process of b-series specimens

Fig. 6.9 shows the time history of the mid-span deflection of RC and B20 subjected to single impact and repeated impacts. Since the deflection history of RC-a was not recorded in the experimental test, the numerical results presented later in this study are adopted for comparison. As compared to the specimens against the single impact, the final residual displacement of specimens subjected to repeated impacts reduced by 9.01% for RC and 27.39% for B20. It was pointed to that, with the same total imparted energy, the single impact was more hazardous than repeated impacts.

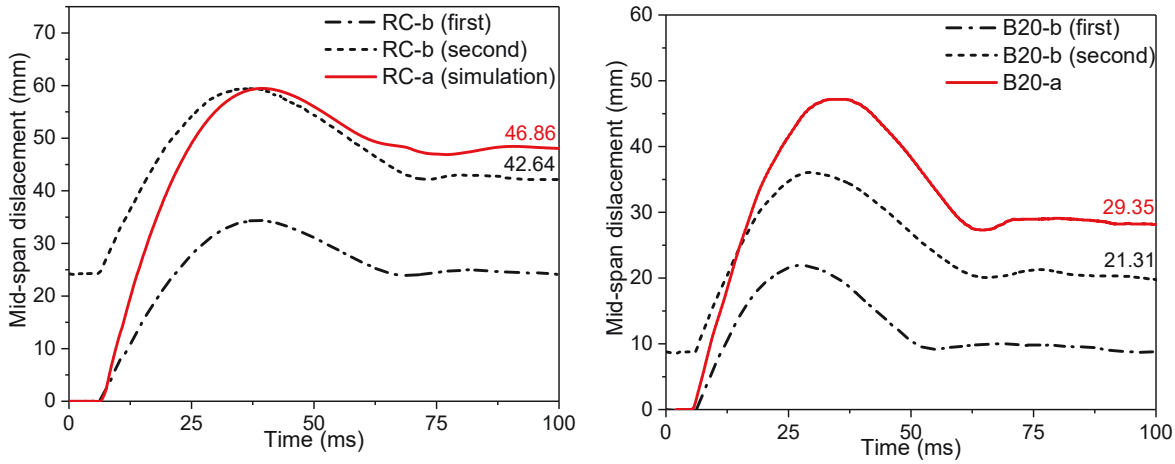

(a) RC (b) B20

Fig. 6.9. Comparison of the displacement time history

Series	Peak impact force (kN)	Peak mid-span *D* (mm)	Residual *D* (mm)	Peak *D* LVDT-1 (mm)	Peak *D* LVDT-2 (mm)
RC-a	212.4	-	-	48.77	32.54
B15-a	208.9	54.03	34.98	42.38	28.86
B20-a	211.3	47.16	29.35	37.33	25.07
T15B15-a	227.4	44.41	30.61	34.58	23.39
RC - b (1st)	137.5	34.41	24.72	26.47	17.11
RC - b (2nd)	108.1	35.19	17.92	28.69	18.62
B20- b (1st)	160.75	21.93	8.77	15.99	10.11
B20- b (2nd)	166.18	27.29	12.53	19.61	11.69

Table 6.5 Lateral impact test results.

The drop hammer impact test data are summarised in Table 6.5. Due to the disintegration of the UHPC layer, the displacement measured from LVDTs and IL-1000 placed underneath the specimen cannot be taken as the deflection of the test beam. Fig. 6.10 shows the comparison of displacement versus time history of RC-b at the location of LVDT 1 measured from LVDT, IL-1000 and PFV in the first impact. Three different sensors were observed to demonstrate consistent displacement versus the time history curves. Thus, the mid-span displacement data of all specimens was used as results from PFV. The impact force and beam deformation versus time curves are to be showed together with FE simulation in the following section.

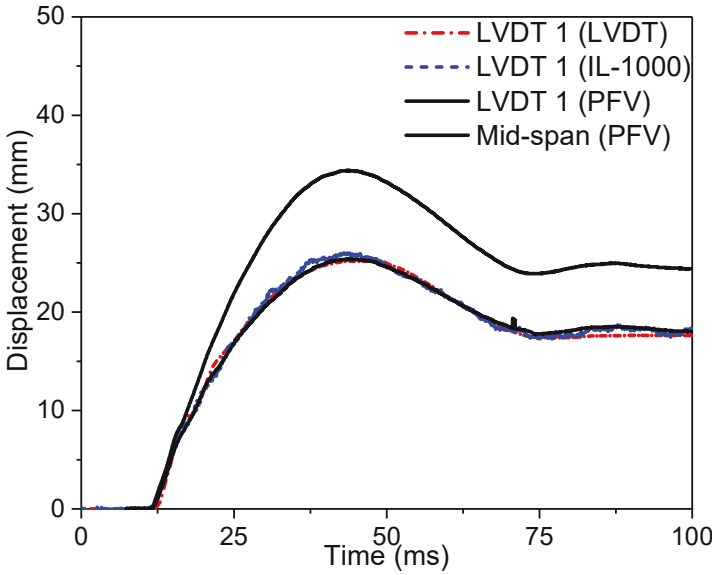

Fig. 6.10. Comparison of the displacement time history of RC-b (first impact)

6.3 Numerical Modelling Tests

6.3.1 Material models

The dynamic response of concrete against impact loading is a rate-dependent, nonlinear and complex process. A number of constitutive models were proposed for

the dynamic behaviour of concrete. Several constitutive models were developed and implemented in LS-DYNA for special purposes, including strain rate effect, damage, etc. Among them, MAT JOHNSON HOLMQUIST CONCRETE (MAT_111, HJC model) was widely adopted to simulate concrete under high pressure, high strains and high strain rate. Wu et al. [185] applied a cohesive element model in HJC concrete model element interfaces to simulate the scattering pattern of RC slabs under internal blast loading. Rong et al. [70] validated strength parameters of the HJC model to simulate Split Hopkinson Pressure Bar tests (SHPB) on cylindrical specimens. MAT CONCRETE DAMAGE REL3 (MAT_73R3, K&C model) was widely used to model reinforced concrete structures under impulsive loading [170, 186]. Xu et al. [187] calibrated the K&C model to simulate reinforced UHPC structures under impact loading by fitting triaxial compression properties with experimental data, deriving the equation of state (EOS) through hydro-static compression test and gaining damage parameters through repeated trial tests. Mao et al. [120] modified strength parameters in the K&C model to simulate the UHPC panels subjected to blast loading, where tension softening behaviour was fitted with the designed strain-stress behaviour of UHPC.

In the aforementioned material models (HJC and K&C), the volumetric increment is independent of the inner incremental flow rule, and EOS is required to calculate plastic volume strain. These material models could not simulate the shear dilatancy with good accuracy. Some other materiel models incorporated volumetric increment into flow rule, and attempted to couple volumetric and shear behaviour. A representative of those models is the MAT CONTINUOUS SURFACE CAP (MAT_159, CSCM model), which has been widely adopted to simulate concrete structures subjected to vehicle collision. Parameter automatic generation capability is

provided in the CSCM_CONCRETE model with an input of only three parameters. As suggested by developers [113, 116], the CSCM_CONCRETE model could be used to simulate the NSC with the strength ranging from 28 to 58 MPa. In this study, CSCM_CONCRETE was applied for NSC. Compared to NSC, limited investigations were performed on the development of UHPC material models. Wei et al. [156, 166] developed a constitutive model to simulate UHPC materials against low-velocity impact loading on the basis of the constitutive theory of the CSCM model. In this study, the UHPC material was modelled by the modified CSCM model (Table 6.6).

Parameter	Magnitude	Parameter	Magnitude	Parameter	Magnitude	Parameter	Magnitude
RO	2500	NPLOT	1	INCRE	0	IRATE	1
ERODE	0	RECOV	0	ITRETRC	0	PRED	0
G (Pa)	1.8E10	K (Pa)	2.5E10	N_H	0	C_H	0
α (Pa)	4.59E7	θ (Pa^{-1})	0.2873	λ (Pa)	3.65E7	β (Pa^{-1})	1.26E-8
α_1 (Pa)	1	θ_1 (Pa^{-1})	0	λ_1 (Pa)	0.4226	β_1 (Pa^{-1})	1.27E-9
α_2 (Pa)	1	θ_2 (Pa^{-1})	0	λ_2 (Pa)	0.5	β_1 (Pa^{-1})	1.27E-9
R	6	X_D (Pa)	6E8	W	0.05		
D_1 (Pa^{-1})	6E-10	D_2 (Pa^{-2})	0				
B	1E2	GFC	1.5E4	D	1E-4	GFT	2E3
GFS	2E3	$pwrc$	5	$pwrt$	1	$pmod$	0
η_{oc}	1.83E-4	N_c	0.504	η_{ot}	1.76E-5	N_t	0.56
$overc$	1.05E8	$overt$ (Pa)	7.76E6	$Srate$	1	$repow$	1

Table 6.6 Material parameters for UHPC overlay.

MAT ELASTIC (MAT_1) was applied to simulate the clamping devices, steel frame and indenter for improving computational efficiency. The nonlinear material model MAT_24 that considered a bilinear strain versus stress curve was adopted to

simulate both the longitudinal and stirrup tendons. Table 6.7 presents parameters defined in material models other than UHPC. In numerical modelling, the strain rate effect is quantified by the dynamic increase factor (DIF), and the DIF of steel reinforcement is defined in Eq. (3.18) as following [123]:

Component	Material model	Parameter	Magnitude
Clamping devices;	MAT_1	Density	7800 (kg/m^3)
Indenter;		Elastic modulus	2E11 (Pa)
Drop weight frame;		Poisson's ratio	0.15
Steel plate			
Longitudinal bars;	MAT_24	Density	7800 (kg/m^3)
stirrup		Elastic modulus	2E11 (Pa)
		Poisson's ratio	0.3
		Yield stress	4E8 (Pa)
		Hardening modulus	2.1E9
		Failure plastic strain	0.15

Table 6.7 Parameters defined in material model.

6.3.2 Numerical simulation drop hammer impact tests

6.3.2.1 Numerical test setup

In the present study, numerical drop hammer impact tests were developed using commercial software LS-DYNA. The numerical model for the drop weight test is shown in Fig. 6.11 (a). Fig. 6.11 (b) – (d) present the modelling of the B15 beam, B20 beam and T15B15 beam, respectively. Solid elements were adopted to model steel components and concrete. Beam elements with 2×2 Gauss Integration were adopted

to simulate the steel reinforcement. The mesh sensitivity test was conducted to investigate the effect of the element size in the analysis. Three different mesh sizes of beams were tested in the study. It is noted that the deflection was found to converge to test data on reducing the element size. To balance the accuracy and efficiency, an element size of 5 mm was selected for steel reinforcement, indenter and concrete.

The contact between the adjacent components was simulated by the CONTACT AUTO SURFACE TO SURFACE keyword. The interfacial surface between NSC and UHPC was modelled by the CONTACT TIEBREAK SURFACE TO SURFACE. In this keyword, the parameters “NFLS” and “SFLS” represented tensile failure tie stress and shear failure tie stress. The values were used from test results (Table 6.3). To improve computational efficiency, the falling process was simplified using the INITIAL VELOCITY GENERATION keyword [188].

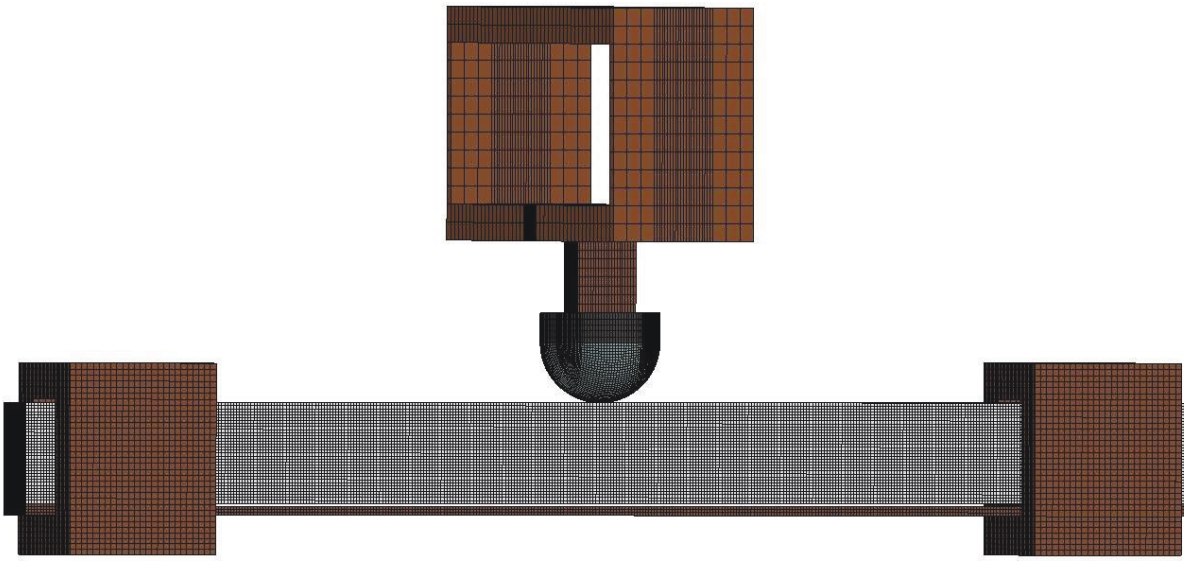

(a) Numerical test setup

(b) B15

(c) B20

(d) T15B15

Fig. 6.11. Finite element model for impact tests

The bind-slip between concrete and bars significantly affect the behaviour of RC structure [101], especially for large deformation under dynamic loading. In the present work, the bond stress-slip behaviour was modelled by the CONTACT 1D: one-dimensional slide line model. In this model, nodes embedded in the rebar beam element was forced to slide along the line of concrete solid element. The model inserted the fictitious springs between slave nodes and corresponding master nodes. These springs provided internal force and allowed the slave nodes to move proportionally along with the master strings. The constitutive stress-slip in the model is represented as follow:

$$\begin{aligned} \tau &= G_s s && \text{for } s \le s_{max} \\ \tau &= \tau_{max} e^{-h_{dmg} D} && \text{for } s > s_{max} \end{aligned} \tag{6.3}$$

where, τ is bond strength; G_s is bond shear modulus; s_{max} is maximum elastic slip; $\tau_{max} = G_s \times s_{max}$; h_{dmg} is damage curve exponential coefficient; D is the plastic displacement, $D = s - s_{max}$. The bond-slip relationship between steel bars and NSC has been evaluated through pull out tests since the 1960s. Shi et al. [189] developed a CONTACT 1D model based on the experimental data to simulate the bod-slip behaviour in the RC column subjected lateral blast test. It was noted that the

developed bond-slip model provided a good prediction of the column response. These recommended parameters were adopted in the present study and listed in Table 6.8. The comparison of the simulation and measured deflection time histories at the location of LVDT 1 for RC-a is shown in Fig. 6.12. From the figure, it was observed that numerical simulation with bond-slip model achieved a better deflection predilection, while simulation with prefect bond showed small plastic deflection.

Bond slip behaviour in RC structures is a complex topic. Real bond-slip between concrete and adjacent steel rebar varies at a local level. Accurate modelling of such behaviour requires micro bond-local slip models. However, such models need numerous computational resources and are difficult to be implemented in the general-purpose finite-element program. Macro models assume constant bond stress over the entire development length of rebar; an example implementation of such model includes the one-dimensional slide line model in LS-DYNA. The slave nodes of a string of rebar beam elements are forced to slide along a master line of nodes attached to concrete elements. Although such model is relatively easy to be implemented, the parameters that define the slide line model require careful validation. In fact, perfect bonding between the steel and the concrete matrix is commonly assumed in the structural dynamic analysis against blast and impact load.

In the present study, the research focus is the effect of strengthening on the impact resistance of RC components. The numerical analysis assumes the perfect bonding between the rebar and concrete for all cases, and the conclusion drawn regarding the strengthening effect will not be affected by the simplified bond-slip assumption.

Parameter	ERR (m)	SIGC (Pa)	GB (Pa/m)	SMAX (m)	EXP
Magnitude	0.012	4E7	3.42E10	6.9E-4	0.18

Table 6.8 Parameters defined in CONTACT 1D.

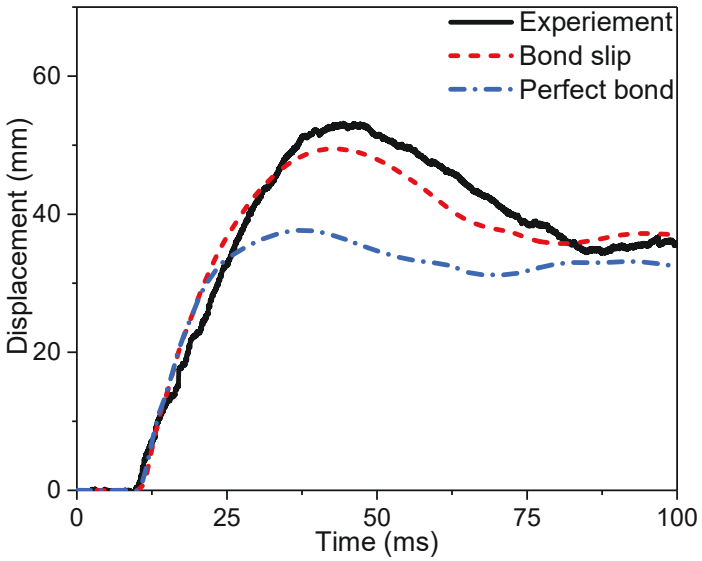

Fig. 6.12. Comparison of the deflection of RC-a at LVDT-1

6.3.2.2 Numerical validation

Impact force and displacement time history for a-series specimens are presented in Fig. 6.13. The impact force history was gained by summing the contact force at the interface between the beam specimen and indenter. The numerical simulation reasonably captured the first peak impact force, demonstrating that the initial contact stiffness between hammer and concrete was appropriately modelled.

The displacement history was estimated from the nodal deflection with the same locations as the measuring points. Other than RC-1, the validation was performed on mid-span deflection. For RC-a, due to the missing of the test data at mid-span, the

numerical validation was conducted based on the displacement history at LVDT-1, and the mid-span displacement history collected from the numerical simulation was also exhibited. The numerical model captured the overall deformation of test specimens with reasonable accuracy.

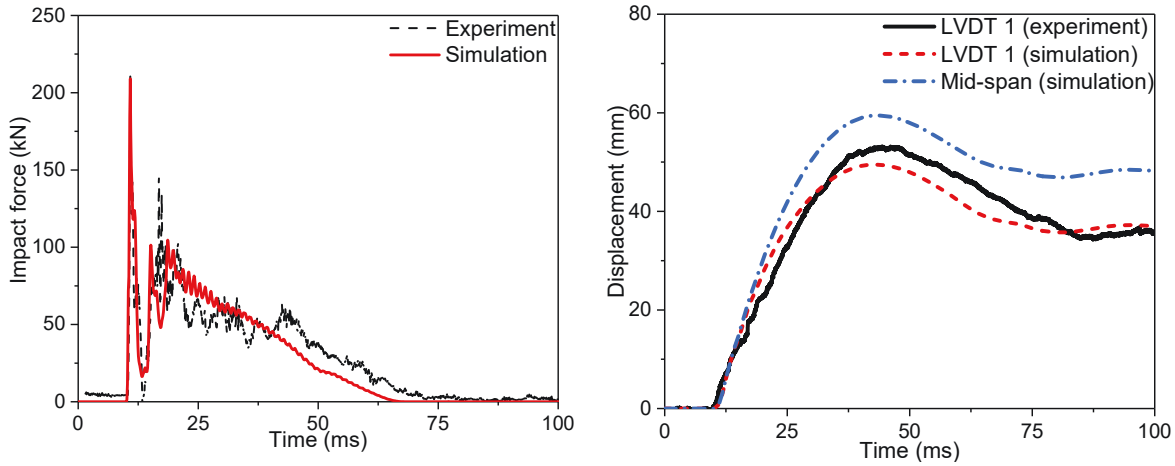

(a) RC-a

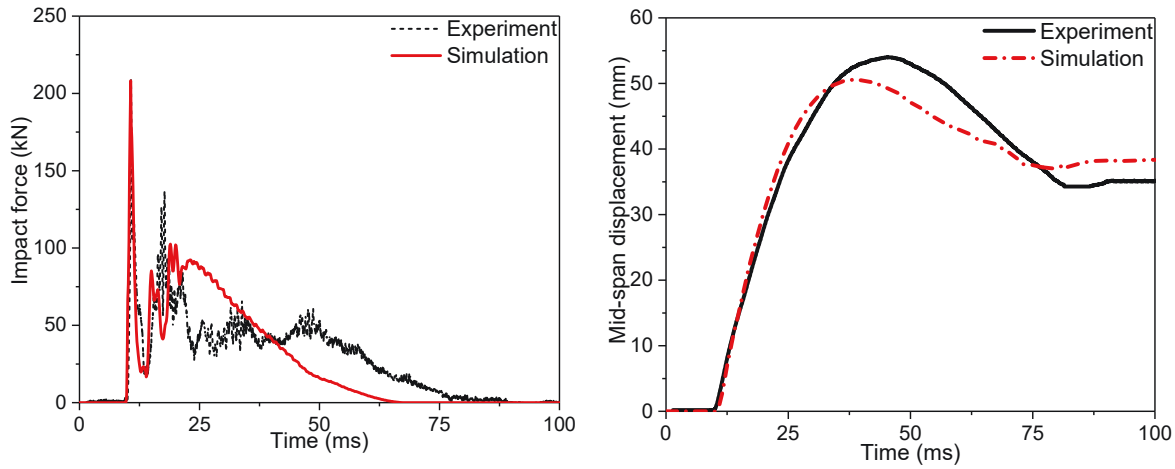

(b) B15-a

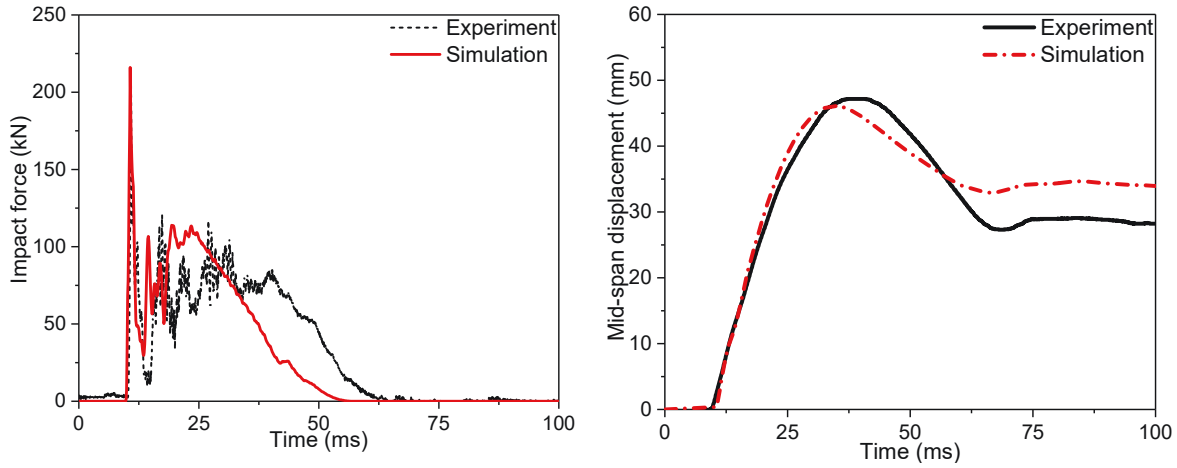

(c) B20-a

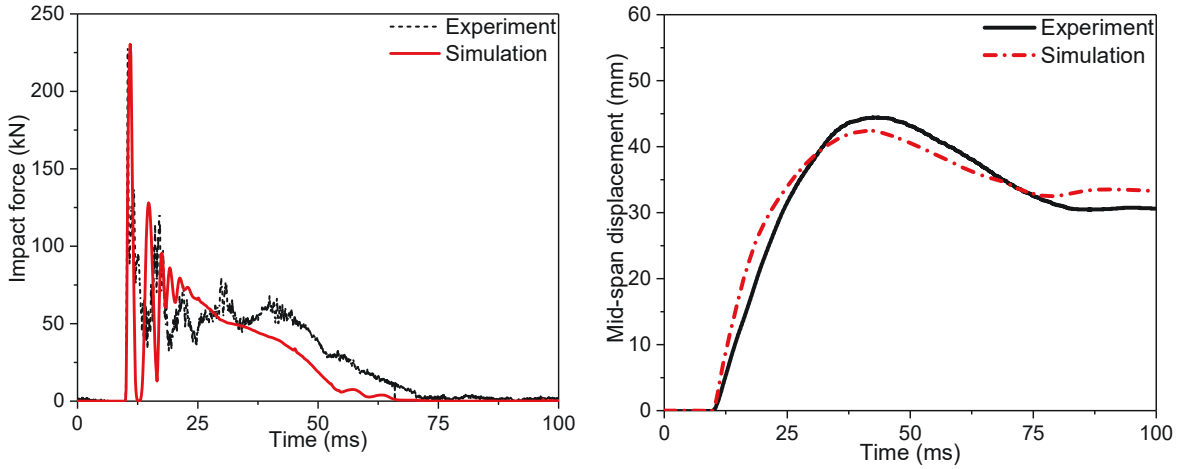

(d) T15B15-a

Fig. 6.13. Experimental and numerical results for a-series beams

Impact force and deflection comparison between experiential and numerical results is listed in Table 6.9. The numerical model well reproduced the dynamic behaviour of test beams with a maximum error of less than 20%. Based on the numerical mid-span deflection data of RC-a, the maximum deflection and residual deflection was decreased by 9.1% and 25.3% in B15-a, decreased by 20.7% and 37.4% in B20-a, and decreased by 25.3% and 34.7% in T15B15-a. Three strengthening methods could enhance resisting performance of RC beams. B20 was

regarded as a better design with consideration of both impact resistance and economic benefit.

Table 6.9 Summary of drop hammer impact test.

No.	Test peak force (kN)	FE peak force (kN)	Error (%)	Test max mid-span (mm)	FE max mid-span (mm)	Error (%)	Test residual mid-span (mm)	FE residual mid-span (mm)	Error (%)
RC-a	212.4	209.1	1.6	-	59.45	-	-	46.86	-
B15-a	208.9	206.2	1.3	54.03	50.56	6.4	34.98	37.81	-8.1
B20-a	211.3	216.1	-0.2	47.16	46.08	2.3	29.35	33.69	-14.8
T15B15-a	227.4	238.4	-4.8	44.41	42.41	4.5	30.61	32.96	-7.6

Fig. 6.14 shows the damage patterns comparison between test and modelling results. The fringe levels varied from 0.3 (minor damage) to 1 (complete damage). The developed numerical model captured the beam damage with reasonable accuracy.

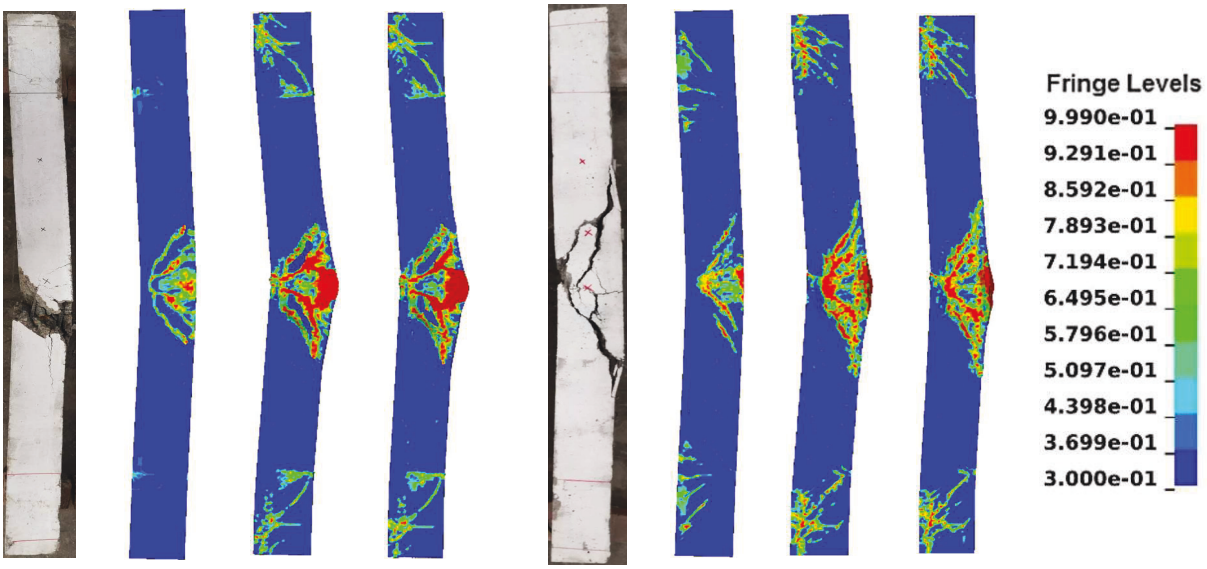

16 ms 43 ms 100 ms 16 ms 38 ms 100 ms

(a) RC-a (b) B15-a

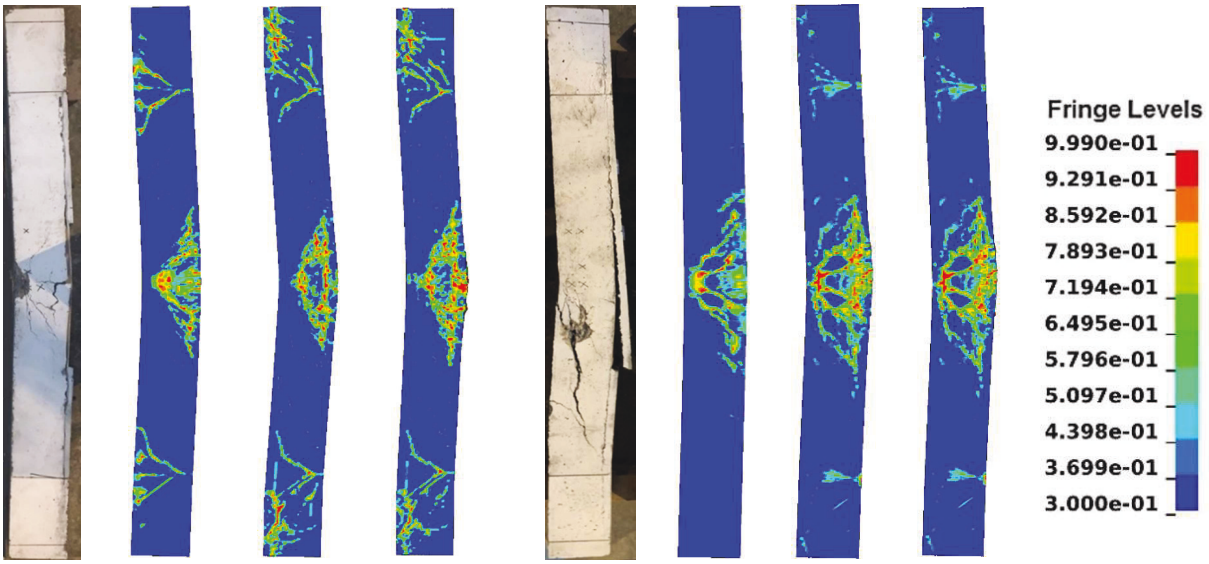

16 ms 33 ms 100 ms 16 ms 42 ms 100 ms

(c) B20-a (d) T15B15-a

Fig. 6.14. Damage patterns comparison

6.3.2.3 Shear force and moment distribution along beam

The time-varying shear force and bending moment distribution along the beam could be obtained from numerical simulation. Fig. 6.15 shows the shear force and bending moment distribution along the beam length of RC-a and B20-a. The impact force was resisted by boundary reaction force and mass inertia. The inertia force was time dependent, and its distribution along the beam was commonly assumed to be linear under impact [168, 169], causing a time-varying shear force distribution. At the beginning of the dynamic process, stress waves generated at the mid-span propagated towards the beam ends. Before the stress waves triggered the boundary reaction, the impact force was mainly resisted by inertia force provided by the partially accelerated beam, resulting in larger amplitudes of shear force concentrated near the mid-span and thus, diagonal shear cracks were generated. This process sustained an extremely short time. As shown in Fig. 6.15 (a) and (c), the shear force at the mid-span increased rapidly at first, and the shear force reached the peak value at 0.5 ms.

At the subsequent impact process, the shear force near the loading points gradually decreased, and its distribution gradually turned into a uniform state. It could be concluded that diagonal shear cracks occurred at the initial stage of the dynamic process. AS 3600 [190] provided the empirical formula to calculate the designed shear capacity for RC members. The shear resistance was contributed to the concrete (V_{uc}) and stirrup (V_{us}). The shear resistance (V_u) is represented as follow:

$$V_u = V_{uc} + V_{us}$$

$$V_c = \beta_1 \cdot \beta_2 \cdot \beta_3 \cdot b_w \cdot d \cdot f_{cv} \cdot \sqrt[3]{\frac{A_{st}}{b_w d}} \tag{6.4}$$

$$V_s = \frac{A_{sv} \cdot f_{sy.f} \cdot d}{s}$$

where, $\beta_1 = 1.1(1.6 - d)$ (d: m) (when β_1 < 1.1, β_1 is taken as 1.1); $\beta_2 = 1$ for beams; $\beta_3 = 1$ in general; b_w presents the beam width; d presents effective depth; $f_{cv} = \sqrt[3]{f_c'}$; f_c' presents compressive strength; A_{st} presents cross-section area of tension reinforcement; A_{sv} presents cross-section area of shear reinforcement; $f_{sy.f}$ presents yield strength of stirrup; s presents spacing of stirrup. In the study, the designed shear capacity for RC beams was 63.61 kN. It was worth noting that, for RC-a, the shear force reached the designed shear capacity at 0.32 ms and kept increasing to 102.1 kN at 0.5 ms. Then, the shear force gradually decreased and dropped below the shear capacity after 3.5 ms at mid-span. During this process, the shear cracks developed rapidly, and damage of concrete occurred to absorb partial imported energy. For B20-a, the shear force reached the capacity at 0.38 ms, then rose to 91.3 kN at 0.5 ms, and reduced beneath the capacity after 0.95 ms. As compared to RC-a, the quick mitigation of the shear force delayed the development of shear cracks.

Fig. 6.15 (b) and (d) exhibit the bending moment distribution diagram. At the beginning of the dynamic process, the bending moment concentrated at the mid-span. With the stress wave propagation, plastic bending hinges moved towards the beam ends. Due to the negative moment induced by the combined effect of impact force and inertia force, the vertical cracks emerged near the boundary, then propagated downward from the compressive side.

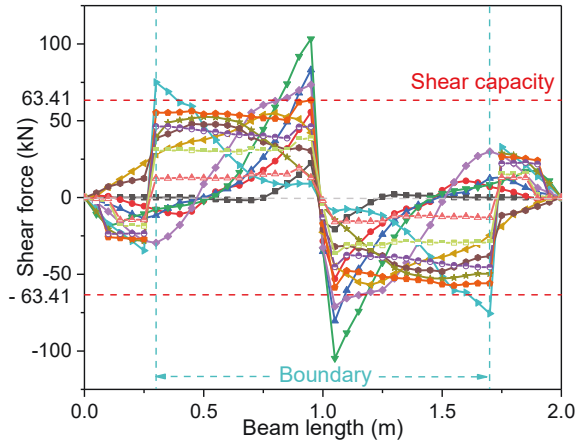

(a) Shear force distribution (RC-a)

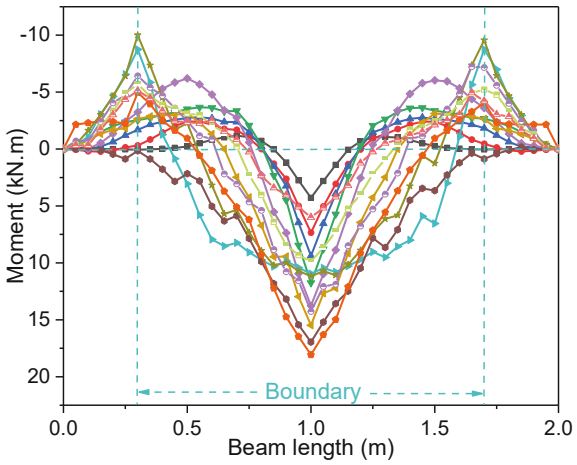

(b) Bending moment distribution (RC-a)

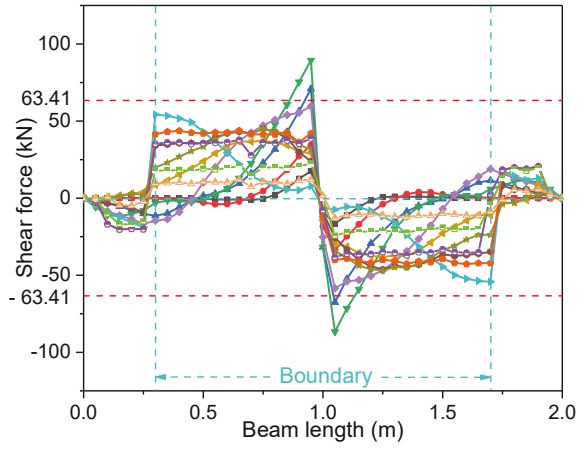

(c) Shear force distribution (B20-a)

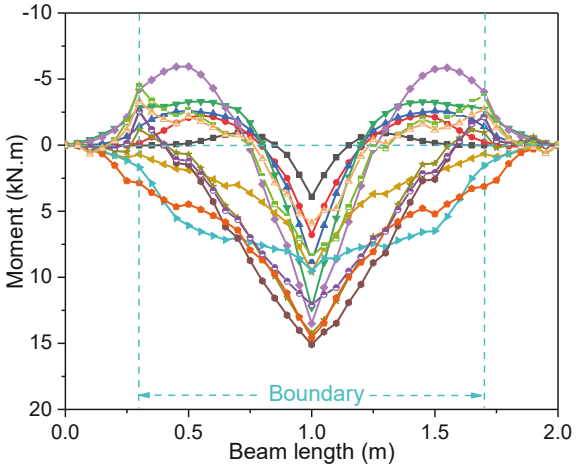

(d) Bending moment distribution (B20-a)

Fig. 6.15 Shear force and bending moment distribution

Fig. 6.16 presents the comparison of distribution diagrams of four specimens. In the diagram, the maximum absolute value of shear force and bending moment on any section during the whole impact process was adopted. For instance, the bending moment of B20-a at 0.5 m ranged from -6.25 kN × m to 5.74 kN × m during the impact process. Thus, the larger absolute value of -6.25 kN × m was used as the maximum bending moment at 0.5 m in the diagram of B20-a. As compared to RC-a, RC-UHPC beams showed an overall lower shear force and bending moment, indicating the UHPC layers could improve the performance of RC beams subjected to impact loading.

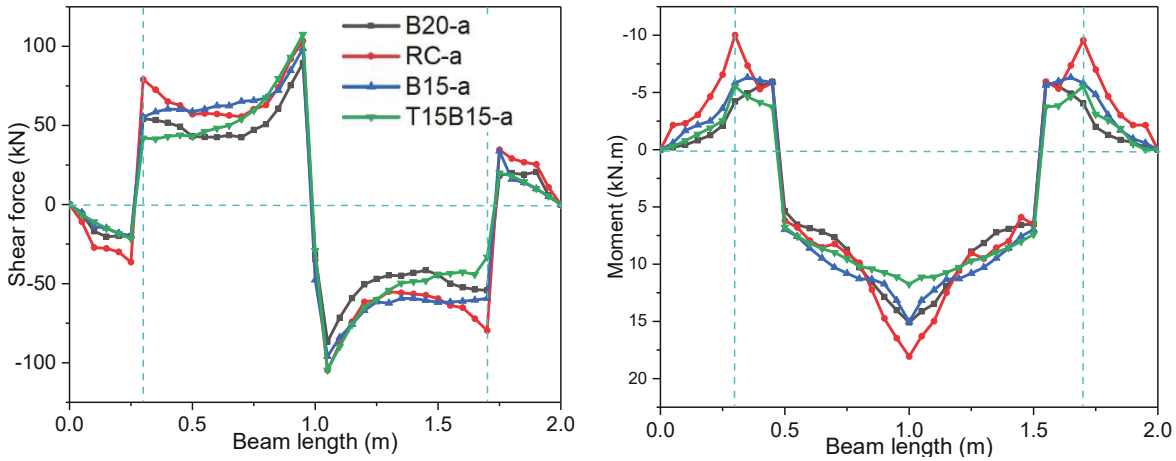

(a) Shear force distribution (b) Bending moment distribution

Fig. 6.16 Shear force and bending moment distribution for all specimens

6.3.2.4 Energy evolution

Fig. 6.17 (a) exhibits the energy absorption time history curve of B20-a. The kinetic energy started from 3.14 kJ, and 59.2% of input energy was converted into the internal energy of the RC beam through plastic fracture of reinforcement and NSC. The kinetic energy of drop hammer that bounced back was 0.23 kJ at the end of the impact test. The UHPC layer absorbed 14.9% of input energy. The energy absorbed

by the UHPC layer occurred at the early stage and was more than that of the internal energy of the RC beam at the same time. As mentioned above, diagonal shear cracks occurred at the initial stage, the introduction of energy-absorption UHPC layer would result in different crack patterns at the subsequent impact process. The UHPC layer effectively strengthened the partially accelerated beam before stress waves triggered the boundary reaction force, restrained the development of Type i shear cracks, and improved the impact resistance. Fig. 6.17 (b) presents the comparison of energy absorption of four test specimens at the end of the impact process. Compared with RC-a, the energy absorbed by RC beams of B15-a, B20-a, and T15B15-a were reduced by 14.6%, 17.7% and 19.9%, respectively. With consideration of both economic benefit and impact performance improvement, B20 was regarded as a better design for strengthening RC beams against impact loading. The influence of the spacing between interfaces was presented in the subsequent parametric study.

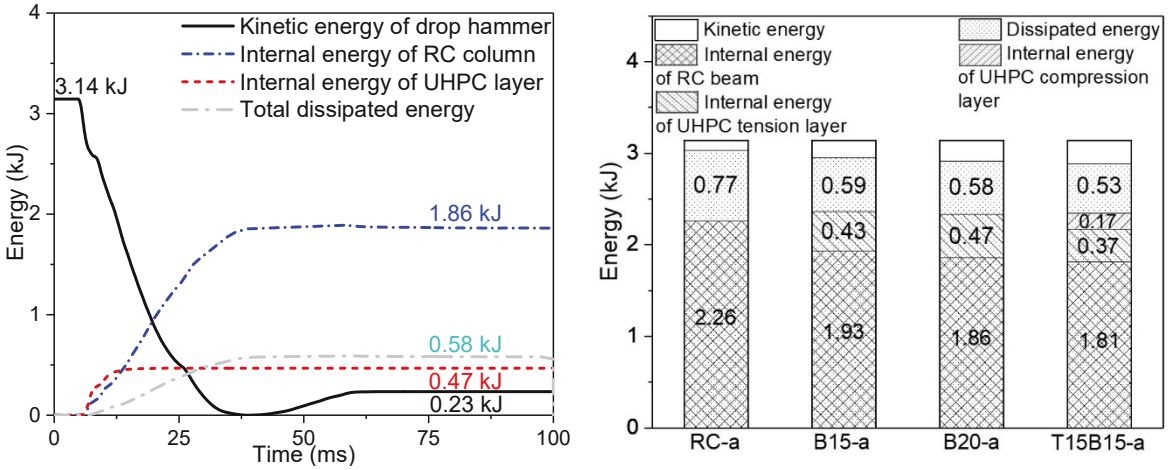

(a) Energy evolution of B20-a (b) Energy evolution of four specimens

Fig. 6.17. Energy evolution of a-series test specimens

6.4 Parametric Study

6.4.1 Numerical simulation matrix

To quantitatively investigate the influence of key design parameters on the impact resistance of RC-UHPC beams with non-bonded interfaces, a parametric study was carried out by using numerical models. Key parameters varied in the numerical models consisted of the length of non-bonded strengthening zone at mid-span = 350 mm, 700 mm, 1050 mm (Fig. 6.18 (a)); the depth of non-attached strengthening zone = 10 mm, 15 mm, 20 mm (Fig. 6.18 (b)); the UHPC layer thickness = 25 mm, 35 mm, 45 mm (Fig. 6.18 (c)). The beam characteristic varied in the parametric study is summarized in Table 6.10. “D” represents the total thickness of the UHPC layer, including the UHPC layer and spacing. The number afterwards represents thickness in mm. “L” and “S” represent the length and thickness of spacing at mid-span.

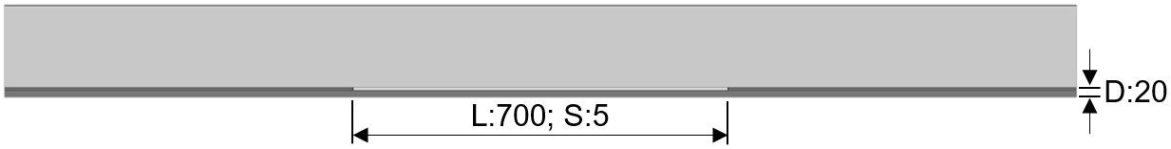

(a) D20L700

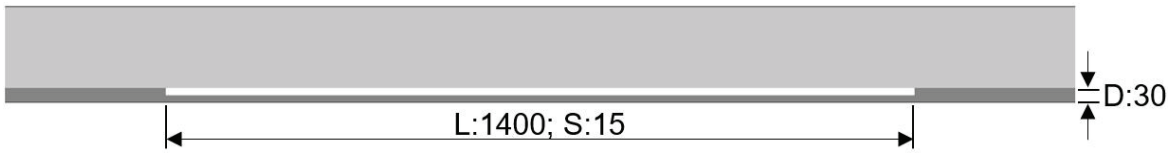

(b) D30S15

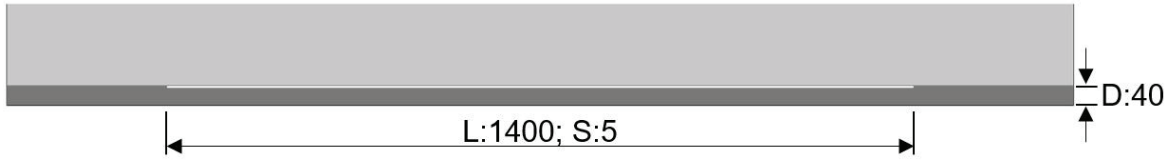

(c) D40S5

Fig. 6.18. Schematic of beam configurations (unit: mm)

Beam type	Variables		
	Strengthening length (mm)	Spacing thickness (mm)	UHPC thickness (mm)
D20L350	350	5	15
D20L700	700	5	15
D20L1050	1050	5	15
D25S10	1400	10	15
D30S15	1400	15	15
D35S20	1400	20	15
D30S5	1400	5	25
D40S5	1400	5	35
D50S5	1400	5	45

Table 6.10 Beam configurations adopted in FE simulation matrix.

6.4.2 Effect of key parameters

6.4.2.1 Effect of spacing length

RC-UHPC beams with different spacing length at mid-span, ranging from 350 mm to 1400 mm, and the RC beam were investigated. Fig. 6.19 shows the comparison of maximum and residual displacement of RC-UHPC beams. By comparison, an increment in the spacing length generally increased the absorbed internal energy of RC beams and the overall deflections. However, the difference among RC-UHPC beams with different spacing lengths was not obvious. The purposes of the spacing between interfaces were to avoid the tensile cracks extending from the RC beam to the UHPC layer and keep the intactness of the UHPC layer at the beginning of the

dynamic process. The lower length limit of 350 mm could still ensure the full development of the energy-absorbing cracks in the UHPC strip. Hence the impact performance was not influenced. Considering both economic benefit and easy manufacture, the design of that RC-UHPC beam with spacing along the whole clear span was recommended.

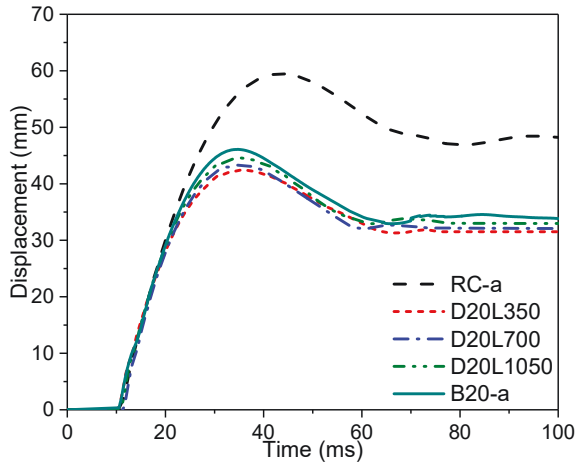

(a) Deflection time histories

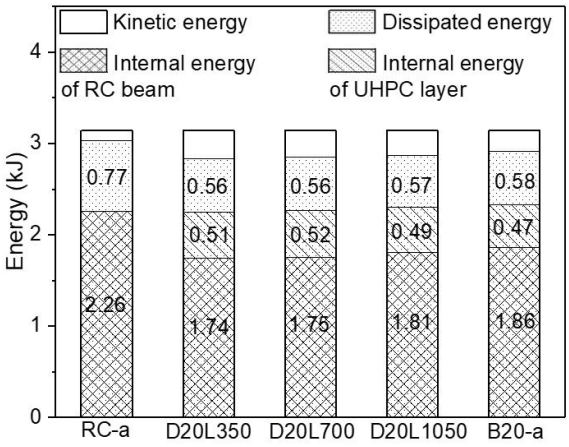

(b) Energy evolution

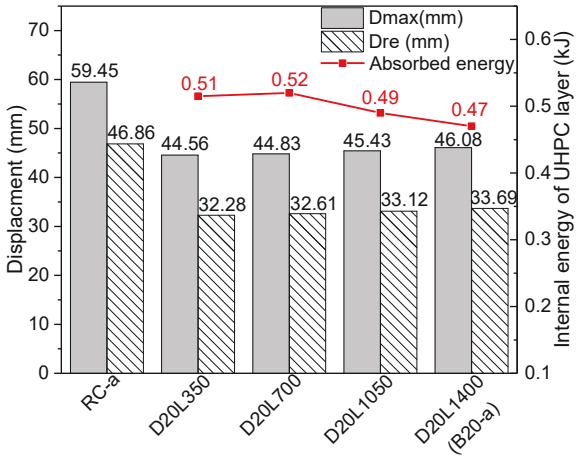

(c) Summary of test results

Fig. 6.19 Effects of spacing length

6.4.2.2 Effect of spacing thickness

The impact resistance for RC beams with a constant 15 mm UHPC layer strengthening but different interfacial spacing, ranging from 5 mm to 20 mm, was examined under impact loading. Fig. 6.20 illustrates the effects of spacing thickness on the RC-UHPC beams. Increasing the interfacial spacing from 5 mm to 20 mm increased overall deflections and the absorbed internal energy of RC beams but decreased the absorbed energy of UHPC layers. UHPC layer could effectively restrain the development of diagonal shear cracks at the beginning of the dynamic process. As the spacing is too large, Type i cracks have developed into the primary predominant cracks and damaged the specimens, and the UHPC layer strengthening in the later stage of the dynamic process was relatively insignificant. Thus, to achieve a better impact resistance, the spacing between the RC beam and UHPC layer was controlled within 10 mm.

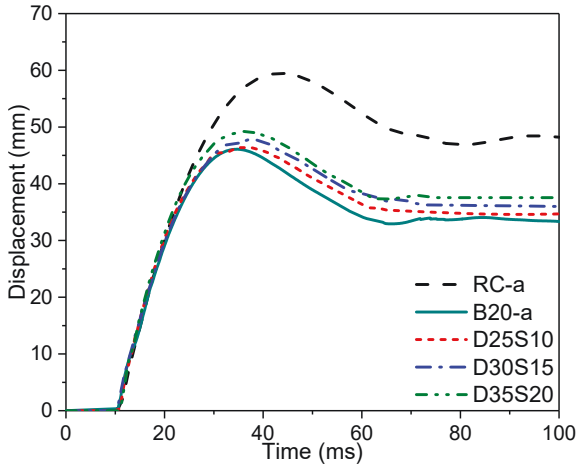

(a) Deflection time histories

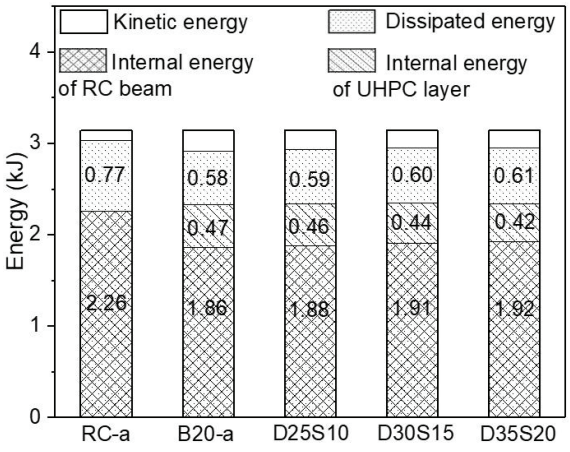

(b) Energy evolution

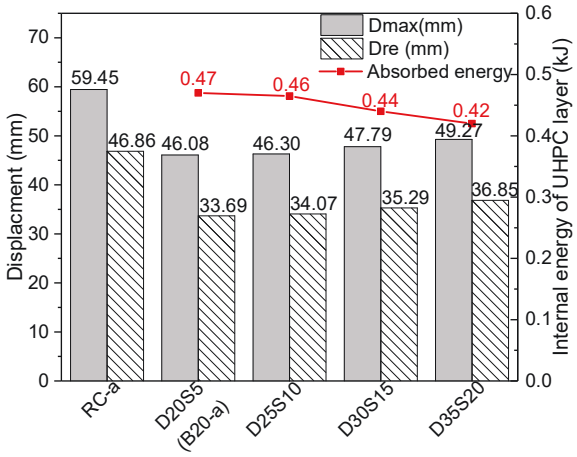

(c) Summary of test results

Fig. 6.20 Effect of spacing thickness

6.4.2.3 Effect of UHPC layer thickness

Four values of the UHPC layer thickness, ranging from 15 mm to 45 mm, were evaluated. Fig. 6.21 presents the effects of layer thickness on the RC-UHPC beams. It is noted that an increase in the UHPC layer thickness significantly reduced overall deflections and the absorbed internal energy of RC beams. More energy was absorbed in the UHPC strengthening layer. The obtained findings indicated that a better impact resistance could be achieved on increasing the UHPC layer thickness, which is expected.

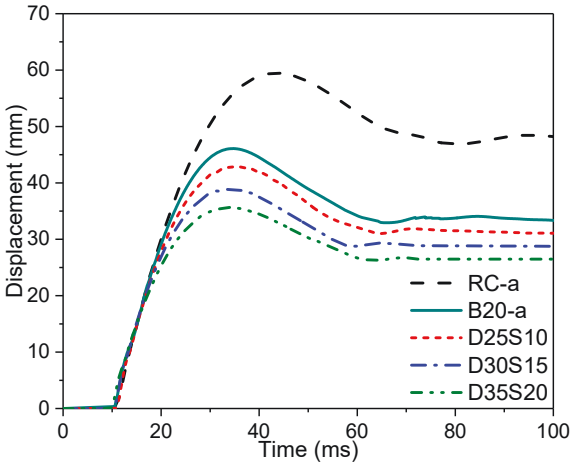

(a) Deflection time histories

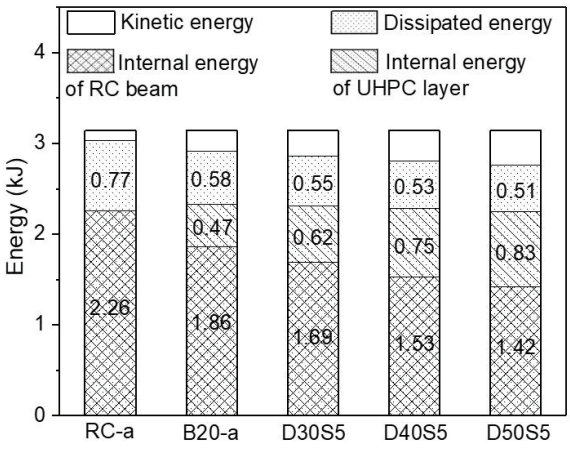

(b) Energy evolution

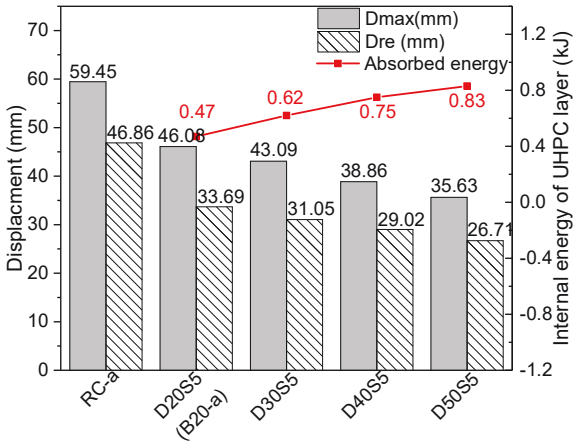

(c) Summary of test results

Fig. 6.21 Effect of UHPC layer thickness

6.5 Summary and Identification of the Gap

Drop hammer impact tests on RC beams and RC beams strengthened by the UHPC layer with three strengthening configurations were performed in the study. Then, high-fidelity FE simulation was developed to further interpret the experimental results. With the findings from experimental and numerical analysis, several conclusions were given:

1. Under the impact loading, evident diagonal shear cracks were developed near the loading point (Type i cracks) in RC beams. This characteristic phenomenon was the main difference between dynamic and quasi-static studies.

2. Different impact energy levels would cause different crack patterns. Under high impact energy, the diagonal shear cracks developed rapidly and formed the shear-plug, causing the shear failure of the specimen. Under relatively low impact energy, Type i cracks were not fully developed. In this situation, Type ii cracks developed into the primary predominant cracks or no more cracks developed.

3. The UHPC layer could absorb a portion of impact energy at the early stage of the impact process, which effectively restrained the development of Type i shear cracks and enhanced impact resistance.

4. Under the impact loading, for the RC-UHPC beam (B15-a), the tensile cracks developed from RC beams would extend in the UHPC layer at the initial stage of the impact process. With designated 5 mm spacing between RC beam and UHPC layer (B20-a), the intactness of the UHPC layer was kept in the beginning stage, and the impact resisting capacity was significantly improved.

5. Increasing spacing length at mid-span exhibited no obvious difference. Further increasing spacing thickness would reduce the impact resistance. Therefore, the design of that RC-UHPC beam with spacing thickness within 10 mm was recommended. A better impact resisting performance could be achieved on enhancing the thickness of the UHPC layer.

Chapter 7

Conclusions and Recommendations for Future Works

7.1 Brief Summary

This thesis brings improvement to the existing understanding of the dynamic behaviour of UHPC and its components against impact loads based on both experimental and numerical studies.

7.2 Conclusion Remarks

In Chapter 3, UHPC columns showed superior crashworthiness. The developed CSCM model could be adopted to simulate UHPC material. The proposed analytical equations can be used to generate the impact mass versus velocity diagram for quick assessment of UHPC column damage after an impact scenario.

In Chapter 4, the fibre hybridization importantly enhanced the static flexural properties of UHPC. The UHPC beams with hybrid fibres exhibited improved impact resistance. The inverse analysis was performed to obtain the adequate tension-softening curves of UHPC. Based on the softening curves, the material fracture energy was calculated.

In Chapter 5, hollow-core and steel wire mesh reinforced UHPC columns demonstrated good impact resistance. For the hollow-core columns, considering both economic benefit and impact resistance, the column with a 15% hollow ratio is considered as a better design. For steel wire mesh reinforced UHPC columns, the reinforcement strengthening the whole section is more effective.

In Chapter 6, The UHPC layer could absorb a portion of impact energy at the early stage of the impact process, which effectively restrained the development of

Type i shear cracks and enhanced impact resistance. With designated 5 mm spacing between RC beam and UHPC layer (B20-a), the intactness of the UHPC layer was kept in the beginning stage, and impact-resisting capacity was significantly improved.

7.3 Recommendations for Future Works

In light of the experience gained in this test program, the following recommendations can be made for future works:

1. The studies on the shear and tensile behaviour under triaxial loading condition is deemed necessary for a more comprehensive understanding of this emerging UHPC material. Fibre reinforcement significantly affected the behaviour of UHPC under triaxial loadings. More experimental triaxial tests were required to investigate its mechanical properties.

2. The bond-slip behaviour between the steel rebar/wire mesh and surrounding UHPC matrix was considered to be the reason for the inaccurate numerical results. As shown in literature, the bond-slip relationship could affect the impact force and deflection period. Further studies need to be performed to develop the bond-slip behaviour in the numerical simulation.

3. The effects of various impact parameters should be evaluated by using various masses and a wide range of velocities. Because the experimental tests are time-consuming and experimental, only a few range of the impact energy was reported. A better understanding of the dynamic behaviour of UHPC components could be achieved by summarizing the test results under various impact energies.

4. The CSCM material model should be developed to simulate the UHPC with hybrid fibres. Limited studies focus on the development of the CSCM model to simulate the UHPC with hybrid fibres in LS-DYNA. Associated parameters could be

modified to fit the experimental curves from compression, four-point and three-point bending tests.

5. UHPC strengthening technology requires further investigation with a consideration of interfacial bonding and performance deterioration of the base RC structure over the service period. The application of UHPC is limited by the raw material cost and lack of guidelines. Adopting UHPC as a strengthening material could greatly promote the impact-resistance performance of RC structures its application in civil constructions.

References

[1] Engineers ASoC. Minimum design loads for buildings and other structures. American Society of Civil Engineers. 1994.

[2] Hao H. Predictions of structural response to dynamic loads of different loading rates. International Journal of Protective Structures. 2015;6:585-605.

[3] Sharma H, Hurlebaus S, Gardoni P. Performance-based response evaluation of reinforced concrete columns subject to vehicle impact. International Journal of Impact Engineering. 2012;43:52-62.

[4] Bache HH. Compact reinforced composite basic principles. 1987.

[5] Cheyrezy M, Maret V, Frouin L. Microstructural analysis of RPC (reactive powder concrete). Cement and Concrete Research. 1995;25:1491-500.

[6] Wu C, Li J, Su Y. Development of ultra-high performance concrete against blasts: from materials to structures: Woodhead Publishing. 2018.

[7] Yoo D-Y, Lee J-H, Yoon Y-S. Effect of fiber content on mechanical and fracture properties of ultra high performance fiber reinforced cementitious composites. Composite Structures. 2013;106:742-53.

[8] Boulekbache B, Hamrat M, Chemrouk M, Amziane S. Flowability of fibre-reinforced concrete and its effect on the mechanical properties of the material. Construction and Building Materials. 2010;24:1664-71.

[9] Yoo D-Y, Zi G, Kang S-T, Yoon Y-S. Biaxial flexural behavior of ultra-high-performance fiber-reinforced concrete with different fiber lengths and placement methods. Cement and Concrete Composites. 2015;63:51-66.

[10] Yoo D-Y, Kang S-T, Yoon Y-S. Effect of fiber length and placement method on flexural behavior, tension-softening curve, and fiber distribution characteristics of UHPFRC. Construction and Building materials. 2014;64:67-81.

[11] Wille K, Kim DJ, Naaman AE. Strain-hardening UHP-FRC with low fiber contents. Materials and Structures. 2011;44:583-98.

[12] Tran NT, Tran TK, Kim DJ. High rate response of ultra-high-performance fiber-reinforced concretes under direct tension. Cement and Concrete Research. 2015;69:72-87.

[13] Su Y, Li J, Wu C, Wu P, Li Z-X. Effects of steel fibres on dynamic strength of UHPC. Construction and Building Materials. 2016;114:708-18.

[14] Skazlić M, Bjegović D. Toughness testing of ultra high performance fibre reinforced concrete. Materials and Structures. 2009;42:1025-38.

[15] Kim DJ, Park SH, Ryu GS, Koh KT. Comparative flexural behavior of hybrid ultra high performance fiber reinforced concrete with different macro fibers. Construction and Building Materials. 2011;25:4144-55.

[16] Yoo D-Y, Kim S-W, Park J-J. Comparative flexural behavior of ultra-high-performance concrete reinforced with hybrid straight steel fibers. Construction and Building Materials. 2017;132:219-29.

[17] Barnett SJ, Millard SG, Schleyer G, Tyas A. Briefing: Blast tests of fibre-reinforced concrete panels. Proceedings of the Institution of Civil Engineers-Construction Materials. 2010;163:127-9.

[18] Aoude H, Dagenais FP, Burrell RP, Saatcioglu M. Behavior of ultra-high performance fiber reinforced concrete columns under blast loading. International Journal of Impact Engineering. 2015;80:185-202.

[19] Yoo D-Y, Banthia N, Kim S-W, Yoon Y-S. Response of ultra-high-performance fiber-reinforced concrete beams with continuous steel reinforcement subjected to low-velocity impact loading. Composite Structures. 2015;126:233-45.

[20] Meng W. Design and performance of cost-effective ultra-high performance concrete for prefabricated elements. 2017.

[21] Lignola GP, Nardone F, Prota A, De Luca A, Nanni A. Analysis of RC hollow columns strengthened with GFRP. Journal of Composites for Construction. 2011;15:545-56.

[22] Hua H, Bo-Quan L, Guo-Hua X, YAN-SHUN L, TIE-QIANG L. Experiment on RC T-type beam bridge strengthened with high strength stainless steel wire mesh and permeabil ity polymer mortar. China Journal of Highway and Transport. 2007;4.

[23] Li J, Wu C, Hao H, Su Y. Experimental and numerical study on steel wire mesh reinforced concrete slab under contact explosion. Materials & Design. 2017;116:77-91.

[24] Meng Q, Wu C, Su Y, Li J, Liu J, Pang J. A study of steel wire mesh reinforced high performance geopolymer concrete slabs under blast loading. Journal of Cleaner Production. 2019;210:1150-63.

[25] Doiron G. Pier repair/retrofit using UHPC—examples of completed projects in north America. International Interactive Symposium on Ultra-High Performance Concrete: Iowa State University Digital Press. 2016.

[26] Brühwiler E. Rehabilitation and strengthening of concrete structures using ultra-high performance fibre reinforced concrete. Proceedings of the 3rd International conference on Concrete Repair, Rehabilitation and Retrofitting (ICCRRR): CRC Press/Balkema. 2012. p. 70-9.

[27] Safdar M, Matsumoto T, Kakuma K. Flexural behavior of reinforced concrete beams repaired with ultra-high performance fiber reinforced concrete (UHPFRC). Composite Structures. 2016;157:448-60.

[28] Noshiravani T, Brühwiler E. Rotation capacity and stress redistribution ability of R-UHPFRC–RC composite continuous beams: an experimental investigation. Materials and Structures. 2013;46.

[29] Ben-Dor G, Dubinsky A, Elperin T. Engineering models of high speed penetration into geological shields. Open Engineering. 2014;4:1-19.

[30] Harik I, Shaaban A, Gesund H, Valli G, Wang S. United States bridge failures, 1951–1988. Journal of Performance of Constructed Facilities. 1990;4:272-7.

[31] Wardhana K, Hadipriono FC. Analysis of recent bridge failures in the United States. Journal of Performance of Constructed Facilities. 2003;17:144-50.

[32] Feldman A, Siess CP. Investigation of resistance and behavior of reinforced concrete members subject to dynamic loading. University of Illinois Engineering Experiment Station. 1956.

[33] Hughes G, Beeby A. Investigation of the effect of impact loading on concrete beams. The Structural Engineer B. 1982;60:45-52.

[34] Kishi N, Nakano O, Matsuoka K, Ando T. Experimental study on ultimate strength of flexural-failure-type RC beams under impact loading. 2001.

[35] Fujikake K, Li B, Soeun S. Impact response of reinforced concrete beam and its analytical evaluation. Journal of Structural Engineering. 2009;135:938-50.

[36] Chen Y, May IM. Reinforced concrete members under drop-weight impacts. Proceedings of the Institution of Civil Engineers-Structures and Buildings. 2009;162:45-56.

[37] Tachibana S, Masuya H, Nakamura S. Performance based design of reinforced concrete beams under impact. Natural Hazards and Earth System Sciences. 2010;10:1069-78.

[38] Kishi N, Mikami H. Empirical Formulas for designing reinforced concrete beams under Impact Loading. ACI Structural Journal. 2012;109.

[39] Ce-idbTG. Ductility of reinforced concrete structures: FIB-International Federation for Structural Concrete; 1998.

[40] Yi W-J, Zhao D-B, Kunnath SK. Simplified approach for assessing shear resistance of reinforced concrete beams under impact loads. ACI Structural Journal. 2016;113.

[41] Zhao D-B, Yi W-J, Kunnath SK. Numerical simulation and shear resistance of reinforced concrete beams under impact. Engineering Structures. 2018;166:387-401.

[42] Kishi N, Mikami H, Matsuoka K, Ando T. Impact behavior of shear-failure-type RC beams without shear rebar. International Journal of Impact Engineering. 2002;27:955-68.

[43] Saatci S, Vecchio FJ. Effects of shear mechanisms on impact behavior of reinforced concrete beams. ACI structural Journal. 2009.

[44] Zhao D-B, Yi W-J, Kunnath SK. Shear mechanisms in reinforced concrete beams under impact loading. Journal of Structural Engineering. 2017;143:04017089.

[45] ASSTO. Bridge design specifications, American Association of State Highway and Transportation Officials. Nevada, USA; 2014.

[46] Wille K, Naaman AE, El-Tawil S, Parra-Montesinos GJ. Ultra-high performance concrete and fiber reinforced concrete: achieving strength and ductility without heat curing. Materials and structures. 2012;45:309-24.

[47] Flatt RJ, Houst YF. A simplified view on chemical effects perturbing the action of superplasticizers. Cement and Concrete Research. 2001;31:1169-76.

[48] Alkaysi M, El-Tawil S, Liu Z, Hansen W. Effects of silica powder and cement type on durability of ultra high performance concrete (UHPC). Cement and Concrete Composites. 2016;66:47-56.

[49] Mazloom M, Ramezanianpour A, Brooks J. Effect of silica fume on mechanical properties of high-strength concrete. Cement and Concrete Composites. 2004;26:347-57.

[50] Duval R, Kadri E. Influence of silica fume on the workability and the compressive strength of high-performance concretes. Cement and Concrete Research. 1998;28:533-47.

[51] Sanchez F, Sobolev K. Nanotechnology in concrete–a review. Construction and Building Materials. 2010;24:2060-71.

[52] Jo B-W, Kim C-H, Tae G-h, Park J-B. Characteristics of cement mortar with nano-SiO2 particles. Construction and Building Materials. 2007;21:1351-5.

[53] Qing Y, Zenan Z, Deyu K, Rongshen C. Influence of nano-SiO2 addition on properties of hardened cement paste as compared with silica fume. Construction and Building Materials. 2007;21:539-45.

[54] Liu X, Chen L, Liu A, Wang X. Effect of nano-CaCO3 on properties of cement paste. Energy Procedia. 2012;16:991-6.

[55] Nazari A, Riahi S. The effects of zinc dioxide nanoparticles on flexural strength of self compacting concrete. Composite Part: B. 2011.

[56] Yang IH, Joh C, Kim B-S. Structural behavior of ultra high performance concrete beams subjected to bending. Engineering Structures. 2010;32:3478-87.

[57] Ferrara L, Ozyurt N, Di Prisco M. High mechanical performance of fibre reinforced cementitious composites: the role of “casting-flow induced” fibre orientation. Materials and Structures. 2011;44:109-28.

[58] Kwon SH, Kang S-T, Lee BY, Kim J-K. The variation of flow-dependent tensile behavior in radial flow dominant placing of Ultra High Performance Fiber Reinforced Cementitious Composites (UHPFRCC). Construction and Building Materials. 2012;33:109-21.

[59] Wille K, Parra-Montesinos GJ. Effect of beam size, casting method, and support conditions on flexural behavior of ultra high-performance fiber-reinforced concret. ACI Materials Journal. 2012;109:379.

[60] Soliman A, Nehdi M. Effect of drying conditions on autogenous shrinkage in ultra-high performance concrete at early-age. Materials and Structures. 2011;44:879-99.

[61] Wille K, Naaman AE, Parra-Montesinos GJ. Ultra-High performance concrete with compressive strength exceeding 150 MPa (22 ksi): a simpler way. ACI Materials Journal. 2011;108.

[62] Wille K, El-Tawil S, Naaman AE. Properties of strain hardening ultra high performance fiber reinforced concrete (UHP-FRC) under direct tensile loading. Cement and Concrete Composites. 2014;48:53-66.

[63] Tanarslan H. Flexural strengthening of RC beams with prefabricated ultra high performance fibre reinforced concrete laminates. Engineering Structures. 2017;151:337-48.

[64] Kang S-T, Lee Y, Park Y-D, Kim J-K. Tensile fracture properties of an Ultra High Performance Fiber Reinforced Concrete (UHPFRC) with steel fiber. Composite Structures. 2010;92:61-71.

[65] Grünewald S. Performance-based design of self-compacting fibre reinforced concrete. 2004.

[66] Yu R, Spiesz P, Brouwers H. Mix design and properties assessment of ultra-high performance fibre reinforced concrete (UHPFRC). Cement and Concrete Research. 2014;56:29-39.

[67] Rossi P. Influence of fibre geometry and matrix maturity on the mechanical performance of ultra high-performance cement-based composites. Cement and Concrete Composites. 2013;37:246-8.

[68] Yoo D-Y, Banthia N, Yoon Y-S. Impact resistance of ultra-high performance fiber-reinforced concrete with different steel fibers. 9th RILEM International Symposium on Fiber Reinforced Concrete–BEFIB2016.

[69] Dawood ET, Ramli M. Mechanical properties of high strength flowing concrete with hybrid fibers. Construction and Building Materials. 2012;28:193-200.

[70] Rong Z, Sun W, Zhang Y. Dynamic compression behavior of ultra-high performance cement based composites. International Journal of Impact Engineering. 2010;37:515-20.

[71] Lai J, Sun W. Dynamic behaviour and visco-elastic damage model of ultra-high performance cementitious composite. Cement and Concrete Research. 2009;39:1044-51.

[72] Fujikake K, Senga T, Ueda N, Ohno T, Katagiri M. Effects of strain rate on tensile behavior of reactive powder concrete. Journal of Advanced Concrete Technology. 2006;4:79-84.

[73] Douglas K, Billington S. Strain rate dependence of HPFRCC cylinders in monotonic tension. Materials and structures. 2011;44:391-404.

[74] Toutlemonde F, Boulay C, Sercombe J, Le Maou F, Renwez S, Adeline R. Characterization of reactive powder concrete (RPC) in direct tension at medium to high loading rates. Proceedings of Concrete under Severe Conditions. 1998;2:887-96.

[75] Wille K, El-Tawil S, Naaman A. Strain rate dependent tensile behavior of ultra-high performance fiber reinforced concrete. High Performance Fiber Reinforced Cement Composites 6: Springer; 2012. p. 381-7.

[76] Tai Y-S, El-Tawil S, Chung T-H. Performance of deformed steel fibers embedded in ultra-high performance concrete subjected to various pullout rates. Cement and Concrete Research. 2016;89:1-13.

[77] Fujikake K, Senga T, Ueda N, Ohno T, Katagiri M. Study on impact response of reactive powder concrete beam and its analytical model. Journal of Advanced Concrete Technology. 2006;4:99-108.

[78] Fan W, Shen D, Yang T, Shao X. Experimental and numerical study on low-velocity lateral impact behaviors of RC, UHPFRC and UHPFRC-strengthened columns. Engineering Structures. 2019;191:509-25.

[79] Xu S, Liu Z, Li J, Yang Y, Wu C. Dynamic behaviors of reinforced NSC and UHPC columns protected by aluminum foam layer against low-velocity impact. Journal of Building Engineering. 2021;34:101910.

[80] Jia P, Wu H, Wang R, Fang Q. Dynamic responses of reinforced ultra-high performance concrete members under low-velocity lateral impact. International Journal of Impact Engineering. 2021;150:103818.

[81] Kusumawardaningsih Y, Hadi MN. Comparative behaviour of hollow columns confined with FRP composites. Composite Structures. 2010;93:198-205.

[82] Pantelides CP, Gibbons ME, Reaveley LD. Axial load behavior of concrete columns confined with GFRP spirals. Journal of Composites for Construction. 2013;17:305-13.

[83] Aiajarmeh O, Manalo A, Benmokrane B, Karunasena W, Mendis P, Nguyen K. Compressive behavior of axially loaded circular hollow concrete columns reinforced with GFRP bars and spirals. Construction and Building Materials. 2019;194:12-23.

[84] Nie J, Wang H, Zhang T, Cai Q, Qin K. Experimental study on flexural behavior of RC beams strengthened with stainless steel wire mesh and permeability polymer mortar. Journal of Building Structures. 2005;2:002.

[85] Brühwiler E, Denarié E, Habel K. Ultra-high performance fibre reinforced concrete for advanced rehabilitation of bridges. Proceedings (eds GL Balasz & A Borosnyoi), fib-Symposium, Budapest2005. p. 951-6.

[86] Brühwiler E, Denarié E. Rehabilitation and strengthening of concrete structures using ultra-high performance fibre reinforced concrete. Structural Engineering International. 2013;23:450-7.

[87] Habel K, Denarié E, Brühwiler E. Experimental investigation of composite ultra-high-performance fiber-reinforced concrete and conventional concrete members. ACI Structural Journal. 2007;104:93.

[88] Yin H, Teo W, Shirai K. Experimental investigation on the behaviour of reinforced concrete slabs strengthened with ultra-high performance concrete. Construction and Building Materials. 2017;155:463-74.

[89] Paschalis SA, Lampropoulos AP, Tsioulou O. Experimental and numerical study of the performance of ultra high performance fiber reinforced concrete for the flexural strengthening of full scale reinforced concrete members. Construction and Building Materials. 2018;186:351-66.

[90] Murthy AR, Karihaloo B, Rani PV, Priya DS. Fatigue behaviour of damaged RC beams strengthened with ultra high performance fibre reinforced concrete. International Journal of Fatigue. 2018;116:659-68.

[91] Al-Osta M, Isa M, Baluch M, Rahman M. Flexural behavior of reinforced concrete beams strengthened with ultra-high performance fiber reinforced concrete. Construction and Building Materials. 2017;134:279-96.

[92] El-Tawil S, Severino E, Fonseca P. Vehicle collision with bridge piers. Journal of Bridge Engineering. 2005;10:345-53.

[93] Thilakarathna HMI, Thambiratnam D, Dhanasekar M, Perera N. Numerical simulation of axially loaded concrete columns under transverse impact and vulnerability assessment. International Journal of Impact Engineering. 2010;37:1100-12.

[94] Kantrales GC, Consolazio GR, Wagner D, Fallaha S. Experimental and analytical study of high-level barge deformation for barge–bridge collision design. Journal of Bridge Engineering. 2015;21:04015039.

[95] Sha Y, Hao H. Nonlinear finite element analysis of barge collision with a single bridge pier. Engineering Structures. 2012;41:63-76.

[96] Lu Y, Zhang L. Analysis of failure of a bridge foundation under rock impact. Acta Geotechnica. 2012;7:57-68.

[97] Saatci S, Vecchio FJ. Effects of shear mechanisms on impact behavior of reinforced concrete beams. American Concrete Institute; 2009.

[98] Wang R, Han L-H, Zhao X-L, Rasmussen KJ. Experimental behavior of concrete filled double steel tubular (CFDST) members under low velocity drop weight impact. Thin-Walled Structures. 2015;97:279-95.

[99] Yang Y-F, Zhang Z-C, Fu F. Experimental and numerical study on square RACFST members under lateral impact loading. Journal of Constructional Steel Research. 2015;111:43-56.

[100]AASHTO LRFD. Bridge design specifications. American Association of State Highway and Transportation Officials, Washington, DC. 2012.

[101] Shi Y, Hao H, Li Z-X. Numerical derivation of pressure–impulse diagrams for prediction of RC column damage to blast loads. International Journal of Impact Engineering. 2008;35:1213-27.

[102] Li J, Wu C, Hao H, Liu Z. Post-blast capacity of ultra-high performance concrete columns. Engineering Structures. 2017;134:289-302.

[103] Li J, Wu C. Damage evaluation of ultra-high performance concrete columns after blast loads. International Journal of Protective Structures. 2018;9:44-64.

[104] ASMT C469, Standard test method for static modulus of elasticity and Poisson's ratio of concrete in compression. Annual Book of ASTM Standards. 2002;4.

[105] ASTM C78. Standard test method for flexural strength of concrete (using simple beam with third-point loading). American Society for Testing and Materials. 2010. p. 19428-2959.

[106] Wu K-C, Li B, Tsai K-C. Residual axial compression capacity of localized blast-damaged RC columns. International Journal of Impact Engineering. 2011;38:29-40.

[107] Zhang R, Zhi X-d, Fan F. Plastic behavior of circular steel tubes subjected to low-velocity transverse impact. International Journal of Impact Engineering. 2018;114:1-19.

[108] Fan W, Yuan W. Numerical simulation and analytical modeling of pile-supported structures subjected to ship collisions including soil–structure interaction. Ocean Engineering. 2014;91:11-27.

[109] Wang W, Morgenthal G. Dynamic analyses of square RC pier column subjected to barge impact using efficient models. Engineering Structures. 2017;151:20-32.

[110] Wang W, Morgenthal G. Reliability analyses of RC bridge piers subjected to barge impact using efficient models. Engineering Structures. 2018;166:485-95.

[111] Wang W, Morgenthal G. Development and assessment of efficient models for barge impact processes based on nonlinear dynamic finite element analyses. Engineering Structures. 2018;175:617-27.

[112] Wang W, Morgenthal G. Parametric studies of pile-supported protective structures subjected to barge impact using simplified models. Marine Structures. 2019;63:138-52.

[113] Murray YD. Users manual for LS-DYNA concrete material model 159. United States. Federal Highway Administration. ; 2007.

[114] Ren G, Wu H, Fang Q, Liu J, Gong Z. Triaxial compressive behavior of UHPCC and applications in the projectile impact analyses. Construction and Building Materials. 2016;113:1-14.

[115] Chen W-F. Plasticity in reinforced concrete: J. Ross Publishing. 2007.

[116] Murray YD, Abu-Odeh AY, Bligh RP. Evaluation of LS-DYNA concrete material model 159. United States. Federal Highway Administration.; 2007.

[117] Guo W, Fan W, Shao X, Shen D, Chen B. Constitutive model of ultra-high-performance fiber-reinforced concrete for low-velocity impact simulations. Composite Structures. 2018;185:307-26.

[118] Williams EM, Graham SS, Reed PA, Rushing TS. Laboratory characterization of Cor-Tuf concrete with and without steel fibers. Engineer Research and Development Centre Vicksburg Ms Geotechnical and Structures Lab; 2009.

[119] JSCE. Recommendations for design and construction of ultra high strength fiber reinforced concrete structures (Draft). JSCE Tokyo, Japan; 2004.

[120] Mao L, Barnett S, Begg D, Schleyer G, Wight G. Numerical simulation of ultra high performance fibre reinforced concrete panel subjected to blast loading. International Journal of Impact Engineering. 2014;64:91-100.

[121] Fujikake K, Senga T, Ueda N, Ohno T, Katagiri M. Nonlinear analysis for reactive powder concrete beams under rapid flexural loadings. Journal of Advanced Concrete Technology. 2006;4:85-97.

[122] Schwer LE, Malvar LJ. Simplified concrete modeling with* MAT_CONCRETE_DAMAGE_REL3. JRI LS-Dyna User Week. 2005:49-60.

[123] Malvar LJ. Review of static and dynamic properties of steel reinforcing bars. Materials Journal. 1998;95:609-16.

[124] MacGregor JG, Wight JK, Teng S, Irawan P. Reinforced concrete: Mechanics and design: Prentice Hall Upper Saddle River, NJ; 1997.

[125] Hosinieh MM, Aoude H, Cook WD, Mitchell D. Behavior of ultra-high performance fiber reinforced concrete columns under pure axial loading. Engineering Structures. 2015;99:388-401.

[126] Brandt AM. Fibre reinforced cement-based (FRC) composites after over 40 years of development in building and civil engineering. Composite Structures. 2008;86:3-9.

[127] Won J-P, Hong B-T, Choi T-J, Lee S-J, Kang J-W. Flexural behaviour of amorphous micro-steel fibre-reinforced cement composites. Composite Structures. 2012;94:1443-9.

[128] Yoo D-Y, Kim J-J, Chun B. Dynamic pullout behavior of half-hooked and twisted steel fibers in ultra-high-performance concrete containing expansive agents. Composites Part B: Engineering. 2019;167:517-32.

[129] Dong W, Li W, Tao Z, Wang K. Piezoresistive properties of cement-based sensors: Review and perspective. Construction and Building Materials. 2019;203:146-63.

[130] Liu J, Wu C, Su Y, Li J, Shao R, Chen G et al. Experimental and numerical studies of ultra-high performance concrete targets against high-velocity projectile impacts. Engineering Structures. 2018;173:166-79.

[131] Krahl PA, Carrazedo R, El Debs MK. Mechanical damage evolution in UHPFRC: experimental and numerical investigation. Engineering Structures. 2018;170:63-77.

[132] Qasrawi Y, Heffernan PJ, Fam A. Dynamic behaviour of concrete filled FRP tubes subjected to impact loading. Engineering Structures. 2015;100:212-25.

[133] Sylaj V, Fam A, Hachborn M, Burak R. Flexural response of double-wythe insulated ultra-high-performance concrete panels with low to moderate composite action. PCI Journal. 2020;65.

[134] Michaud D, Fam A, Dagenais M-A. Development length of sand-coated GFRP bars embedded in Ultra-High performance concrete with very small cover. Construction and Building Materials. 2021;270:121384.

[135] Marković I. High-performance hybrid-fibre concrete: development and utilisation: IOS Press; 2006.

[136] Farhat F, Nicolaides D, Kanellopoulos A, Karihaloo BL. High performance fibre-reinforced cementitious composite (CARDIFRC)–Performance and application to retrofitting. Engineering Fracture Mechanics. 2007;74:151-67.

[137] Fantilli AP, Kwon S, Mihashi H, Nishiwaki T. Synergy assessment in hybrid Ultra-high performance fiber-reinforced concrete (UHP-FRC). Cement and Concrete Composites. 2018;86:19-29.

[138] Amin A, Foster SJ, Muttoni A. Derivation of the σ-w relationship for SFRC from prism bending tests. Structural Concrete. 2015;16:93-105.

[139] Amin A, Foster SJ. Predicting the flexural response of steel fibre reinforced concrete prisms using a sectional model. Cement and Concrete Composites. 2016;67:1-11.

[140] Simo JC, Oliver J, Armero F. An analysis of strong discontinuities induced by strain-softening in rate-independent inelastic solids. Computational Mechanics. 1993;12:277-96.

[141] ASTM C469. Standard test method for static modulus of elasticity and Poisson's ratio of concrete in compression. Amercian Society for Testing and Materials. 2014.

[142] Yu R, Spiesz P, Brouwers H. Static properties and impact resistance of a green Ultra-High Performance Hybrid Fibre Reinforced Concrete (UHPHFRC): experiments and modeling. Construction and Building Materials. 2014;68:158-71.

[143] Graybeal BA. Material property characterization of ultra-high performance concrete. United States. Federal Highway Administration. Office of Infrastructure. 2006.

[144] ASTM C78. Standard test method for flexural strength of concrete (using simple beam with third-point loading). American Society for Testing and Materials. 2010.

[145] RILEM. Determination of the fracture energy of mortar and concrete by means of three-point bend tests on notched beams. Materials and Structures. 1985.

[146] ASTM C1609. Standard Test Method for Flexural Performance of Fiber-Reinforced Concrete (Using Beam with Third-Point Loading). Amercian Society for Testing and Materials. 2012.

[147] Zhang J, Leung CK, Xu S. Evaluation of fracture parameters of concrete from bending test using inverse analysis approach. Materials and Structures. 2010;43:857-74.

[148] Olesen JF. Fictitious crack propagation in fiber-reinforced concrete beams. Journal of Engineering Mechanics. 2001;127:272-80.

[149] Soetens T, Matthys S. Different methods to model the post-cracking behaviour of hooked-end steel fibre reinforced concrete. Construction and Building Materials. 2014;73:458-71.

[150] Almusallam T, Ibrahim S, Al-Salloum Y, Abadel A, Abbas H. Analytical and experimental investigations on the fracture behavior of hybrid fiber reinforced concrete. Cement and Concrete Composites. 2016;74:201-17.

[151] JSCE. Recommendations for design and construction of ultra high strength fiber reinforced concrete structures. JSCE Tokyo (Japan); 2004.

[152] Tada H, Paris P, Irwin G. The analysis of cracks handbook. New York: ASME Press. 2000;2:1.

[153] Wu Z, Shi C, He W, Wang D. Static and dynamic compressive properties of ultra-high performance concrete (UHPC) with hybrid steel fiber reinforcements. Cement and Concrete Composites. 2017;79:148-57.

[154] Wu Z, Shi C, He W, Wu L. Effects of steel fiber content and shape on mechanical properties of ultra high performance concrete. Construction and Building Materials. 2016;103:8-14.

[155] Grünewald S. Performance-based design of self-compacting fibre reinforced concrete. Delft University Press. 2004.

[156] Wei J, Li J, Wu C. Behaviour of hollow-core and steel wire mesh reinforced ultra-high performance concrete columns under lateral impact loading. International Journal of Impact Engineering. 2020;146:103726.

[157] Pham TM, Hao H. Axial impact resistance of FRP-confined concrete. Journal of Composites for Construction. 2017;21:04016088.

[158] Pham TM, Hao Y, Hao H. Sensitivity of impact behaviour of RC beams to contact stiffness. International Journal of Impact Engineering. 2018;112:155-64.

[159] Pham TM, Chen W, Hao H. Review on Impact Response of Reinforced Concrete Beams: Contemporary Understanding and Unsolved Problems. Advances in Structural Engineering. 2021:(Under review).

[160] Mangat P. Tensile strength of steel fiber reinforced concrete. Cement and Concrete Research. 1976;6:245-52.

[161] Shah SP, Rangan BV. Fiber reinforced concrete properties. Journal Proceedings. 1971. p. 126-37.

[162] Shishegaran A, Khalili MR, Karami B, Rabczuk T, Shishegaran A. Computational predictions for estimating the maximum deflection of reinforced concrete panels subjected to the blast load. International Journal of Impact Engineering. 2020;139:103527.

[163] Meng W. Design and performance of cost-effective ultra-high performance concrete for prefabricated elements. Civil Engineering Commons. 2017.

[164] ASTM C469. Standard test method for static modulus of elasticity and Poisson's ratio of concrete in compression. Annual Book of ASTM Standards. 2002;4:469.

[165] ASTM C78. Standard test method for flexural strength of concrete (using simple beam with third-point loading). American Society for Testing and Materials2010. p. 19428-2959.

[166] Wei J, Li J, Wu C. An experimental and numerical study of reinforced conventional concrete and ultra-high performance concrete columns under lateral impact loads. Engineering Structures. 2019;201:109822.

[167] Aoude H. Structural behaviour of steel fibre reinforced concrete members. ProQuest Dissertations Publishing. 2009.

[168] Cotsovos D, Stathopoulos N, Zeris C. Behavior of RC beams subjected to high rates of concentrated loading. Journal of structural engineering. 2008;134:1839-51.

[169] Cotsovos DM. A simplified approach for assessing the load-carrying capacity of reinforced concrete beams under concentrated load applied at high rates. International Journal of Impact Engineering. 2010;37:907-17.

[170] Pham TM, Hao H. Plastic hinges and inertia forces in RC beams under impact loads. International Journal of Impact Engineering. 2017;103:1-11.

[171] Voo YL, Foster SJ. Variable engagement model for the design of fibre reinforced concrete structures. Engineering Conferences International. 2003.

[172] Voo YL, Foster SJ, Gilbert RI. Shear strength of fiber reinforced reactive powder concrete prestressed girders without stirrups. Journal of Advanced Concrete Technology. 2006;4:123-32.

[173] Voo YL, Poon WK, Foster SJ. Shear strength of steel fiber-reinforced ultrahigh-performance concrete beams without stirrups. Journal of Structural Engineering. 2010;136:1393-400.

[174] Fan W, Liu B, Consolazio GR. Residual capacity of axially loaded circular RC columns after lateral low-velocity impact. Journal of Structural Engineering. 2019;145:04019039.

[175] Manual LS-DYNA Keyword, Volume I. Version 971. Livermore Software Technology Corporation. 2007;7374:354.

[176] AS1012.2. Methods of testing concrete. Standards Australia. 2014.

[177] ASTM C469. Standard Test Method for Static Modulus of Elasticity and Poisson's Ratio of Concrete in Compression. Annual Book of ASTM standards. 2002;4.

[178] ASTM C78. Standard Test Method for Flexural Strength of Concrete (Using Simple Beam with Third-Points Loading. 2015.

[179] ASTM C882. Standard Test Method for tensile properties of thin plastic sheeting. ASTM International, West Conshohocken, Pennsylvania, USA. 2002.

[180] Harris DK, Munoz MAC, Gheitasi A, Ahlborn TM, Rush SV. The challenges related to interface bond characterization of ultra-high-performance concrete with implications for bridge rehabilitation practices. Advances in Civil Engineering Materials. 2015;4:75-101.

[181] Valikhani A, Jahromi AJ, Mantawy IM, Azizinamini A. Numerical modelling of concrete-to-UHPC bond strength. Materials. 2020;13:1379.

[182] ASTM C546. Guide to materials selection for concrete repair. American Concrete Institute; 2004.

[183] ASTM C496. Standard test method for splitting tensile strength of cylindrical concrete specimens. 2004;4:5.

[184] Sprinkel MM, Ozyildirim C. Evaluation of high performance concrete overlays placed on Route 60 over Lynnhaven Inlet in Virginia. Virginia Transportation Research Council; 2000.

[185] Wu Z, Zhang P, Fan L, Liu Q. Debris characteristics and scattering pattern analysis of reinforced concrete slabs subjected to internal blast loads–a numerical study. International Journal of Impact Engineering. 2019;131:1-16.

[186] Pham TM, Hao H. Influence of global stiffness and equivalent model on prediction of impact response of RC beams. International Journal of Impact Engineering. 2018;113:88-97.

[187] Xu S, Wu P, Wu C. Calibration of KCC concrete model for UHPC against low-velocity impact. International Journal of Impact Engineering. 2020;144:103648.

[188] Wang Y, Lu J, Zhai X, Xue B, Zhi X. Response of energy absorbing connector with polyurethane foam and multiple pleated plates under impact loading. International Journal of Impact Engineering. 2019;133:103356.

[189] Shi Y, Li Z-X, Hao H. Bond slip modelling and its effect on numerical analysis of blast-induced responses of RC columns. Structural Engineering and Mechanics. 2009;32:251-67.

[190] AS 3600. Concrete Structures. Standards Australia Limited Sydney, NSW. 2018.